2008-07-09

Analog Feedback Control of an Active Sound Transmission Control Module

Jason Derek Sagers
Brigham Young University - Provo

ANALOG FEEDBACK CONTROL OF AN ACTIVE SOUND TRANSMISSION CONTROL MODULE

by

Jason D. Sagers

A thesis submitted to the faculty of

Brigham Young University

in partial fulfillment of the requirements for the degree of

Master of Science

Department of Mechanical Engineering

Brigham Young University

August 2008

BRIGHAM YOUNG UNIVERSITY

GRADUATE COMMITTEE APPROVAL

of a thesis submitted by

Jason D. Sagers

This thesis has been read by each member of the following graduate committee and by majority vote has been found to be satisfactory.

Date	Jonathan D. Blotter, Chair
Date	Timothy W. Leishman
Date	Mark B. Colton

BRIGHAM YOUNG UNIVERSITY

As chair of the candidate's graduate committee, I have read the thesis of Jason D. Sagers in its final form and have found that (1) its format, citations, and bibliographical style are consistent and acceptable and fulfill university and department style requirements; (2) its illustrative materials including figures, tables, and charts are in place; and (3) the final manuscript is satisfactory to the graduate committee and is ready for submission to the university library.

Date

Jonathan D. Blotter
Chair, Graduate Committee

Accepted for the Department

Matthew R. Jones
Graduate Coordinator

Accepted for the College

Alan R. Parkinson
Dean, Ira A. Fulton College of Engineering and Technology

ABSTRACT

ANALOG FEEDBACK CONTROL OF AN ACTIVE SOUND TRANSMISSION CONTROL MODULE

Jason D. Sagers

Department of Mechanical Engineering

Master of Science

This thesis provides analytical and experimental proof-of-concept for a new feedback-controlled sound transmission control module for use in an active segmented partition (ASP) array. The objective of such a module is to provide high transmission loss down to low audible frequencies while minimizing the overall mass of the module. This objective is accomplished in the new module by using actively controlled panels in conjunction with analog feedback controllers. The new module also overcomes two limitations that exist in current ASP modules: the inability to control broadband random-noise and the lack of bidirectional control through the module. Overcoming these limitations represents an important advancement in the research area of actively controlled partitions and broadens the number of potential applications for ASP arrays.

Analogous circuit models were developed and used to predict the performance of the new ASP module under feedback control. The preliminary design consists of two loudspeaker drivers mounted back-to-back in a duct, with two decoupled analog feedback controllers connected to reduce the vibration of the loudspeaker cones. It was found that the classical analogous circuit model of a loudspeaker proved inadequate for modeling the low- and mid-frequency transmission loss due to resonance effects of the loudspeaker surround. An enhanced model of a loudspeaker was then used to account for this phenomenon and more accurately predict the transmission loss behavior.

An experimental proof-of-concept module was constructed using two 10 cm diameter loudspeaker drivers, two accelerometers, and other off-the-shelf materials. The two analog feedback controllers used in the module were designed and built using measured frequency response function techniques. The passive and active transmission loss of the module was measured using a plane-wave tube. Transmission loss of broadband random-noise in excess of 50 dB was achieved between 100 Hz and 2 kHz. The experimental transmission loss results validated the numerical model and showcased the transmission loss performance of the new module design.

ACKNOWLEDGMENTS

I would like to thank all those who have supported me during this project. I first recognize Jonathan Blotter for his role as my graduate advisor. His example of friendship, enthusiasm, and kindness was noticed and appreciated. I am also indebted to Timothy Leishman for his technical expertise on this project. We spent many hours together discussing the subtleties of this research. I also thank Mark Colton for his early discussions on feedback control strategies.

I acknowledge those groups who have assisted me financially throughout my graduate experience, including the Department of Mechanical Engineering, the Department of Physics and Astronomy, and the Rocky Mountain Space Grant Consortium. This financial support made it possible for me to focus solely on the research project at hand.

Finally, I would like to thank my sweet wife, Alicia, for her patience, perseverance, and love. She happily supported me in this work despite me spending many late nights and weekends away from home. I recognize that she sacrificed many things so that I could successfully complete this project.

TABLE OF CONTENTS

LIST OF TABLES

LIST OF FIGURES

1 INTRODUCTION

This chapter provides an introduction to the control of sound through partitions and describes several applications for active partitions. It also states the research objectives, introduces each of the chapters, and reviews the research contributions of the thesis.

1.1 PASSIVE PARTITIONS

There has long been interest in the use of partitions (also called panels, walls, barriers, and leaves) to reduce sound transmission into noise sensitive environments [1-3]. The partition serves as a frequency-dependent mechano-acoustic filter, modifying the amplitudes of the incident sound waves as they travel through the partition from the source side to the receiving side. The effectiveness in reducing the acoustic energy of the incident noise as it travels through the partition is often determined by transmission loss (TL) measurements.

Passive partitions have several advantageous qualities. First, they are relatively inexpensive and can be constructed from common building materials such as concrete, cinder-block, stone, brick, wood, and drywall. Second, they can provide reasonable TL at mid to high frequencies (500 Hz to 10 kHz), depending on the materials and construction. Third, the installation of a passive partition is usually simple and its performance is consistent over its lifetime. Passive partitions are a viable solution when

exceptional low-frequency TL is not required and the weight of the partition is not a critical concern.

The primary disadvantage of passive partitions is that the TL at low frequencies is severely degraded due to resonance effects of the partition. A common method to increase the TL of a partition above its resonance frequency is to add mass. As a rule-of-thumb, the TL is increased by 6 dB with every doubling of mass (known as the normal-incidence mass-law [4, pg. 148]). Increasing the mass of the partition is tolerable in some applications such as construction of single-story buildings, ground-level acoustic screens and fences, and small machinery enclosures. However, this solution is not efficient for applications where increased weight cannot be tolerated, such as in aerospace vehicles, rocket payload fairings, submarine hulls, large ceiling structures, high-rise buildings, etc.

Other passive methods such as absorptive foams, mounting brackets, and rubber isolators have been researched and marketed with some success. Such products are currently used in residential and commercial construction for internal sound absorption and vibration isolation. However, as a general result, the improvement in sound isolation produced by these methods still lacks at low frequencies.

1.2 ACTIVE PARTITIONS

Active control strategies have been explored to improve the otherwise poor TL of passive partitions at low frequencies. An active partition involves some means of sensing the excitation, vibration, and radiation of the partition as well as some means of actuating, or forcing, the partition to move in a desirable way. The desired movement is achieved by using an active controller, whose objective is to reduce the radiated sound on

the receiving side of the partition. Several different sensing, control, and actuation schemes have been proposed to achieve this objective, all with varying levels of success.

One potential advantage of active control is increased low-frequency TL through a lightweight partition. This could be realized by using lightweight structures in conjunction with lightweight actuators. The weight of the structures, sensors, actuators, and other electrical components would be included in the overall weight of the partition, but in principle, the overall weight of the active partition should be much less than that of a passive partition with the same low-frequency TL. The improved low-frequency TL of the active partition comes at the expense of electrical power instead of mass.

Two of the current challenges with active partitions include their relatively high cost and relatively small increase in the TL achieved to date by most researchers. Although active partitions are not currently available on the market, the design and cost of future products can be inferred from the literature. The up-front cost of an active partition includes materials, sensors, actuators, and active controllers (digital or analog). An active partition also requires electrical power, and this cost is incurred throughout the life of the partition. With some active partitions, these additional costs can seem excessive when the increase in the TL is only a few dB over narrow frequency bands. However, in some situations, high-performance active partitions would justify the cost.

1.2.1 APPLICATIONS FOR ACTIVE PARTITIONS

The primary applications for active partitions are found in situations where low-frequency sound isolation is required from a lightweight partition. One such application (which initially spurred the research field of active partitions) is reducing the noise inside

aircraft cabins [5]. Much of the noise that exists in aircraft cabins is generated by external, low-frequency sources (i.e., engines, flow-induced noise, etc.) and is transmitted through the walls and floor of the passenger compartment. A lightweight trim panel with superb sound isolation performance could greatly increase passenger comfort. However, the weight of the panel is crucial since it directly affects the fuel economy and flight performance of the aircraft.

A similar aerospace application is found in rocket payload fairings. Sensitive payloads can be damaged by the extremely high acoustic sound field which impinges upon the fairing during launch [6]. Since much of the acoustic energy in a rocket launch is found in low-frequency bands, an effective lightweight partition would find widespread use in protecting these fragile multi-million dollar payloads from damage caused by high-amplitude acoustic pressure.

Other vehicles such as trains, subways, buses, boats, cars, tractors, bulldozers, and other earth-moving equipment could also benefit from active partition technology. In each case, the primary application would be to quiet passenger compartments without degrading the fuel economy of the vehicle. However, secondary applications might also exist. Some military vehicles may be able to use active partitions for stealth applications. For example, an active partition could be implemented between the engine room and the hull of a submarine ship to reduce detection of the acoustic signature of the vessel.

Numerous architectural applications exist for effective lightweight partitions. One such application is for sound-sensitive buildings such as research laboratories, recording studios, hospitals, and libraries located in noisy environments. For example, the low-frequency sound that is generated when aircraft take off and land is readily

transmitted through the roofs of these buildings. Adding mass to a roof is costly because of the substantial infrastructure required to support it. Lightweight active partitions could be introduced as part of the structure of these buildings and would provide the required sound isolation. Noise from other sources such as construction sites, manufacturing plants, transportation noise, and public gatherings could also be attenuated.

A similar architectural application would exist with high-rise buildings where weight penalties increase with each story. High-amplitude acoustic noise can be trapped between high-rise buildings and propagate to the upper floors. Lightweight active partitions could be introduced as either interior or exterior boundaries and provide increased sound isolation without substantial weight penalties.

1.2.2 CLASSIFICATION OF ACTIVE CONTROL APPROACHES

Most of the active control approaches that have been utilized to improve the TL of partitions at low frequencies fall under two main classifications: active structural acoustic control (ASAC) and active segmented partitions (ASPs). This section provides a brief description of each classification. The past and current research for ASAC and ASP approaches will be discussed further in Chapter 2 of this thesis.

The ASAC classification includes active control approaches where a continuous panel is actuated in such a way as to reduce the acoustic radiation into the receiving space. It can be implemented by locating several actuators over the continuous panel and by locating the sensors either on the panel or in the receiving space. A control algorithm is then used which alters the radiating mode shapes of the panel and the partition becomes a less effective acoustic radiator. The challenges with the ASAC approaches

include the typical necessity for several fully-coupled controllers, the spatial control spillover that results when using a continuous transmitting panel, and the minimal attenuation that has been achieved to date in narrow frequency bands.

An alternative classification, called active segmented partitions (ASPs), includes active control approaches where a partition is subdivided into an array of small modules that are mechanically segmented and in some cases acoustically segmented. The segmentation simplifies the control scheme by allowing a long-wavelength (i.e., uniform pressure) assumption to exist in the exposed module surfaces and cavities. Consequently, fewer and less sophisticated sensors, actuators, and controllers can be used. The result can be a more effective partition at a lower cost. The segmentation also allows the researcher to focus on the design of an individual ASP module before progressing to an entire array. Although the construction of an ASP array contains a few design challenges of its own, the physical configuration and control strategy for the module can be investigated on a smaller scale with reasonable assurance that the module will still be effective when used in the array.

In some cases, ASP approaches have produced higher TL than ASAC approaches. Although high TL has been achieved at low frequencies, the limitations of current ASP modules are the inability to control broadband random-noise and bidirectional transmission through the module.

1.3 THESIS OBJECTIVES

The primary objective of this research is to design a new ASP module that will produce high bidirectional TL of either tonal or random-noise at low frequencies through

active control. Above the active control bandwidth, the module will also take advantage of the high TL that is inherently achieved by well-designed passive partitions at mid to high frequencies. Through the use of effective decoupled analog feedback controllers, the new module will overcome the previously mentioned limitations of current ASP modules. A second objective of this research is to produce analytical models that accurately predict the TL through the module. In order for the TL predicted by the analytical models to agree with experimental TL measurements, a third objective is required. An experimental parameter extraction routine must be developed for an enhanced loudspeaker model. A final objective is to construct a proof-of-concept ASP module, measure its TL performance, and compare it to theoretical predictions.

In order to provide a glimpse of where this thesis fits into the broader research picture, an overview of the research areas for passive and active partitions is shown in Figure 1-1. The thesis objectives are also shown.

The thesis objectives will be accomplished by following the systematic research approach shown in Figure 1-2. This approach involves reviewing the past research in the area, hypothesizing a new control strategy, creating analytic models to predict the TL performance of an actively controlled module, and validating both the control strategy and the analytic models by testing proof-of-concept hardware. This approach will likely be an iterative process. Improvements in the control strategy can be made as new information is gathered during the modeling and validation stages.

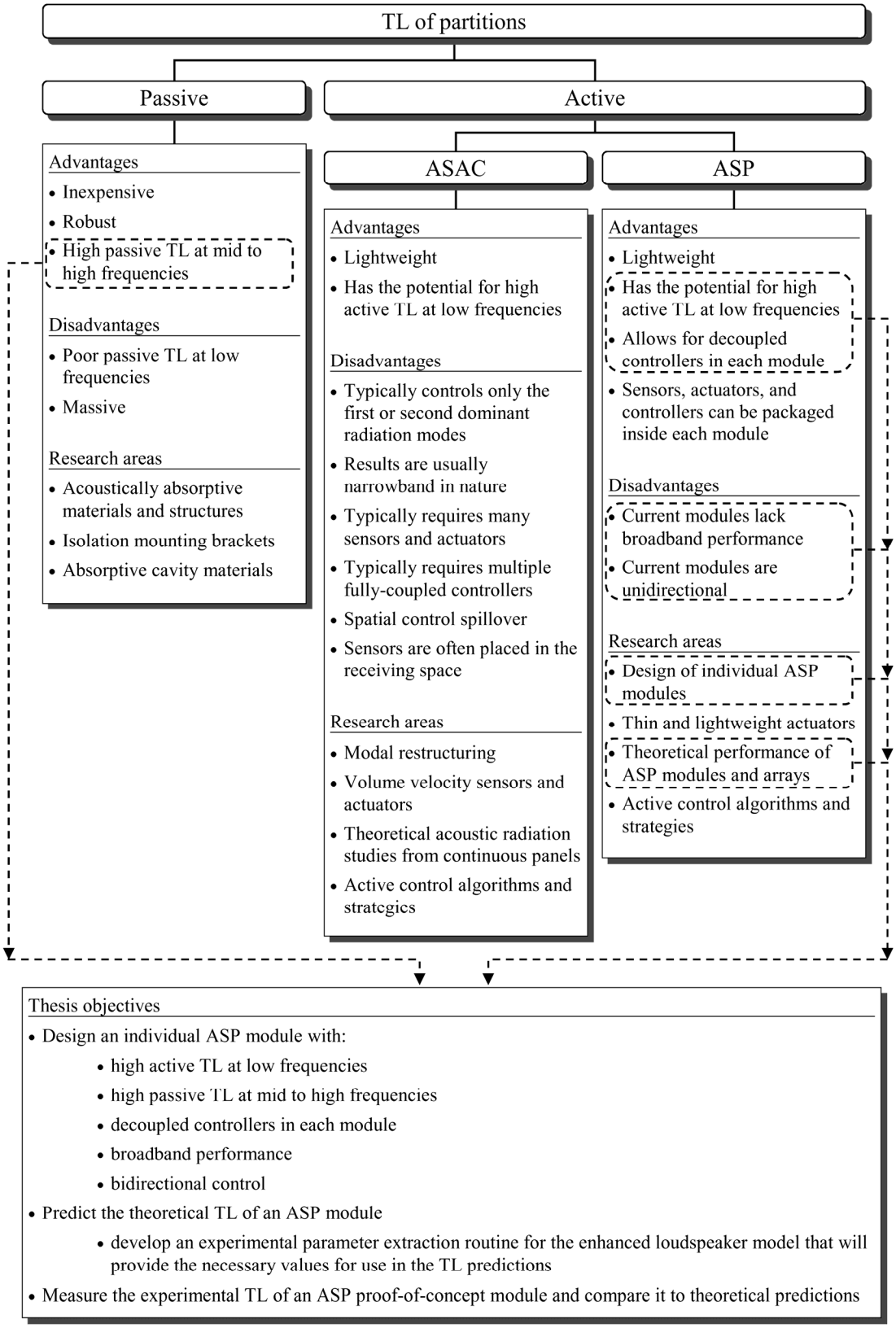

Figure 1-1. Overview of research areas and thesis objectives.

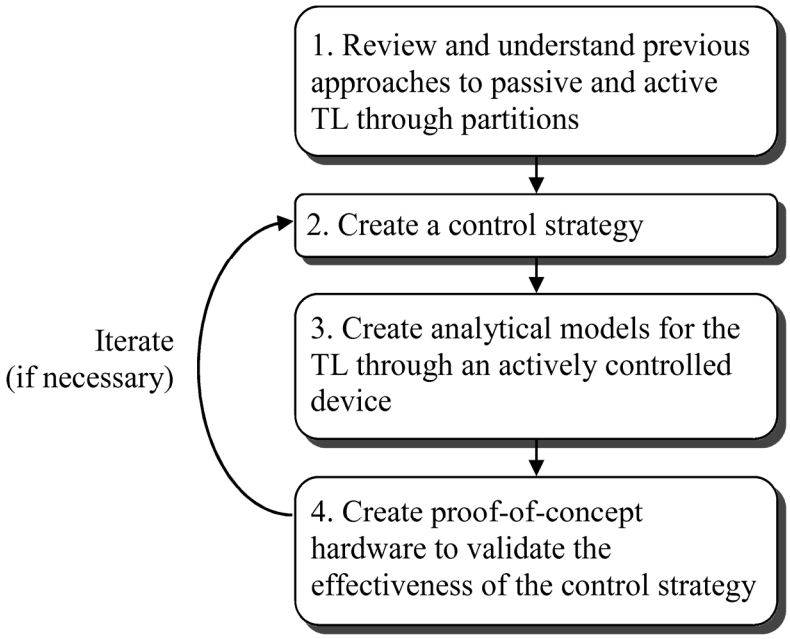

Figure 1-2. Systematic approach for accomplishing thesis objectives.

1.4 THESIS CONTRIBUTIONS

This thesis provides several new contributions to the research area of active partitions. The primary contribution is contained in the development of a new proof-of-concept ASP module with exceptional TL at low frequencies. This module possesses a unique design and demonstrates capabilities that have not been achieved by any other ASP module:

- The module uses panel control with two decoupled analog feedback controllers.
- The module demonstrates bidirectional TL performance.
- The module demonstrates broadband random-noise TL performance.

A second contribution of this thesis is contained in the development of the analytical models for the new ASP module. A complete set of modeling equations was derived for four variations of the same module design. These four models helped to uncover several important characteristics of the ASP module and controllers, including the effect of the acoustic coupling strength between panels, the effect of the flanking path through the surround, and the slight degradation in the TL near the instability points of the feedback controller. These models also allow future designers to predict the TL performance of an ASP module with similar construction but different model parameters and different controllers. The four analytical models are:

- Feedback control of a single-panel partition using the classical loudspeaker model.
- Feedback control of a single-panel partition using the enhanced loudspeaker model.
- Feedback control of a double-panel partition using the classical loudspeaker model.
- Feedback control of a double-panel partition using the enhanced loudspeaker model.

A final contribution of this thesis is contained in the laser-based parameter extraction routine that was developed to determine the model parameters for use in an enhanced model of a loudspeaker. This is the first parameter extraction routine for the enhanced loudspeaker model that has been published in the literature. This contribution will permit researchers to more accurately measure and model loudspeaker surround resonances and to predict the effect of this resonance for various applications. It will also

serve as a springboard for other parameter extraction techniques for the enhanced loudspeaker model.

1.5 THESIS OUTLINE

The remainder of this thesis is divided into specific topics related to the modeling and performance of the new proof-of-concept ASP module. Three of the chapters (4, 5, and 6) represent work that will be submitted for journal publication.

Chapter 2 describes the mechanisms of sound transmission through single- and double-panel partitions. This chapter also introduces the necessary technical foundation for quantifying the sound isolation performance of partitions. The last section of Chapter 2 is a literature review which outlines the related ASAC and ASP research.

Chapter 3 discusses preliminary experimental work done on existing ASP hardware. The existing hardware represented the most effective ASP module configuration to date. Although high TL through the module was achieved using a digital feed-forward controller, the two primary drawbacks to this configuration were the lack of broadband random-noise control and the unidirectional TL performance. To address the limitation of broadband control, the feasibility of using an analog feedback controller in conjunction with the existing hardware was explored. The purpose of this work was to combine the positive qualities of the existing hardware with the potentially advantageous qualities of an analog feedback controller. The associated difficulties with the existing hardware while using an analog feedback controller were identified. The results of the work presented in Chapter 3 indicated that a new module design was needed.

The physical components of many ASP modules resemble those found in a moving-coil loudspeaker. In order to create an accurate analytical model of a new ASP module, the classical model of a loudspeaker had to be discarded in favor of an enhanced loudspeaker model. The enhanced model introduced an additional degree of freedom so that the surround of the loudspeaker could vibrate even if the cone was actively controlled such that it could not vibrate. However, the major drawback to the enhanced model was the lack of a measurement method that could be used to extract all of the required parameter values. Chapter 4 introduces a novel parameter extraction routine that was required for the enhanced model. The accuracy of the method is verified in the chapter by predicting the on-axis acoustic pressure for several loudspeakers and comparing the predictions to measured data. The method is also verified indirectly in Chapters 5 and 6 by using the enhanced model and the enhanced parameters to accurately predict the TL through the new ASP module.

A new design for an ASP module is proposed in Chapter 5. The basic design consists of two loudspeaker drivers mounted back-to-back in a duct with two decoupled analog feedback controllers designed to reduce the vibration of each "panel" (i.e., each loudspeaker cone). The analogous circuit representations which model the new ASP module are presented. Four variations of the same model are presented, with each model containing various degrees of complexity. The simpler models use the classical model of a loudspeaker and illustrate fundamental behaviors of the ASP module. The more complex models use the enhanced model of a loudspeaker and are required to accurately model the TL. The TL predictions of the complex models are compared with those of the simple models and the effect of the surround resonance is illustrated.

Chapter 6 discusses the design, construction, and measurement of a new proof-of-concept ASP module. Design choices for the physical construction of the module are explained. The TL measurement apparatus is introduced and qualified. The measured TL is compared to that predicted by the analogous circuit model in Chapter 5.

Conclusions about the performance of the new ASP module (i.e., the active control scheme and the module hardware) are presented in Chapter 7. Future research work in this area is also discussed.

2 BACKGROUND AND LITERATURE REVIEW

This chapter gives background information that is helpful in understanding sound transmission through partitions. Previous research in the area of actively controlled partitions is also outlined.

2.1 NOMENCLATURE

c	Speed of sound in the fluid medium
d	Separation distance between two panels in a double-panel partition
k	Acoustic wavenumber, = ω/c
l	Arbitrary length
m_1	Mass per unit area of panel 1 in a double-panel partition
m_2	Mass per unit area of panel 2 in a double-panel partition
$\hat{p}_{flanking}$	Complex acoustic pressure from a flanking path
$\hat{p}_i$	Complex acoustic pressure incident upon a partition
$\hat{p}_t$	Complex acoustic pressure transmitted through a partition
p_{rms}	Root-mean-square pressure amplitude
$\hat{u}_P$	Complex surface velocity of a partition
Π	Acoustic sound power
$<\Pi_i>_t$	Time-averaged acoustic sound power incident upon a partition
$<\Pi_t>_t$	Time-averaged acoustic sound power transmitted through a partition

λ_k Stiffness ratio, equals mechanical stiffness divided by air gap stiffness

ρ_o Ambient density of the fluid medium

2.2 BACKGROUND

This section provides background material relative to the transmission of sound through single- and double-panel partitions. It also discusses four common metrics used to quantify the effectiveness of partitions as acoustic barriers.

2.2.1 MECHANISM OF SOUND TRANSMISSION THROUGH SINGLE-PANEL PARTITIONS

Both single- and double-panel partitions have been used to acoustically isolate a source space from a receiving space. A single-panel partition is one in which there is only a single continuous layer of material along the thickness of the partition. The mechanism of sound transmission through a single-panel partition is a simple but important phenomenon to understand. Suppose a partition separates a source space from a receiving space as shown in Figure 2-1. An acoustic disturbance in the source space creates a complex pressure amplitude $\hat{p}_i$ that is incident upon the partition. When the pressure impinges upon the partition, it imparts a force upon it causing it to vibrate with some complex velocity $\hat{u}_P$. In turn, the vibrating partition compresses the fluid that is adjacent to it in the receiving space and radiates sound with pressure $\hat{p}_t$. It is in this way that sound is transmitted from the source space to the receiving space through the partition.

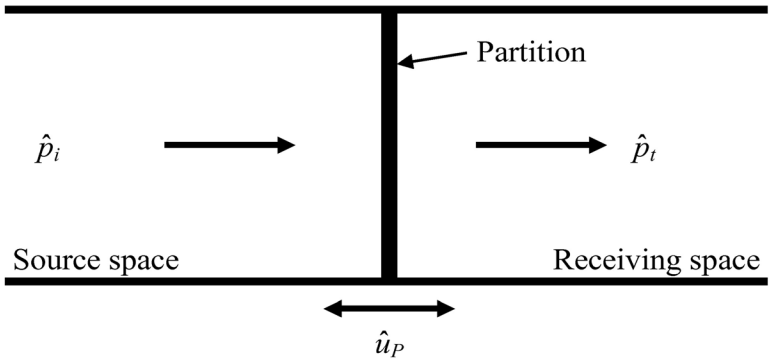

Figure 2-1. A partition separating a source space from a receiving space.

In general, passive single-panel partitions can provide reasonable TL (20-30 dB) over mid- to high-frequency ranges (500 Hz to 10 kHz). However, it should be noted that the TL is degraded at frequencies near the structural resonance of the partition. The mechanical properties (mass, stiffness, and damping) of the partition affect the sound transmission in the vicinity of the structural resonance. The partition is said to be stiffness-controlled below the resonance frequency and mass-controlled above the resonance frequency. In the low-frequency mass-controlled region, a common passive method used to increase the TL is simply to add mass to the panel. The normal-incidence mass law indicates that a 6 dB increase in the TL will be realized for each doubling of the mass [4, pg. 148].

2.2.2 MECHANISM OF SOUND TRANSMISSION THROUGH DOUBLE-PANEL PARTITIONS

A double-panel partition is one in which two layers of material are separated by a cavity. There are two mechanisms by which sound is transmitted through a double-panel partition [7, sec. 11.4.5]. The first mechanism is the transmission of vibrational energy directly through the mechanical linkages of the structure (e.g., in one standard wall

construction, energy would transmit from one drywall panel, through the studs, and into the other drywall panel). The direct mechanical path will degrade the TL at frequencies near the structural resonance of the composite structure.

The second mechanism of sound transmission is the similar to the single-panel partition. However, in the case of a double-panel partition, the vibro-acoustic path is longer because it includes passage through the air cavity as well as a second panel before it reaches the receiving space. The extended vibro-acoustic path gives rise to a structural-acoustic resonance. The air in the cavity acts like a spring at frequencies where the wavelength of sound is much larger than the depth of the cavity. This spring effect couples the two panels together and produces what is known as the mass-air-mass resonance frequency f_o given by Fahy [4, sec. 4.7]:

$$f_o = \frac{1}{2\pi}\left[\left(\frac{\rho_0 c^2}{d}\right)\left(\frac{m_1 + m_2}{m_1 m_2}\right)\right]^{1/2}, \qquad \textbf{(2.1)}$$

where m_1 and m_2 are the mass per unit area of each panel, and d is the separation distance between the panels. As with the structural resonance of the single-panel partition, the consequence of the mass-air-mass resonance is that sound energy is transmitted through the partition with little or no attenuation in the vicinity of the resonance. At frequencies below the mass-air-mass resonance, the double-panel partition behaves like a single-panel partition (with a total mass equal to the sum of the individual panel masses). In this mass-controlled region, the effect of doubling the total mass of a double-panel partition produces results that are similar to the normal-incidence mass law.

2.2.3 TRANSMISSION LOSS EXAMPLE FOR SINGLE- AND DOUBLE-PANEL PARTITIONS

As an example, consider the measured TLs for a single- and a double-panel partition (constructed from 16 mm thick drywall panels and standard wooden studs, no absorptive material in the cavity) shown in Figure 2-2.

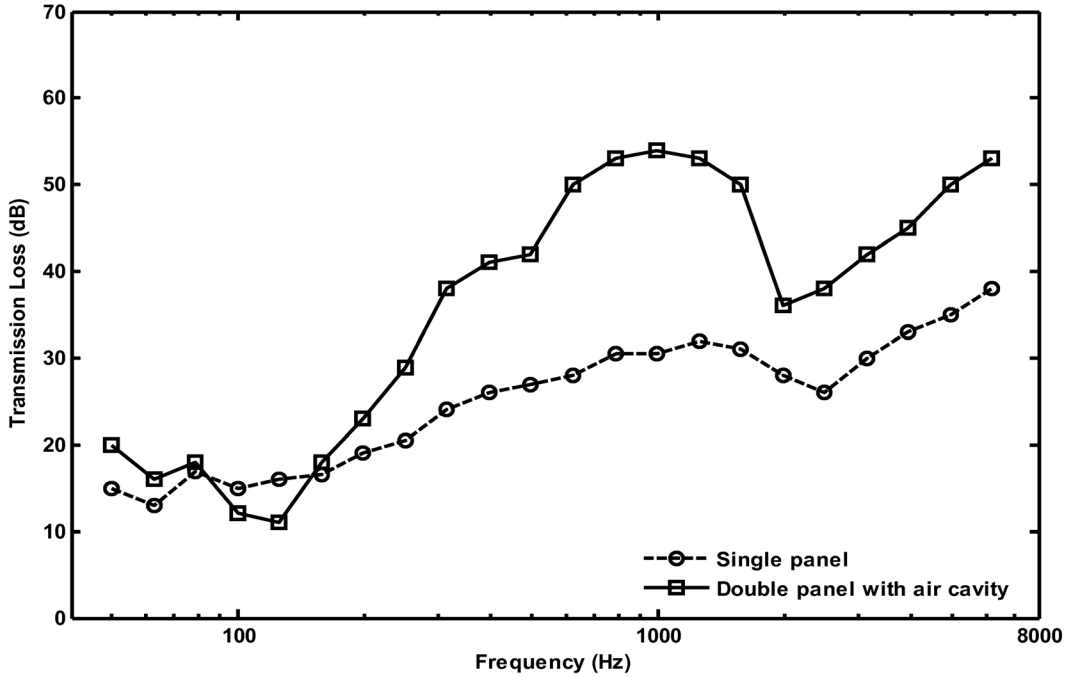

Figure 2-2. Example of the sound TL through passive single- and double-panel partitions. (Adapted from Leishman [8, pg. 5]).

The structural resonance of the single-panel partition occurs near 100 Hz. The detrimental effect of this resonance on the TL is observed at nearby frequencies. The single-panel partition performs reasonably well at mid to high frequencies, with the TL of the single-panel partition exceeding 20 dB at all frequencies above 300 Hz. Adding a second panel to the partition further improves the TL performance at mid to high

frequencies but actually reduces the low-frequency TL near 100 Hz. This is due to both the mechanical resonance of the system as well as the mass-air-mass resonance.

For the example shown, the mass of the single-panel partition is estimated at 12 kg/m2 while the mass of the double-panel partition is estimated at 24 kg/m2. It is apparent that any appreciable change in the TL using the mass law represents a significant increase in the overall mass. Such an increase in mass is prohibitive in many applications.

2.2.4 METRICS FOR THE PERFORMANCE OF ACOUSTIC BARRIERS

A partition possesses intrinsic characteristics (such as mass, stiffness, and damping) that dictate how it will vibrate as a function of frequency in the presence of an acoustic disturbance. In this context, the partition can be viewed as a frequency-dependent acoustic filter. When the partition is intended to be an acoustic barrier, its qualitative effectiveness is described by how much the disturbing sound is quieted as it passes through the partition. Several different quantitative metrics are used in the literature; four of the most common are attenuation in sound pressure, insertion loss, TL, and sound transmission class.

2.2.4.1 ATTENUATION IN SOUND PRESSURE

Attenuation in sound pressure is defined as the difference between two root-mean-square (rms) sound pressure measurements taken at fixed position(s) in the receiving space. The first measurement is made without the partition and the second

measurement is made with the partition in place. The attenuation provided by the partition may then calculated by

$$Attenuation\,(\mathrm{dB}) = 20\log_{10}\left[\frac{p_{\mathrm{rms,\ without\ partition}}}{p_{\mathrm{rms,\ with\ partition}}}\right]. \qquad \textbf{(2.2)}$$

This metric only provides a crude measure of the effectiveness of the partition (which can be misleading in many instances, including most active control situations). This is because the pressure in the receiving space is a complicated function of spatial position. It is easily possible to locally attenuate the pressure at some field points in the receiving space while amplifying it at other points.

The attenuation in sound pressure metric is also flawed because it depends strongly on the nature of the source and receiving spaces. For example, suppose an acoustic flanking path were present in the measurement setup as shown in Figure 2-3. The presence of this flanking path can significantly reduce the measured attenuation that the partition can provide. Although this metric is used widely in the literature, it is neither a rigorous nor global measure of the acoustic effectiveness of the partition.

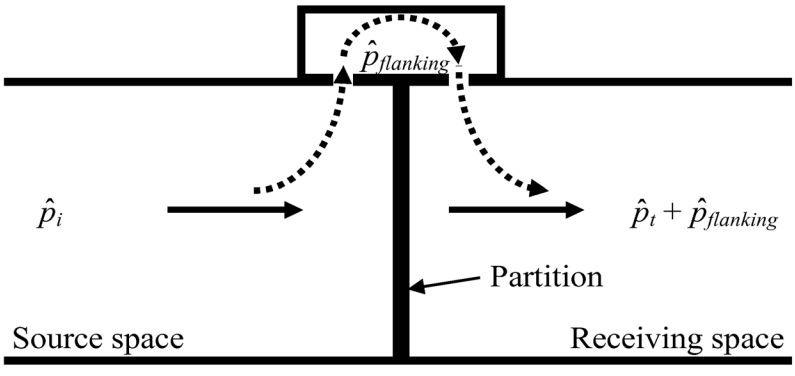

Figure 2-3. An acoustic flanking path between a source and receiving space.

2.2.4.2 INSERTION LOSS

A slightly more accurate metric than attenuation in sound pressure is insertion loss (IL). The IL may be defined as the difference between two time-averaged sound power measurements taken in the receiving space. The first measurement is made without the partition and the second is made after the partition is inserted into the test apparatus. The IL is then calculated by the following equation [9].

$$\mathrm{IL\,(dB)} = 10\log_{10}\left[\frac{\left\langle \Pi_{\text{without partition}} \right\rangle_t}{\left\langle \Pi_{\text{with partition}} \right\rangle_t}\right]. \qquad \textbf{(2.3)}$$

In many cases, this metric is more suitable than attenuation in sound pressure because the sound power is a global measurement which accounts for any change in acoustic energy flow into the receiving space. However, since the IL does not account for changes in the sound power of the source space when the partition is put in place, it is still not an ideal measurement of the performance of the partition. If there is a build-up of sound power in the source space after the partition is inserted, the second IL measurement $\langle \Pi_{\text{with partition}} \rangle_t$ will not account for the increase in sound power incident upon the partition. As a result, the performance of the partition might be misrepresented. It should also be mentioned that the insertion loss measurement is usually a function of frequency.

2.2.4.3 TRANSMISSION LOSS

The TL is the most accurate metric for characterizing the effectiveness of a partition. The TL of the partition is defined in terms of the time-averaged incident sound

power $<\Pi_i>_t$ measured in the source space and the time-averaged transmitted sound power $<\Pi_t>_t$ measured in an anechoic receiving space according to the following equation [8, pg. 141, 10, pg. 279]:

$$\mathrm{TL\ (dB)} = 10\log_{10}\left(\frac{\langle \Pi_i \rangle_t}{\langle \Pi_t \rangle_t}\right). \qquad \textbf{(2.4)}$$

The TL metric is more general than the IL metric because both the incident and transmitted sound powers are measured directly. The TL metric allows for a characterization of the partition that does not depend on the nature of the source space. It should be noted that the TL is also typically measured as a function of frequency.

The problem of acoustic flanking paths can still negatively affect the TL measurement, particularly when trying to measure partitions with very high TLs. Care must be taken to eliminate these paths from the measurement apparatus in order to produce accurate measurements of the TL.

2.2.4.4 SOUND TRANSMISSION CLASS

The sound transmission class (STC) is a common metric used in the architectural community. It is an integer-number classification of how well a partition attenuates airborne sound. The STC rating by itself is not a function of frequency, although it is computed from frequency-dependent TL data. The method for computing the STC given by Kinsler and Frey [11, pg. 380] is repeated here in a condensed form:

- Measure the third-octave band TL between 125 Hz and 4.0 kHz.
- Plot the third-octave band TL data points.
- The STC curve consists of 3 contiguous lines plotted on top of the third-octave band TL data:
    - a line which increases 15 dB from 125 Hz to 400 Hz.
    - a line which increases 5 dB from 400 Hz to 1.25 kHz.
    - a line which increases 0 dB from 1.25 kHz to 4.0 kHz.
- Adjust the STC curve such that the maximum deficiency (deviation of the data below the STC curve) at any one frequency does not exceed 8 dB and the total deficiency at all frequencies does not exceed 32 dB.
- The STC of the partition is then the value of the TL corresponding to the intersection of the STC curve with the 500 Hz ordinate.

An example of an STC rating (after [11, Fig. 13.13.1]) is shown in Figure 2-4. The third-octave band TL data are plotted (o's) and the three lines of the STC curve are shown in this figure. The three lines of the STC plot have already been adjusted to meet the aforementioned deficiency criteria. The STC rating is the level of the TL at the point where a vertical line extended from 500 Hz crosses the STC curve. In this example, the partition has an STC rating of 42 dB.

The STC was created to give a convenient single-number classification for the acoustic effectiveness of a partition. The shortcoming in this rating system is the underlying tolerance for poor TL performance at low frequencies. This is manifest in two ways. First, no TL data below the 125 Hz third-octave band are used to locate the

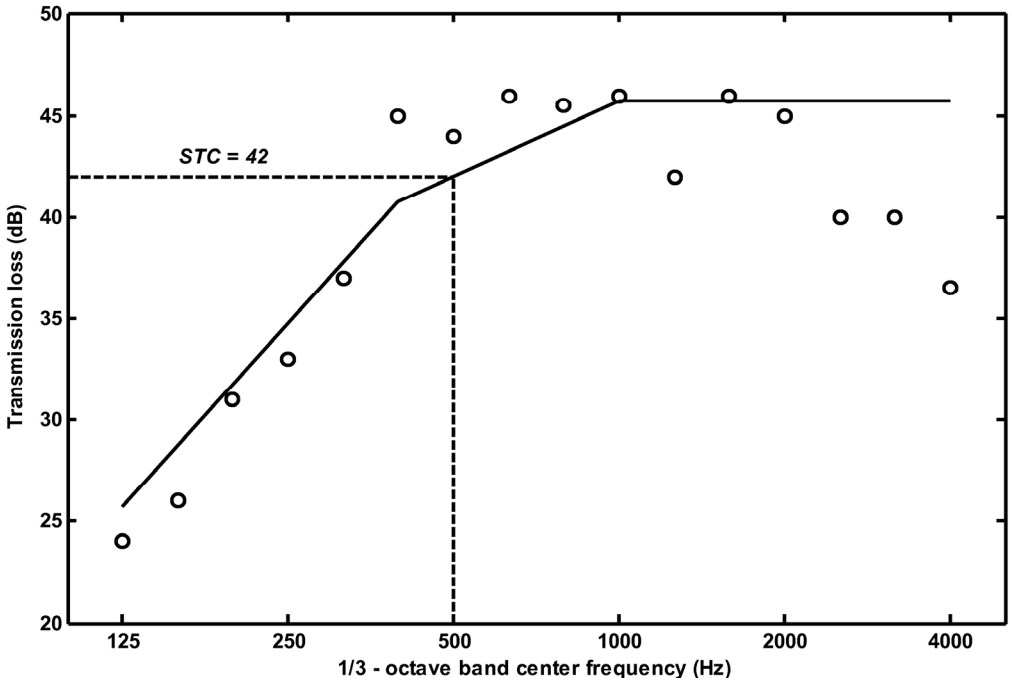

Figure 2-4. Example of the determination of the sound transmission class (STC) (after [11, Fig. 13.13.1]).

STC curve—the low-frequency data below this band are ignored. Second, the first line of the STC curve allows for a generous 15 dB rise in the TL between 125 Hz and 400 Hz. As a result, this metric does not effectively differentiate between a partition with excellent TL at low frequencies and a partition with poor TL at low frequencies. Although widely used in architectural acoustics, the STC rating will not be used as a metric in this research.

2.3 LITERATURE REVIEW

This section gives a review of prior research conducted in the area of sound transmission through active panels. The review provides a sampling of the different control strategies and the subsequent experimental results. Single- and double-panel

partitions are discussed in two separate sections. There is also a third section outlining the major research results with ASPs.

2.3.1 SINGLE-PANEL ACTIVE PARTITIONS

The historic motivation for much of the research in the area of active partitions involves quieting aircraft cabins. Much of the research that was reviewed for this thesis targeted this application and lightweight single-panel partitions were often used. Early researchers coined the term "active structural acoustic control" (ASAC), referring to an approach wherein structure-borne radiation at low to mid frequencies is minimized by directly applying forces to a continuous radiating panel [12]. Stated differently, the approach involves actuating a transmitting panel in such a way as to minimize the acoustic radiation into the receiving space.

One method of ASAC implementation, called modal restructuring, involves placing several sensor and actuator pairs over the surface of the transmitting panel with the purpose of altering the radiating mode shapes. In this way, the panel is forced to become a less efficient acoustic radiator at certain panel resonance frequencies. Such a method was introduced in 1991 by Fuller [13] when he controlled the (1,1), (2,1), and (3,1) modes of a rectangular steel plate with multiple force sources. He reduced the magnitudes of three tones in the receiving space (85, 182, and 354 Hz). The results were reported in terms of attenuated pressure in the directivity patterns measured in the receiving space. The results varied from 35 dB at the 85 Hz mode of the plate to 20 dB at the 354 Hz mode. However, no reductions in the transmitted sound pressure were reported at other frequencies.

Subsequent researchers noted the impracticality of direct-force actuation in relation to the active control of aircraft fuselages. In 1993, Thomas et al. [14] noted that it would require massive inertial shakers with severe weight penalties because conventional force-sources would have nothing to react against. As an alternative, he proposed actuating the trim panels inside the fuselage of an aircraft. This would allow the electromechanical actuator to be placed between the frame of the aircraft and the trim panel. Thomas' method produced an average attenuation of 10 dB (measured at 24 microphone positions in the receiving space) over the narrow frequency band of 81 to 84 Hz. The reductions in sound pressure were admitted by the author to be quite low and limited to a very narrow frequency band. Little attenuation was seen at any other frequency. However, a major contribution of Thomas' work was the idea of composite, or mechanically segmented, partitions. Active segmented partitions will be discussed further in Section 2.3.3.

Theoretical examinations of the structural radiation efficiencies of rectangular plates began to develop in 1993. Elliott and Johnson [15] demonstrated that the lower order radiation modes (the piston mode and the first two rocking modes) dominated the radiated acoustic power at low values of kl. The parameter kl is a product of the acoustic wavenumber k (which represents the phase change in radians per unit length [4, pg. 4]) and the plate length l. Consequently, kl represents the phase change across a plate of arbitrary length l. Elliott and Johnson suggested that the first structural mode of the plate accounted for 99% of the radiated acoustic power up to a kl value of 0.5 and that the first three modes accounted for 99% of the radiated power up to $kl = 2$. If these modes could

be effectively controlled, a 20 dB reduction in global sound power could be achieved up to a prescribed frequency.

Because of the findings of Elliott and Johnson, the ASAC approaches began to shift toward "volume velocity cancellation." Volume velocity refers to the flow rate of the acoustic medium through a specified area *S* in the direction of the surface normal vector [16, pg. 10]. In 1995, Elliott and Johnson suggested that the amplitude of the first radiation mode is approximated by the net volume velocity of the panel at low frequencies [17]. Control schemes began to focus on minimizing the net volume velocity produced by the panel. This presented a much simpler control scheme which required far fewer sensors and actuators. However, the phenomenon of control spillover began to be evident wherein the control actuator excites structural modes that were not originally excited by the primary disturbance source. As a result, the control effort had to be bounded so that it would not increase the radiated sound power of the residual modes. It was proposed that a single sensor and actuator pair could be used without the spillover effect if they were "volume velocity" sensors and actuators (i.e., a spatially distributed sensor and/or actuator).

Subsequent experimental efforts focused on reducing the volume velocity of composite panels. These studies were still among the first to use the idea of segmented partitions. In 1998, Pierre et al. [18] noted that it was impractical to have the error sensors for the control algorithm located in the acoustic space on the receiving-side of the partition. Instead, their research efforts focused on control strategies that only used sensors mounted on the vibrating surface of the composite panel. In this study, an electro-magnetic loudspeaker was used to actuate a panel and accelerometers were used

to estimate the volume velocity. The panel was a composite panel possessing two radiating areas—the rectangular area of the panel and the circular area of the loudspeaker mounted in the panel. The loudspeaker was excited by a signal from a feed-forward controller so that the net displacement of the panel was minimized. A reduction in radiated sound power of 10 dB was achieved in the 200 Hz and 250 Hz third-octave bands when active control was used. Similar results were obtained in the year 2000 by Hirsch et al. [19, 20] inside a cylindrical test environment.

By about the year 2000, many of the variations on physical configurations had been explored, so much of the research effort turned to the design and implementation of better active controllers. The increasing power of digital signal processors (DSPs) caused digital control schemes to flourish. A detailed comparison between rate feedback, linear quadratic Gaussian feedback (LQG), and adaptive feed-forward (xLMS) control was performed on the same structure by Bingham et al. [21]. The differences in the reduced acoustic radiation from one controller to the next were minimal (on the order of 1-4 dB). The more significant contribution of the paper is its discussion of the advantages, disadvantages, challenges, and practical bandwidth limits of each control scheme. A rate feedback controller is simple to implement and good results can be achieved with a low-order controller. However, the performance of this controller had strong dependence on the sensor location and it had the smallest usable bandwidth of the three controller types. The LQG controller had a slightly wider bandwidth than rate feedback, but the design of the controller required an accurate model of the system at all frequencies and was of much higher order. The feed-forward xLMS controller had the ability to track dynamic changes in the system but it also required advanced knowledge of the disturbance signal

and an accurate broadband model of the system. The study did not comment on which was the "best" controller because the performance depended heavily on the architecture and application of the particular system. A similar study was performed by Petitjean [22] in 2002.

As another example, a self-proclaimed "smart panel" was introduced in a series of papers by Gardonio et al. [23-25], wherein 16 sensor and actuator pairs were evenly spaced over the surface of a plate. Each sensor and actuator pair had an independent channel of analog feedback control. Despite having the entire plate swamped with active control potential, only 5 dB attenuation in radiated sound power was achieved in a half dozen third-octave bands.

In general, receiving-side attenuations with single-panel ASAC methods have been small (5-10 dB). Additionally, comparing the performance of one ASAC implementation to another is difficult because the measurement techniques have been inconsistent. Finally, the major drawbacks to the ASAC approach are the large number of fully-coupled controllers, the frequent need for microphones as error sensors in the receiving space, and the spatial control spillover that inevitably results when attempting modal restructuring.

2.3.2 DOUBLE-PANEL ACTIVE PARTITIONS

The development of double-panel active partitions was concurrent with that of single-panel partitions. However, because the physical configurations and control strategies are different, the literature review for double-panel partitions is treated in a separate section.

It was noted in Section 2.2.2 that the low-frequency degradation in the TL of a double-panel partition is caused in part by the mass-air-mass resonance phenomenon wherein the air between the panels acts as a spring. Instead of controlling a plate resonance in the case of a single panel, many of the approaches for controlling the double-panel setup involve actively controlling the cavity resonance effects [26].

In 1995 Sas et al. [27] performed a study wherein the acoustic response inside the cavity of a double-wall structure was actively controlled by a number of internally mounted loudspeakers. The results of the study were reported in terms of the frequency-dependent IL of the device under test. The highest experimental ILs occurred at resonance frequencies of the cavity with a maximum of 40 dB at 105 Hz. However, noise reductions were typically only a few dB at anti-resonances and in the frequency bands between resonances.

Pan and Bao performed a number of analytical and experimental studies on double-panel partitions. The first reported study in 1997 [28] compared a variety of physical configurations that were possible in a double-panel setup: (1) acoustic cavity control, (2) vibrating panel control, and (3) active noise control in the receiving room. They reported that panel control and cavity control produced much better results in terms of the spatially averaged attenuation in sound pressure measured in the receiving space. Further comparison of cavity and panel control led them to conclude that "cavity control is effective in attenuation of broadband noise and panel control is not." Their second published paper in 1998 was an analytical study on the same three physical configurations [29]. This paper gives equations for the control forces that should be used in each configuration. Their third paper, also published in 1998, focused on the effect of

a structural coupling path between the opposing faces of the partition [30]. They concluded that cavity control was still effective at low frequencies despite the presence of a structural transmission path. They also concluded that the added stiffness to the panels caused beneficial modal restructuring at high frequencies. Later, in 2005 and 2006, Li and Cheng [31, 32] revisited this topic with a more complete analysis of the effect of a mechanical link. They concluded that the stiffness of the mechanical link and the stiffness of the air gap were the two parameters that determined the most dominant transmission path. A stiffness ratio λ_k was introduced and was defined as the mechanical stiffness divided by the air gap stiffness. The acoustic coupling path dominated when λ_k was less than 0.1 while the mechanical coupling path dominated when λ_k was greater than 10. Both coupling paths were present in the intermediate region.

Researchers involved with Elliott tried to extend his notion of volume velocity cancellation to the double-panel partition. In 1998, Pan et al. [33] applied this approach experimentally on a pair of small plates separated by a 100 mm air gap. They found that the transmission of sound power through a double-panel partition could be reduced at frequencies lower than 350 Hz and that absorption could be added in the cavity to improve the passive TL at higher frequencies.

Several analytical and experimental papers emerged which studied cavity control methods within a double-panel partition. Researchers continued to assert that "active cavity control with control loudspeakers in the cavity appears to be the best solution for reducing the sound transmission through the double-panel set-up" [34, 35]. This was attributed to the strong (0,0,0) cavity mode and its domination of the radiated acoustic power.

However, it should be noted that most of the experimental implementations of cavity control up to this time used a feed-forward active control scheme. Feed-forward schemes require foreknowledge of the disturbance signal. This convenient reference signal is not realistic in many situations. At ACTIVE 99, Paurobally et al. [36] presented a paper where analog feedback control was used to minimize volume velocity within the cavity of a double panel partition. Active control loudspeakers were mounted inside of the cavity and a microphone in the cavity served as the error sensor. The authors found that the pressure response at the error microphone was not suitable for feedback control of a wide bandwidth due to the gain and phase margin requirements of the controller. As a result, they built two separate controllers to control the major cavity responses at 55 and 171 Hz. With the 55 Hz controller, an average of 10 dB attenuation of pressure was achieved in the receiving room measured at several microphone locations. It should be noted, however, that there was significant control spillover at frequencies outside of the control band. With the 171 Hz controller in place, only increases in the pressure were measured in the receiving room under active control. This study was the first to highlight the difficulty of control spillover that was associated with feedback cavity control.

Carneal and Fuller presented work on double-panel partitions in 1995 and again in 2000, with proposals to use PZT actuators on the radiating panel to change its effective bending stiffness [37, 38] (recall that radiating panel control is the second of three physical configuration strategies identified by Pan and Bao [28]). Their approach was the same as it was for the single-panel case except that the PZT actuators would be used to locally increase the effective stiffness of the plate instead of using direct force actuation. TL improvements near 30 dB were seen over several low-frequency bands that were

approximately 100 Hz wide. It was concluded that the increased stiffness of the plate lowered the modal density inside the cavity and led to a much easier active control problem. As an editorial aside, it should be noted that the panel control approaches proposed by Fuller were generally more successful than cavity control approaches (both in terms of increased TL and control bandwidth). However, studies continued to emerge where the authors concluded that "theoretical and experimental works have shown that cavity control should be preferred to panel control. The increasing amount of experimental work based on cavity control tend to validate this fact" [39, pg. 5].

Recently, thin panel actuators have emerged as a new approach to the control of a double-panel partition. These actuators differ from conventional loudspeaker actuators which operate primarily in piston mode. The thin panel actuators enable a panel to vibrate flexibly as a distributed structure [40-43]. A transparent version of the thin panel actuator has even been manufactured for window applications [44]. However, the current crippling drawback to these actuators is the very poor sound power output at low frequencies. Consequently, they have not found widespread use in active double-panel partitions.

2.3.3 ACTIVE SEGMENTED PARTITIONS

The research presented in the previous sections falls under the general classification of ASAC control. The classification of ASPs is also evident in the literature. The distinction between ASAC and ASP approaches is subtle but important. The latter subdivide a large continuous panel into several individual modules which are mechanically and/or acoustically segmented from one another while ASAC more

generally refers to the reduction in sound radiation from the surface of continuous panels. The mechanical segmentation found in ASPs reduces the spatial control spillover that exists for continuous panels. Acoustic segmentation is possible for double-panel ASPs, allowing for a long-wavelength (i.e., nearly uniform pressure across spatial dimensions) assumption to exist in module cavities. Such segmentation can also assume the long-wavelength assumption holds for exposed module surfaces. This simplifying assumption enhances the possibility of independent control of each module, thus addressing the impracticality of a large number of fully-coupled controllers that typically exists for ASAC control. Furthermore, the double-panel ASP approach locates the error signal sensors inside the partition and does not require the placement of microphones or other sensors in the receiving space.

Some of the ASAC research presented earlier can also be loosely categorized as ASP research. The previously discussed studies of Thomas [14], Pierre [18], Hirsch, [19, 20], and Bingham [21] all utilized composite panels, which are mechanically segmented panels with multiple discrete areas and surface velocities. Composite panels showed promise because each radiating area of the panel could be independently sensed and actuated. However, all of these studies used single-panel partitions which were still acoustically coupled despite being mechanically segmented. The acoustic interaction between adjacent areas in the composite panel often required fully-coupled controllers.

An effective double-panel ASP (with acoustic segmentation in addition to mechanical segmentation) was implemented by Leishman et al. [8, 45-48]. Several different designs for individual ASP modules were published in 2005 [46]. This paper used analytical models to explore two single-panel designs and two double-panel designs.

The single-panel designs consisted of an actuator, a transmitting diaphragm, and interstitial supports. One of the designs assumed that the diaphragm vibrated snugly (without friction) within the interstitial supports, while the other included a resilient surround which connected the diaphragm to the interstitial support. The transmitting diaphragm was directly forced by the actuator. It was predicted that both single-panel designs produced an actively controlled TL in excess of 25 dB above 600 Hz but were unable to provide more than 15 dB of TL near the primary resonance of the panel.

The double-panel designs used an active composite panel on the source-side of the module and a passive panel on the transmitting-side of the module. The active composite panel consisted of a circular control loudspeaker mounted in a larger, square, honeycomb panel. The loudspeaker was actuated to reduce the normal vibration of the passive transmitting panel or to reduce the acoustic pressure inside the cavity. The two double-panel designs presented in this theoretical paper predicted infinite TL under active control.

Using this double-panel configuration and a digital feed-forward controller, Leishman et al. achieved experimental TL results near 80 dB over a band of 40 Hz to 1.0 kHz for an individual double-panel ASP module [47]. Two different error sensors were investigated (a microphone located in the cavity and an accelerometer mounted to the center of the transmitting panel) and similar TL results were obtained in both cases. Although the module had high TL, it also had several limitations that were noted in the paper. First, the digital feed-forward controller required a time-advanced reference signal. Second, the digital controller could only effectively attenuate sinusoidal or narrowband disturbances (i.e., it lacked broadband random-noise control). Third, the

digital controller had a slow convergence rate and had a difficult time tracking the swept-sine disturbances. Finally, the module was unidirectional and could not produce TL in both directions. Despite these limitations, the double-panel prototype module represented the first active partition with very high TL at low frequencies and produced (by far) the best experimental results to date. Leishman concluded the paper by stating that "additional work is required to assess normal-incidence TL characteristics of other ASP module configurations and multiple modules mounted in ASP arrays."

The second half of this statement was addressed in [48] by constructing an ASP array using four of the previously mentioned double-panel modules. Each module in the array possessed its own digital feed-forward controller. The array was tested using both centralized and decentralized control. Centralized control was implemented by using a four channel multiple-input/multiple-output (MIMO) controller, while decentralized control was implemented by using four independent single-input/single-output (SISO) controllers. The experimental ASP array under SISO control produced TL results near 55 dB over a band of 40 Hz to 300 Hz. Surprisingly, the SISO controllers produced an average TL that was 6 dB higher than the MIMO controller. This result emphasized the fact that the acoustic segmentation within the double-panel ASP allowed decoupled controllers to function simultaneously for the modules. It should be noted that the same limitations manifested by the individual ASP module were still exhibited in the array.

Other ASP module configurations have not yet emerged in the literature. New designs may be able to overcome some of the aforementioned limitations that are present in the published ASP designs. In particular, since analog feedback controllers are typically better suited for controlling broadband random-noise, they should be

investigated with the existing ASP modules. Other ASP module designs should also be explored to see if bidirectional TL is obtainable. ASP arrays have a promising future if these limitations can be overcome while still producing high TL at low frequencies.

3 FEEDBACK CONTROL OF AN ASP ARRAY

This chapter presents experimental work done on an existing ASP array. The steps for designing an analog feedback controller are outlined and the TL for the ASP array under feedback control is measured.

3.1 NOMENCLATURE

a	Gain of a first-order analog controller
c	Speed of sound in the fluid medium
c_1	Complex frequency response function of controller 1
c_2	Complex frequency response function of controller 2
C_1	Electrical capacitor in a first-order analog controller
$C(f)$	Complex frequency response function of an arbitrary controller
d	Acoustic propagation distance between a control source and error sensor
$d(f)$	Frequency-dependent disturbance signal
$e(f)$	Frequency-dependent error signal
f	Frequency (Hz)
G_M	Gain margin of $L(f)$
$L(f)$	Complex frequency response of the open loop system, = $C(f)P(f)$
p_n	n^{th} pole of $C(f)$
$P(f)$	Plant frequency response function

R_{IN} Electrical resistor in a first-order analog controller

R_1 Electrical resistor in a first-order analog controller

R_2 Electrical resistor in a first-order analog controller

s Laplace domain frequency, = $\sigma + j\omega$

S Arbitrary surface area

S_p Surface area of the honeycomb panel

S_s Surface area of the loudspeaker diaphragm

$\hat{u}_p$ Complex surface velocity of the honeycomb panel

$\hat{u}_s$ Complex surface velocity of the loudspeaker diaphragm

$\hat{U}_p$ Complex volume velocity of the honeycomb panel, = $\hat{u}_p S_p$

$\hat{U}_s$ Complex volume velocity of the loudspeaker diaphragm, = $\hat{u}_s S_s$

z_n n^{th} zero of $C(f)$

φ_{AP} Phase shift caused by acoustic propagation

ω Angular frequency (rad/s), = $2\pi f$

φ_M Phase margin of $L(f)$

3.2 INTRODUCTION

The purpose of this chapter is to combine the positive qualities of existing ASP hardware with the potentially advantageous qualities of an analog feedback controller. In particular, it will demonstrate whether analog feedback control is feasible in a double-panel partition that uses an active composite source-side panel with a passive transmitting-side panel.

ASPs have shown the potential for high TL at low frequencies. As discussed in the previous chapter, an individual double-panel ASP module [47] produced an average TL of nearly 80 dB over a band of 40 Hz to 1 kHz. It has also been demonstrated that several of these modules can be combined to form an effective ASP array with similar TL performance [48]. Unfortunately, both the individual ASP module and the ASP array had a few limitations that restricted the number of potential applications. The primary limitation was the lack of broadband random-noise control. The digital feed-forward controller used in conjunction with the existing ASP module was only capable of attenuating tonal or narrowband disturbances. While some applications exist where the acoustic field is dominated by single-frequency noise, other applications require the ability to attenuate broadband noise. A secondary limitation of the control scheme was the need for a time-advanced reference signal for the feed-forward controller. There are some applications where this reference signal can be readily obtained (such as microphones placed upstream in ducts and tachometer signals from rotating machinery), but there are many other applications in which this reference signal is unavailable or uneconomical (such as for multiple sound sources impinging upon an ASP array, moving sound sources, and flow-induced disturbances [49, pg. 272]).

As a general trend, feed-forward controllers have produced better attenuation in applications involving tonal disturbances and feedback controllers have produced better attenuation in applications involving broadband disturbances. Since many active partition applications require the attenuation of broadband random-noise, a feedback controller should be considered for use with an ASP module. Additionally, feedback active control must be used instead of feed-forward control when no time-advanced error signal is

available. However, the challenge with feedback control involves trying to sense the disturbance, condition the signal, and actuate the secondary source before the original disturbance leaves the plant and can no longer be attenuated. The desired attenuation will not occur unless the output signal from the secondary source is sufficiently correlated with the original disturbance.

A commonly known challenge with digital controllers is the latency involved in the DSP chip as well as the latency involved in the necessary analog-to-digital (A/D) and digital-to-analog (D/A) converters and low-pass filters [50, pg. 194, 51]. This latency is much less of a problem when feed-forward control is used because an inherent time lag in the physical system already exists between the first detection of the disturbance signal and the time at which the secondary source must be actuated. However, the processing latency can significantly degrade the effectiveness of a feedback controller. A discussion of how the latency in the plant and controller affects the maximum possible attenuation of a digital feedback active control scheme is by given by Green in chapter 2 of his thesis [52]. Of all the delay present in his system, 26% was due to acoustic propagation time, 56% was due to the DSP and the accompanying anti-aliasing and reconstruction filters, and 18% was due to all other electronics and transducers.

Analog controllers can have extremely low latency times. As a result, they are well suited for many feedback control applications, including the active control of sound through partitions. Since the double-panel ASP array referenced previously was available at BYU, the first task of this thesis project was to implement an independent analog feedback controller with each module in the array.

3.3 DESCRIPTION OF THE EXISTING ASP HARDWARE

Leishman et al. performed experimental TL measurements through the array of four ASP modules [48]. It consisted of a 2 x 2 arrangement of individual modules, measuring 0.55 m by 0.55 m in overall outside dimensions. The array was constructed with two interlocking halves so that access to the air cavity was possible. The half of the module closest to the disturbance source is referred to as the source side, while the other half of the module is referred to as the transmitting side. The source side and transmitting side of the ASP array are secured to each other by latching mechanisms to form an airtight seal. A photograph of the open ASP array is shown in Figure 3-1 (further detail of both the source side and transmitting side will be shown in Figure 3-2, Figure 3-3, and Figure 3-4).

Figure 3-1. Photograph of Leishman's ASP array. Photographs reprinted with permission from [48]. Copyright 2005, Acoustical Society of America.

Each module in the array consisted of two panels (designated the source-side panel and the transmitting-side panel), separated by an air cavity. The source-side panel of each module was a composite panel similar in some ways to that used by Pierre [18].

It consisted of a square aluminum honeycomb sandwich panel with a 10 cm diameter loudspeaker mounted in the center. The loudspeakers were Aura Sound NS4-8A full-range drivers and were specially selected for their lightweight neodymium magnets. The orientation of the speaker was such that the magnet structure of the loudspeaker faced the exterior of the closed ASP module (toward the source space) while the cone faced toward the cavity. A resilient compressed foam-rubber surround connected the honeycomb panel to the interstitial support structure. A secondary spider suspension was added on the exterior of the source-side panel to support the weight of the magnet and to help reduce any rotational motion of the panel. A photograph of the exterior and interior faces of the source-side panel is shown in Figure 3-2.

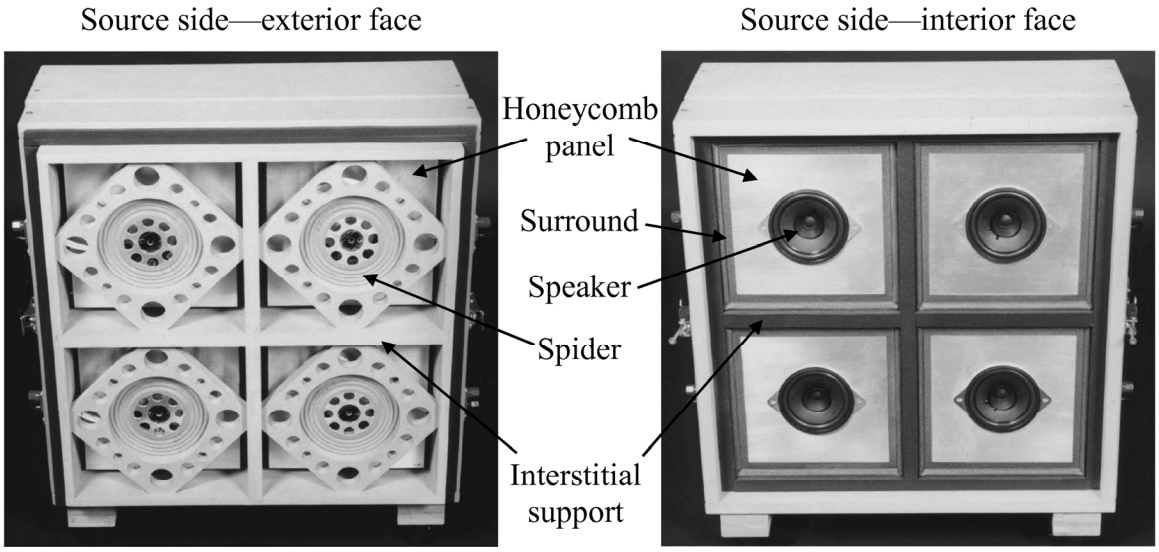

Figure 3-2. Photographs of the exterior and interior faces of the source-side panel from Leishman's ASP array. Photographs reprinted with permission from [48]. Copyright 2005, Acoustical Society of America.

The transmitting panel of each module in the array was also constructed from an aluminum honeycomb sandwich panel. An aluminum fin assembly was glued to the interior face of the transmitting-side panel. The other end of the fin assembly was supported by a spider suspension to help constrain the panel to piston-like motion. Once again, a resilient surround was used to connect the honeycomb panel to the interstitial support. A photograph of the exterior (toward the receiving space) and interior (toward the cavity) faces of the transmitting-side panel is shown in Figure 3-3. The spider is easily visible on the interior face of the transmitting side but the support fins are slightly harder to see. Both the interior and exterior faces of the transmitting panel are smooth surfaces.

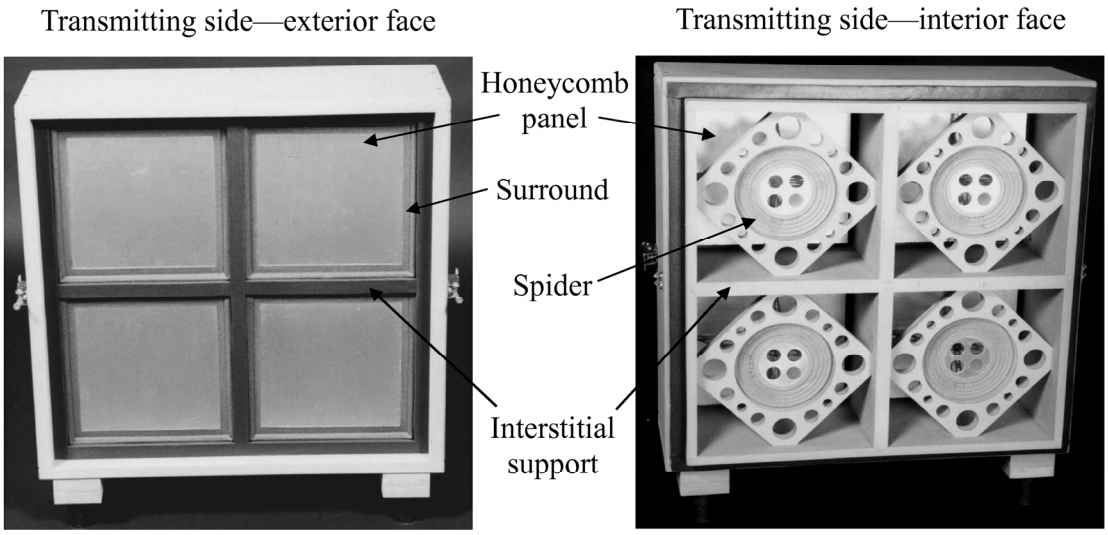

Figure 3-3. Photographs of the exterior and interior faces of the transmitting-side panel from Leishman's ASP array. Photographs reprinted with permission from [48]. Copyright 2005, Acoustical Society of America.

Because some of the details of the module are difficult to see in the photographs, a labeled schematic cutaway view of the assembled ASP array is shown in Figure 3-4.

This view illustrates some of the internal features of two ASP modules. The composite source-side panel is shown as the left half of the module and the passive transmitting-side panel is shown as the right half of the module. The secondary spider suspensions, the resilient surrounds, and the aluminum fins are more clearly seen.

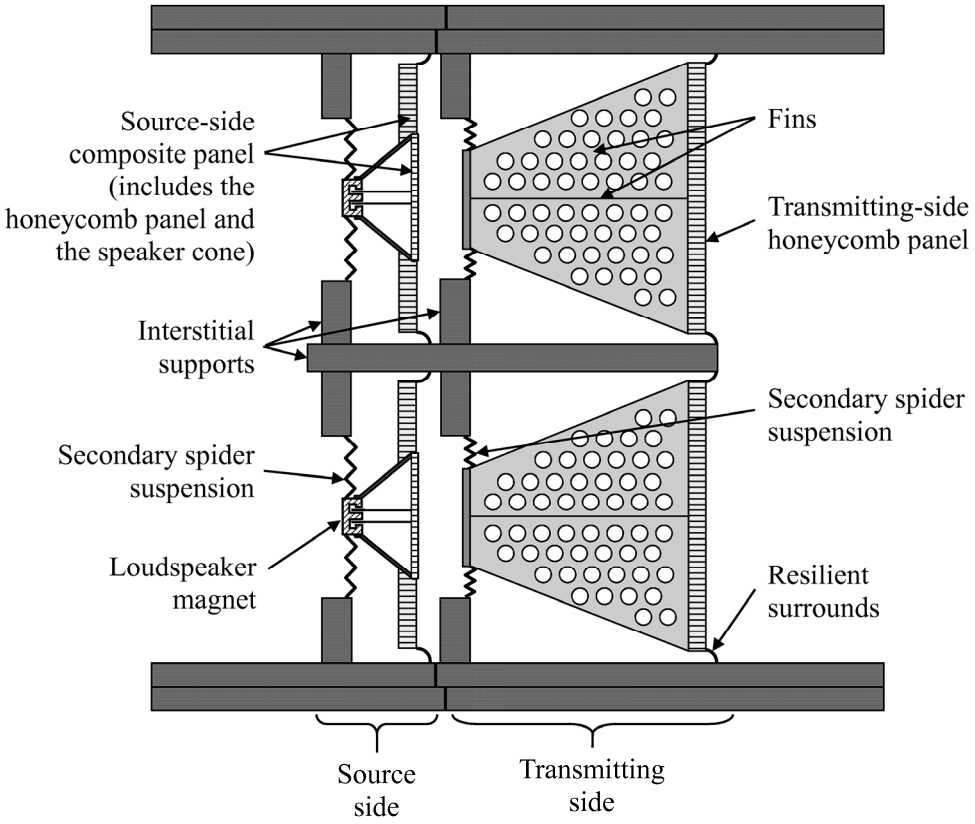

Figure 3-4. Schematic cutaway view of Leishman's ASP array (after [8, Fig. 8.9]).

3.4 ACOUSTIC CONSIDERATIONS OF THE MODULE HARDWARE

Several important acoustic factors were considered when designing the module. It is critical that these factors are addressed in any ASP design if high TL is to be achieved. The most important factors are presented in this section.

The first factor of importance is contained in the idea of the segmented partition. The purpose of segmentation is to maintain a relatively uniform pressure on the surface of the panels and inside the cavity up to a sufficiently high frequency. This aligns with the findings of Elliott and Johnson that the first structural mode of the plate accounted for 99% of the radiated acoustic power up to a *kl* value of 0.5 [15]. Maintaining small panel and cavity dimensions compared to an acoustic wavelength greatly simplifies the sensing and actuation schemes for active control. On this hardware, the dimensions of the panels were 22.9 cm by 22.9 cm and the depth of the airspace was approximately 19.0 cm.

A second factor of importance was adding further means to constrain both the source-side and transmitting-side panels to exhibit piston-like motion. The secondary spider suspensions used in the hardware behave like the spider suspension on a loudspeaker driver. The circular spider provides a centering force to either the loudspeaker magnet (in the case of the source-side panel) or the base of the fins (in the case of the transmitting-side panel) should they start to displace away from their center position. This consideration helps to reduce rotational motion of the panels. Both the spider suspensions and the aluminum fins are assumed to be acoustically transparent.

The third factor of importance was the connection between the panels and the interstitial support structure. Piston-like behavior is difficult to accomplish if the panels are rigidly connected to the interstices, e.g. through clamped or simply-supported boundary conditions. The mechanical coupling path through the interstitial supports is also increased for any type of rigid connection. The use of resilient connections isolates the modules from the interstitial supports (thus breaking a mechanical coupling path) and

allows for piston-like motion of the panels. The resilient connections used on this hardware were half-roll compressed foam-rubber surrounds.

A fourth factor of importance is the construction of the panels. One of the overall goals of the research is to reduce the mass of the partition. However, the panels need to possess sufficient stiffness so that higher order bending modes do not dominate their vibrational behavior. Consequently, the panels need to be both stiff and lightweight. To accomplish this, aluminum honeycomb sandwich panels were used. The honeycomb interior significantly reduced the overall mass of the panel while the sandwich layup produced high stiffness in bending. The stiffness of the transmitting panel was increased further by adding the rigid fin supports to the inside of the panel. The average mass of the four transmitting panels was 87 grams, including their support fins. The first bending mode frequency for the transmitting panels was reported to be near 1 kHz.

A final factor of importance exists, which is only pertinent to this particular module configuration. The existing ASP module indirectly uses a volume velocity approach to increase the TL through the partition. Volume velocity refers to the flow rate of the acoustic medium through a specified area S in the direction of the surface normal vector [16, pg. 10]. At low frequencies, the amplitude of the first radiation mode (this is also the dominant radiation mode since the panel is constrained to piston-like motion and is designed to have high stiffness in bending) is approximated by the net volume velocity of the transmitting panel [17]. The volume velocity of a uniformly vibrating surface is equal to the product of its surface area and the normal surface velocity vector. In addition, consider the composite panel shown in Figure 3-5. The volume velocity of the honeycomb panel $\hat{U}_p$ is equal to the product of its surface area S_p and the normal surface

velocity $\hat{u}_p$. A similar volume velocity can be written for that of the loudspeaker cone: $\hat{U}_s = \hat{u}_s S_s$. The net volume velocity into the cavity (for the entire composite panel) can be zero if $\hat{U}_p$ and $\hat{U}_s$ are equal in magnitude but opposite in phase relative to one another. If zero net volume velocity into the cavity could be achieved at each frequency, there would be no net acoustic force impinging upon the transmitting-side panel and vibration would not be induced. This would result in an ASP module with high TL under active control.

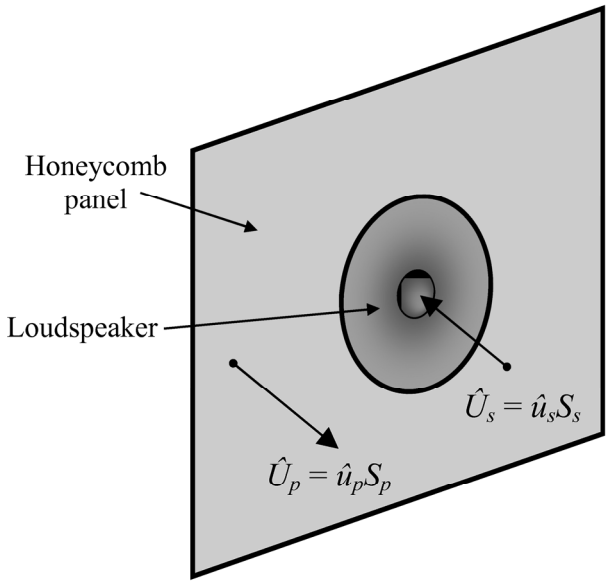

Figure 3-5. Composite panel with two radiating surface areas.

3.5 SENSING AND ACTUATION FOR ACTIVE CONTROL

Measuring the acoustic pressure in the cavity with a microphone can also provide an error signal that is approximately proportional to the net volume velocity of the source-side composite panel. This assumes that the pressure is approximately uniform at all locations inside the cavity (this assumption is valid at low frequencies). Although many microphone locations are possible, some locations are more prudent than others. For example, the

microphone should not be placed in the acoustic near-field of the loudspeaker where it might detect evanescent waves or be positioned on a pressure null in the field. The microphone should not be placed on the pressure node of a mode inside the cavity. These two considerations suggest the microphone should be placed in a corner of the cavity away from the loudspeaker. On the other hand, the control bandwidth becomes limited as the distance between the microphone and loudspeaker is increased. The added acoustic propagation distance is manifest as a phase shift in the plant frequency response function. The pure phase shift (in degrees) caused by acoustic propagation at frequency f, over a distance d, with speed of sound c, is given by

$$\phi_{\mathrm{AP}} = -360\frac{fd}{c}. \qquad \textbf{(3.1)}$$

Suppose for example that the distance between the loudspeaker and the microphone was 10 cm. The phase shift at 1 kHz caused solely by the acoustic propagation time would be -105°. This represents a significant phase shift when trying to perform feedback control. High phase shifts limit the control bandwidth by causing instabilities in the system at lower frequencies. The amount of phase shift that can be tolerated depends on the frequency response function of the plant.

3.6 FEEDBACK CONTROL THEORY

A brief discussion of feedback control theory is provided in this section. It is intended to provide enough material on the subject so that the control theory used in this thesis may be understood.

3.6.1 FEEDBACK CONTROL BLOCK DIAGRAM

A schematic diagram of the feedback control arrangement for an individual ASP module is shown in Figure 3-6. The disturbance pressure impinges upon the source-side panel of the module. The disturbance is then transmitted into the cavity where it is sensed by the microphone. The electrical output of the microphone is designated the error signal and becomes the input to the feedback controller. The output of the feedback controller is then fed through a variable-gain power amplifier and into the control source (loudspeaker). If the controller works as anticipated, the pressure inside the cavity will be reduced.

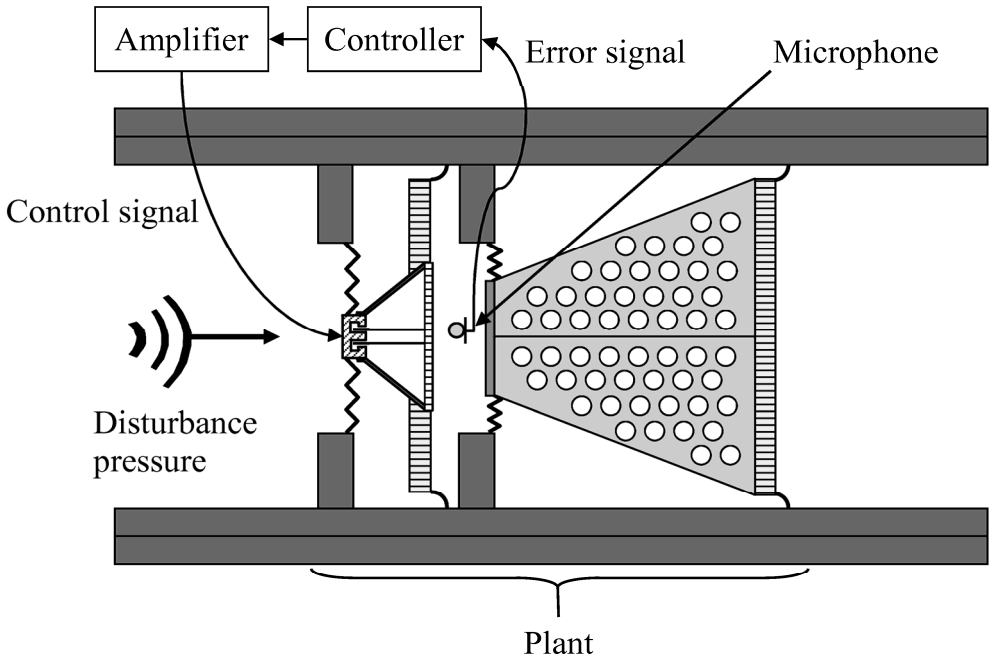

Figure 3-6. Schematic diagram of the feedback control arrangement.

For feedback active cavity control in the existing module, the actuator is a loudspeaker in the source-side panel and the error sensor is a microphone located inside the cavity. The loudspeaker and the microphone, along with the mechano-acoustic

coupling path between them, constitute a "plant" in the control literature. Formally, the plant is defined for active control schemes as "the system between the input to the secondary actuator and the output of the sensor used to measure the residual error signal" [49, pg. 105]. The plant frequency response function $P(f)$ can then be written as:

$$P(f) = \frac{\text{Microphone Output}}{\text{Actuator Input}}. \tag{3.2}$$

The arrangement shown in Figure 3-6 can also be represented by the block diagram form of Figure 3-7. Block diagrams provide a simpler representation of the critical dynamics. The dynamics of the controller are represented by $C(f)$, the dynamics of the plant by $P(f)$, the disturbance signal is $d(f)$, and the error signal is $e(f)$. The designation (f) indicates that these quantities are functions of frequency.

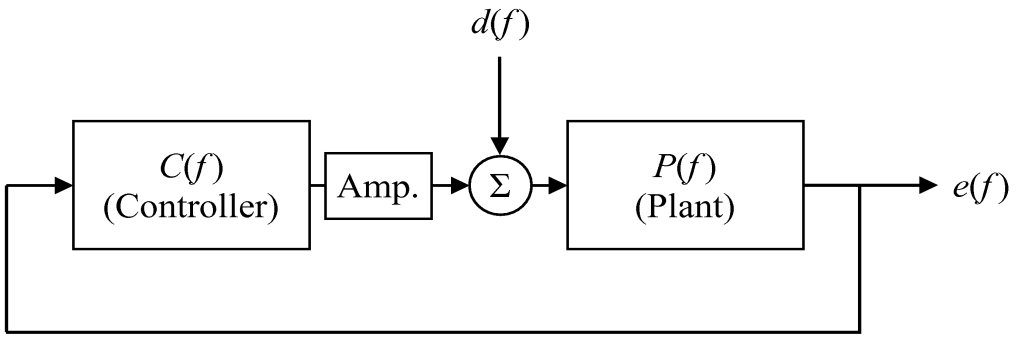

Figure 3-7. Block diagram of a positive-feedback system with no reference signal.

Again, consider a disturbance pressure $d(f)$ that impinges upon the plant. As the disturbance passes through the plant, it is sensed by the microphone and then relayed as an electrical signal into the controller. The controller will then impose a predefined

frequency-dependent filter $C(f)$ upon the disturbance signal. The objective of $C(f)$ is to condition the original disturbance signal in order to make it a suitable cancellation signal to send to the control actuator. The variable-gain power amplifier (amp) is shown in the block diagram but it is assumed to not have any frequency-dependent dynamics. The conditioned control signal is then fed into the plant, where it drives the control actuator and is converted to a secondary pressure wave. The secondary pressure wave propagates to the error sensor. The error signal $e(f)$ then becomes the sum of the current disturbance pressure and the current control pressure.

The frequency-dependent dynamics of the plant $P(f)$ depend on the dynamics of the sensors and actuators, on the physical properties of the panels and surrounds, and on the position of these elements within the module. For the existing ASP module, most of these factors were already determined. For example, the loudspeakers were permanently affixed in the source-side panel, the module dimensions were already chosen, and the physical properties of the panels, surrounds, and spider suspensions were set. Although constructing a new ASP module with new components could change $P(f)$, the purpose of this initial research was to explore the possibility of using a feedback controller with the existing hardware. The primary focus was to design an effective analog feedback controller.

3.6.2 FREQUENCY RESPONSE CONTROLLER DESIGN METHOD

Several approaches exist for designing feedback controllers: the root locus method, the state space method, and the frequency response method. A few excellent books on controller design are referenced for the reader [49, 50, 53]. The root locus and

state space methods rely on precise analytical models of the plant. For most systems, models only accurately describe the low-frequency dynamics of the plant. Significant uncertainty can exist in the model at high frequencies, leading to system instability.

A more practical approach to the design of control systems is the frequency response method. In this approach, $P(f)$ is measured directly so that the plant dynamics are known at all frequencies. A controller is then designed to attenuate the disturbance over some control bandwidth. Guidelines can then be used to make sure that the designed controller will remain stable during operation. If stable performance is predicted, the controller can be built and tested with the plant. If the desired active control performance is not achieved, either a new controller or a new plant can be designed. These steps are summarized in Table 3-1.

Table 3-1. Steps of the frequency response controller design method.

1. Measure the frequency response function of the plant, $P(f)$
2. Design a controller $C(f)$ to satisfy the control objectives
3. Analytically verify the stability of the controller using $L(f) = C(f)P(f)$
4. Build a prototype controller
5. Test the prototype controller with the plant
6. Iterate on the controller design or create a new plant

The first step in the design method is to measure the FRF of the plant $P(f)$. This measurement can be made with a two-channel FFT analyzer that can compute $P(f)$

according to Eq. (3.2). Care should be taken to ensure that the measurement is accurate and that it represents the general operating conditions of the plant. If the plant will see many different operating conditions, the worst-case conditions might be measured for controller design purposes. The plant FRF $P(f)$ is then plotted on a Bode plot (which shows the magnitude on an upper plot and the phase on a lower plot). The Bode plot is typically displayed with a logarithmic frequency axis. An example of $P(f)$ for a fictitious plant is shown in Figure 3-8. As is usually the case with physical systems, the low-frequency dynamics are relatively smooth, but severe fluctuations can exist in the plant at higher frequencies.

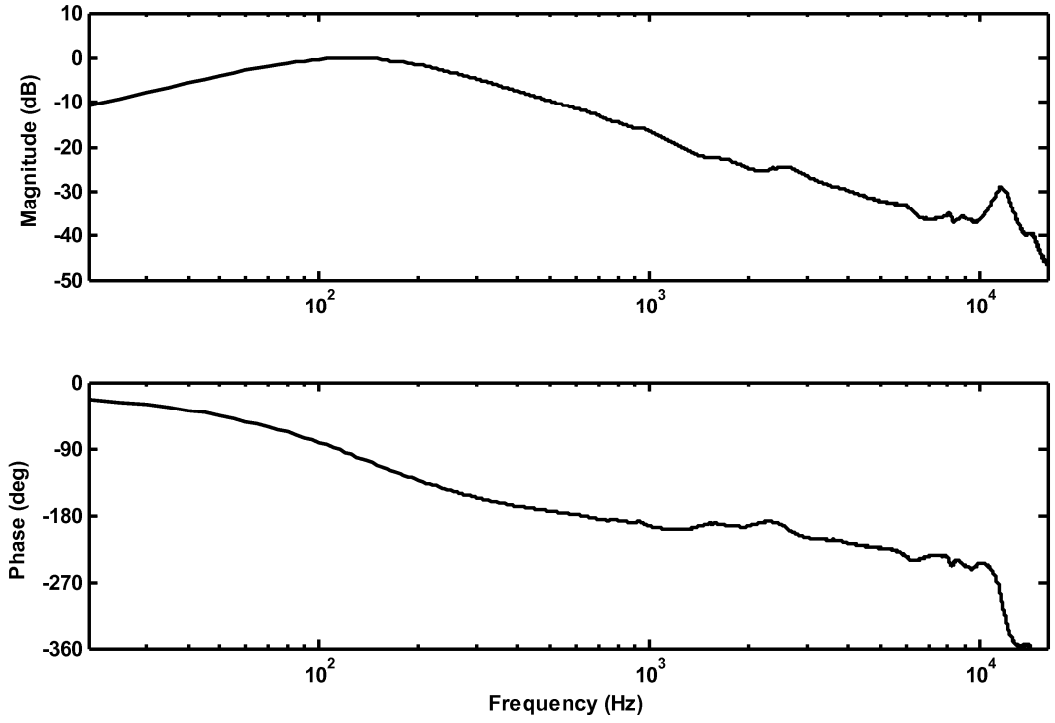

Figure 3-8. Example $P(f)$ of a fictitious plant.

The second step is to design a controller $C(f)$ for use with the measured plant. The function $C(f)$ is designed to meet some desired control objective. A general mathematical representation of $C(f)$ can be written as

$$C(f) = \frac{(s-z_1)(s-z_2)(s-z_3)...}{(s-p_1)(s-p_2)(s-p_3)...}. \quad \textbf{(3.3)}$$

The poles (zeros of the denominator) and zeros (zeros of the numerator) can be entirely real or can come in complex conjugate pairs. The number of poles of the FRF determines the order of the filter. An analog controller of any order can be constructed, although the complexity of the circuit increases with increasing order. The position of the poles and zeros on the s-plane determines the shape of the controller FRF. In order for the controller to be physically realizable (i.e., to have a causal impulse response), all of the poles and zeros must be located in the left-half of the s-plane. The SISOTOOL toolbox in MATLAB can be helpful in designing a controller because the shape of the controller FRF is dynamically displayed in a graphical user interface (GUI) while the designer positions the poles and zeros in the s-plane. If SISOTOOL is not available, a graph of $C(f)$ is still easily obtainable using MATLAB or other mathematical software packages. Ultimately, the shape of $C(f)$ is left to the designer.

It should be noted from Eq. (3.3) that the magnitude and phase of $C(f)$ are determined by a single complex FRF. As a result, the magnitude and the phase response of the controller cannot be adjusted independently [50, pg. 219]. This represents a tradeoff between the gain and phase response of the controller that must be faced during the design process. Increasing the low-frequency gain of the controller will also increase

the amount of phase lag that is introduced into the system and thus reduce the upper frequency limit of the active control bandwidth. In a similar fashion, increasing the active control bandwidth will decrease the maximum gain of the controller.

In the case of the ASP module, the primary objective is to produce high attenuation at relatively low frequencies. A secondary objective is to have the module gracefully transition back into a passive state above the active control bandwidth. A logical controller for this application would then have some characteristics of a low-pass filter. Suppose that a controller has been designed for the fictitious plant of Figure 3-8. The Bode plot of a possible $C(f)$ is shown in Figure 3-9 and represents a low-pass filter with roughly 40 dB amplification in the pass band. Its phase starts at 0°, reaches a minimum of -80° near 1 kHz, and then returns to 0° at higher frequencies. The corner-frequencies (the frequencies at which the magnitude of $C(f)$ changes slope on the Bode plot) can be adjusted by shifting the location of the poles and zeros.

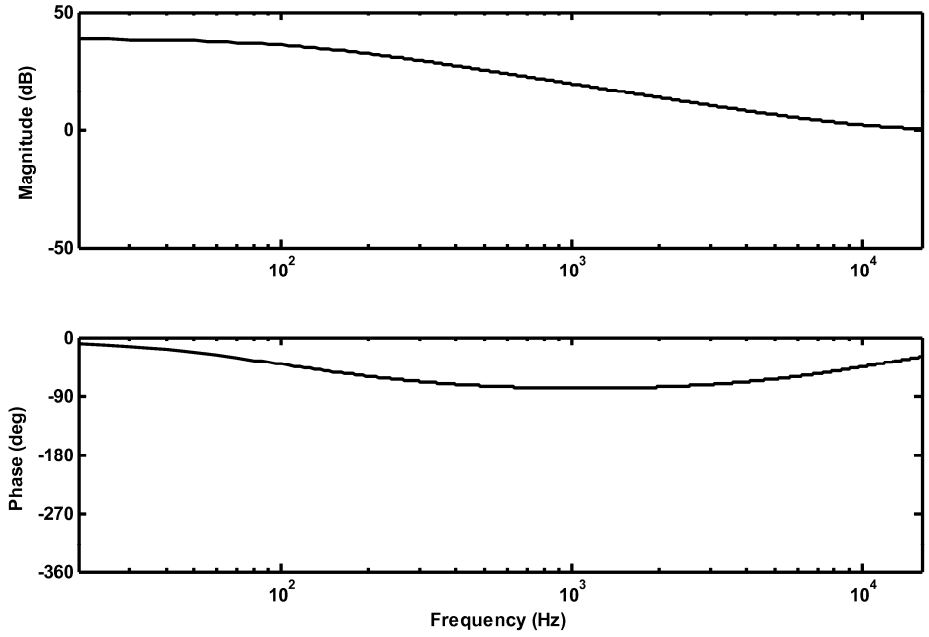

Figure 3-9. Example $C(f)$ of a fictitious controller.

The third step of the controller design process is to analytically verify the stability of the controller when used with the plant. The stability of the controller cannot be determined independent of the plant. For the frequency response design method, this is often accomplished by graphically examining certain characteristics of the open-loop system $L(f)$. The function $L(f)$ is defined as the series combination of $C(f)$ and $P(f)$. In the frequency domain, the series combination is implemented by multiplying the controller FRF by the plant FRF:

$$L(f) = C(f)P(f). \tag{3.4}$$

The $L(f)$ for the fictitious system is shown on a Bode plot in Figure 3-10. The low-frequency magnitude of the system response has been increased dramatically by the controller (compare to Figure 3-8). Also note that the controller has only slightly increased the magnitude at high frequencies. However, it has modified the total phase of the system (again compare to Figure 3-8).

At this point, the stability margins can be determined for the *closed-loop* system (i.e., the system under feedback control) by analyzing the plot of the *open-loop* system, $L(f)$. The gain margin G_M is defined as the magnitude of the open-loop system response at the frequencies where the phase crosses 0° and -360° for the first time [53, pg. 353]. A positive gain margin (and thus a stable system) results when the magnitude of the open-loop system response is less than 0 dB at the 0° and -360° crossing points. Conversely, a negative gain margin (and thus an unstable system) results when the magnitude of the open-loop system response is greater than 0 dB at the 0° and -360° crossing points. The

phase of $L(f)$ shown in Figure 3-10 first crosses the -360° point near 5.7 kHz. The corresponding dB magnitude at this frequency is -10 dB, so by definition this is a positive gain margin of 10 dB. This metric says that the gain of the controller could be increased by 10 dB before system instability occurs. Because the phase does not cross 0° on the low-frequency end, there is less worry about system instability at low frequencies for this fictitious plant. As a rule-of-thumb, gain margins greater than 6 dB are employed in controller design [54, Ch. 5].

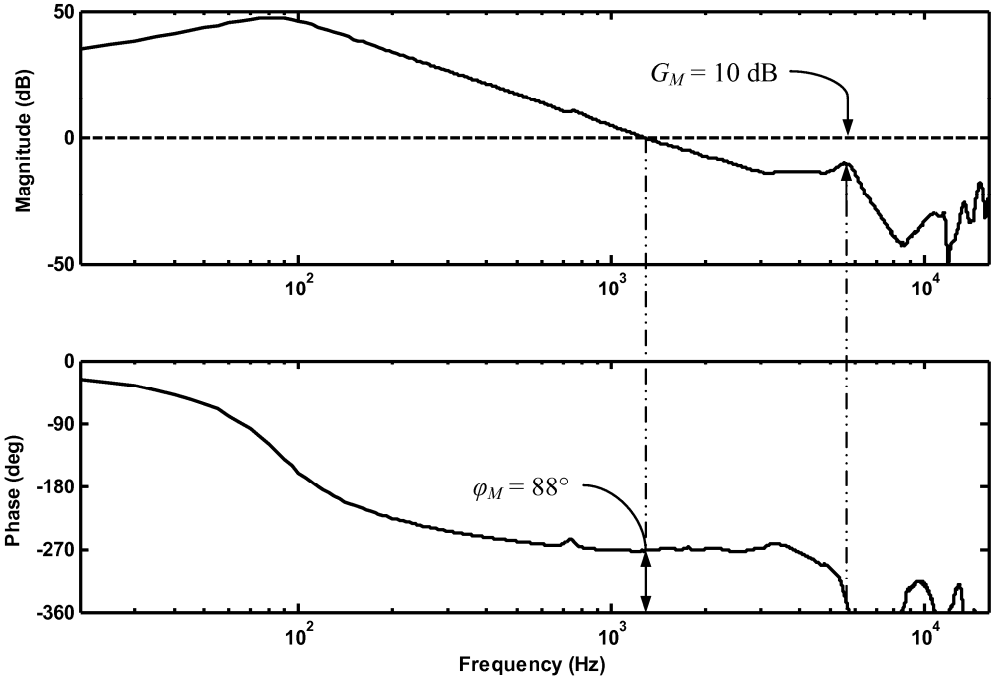

Figure 3-10. Example $L(f)$ for a fictitious plant and controller.

The phase margin φ_M is defined as the difference between the phase response of the open-loop system and the nearest bounding phase line when the magnitude response is 0 dB [50, pg. 217]. The magnitude of the system in Figure 3-10 crosses 0 dB near 1.2 kHz and the corresponding phase at this frequency is -270°. The corresponding phase

margin at this frequency is 90°. Typical phase margins of 30° to 60° are employed in controller design [53, pg. 357, 55, pg. 218, 56]. The gain margin and the phase margin are not independent measures of stability but both are often referred to in controller design theory. The controller must be redesigned if proper stability margins are not met.

After proper stability margins have been ensured, the effectiveness of the controller can be estimated. The amount of attenuation at the error sensor that can be obtained during active feedback control is represented by the amplitude of $L(f)$. In Figure 3-10, approximately 50 dB of attenuation will occur at the error sensor at 85 Hz. The amount of attenuation will taper off with increasing frequency until no attenuation is realized at 1.2 kHz. This frequency represents the upper frequency limit of the active control band. If further attenuation is desired at low frequencies, the shape of $C(f)$ must be adjusted to have higher gain at low frequencies. However , one must keep in mind that this change to the controller will increase the phase lag and will thus lower the active control bandwidth.

The fourth step in the controller design process is to build a prototype of the analog controller. Both "passive" and "active" electrical circuits can be used as controllers. The typical electrical components of analog controllers include resistors, capacitors, and inductors. Active electrical circuits may also include operational amplifiers (op-amps). Hundreds of designs for electrical circuits exist; each design has some distinct shape or performance. Two books which have been of particular value in designing analog controllers are *Analog Filters* by Su [57] and *Active RC Filter Design* by Herpy and Berka [58].

The FRF of the prototype controller $C(f)$ can be measured directly using a two-channel FFT analyzer and then compared to the $C(f)$ for the analytical controller. Tolerances on electrical circuit components are known to range anywhere from five to twenty-five percent. Care should then be taken when building the controller so that the tolerances do not alter the desired FRF.

The fifth step in the design process is to test the controller. The effectiveness of the controller can be evaluated by using it with the plant under experimental conditions. The effectiveness is quantified by how well the closed-loop system response meets the control objectives. An example of some control objectives could be attenuation at the error sensor, achievable transmission loss, and/or adequate stability margins. In the case of this work, the effectiveness will be quantified by the increase in the TL of the array between passive and active states.

The final step in the design process is to iterate on the controller design. In some cases, the control objectives will not be met and the controller design must be adjusted. These changes might include modifying the gain of $C(f)$ and/or modifying the entire shape of $C(f)$ (e.g., switching from a low-pass filter to a band-pass filter). In other cases, an analog controller of any shape might not provide adequate results when used with a particular plant. In these cases, modifications to the plant must be made to make it more controllable.

3.7 PLANT MEASUREMENTS

The controller design method was used on the existing hardware from Leishman's ASP array. To begin, $P(f)$ was measured for just one of the four modules in the array.

Because the flexibility of moving the microphone within the cavity was available, $P(f)$ was measured with several different microphone locations. The microphone location with the lowest phase delay (as discussed in Section 3.3) was selected. The microphone was located on axis with the control loudspeaker at a distance of approximately 2.5 cm from the cone. The measurement of $P(f)$ with the microphone at this location is shown as the solid line (no fiberglass) in Figure 3-11.

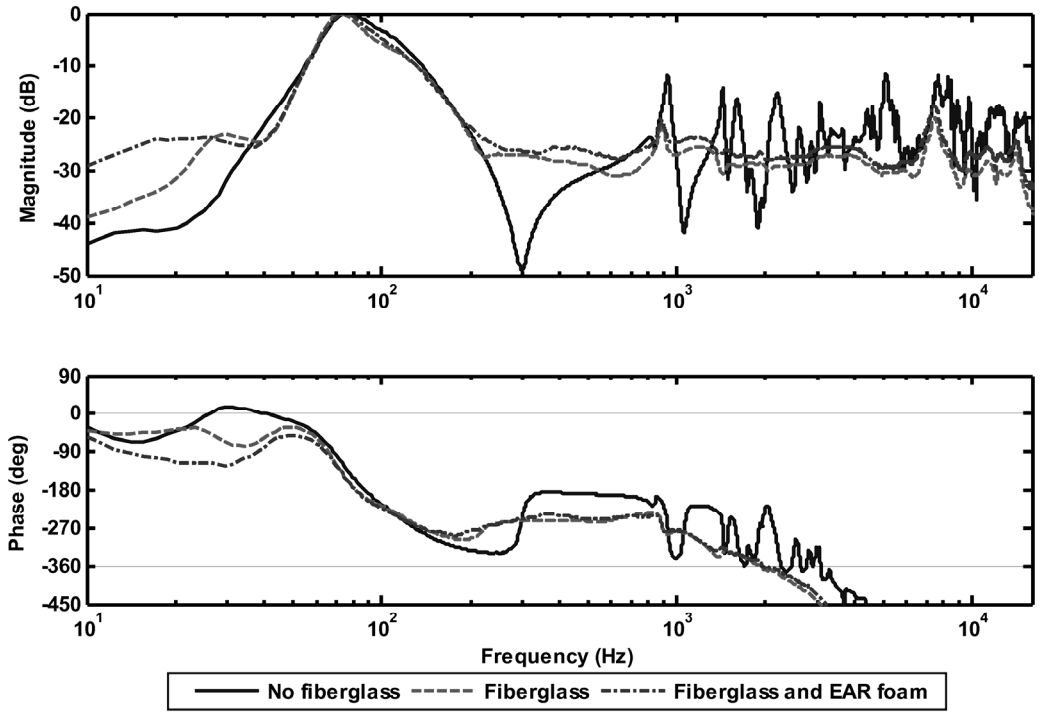

Figure 3-11. Measured $P(f)$ for one module in Leishman's ASP array with various plant modifications.

The original plant (without modifications) presented several control challenges. The first was the strong cavity resonances that are evident by the wild fluctuations in $P(f)$. These resonances make it very difficult to implement a stable analog controller that can provide any sizeable attenuation of the disturbance pressure. Wheeler [59] noticed

similar cavity resonances in an actively controlled headset and successfully used absorptive material in the cavity to reduce the resonances in the mid-frequency band. Such a tactic was tried with the ASP module and the measurement of $P(f)$ with absorptive fiberglass batting placed throughout the entire volume of the cavity is shown as the dashed curve in Figure 3-11 (fiberglass). The acoustic cavity resonances are significantly damped by the fiberglass fill.

The second challenge was that the low-frequency phase response was very near 0° at frequencies less than 20 Hz. To alleviate this undesirable characteristic of the plant, four blocks of EAR CF-40025 foam were placed between the source-side aluminum honeycomb panel and the interstitial support structure to which the spider was connected. This modification to the plant is shown in Figure 3-12. The foam increased the low-frequency damping of the source-side panel without affecting the high-frequency performance. This addition to the plant increased the phase margin below 20 Hz by 80°. The dash-dot curve in Figure 3-11 shows this measurement configuration.

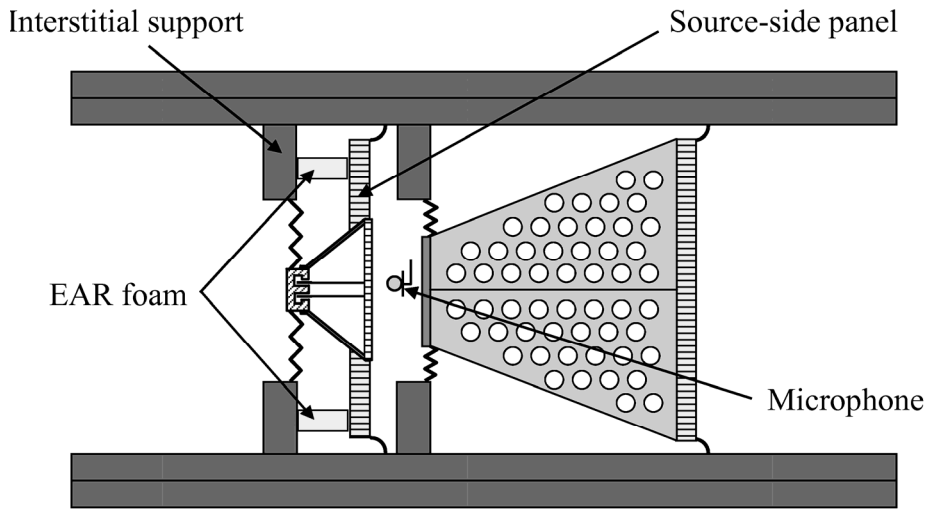

Figure 3-12. Location of the EAR foam used in the plant modification.

Similar FRF measurements were measured for each of the four modules in the ASP array. The measured frequency response functions for all four plants (designated P1-P4) with fiberglass fill and the EAR foam modification are shown in Figure 3-13. It was thus found that the measured plants were very similar to each other at lower frequencies. Consequently, the same controller design could be used for each module in the array.

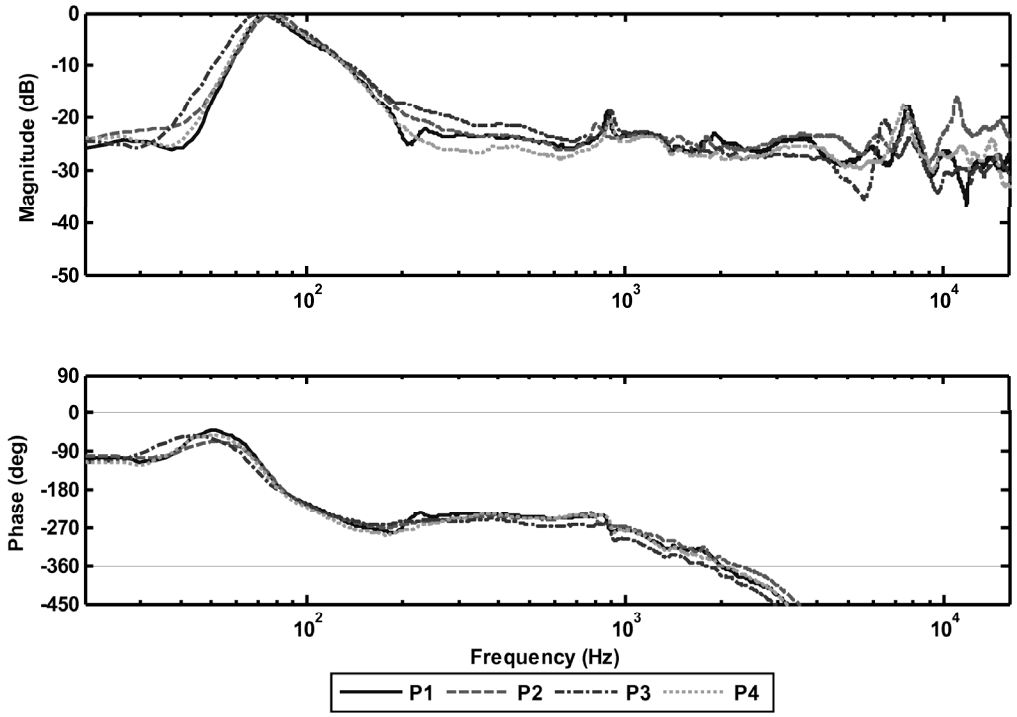

Figure 3-13. Measured *P*(*f*) for all four modules in Leishman's ASP array.

3.8 CONTROLLER DESIGN

The second and third steps in the design process are to design a controller to meet the necessary control objectives and verify the stability of the controller. An analog controller was designed based on the measured *P*(*f*)'s. The controller was a first-order

active lag filter (i.e., a low-pass filter). The electrical circuit for the analog controller is shown in Figure 3-14. The electrical components of the controller consisted of three resistors, a capacitor, and an op-amp. A very simple controller design was chosen since this was the first attempt at building an analog filter for use in the ASP module.

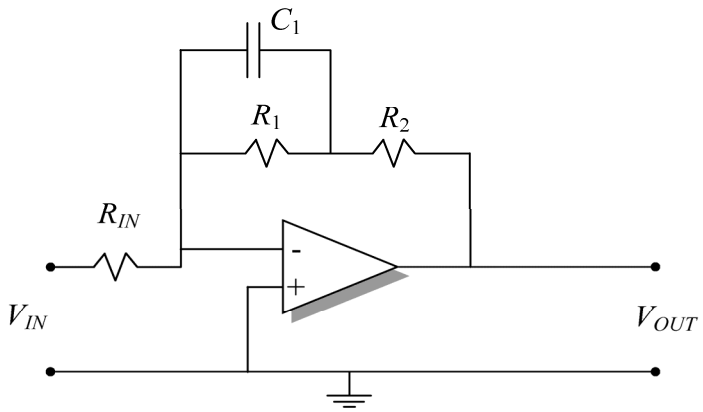

Figure 3-14. Circuit schematic for a first-order active controller.

The controller shown in Figure 3-14 produces a transfer function defined by Eqs. (3.5) through (3.8). The gain of the controller (represented by a) shifts the magnitude of $C(f)$ on the Bode plot without altering the shape of the magnitude or phase curves. The zero and pole of the controller (z and p respectively) determine the corner-frequencies for the low-pass filter.

$$\frac{V_{OUT}}{V_{IN}} = -a\frac{s+z}{s+p}, \tag{3.5}$$

$$a = \frac{R_2}{R_{IN}}, \tag{3.6}$$

$$z = \frac{R_1 + R_2}{R_1 R_2 C_1}, \tag{3.7}$$

$$p = \frac{1}{R_1 C_1}. \tag{3.8}$$

The gain a of the controller was not critical since a variable-gain power amplifier was used in-line after the controller in the active control setup. The resistor and capacitor values used to produce the desired controller are listed in Table 3-2. The tolerance on the resistors was ± 5% and the tolerance on the capacitors was ± 10%.

Table 3-2. Resistor and capacitor values used in the controllers.

Parameter	Value	Units
R_{IN}	9,800	Ω
R_1	13,812	Ω
R_2	1,351	Ω
C_1	0.047	μF

The analytical $C(f)$ of the designed controller is shown in Figure 3-15. It is a low-pass filter with a low-frequency gain of approximately 20 dB. The maximum phase lag introduced is 56°, which occurs near 900 Hz. The position of the pole and zero was judiciously made so that the low-frequency magnitude of the controller was as large as possible to as high of frequency as possible. The phase lag introduced by the controller was controlled so that the system would remain stable. This controller should provide attenuation of low-frequency pressure disturbances while not attempting to actively control high-frequency pressure disturbances.

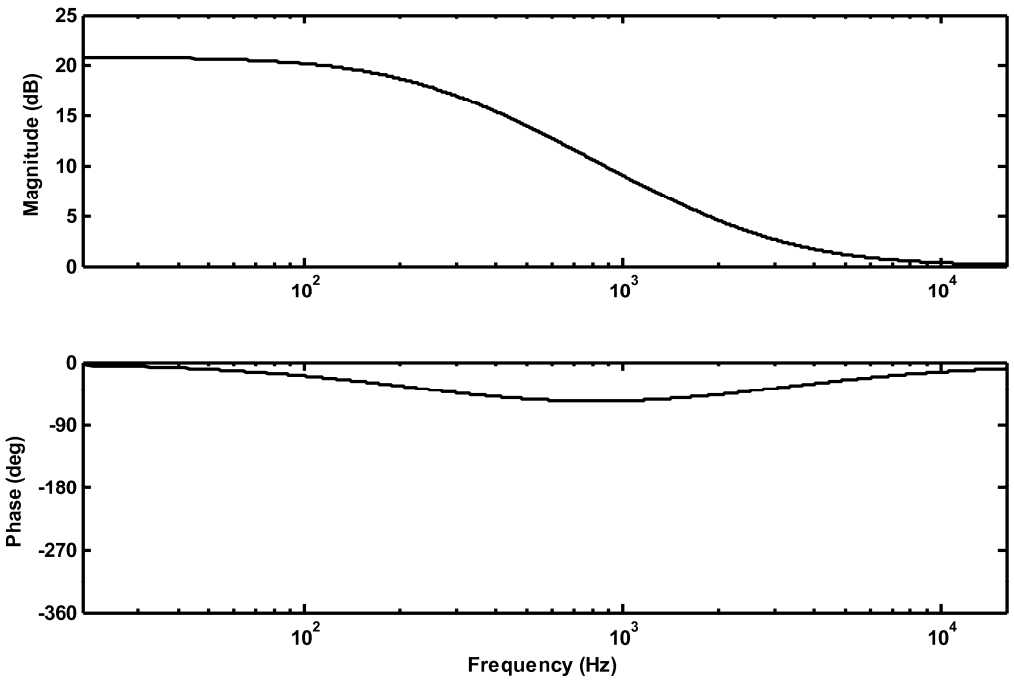

Figure 3-15. Controller *C*(*f*) for the first-order analog controller.

The function *L*(*f*) was computed for each module in the array to ensure that adequate stability margins were employed. Using the controller response *C*(*f*) shown in Figure 3-15, the phase margin at frequencies less than 30 Hz was 90° and the phase margin of *L*(*f*) at 320 Hz was 60°. The minimum gain margin occurred at 1.1 kHz and was 10 dB. These stability margins meet the rule-of-thumb guidelines given earlier of a 6 dB gain margin and at least a 30° phase margin. The analytical *L*(*f*) shown in Figure 3-16 predicts that stable feedback control is possible with a control bandwidth of 0 Hz to 320 Hz. The stability of the closed-loop system is ensured because the predicted dB magnitude of *L*(*f*) is less than 0 dB at all frequencies where the phase is more negative than -360°.

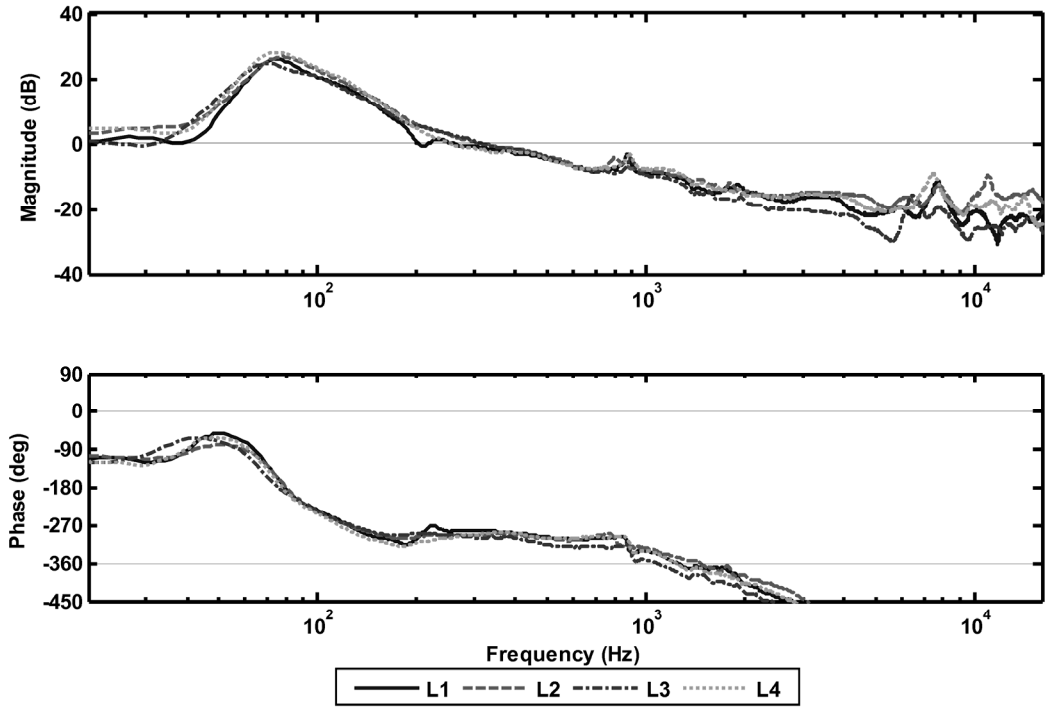

Figure 3-16. Analytical *L*(*f*) for Leishman's ASP hardware with a feedback controller.

The fourth step in the design process is to build a prototype controller. The resistor and capacitor values used to produce the low-pass filter were shown previously in Table 3-2. The controllers were built on a breadboard so that components could easily be changed if necessary. The op-amp was a National Semiconductor LM837N quad operational amplifier chip (i.e., four op-amps per chip). The supply voltage for the op-amp chip was provided by a Tektronix laboratory DC power supply. Four identical copies of the controller were constructed, one for each module. A photograph of the controllers is shown in Figure 3-17. Two, two-channel, Electro Voice 7100 power amplifiers were used in-line after the controller to more easily adjust the gains of each controller (not shown).

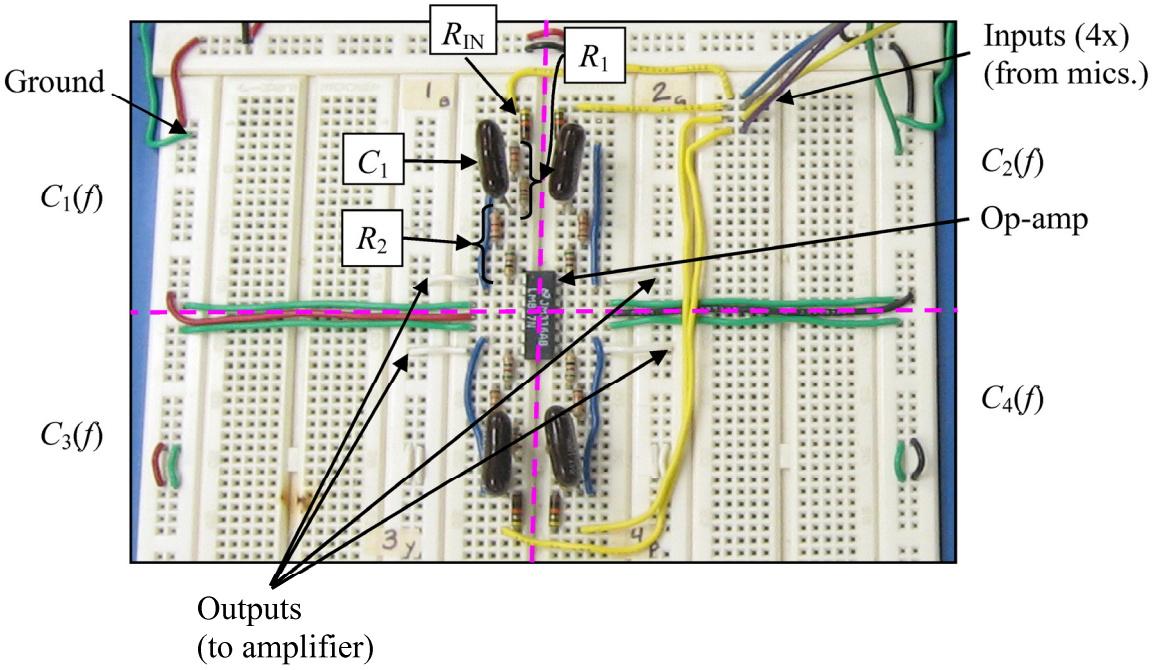

Figure 3-17. Photograph of the analog controllers used with Leishman's ASP array.

3.9 MEASUREMENT SETUP

The fifth step in the controller design process is to test the prototype controller with the plant. A measurement apparatus was used to determine the normal-incidence TL through the ASP array under analog feedback control. The measurement apparatus was a plane-wave tube consisting of several parts. The primary disturbance source was composed of a 25.4 cm diameter loudspeaker in a sealed box and was located at the left end of the tube. Identical source and receiving tubes of 2.44 m lengths were located on each side of the ASP array. The microphones needed to measure the TL were located in the top walls of the source and receiving tubes. An anechoic termination was the final piece of the measurement apparatus. It was located on the far end of the receiving tube. The total length of the device was approximately 9 m. A schematic of the TL measurement system is shown in Figure 3-18.

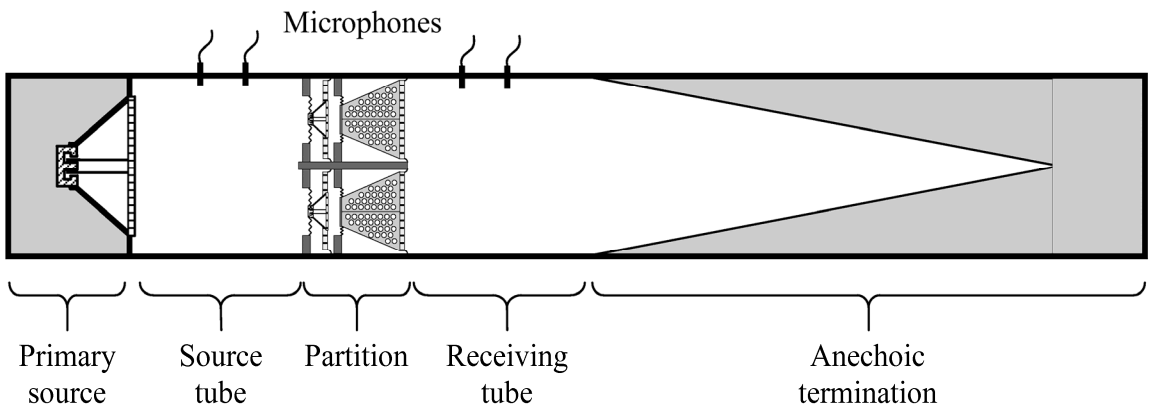

Figure 3-18. Schematic of the TL measurement apparatus used to test Leishman's ASP hardware.

The TLs of the array was determined using the two-microphone transfer-function technique developed by Chung and Blaser [60, 61]. This method allows the sound fields on either side of the module to be decomposed into incident and reflected components. This is necessary to accurately determine the sound powers incident upon and transmitted through the array and therefore the TL. It should be noted that the accuracy of the transfer functions requires a careful calibration of both the gain and phase of each microphone pair used in the measurement (see [60], [62], and [63]).

The useable bandwidth of the TL measurement apparatus was approximately 40 Hz on the low end and 300 Hz on the high end. The lower bandwidth limit was due to the breakdown of the anechoic termination at frequencies below 40 Hz. The upper bandwidth limitation was due to the first cross-mode frequency of the rectangular duct. It should be noted that the effect of axial resonances of the upstream duct were inconsequential in the measurement apparatus because of the two-microphone transfer-function technique.

A photograph of the disturbance source, ASP array, and electrical hardware (without the source tube, receiving tube, and anechoic termination) is shown in Figure 3-19. For the testing of the prototype controllers, all of the electrical hardware was located outside of the module (as shown). In a production unit, the required electronics could be packaged to fit within each individual module.

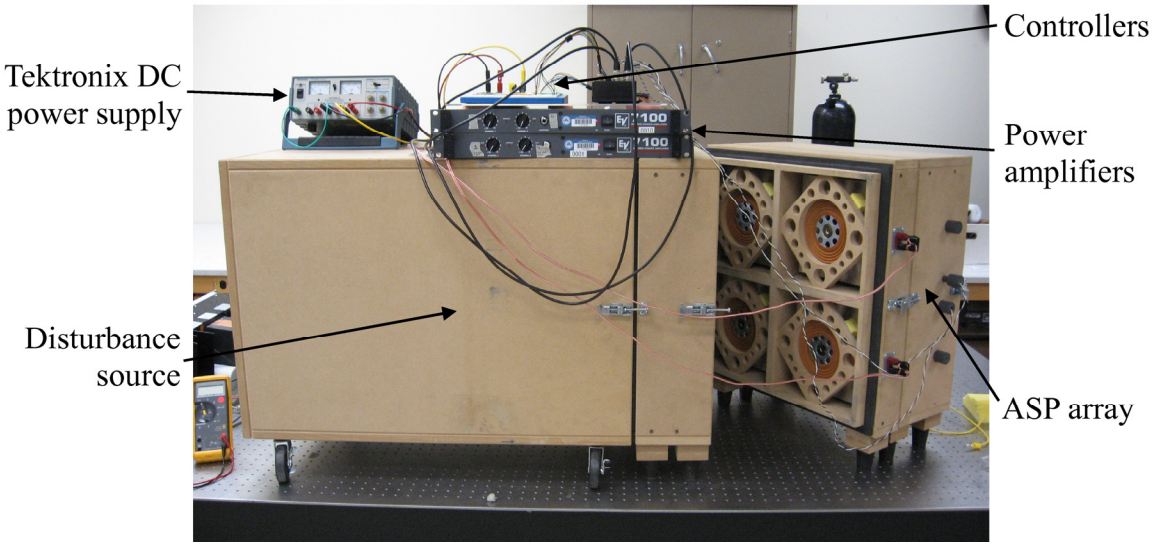

Figure 3-19. Leishman's ASP hardware, including disturbance source (center), ASP array (right), and electrical hardware (top).

3.10 MEASURED TL PERFORMANCE

The passive and active TL through the double-panel ASP array with the EAR foam was measured using the measurement apparatus described in the previous section. The active TL was measured while active control was performed in all four modules. The normal-incidence TL results are shown in Figure 3-20.

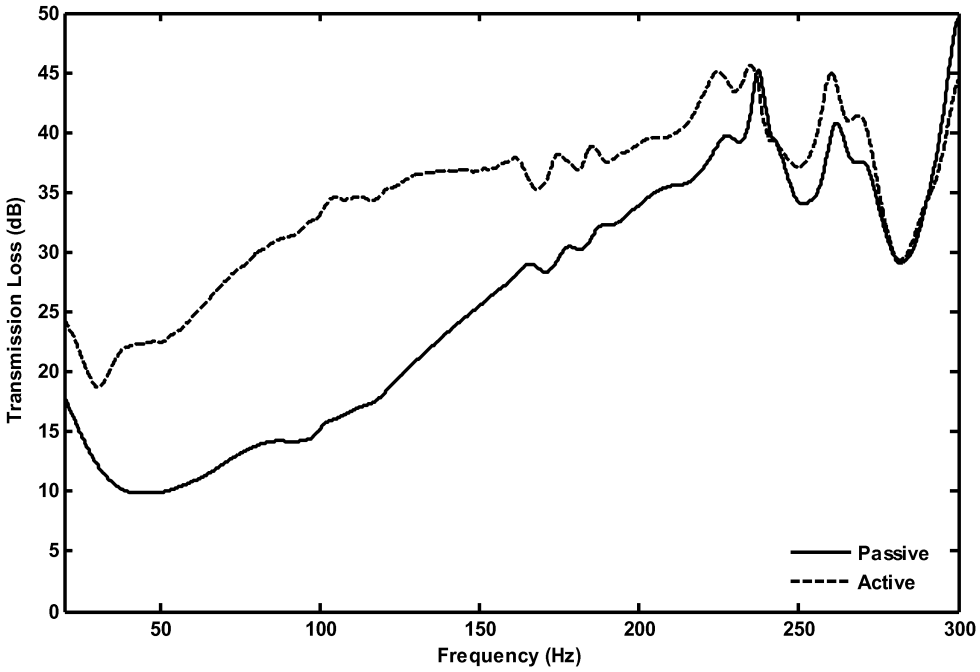

Figure 3-20. Measured TL for Leishman's ASP array with feedback cavity control.

In the passive mode, the array demonstrated the recognizable characteristics of a double-panel partition. The mass-air-mass resonance frequency of the device occurred near 50 Hz shown by the dip in the TL plot. The TL increases at roughly 18 dB per octave above the resonance frequency until approximately 240 Hz.

When the active control was turned on, the TL increased over the majority of the active control bandwidth. The difference in the TL between passive and active states increased from 7 dB at 20 Hz, up to 20 dB at 100 Hz, whereupon it decreased almost linearly to 0 dB by 300 Hz. These results are in accordance with the predicted open-loop system of Figure 3-16. The active TL was 2 to 4 dB less than the passive TL near 240 Hz and again at 300 Hz. Although the feedback TL results presented here are less than the TL results presented by Leishman [48], they still represent a sizeable improvement over many of the

results common in the literature. In addition, the results presented here were obtained with a broadband random-noise disturbance.

It is believed that the performance of the active partition was limited by the acoustic response of the loudspeaker below 80 Hz. The free-air resonance frequency of the Aura Sound NS4-8A drivers used in the module was near 80 Hz, and the magnitude of the pressure response function rolls off significantly below this frequency. In addition, the maximum low-frequency gain of the controller was limited by the stability margins described earlier. Increasing the gain of the controller would cause instability to occur.

The existing ASP array was also tested in a reverse orientation by rotating the module 180° in the measurement tube so that the transmitting panel was now facing the disturbance source as shown in Figure 3-21 (compare to Figure 3-18). This measurement was conducted to determine if the current hardware was bidirectional, or capable of the same TL in either direction through the module. The results from the reversed orientation TL measurement are shown in Figure 3-22.

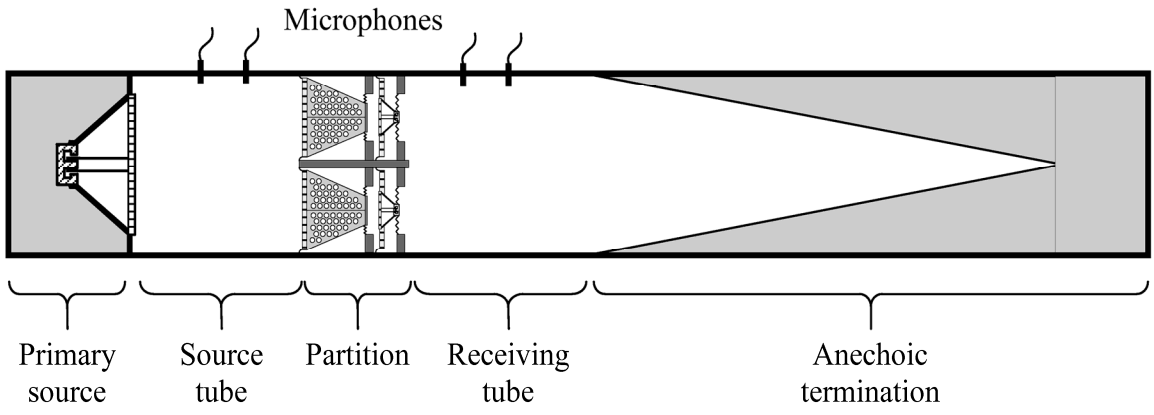

Figure 3-21. Schematic of the TL measurement apparatus used to test Leishman's ASP hardware.

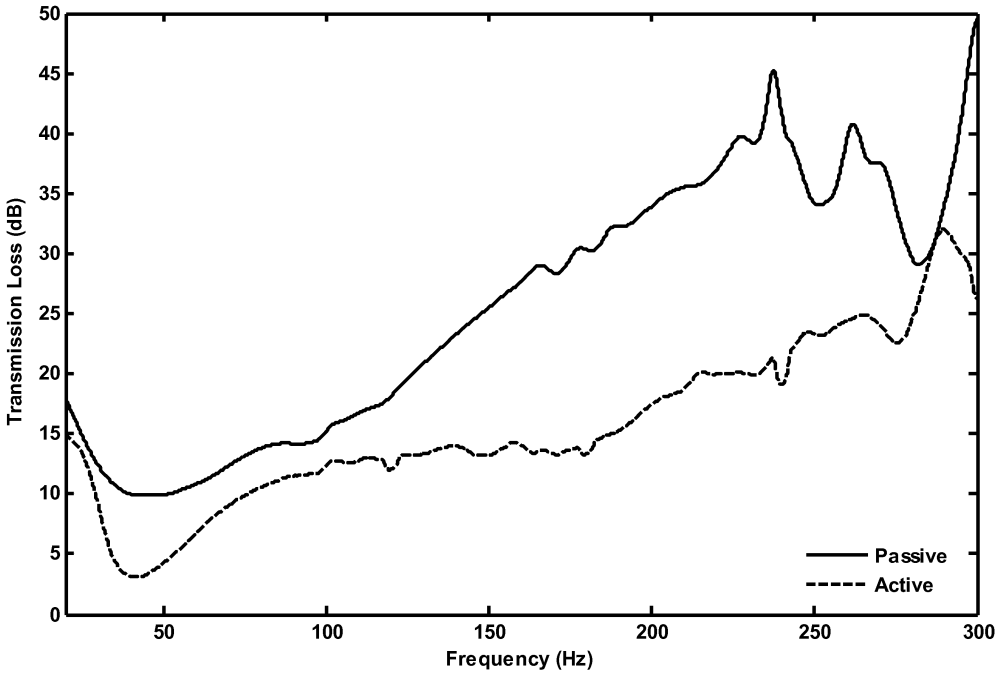

Figure 3-22. Measured TL for Leishman's ASP array in a reversed orientation with feedback cavity control.

The TL for the passive array in the reversed orientation was basically identical to the passive array in the original orientation. However, the active TL for the reversed array was much worse than the passive reversed array, indicating that the use of active control is this orientation produces worse results than simply using the module in its passive state.

It is apparent that this unidirectional behavior has to do with the sequence in which the disturbance pressure interacts with the array modules. In the reversed orientation, the incident pressure first interacts with the passive transmitting-side panel. When the disturbance reaches the pressure microphone inside the cavity, the loudspeaker works to minimize the pressure amplitude back upstream in the cavity. Although this may help to reduce the volume velocity amplitude of the transmitting-side panel looking

into the cavity, it is not guaranteed to produce zero net volume velocity on the downstream side of the ASP array. This characteristic proved to be an unfortunate drawback to the modules used in the existing ASP array.

3.11 PERFORMANCE NOTES

Although the previous lack of broadband random-noise control was overcome with the feedback controller, the existing hardware still produced only unidirectional TL performance. Many practical applications for ASP arrays necessitate bidirectional TL performance. With the cavity control approach, adding multiple control sources does not improve the bidirectional performance because only a single error sensor can be used – two error sensors does not add anything extra (remember that the pressure field is assumed uniform within the cavity). Trying to implement a bidirectional controller with a single error microphone could lead to a complex control scheme where the actuators end up fighting against one another.

The second limitation with the existing hardware and analog feedback control is the relatively mediocre improvement in the low-frequency TL. While the increase in the TL is substantial compared to the research reviewed in the literature section of this thesis, it pales in comparison to the maximum 55 dB achieved with the feed-forward controller on the same hardware. It should be noted, however, that Leishman's TL results were measured with single-frequency disturbances *and* feed-forward control whereas the results presented here used a broadband disturbance source and feedback control.

Step six of the controller design method suggests looping back through the design process if the control objectives were not accomplished. This is a logical step if the

performance of the controller is to blame for the missed objectives. A second alternative is to create a new module which could work better with the desired controller. Because of the inherent tradeoff between the gain of the controller at low frequencies and the maximum control bandwidth, the stability criterion for the feedback controller suggested that higher TL would be difficult to obtain with this hardware and an analog feedback controller. As a result, a new ASP module design will be presented in Chapter 5 of this thesis.

3.12 CONSIDERATIONS FOR FUTURE DESIGNS

Many practical applications would require a bidirectional ASP array. This means that the ASP array would be capable of minimizing sound transmission in both directions through the partition. Since the existing array does not possess this characteristic, a new module design is necessary. One of two design approaches could be utilized:

- Use cavity control but move the control source from the receiving-side panel into a symmetric position inside the cavity.
- Use panel control on one or both of the panels.

The drawback to the first design approach is the acoustic propagation delay introduced by having a non-collocated sensor and actuator pair. The propagation delay is recognized as a phase lag in $P(f)$ and subsequently limits the control bandwidth. This delay was manifest in the existing ASP hardware and was a limiting factor in the magnitude of the achievable active TL. The advantage of the design is that only a single sensor and actuator pair are required.

The drawback to the second design approach is that two sensor and actuator pairs would be needed—one for each panel. However, it is hypothesized that direct actuation of a two panel system might better lend itself to bidirectional control. Another advantage to this design approach is that the sensor and actuator pairs could be collocated (no acoustic propagation delay), improving the odds that an analog feedback controller could be effective. It would be desirable to have two independent controllers but one concern is that a fully-coupled MIMO controller would be necessary to counteract the acoustic coupling between the two panels. On the other hand, controlling both panels simultaneously might also have synergistic effects that improve the overall TL through the device.

The design of a two channel panel control scheme for a new ASP module will be discussed further in chapter 5. Analogous circuit models will be developed and used to predict the TL performance of the new module. Chapter 4 discusses a new method developed to measure parameter values for an enhanced model of a loudspeaker. It is presented first so that the enhanced model can be used in chapter 5.

4 AN EXPERIMENTAL PARAMETER EXTRACTION METHOD FOR AN ENHANCED LOUDSPEAKER DRIVER MODEL

This chapter presents a paper submitted to the Journal of the Audio Engineering Society. The formatting of the paper has been modified to meet the formatting requirements of this thesis.

4.1 CONTRIBUTING AUTHORS AND AFFILIATIONS

Jason D. Sagers
Department of Mechanical Engineering, 435 CTB, Brigham Young University, Provo, UT 84602; email: jsagers@byu.edu

Timothy W. Leishman
Department of Physics and Astronomy, N247 ESC, Brigham Young University, Provo, UT 84602; email: tim_leishman@byu.edu

Jonathan D. Blotter
Department of Mechanical Engineering, 435 CTB, Brigham Young University, Provo, UT 84602; email: jblotter@byu.edu

4.2 ABSTRACT

The classical model of a moving-coil loudspeaker driver contains a single degree of freedom and consequently only predicts a single resonance where both the cone and the surround move together in phase. An enhanced model of a moving-coil loudspeaker possesses two degrees of freedom and can predict the resonance state where the cone and surround are moving out of phase with each other. Several measurement methods exist to extract the parameters for use in the classical model but no measurement methods

currently exist to extract the parameters for the enhanced model. This paper introduces a scanning laser-based parameter extraction method for the enhanced model. The steps used to extract the parameters are described and extracted parameters are reported for seven different loudspeakers. The utility of the method is validated by using the enhanced model and the extracted parameters to predict the radiated on-axis pressure for the seven loudspeakers. The model predictions are compared to experimental data and the reduction in the sum of the squared error between the enhanced model and the classical model is reported.

4.3 NOMENCLATURE

a Effective radius of the cone (cone radius plus half of the surround width)

b Total radius of the moving-coil loudspeaker (measured to the outside edge of the surround)

BL Force factor of the moving-coil loudspeaker

c Speed of sound in the fluid medium

C_{MS} Effective mechanical compliance (classical model)

$C_{M\mathrm{n}}$ Effective mechanical compliance of the n^{th} element (enhanced model)

$C_{M\mathrm{mn}}$ Effective mechanical compliance coupling the m^{th} and n^{th} elements ($m \neq n$) (enhanced model)

$\hat{e}_g$ Complex control voltage of the moving-coil loudspeaker

f_s Primary cone resonance frequency of a loudspeaker (Hz)

f_{surr} Primary surround resonance frequency of a loudspeaker (Hz)

G_A Acoustic ground (ambient reference pressure)

G_M	Mechanical ground (zero reference velocity)
j	$\sqrt{-1}$
L_E	Electrical inductance of the voice coil in the moving-coil loudspeaker
m	Ratio of loudspeaker radii, = b/a
M_{MD}	Effective mechanical mass (classical model)
$M_{M\mathrm{n}}$	Effective mechanical mass of the n^{th} element (enhanced model)
$\hat{p}_A$	Complex acoustic pressure on the back of the loudspeaker cone (classical model)
$\hat{p}_B$	Complex acoustic pressure on the front of the loudspeaker cone (classical model)
$\hat{p}_{A,e}$	Complex acoustic pressure on the back of the loudspeaker cone (enhanced model)
$\hat{p}_{B,e}$	Complex acoustic pressure on the back of the surround (enhanced model)
$\hat{p}_{C,e}$	Complex acoustic pressure on the front of the loudspeaker cone (enhanced model)
$\hat{p}_{D,e}$	Complex acoustic pressure on the front of the surround (enhanced model)
R_E	Electrical resistance of the voice coil in a moving-coil loudspeaker
R_{MS}	Effective mechanical resistance (classical model)
$R_{M\mathrm{n}}$	Effective mechanical resistance of the n^{th} element (enhanced model)
$R_{M\mathrm{mn}}$	Effective mechanical resistance coupling the m^{th} and n^{th} elements ($\mathrm{m} \neq \mathrm{n}$) (enhanced model)
S_D	Surface area of the cone (classical model), = πa^2
S_{n}	Surface area of the n^{th} element (enhanced model)
$\hat{u}_D$	Complex normal velocity amplitude of the cone (classical model)
$\hat{u}_{\mathrm{n}}$	Complex normal velocity amplitude of the n^{th} element (enhanced model)
Z_{A1}	Acoustic impedance substitution
Z_{A2}	Acoustic impedance substitution

Z_{A3} Acoustic impedance substitution

Z_{A11} Self acoustic impedance of circular piston 1

Z_{A12} Mutual acoustic impedance between circular piston 1 and concentric annular piston 2

Z_{A22} Self acoustic impedance of annular piston 2

Z_{A33} Self acoustic impedance of circular piston 3

Z_E Total electrical impedance of the loudspeaker, $= R_E + j\omega L_E$

Z_{M1} Mechanical impedance substitution (enhanced model)

Z_{M2} Mechanical impedance substitution (enhanced model)

Z_{M12} Mechanical impedance substitution (enhanced model)

ρ_o Ambient density of the fluid medium

ω Angular frequency (rad/s), $= 2\pi f$

4.4 INTRODUCTION

Research interest in the development of high-fidelity loudspeakers has existed for most of the twentieth century. Beranek gives an excellent history of the evolution of loudspeaker design from 1915 to 1954 [64]. In this paper, Beranek discusses the fact that although the direct-radiator loudspeaker was invented in 1877, it did not prove to be a "faithful" device until Rice and Kellogg discovered the importance of shifting the resonance frequency of the diaphragm to the low-end of the frequency spectrum (circa 1925). When this design change was implemented, a much flatter response was achieved in the frequency band above the cone resonance frequency.

The low-frequency pressure response of loudspeakers can be predicted with dynamical system analogies. Beranek published his book, *Acoustics*, in 1954 [16] in which several chapters were devoted to analogous circuit modeling techniques for direct-radiator loudspeakers. Although he was not the first researcher to use analogous circuits to model loudspeakers [65, 66], his presentation formed the basis for the long standing analogous circuit model of a moving-coil loudspeaker. This model will be referred to in this paper as the "classical" model. Not only was the model a powerful tool that allowed for systematic design improvements of the loudspeaker drivers themselves, but it also provided a useful way to model the loudspeaker driver as an element of a larger acoustical system [67].

The classical model is a single degree of freedom system with lumped-element parameters which combine the physical properties of several loudspeaker elements into a single modeled value. The result of this approximation is a model which can only predict a single resonance frequency for the loudspeaker system. Although the classical model is usually accurate in describing the measured pressure response of the loudspeaker in the vicinity of its free-air cone resonance, f_s, the limitation of the classical model is that it cannot predict any other resonances above f_s. There are many undulations in the acoustic frequency response spectrum which remain unexplained by the classical model.

One resonance of particular importance is the second system resonance of the loudspeaker where the surround and cone are moving out of phase. This will be referred to in this paper as the primary resonance of the surround. Olson et al. [68] noted that this behavior could cause significant undulations in the radiated acoustic pressure. Since this phenomenon cannot be predicted with the classical model, it is more difficult to make

systematic design changes to improve the acoustic response of the loudspeaker at this resonance frequency. Although this phenomenon was identified by Olson more than half a century ago, little research has been conducted to model this effect with analogous circuit techniques.

The effect of the surround resonance is important to other research fields as well. In some active TL devices, a loudspeaker-like setup is used wherein a stiff panel is connected to a rigid interstitial support using a resilient material (similar to that of a loudspeaker surround). The resilient connection serves both to reduce the mechanical flanking path from one panel through the interstitial support into another panel and to provide an airtight seal around the panel. An electromechanical actuator is used in conjunction with an active control scheme to drive the normal surface velocity of the panel to zero. In this way, the panel does not vibrate and will not transmit sound pressure from one side of the panel to the other. However, because the resilient connection introduces an additional degree of freedom into the system, it is permitted to vibrate even if the panel does not move. In the event that this occurs, sound will transmit through the resilient connection and degrade the TL of the partition.

A more complete model of a loudspeaker, presented by Leishman [46], possesses two degrees of freedom. This model will be referred to in this paper as the "enhanced" model of a loudspeaker. In the enhanced model, the surround is represented as a separate mass with an accompanying radiating area. New compliance and resistance elements are introduced in the model which couple the surround to the cone. The result is a loudspeaker model with two degrees of freedom and the ability to predict a surround resonance.

Many techniques exist to extract the lumped-parameter values for use in the classical model [69-88]. These techniques include electrical impedance measurements, plane-wave tube measurements, and laser transducer measurements. The classical model parameters can be extracted from one or more measurements of the loudspeaker and are typically determined via a curve-fit. The extracted classical model parameters can then be used directly and effectively in a classical analogous circuit model to predict the acoustic behavior over low- to mid-frequency ranges, depending on the properties of the loudspeaker.

The current drawback to the enhanced model is the lack of a measurement method to extract the enhanced model parameters. If these parameters could be obtained experimentally for an arbitrary loudspeaker driver, it would then be possible to use the enhanced model to better predict loudspeaker behavior and to make systematic design changes that improve its fidelity. The purpose of this paper is to introduce a parameter extraction method so that enhanced loudspeaker parameters can be determined experimentally.

4.5 PARAMETER EXTRACTION METHOD

The parameter extraction method developed in this paper can be divided into six steps. The steps are listed in Table 4-1. Each of these steps will be described in detail in a separate section. For illustrative purposes for steps 3-6, results from an actual loudspeaker will accompany the description to highlight points of interest. The parameter extraction method will then be used to extract parameters for seven different loudspeakers.

Table 4-1. Six step process for extracting enhanced loudspeaker parameters.

1. Develop enhanced model loudspeaker equations
2. Directly measure five loudspeaker parameters: a, b, BL, R_E, *and* L_E
3. Measure $(\hat{u}_1/\hat{e}_g)$ and $(\hat{u}_2/\hat{e}_g)$ at several points using a scanning laser
4. Compute $(\hat{u}_1/\hat{e}_g)_{avg}$ and $(\hat{u}_2/\hat{e}_g)_{avg}$ for the measured data
5. Determine f_{surr} to use as a constraint in the curve-fit
6. Curve-fit to extract the unknown loudspeaker parameters: M_{M1}, M_{M2}, C_{M1}, C_{M2}, C_{M12}, R_{M1}, R_{M2}, and R_{M12}

4.5.1 STEP 1: DEVELOP ENHANCED MODEL LOUDSPEAKER EQUATIONS

This section provides a detailed overview of the classical and enhanced loudspeaker models. The equations needed for the parameter extraction method are also presented.

4.5.1.1 OVERVIEW OF THE CLASSICAL MODEL AND THE ENHANCED MODEL

The classical lumped-parameter loudspeaker model is widely used in many areas of acoustic-related research and in the audio engineering community. The model is straightforward to use because of the small number of loudspeaker parameters that it requires and the fact that the parameter extraction techniques are well established. However, one limitation of the classical model is that it only provides an accurate estimation at low frequencies where the lumped-parameter approximation is valid.

The long standing classical model of a moving-coil loudspeaker [16, 67] uses seven key parameters to approximate the electro-mechano-acoustical elements of the actual loudspeaker: the force factor BL, the effective mechanical compliance C_{MS}, the electrical inductance of the voice-coil L_E, the effective mechanical mass M_{MD}, the electrical resistance of the voice-coil R_E, the effective mechanical resistance R_{MS}, and the effective surface area of the cone S_D. The mechanical components that the key parameters represent in the model are shown in Figure 4-1. A resilient surround connecting the basket to the cone is not shown in this figure since it is not accounted for in the model. The voltage input to the loudspeaker is represented by $\hat{e}_g$ and the presumably uniform normal surface velocity of the cone is represented by $\hat{u}_D$.

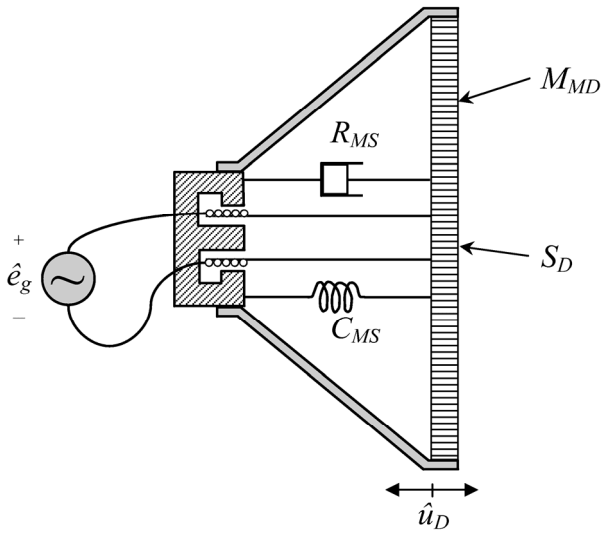

Figure 4-1. Key mechanical components of the classical model of a loudspeaker.

The classical model uses a simplifying lumped-element approximation in four of the parameters: C_{MS}, M_{MD}, R_{MS}, and S_D. This approximation combines several physical elements of the loudspeaker into single modeled parameters. The mechanical compliances of the

spider and surround are combined to create the overall compliance, C_{MS}. In a similar fashion, R_{MS} represents the combined resistances of both the spider and surround. The mechanical masses of the voice coil, former, cone, leads, dust cap, adhesives, and both suspensions are combined to create the total moving mass, M_{MD}. The classical model of a loudspeaker only has one radiating surface, S_D, so the effective radius a is usually measured from the center of the cone to the middle of the surround.

The multiple-domain analogous circuit representing the time-harmonic behavior of the loudspeaker is shown in Figure 4-2. The two gyrators represent the necessary connection between the acoustic impedance domain and the mechanical mobility domain. The electrical components of the moving-coil driver have been transformed into the mechanical mobility domain and are shown in the figure as an ideal current source in parallel with the internal electrical impedance of the driver. The acoustic radiation impedance Z_{AR} seen by the front and back of the cone is assumed to be equal (sides B and A respectively).

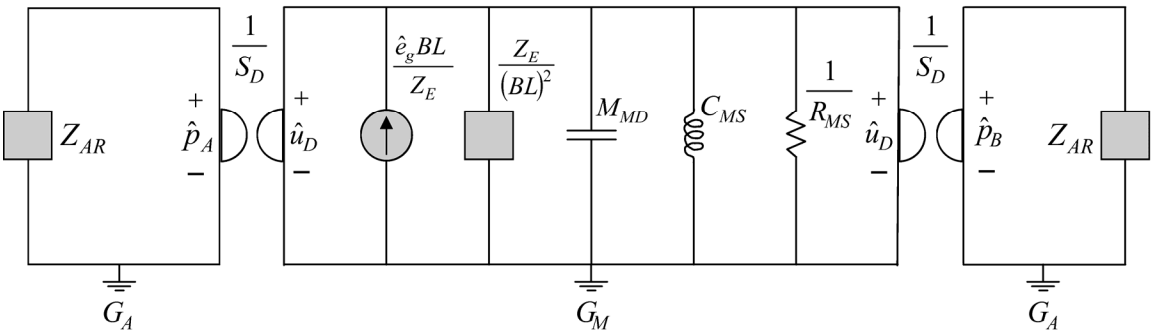

Figure 4-2. Multiple-domain analogous circuit representing the key mechanical components of the classical model shown in Figure 4-1.

In contrast to the classical model, the enhanced model contains individual element representations for each of the physical components. For example, the effective mass of the cone (M_{M1}) is separate from the effective mass of the surround (M_{M2}). There is also a compliance and resistance value for the spider (C_{M1} and R_{M1}). There is a compliance and resistance value connecting the basket to the outer perimeter of the surround (C_{M2} and R_{M2}) and a separate compliance and resistance value connecting the inside perimeter of the surround to the outside perimeter of the cone (C_{M12} and R_{M12}). The enhanced model has two radiating surface areas: the presumably uniform surface velocity of the cone (represented by $\hat{u}_1$) and the presumably uniform surface velocity of the surround (represented by $\hat{u}_2$). The addition of these extra parameters gives the enhanced model two degrees of freedom whereas the classical model only has one. The mechanical components of the enhanced model are shown in Figure 4-3.

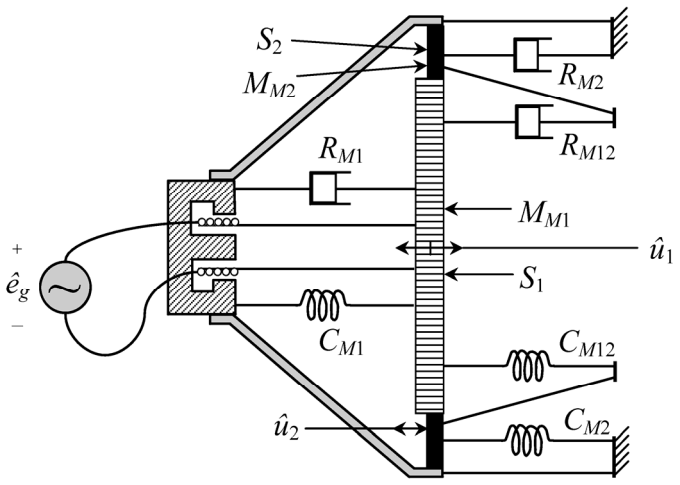

Figure 4-3. Key mechanical components of the enhanced model of a loudspeaker.

The multiple-domain analogous circuit representing the time-harmonic behavior of the loudspeaker is shown in Figure 4-4. The four gyrators represent the necessary connection between the acoustic impedance domain and the mechanical mobility domain. As with the circuit for the classical model, the electrical components of the moving-coil driver are shown in the mechanical mobility domain as an ideal current source in parallel with the internal electrical impedance of the driver. Note that the self and mutual acoustic radiation impedances (Z_{A11}, Z_{A22}, and Z_{A12}) of the two radiating areas are included in the acoustic domain sections of the circuit.

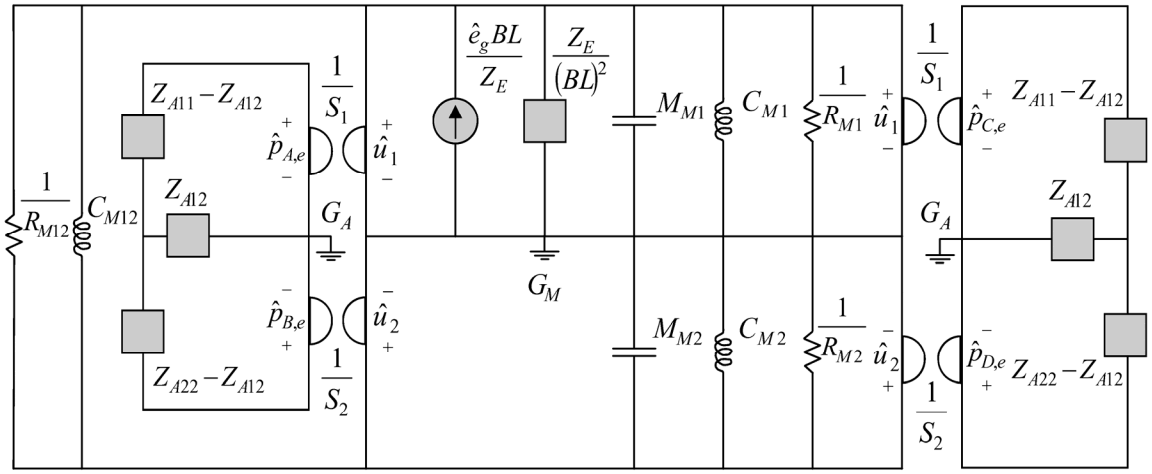

Figure 4-4. Multiple-domain analogous circuit representing the components of the enhanced model shown in Figure 4-3.

The enhanced model represents an improvement in modeling capability by eliminating the need for the lumped-parameter assumption in the radiating elements. This will allow the model to predict two system resonances. However, it still assumes that the cone and the surround both move as uniformly vibrating surfaces. As a result, the enhanced model will not predict undulations in the acoustic frequency response

spectrum which correspond to violations of the uniform vibration assumption (i.e., resonances where the cone and surround break-up into modal patterns).

4.5.1.2 ENHANCED LOUDSPEAKER MODEL EQUATIONS

The characteristic response quantities from the analogous circuit model are the uniform surface velocities of the cone and surround ($\hat{u}_1$ and $\hat{u}_2$ respectively). These quantities are represented as potential quantities in the mechanical mobility domain of Figure 4-4. The equations derived from the analogous circuit model can easily be represented as mobility FRFs (i.e., $\hat{u}_1$ and $\hat{u}_2$ divided by $\hat{e}_g$) which will later be utilized in the parameter extraction method. These equations will be presented in this section.

Nodal analysis techniques can be used with the circuit shown in Figure 4-4 to produce equations for $\hat{u}_1/\hat{e}_g$ and $\hat{u}_2/\hat{e}_g$. The development of these equations is too lengthy to include in this paper so only the equations required to model the response of the loudspeaker are reported. The mobility FRFs are

$$\frac{\hat{u}_1}{\hat{e}_g} = \frac{BL}{Z_E}\left(\frac{Z_{A3}}{Z_{A1}Z_{A3} - Z_{A2}^2}\right), \tag{4.1}$$

$$\frac{\hat{u}_2}{\hat{e}_g} = \frac{BL}{Z_E}\left(\frac{Z_{A2}}{Z_{A1}Z_{A3} - Z_{A2}^2}\right). \tag{4.2}$$

Equations (4.1) and (4.2) contain three impedance substitutions (Z_{A1}, Z_{A2}, and Z_{A3}) which were defined so that the equations could be displayed in compact form. The definition of these impedance substitutions are

$$Z_{A1} = 2Z_{A11}S_1^{\,2} + Z_{M1} + Z_{M12}\,, \tag{4.3}$$

$$Z_{A2} = Z_{M12} - 2Z_{A12}S_1S_2\,, \tag{4.4}$$

$$Z_{A3} = 2Z_{A22}S_2^{\,2} + Z_{M2} + Z_{M12}\,. \tag{4.5}$$

Likewise, Eq. (4.3) through Eq. (4.5) contain mechanical impedance substitutions which are defined as

$$Z_{M1} = \frac{BL^2}{Z_E} + R_{M1} + \frac{1}{j\omega C_{M1}} + j\omega M_{M1}\,, \tag{4.6}$$

$$Z_{M2} = R_{M2} + \frac{1}{j\omega C_{M2}} + j\omega M_{M2}\,, \tag{4.7}$$

$$Z_{M12} = R_{M12} + \frac{1}{j\omega C_{M12}}\,. \tag{4.8}$$

Equations (4.3) through (4.5) also contain three acoustic radiation impedance terms: Z_{A11}, Z_{A22}, and Z_{A12}. The radiation impedance felt by the loudspeaker during the parameter extraction method will affect the measured surface velocities. Consequently, it is important to include an appropriate model of the radiation impedances. The radiation impedances depend on the mounting condition of the loudspeaker. For this research, the loudspeakers under test were mounted in a large baffle (2.5 m x 2.5 m) located in a fully anechoic chamber. This mounting configuration was chosen because of the possibility for an analytical solution for radiation impedances. Other mounting conditions could also be used as long as the radiation impedances are properly accounted for.

The self and mutual radiation impedances for a piston and a concentric annular piston may be used to model a loudspeaker. The radiation impedances for a circular piston with a concentric annular piston mounted in an infinite baffle were solved by Stepanishen [89-91] and a similar development was also given by Thompson [92]. A diagram of this configuration is shown in Figure 4-5. The inner piston (white) has a radius a and will be designated by the number 1 in the mathematical equations that will follow. The concentric annular piston (shaded) has outer radius b and inner radius a and will be designated by the number 2. One additional piston is needed in order to develop the equations for the radiation impedances. This piston comprises both of the previous pistons, has a total radius b, and will be designated by the number 3.

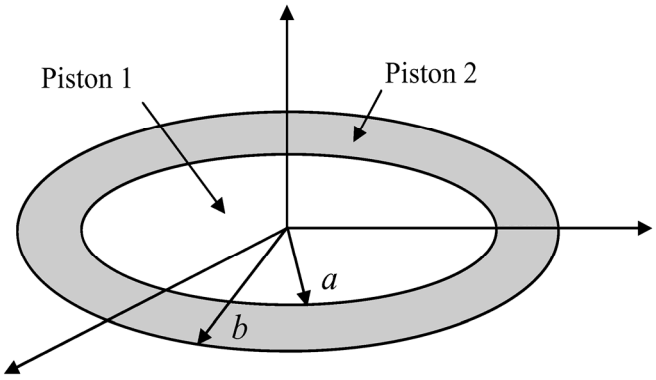

Figure 4-5. A circular piston (white) surrounded by an annular piston (shaded).

The self acoustic impedances of pistons 1 and 3 are well known [11, pg. 186] and are defined in Eq. (4.9) and Eq. (4.10) where J_1 is the Bessel function of the first kind and order and H_1 is the Struve function of first order.

$$Z_{A11} = \left(\frac{\rho_0 c}{\pi a^2}\right)\left(1 - \frac{J_1(2ka)}{ka} + j\frac{H_1(2ka)}{ka}\right), \quad \textbf{(4.9)}$$

$$Z_{A33} = \left(\frac{\rho_0 c}{\pi b^2}\right)\left(1 - \frac{J_1(2kb)}{kb} + j\frac{H_1(2kb)}{kb}\right). \quad \textbf{(4.10)}$$

The mutual acoustic impedance between pistons 1 and 2 was developed by Stephanishen and is repeated here in terms of the acoustic impedance Z_{A12} where $m = b/a$ [91, Eq. 23]:

$$Z_{A12} = \left(\frac{\rho_o c}{\pi a^2}\right)\left[\frac{J_1(2ka)}{ka} - j\frac{H_1(2ka)}{ka} - \frac{1}{\pi}e^{-jkb}\int_0^{\pi}\left[\frac{\sqrt{4m^2 - 4m\cos(\theta) - \sin^2(\theta)}}{m - \cos(\theta)}e^{jka\cos(\theta)}\sin^2(\theta)\right]d\theta\right]. \quad \textbf{(4.11)}$$

There is an error in Eq. (22) and Eq. (23) of Stepanishen's 1974 paper that was found by the authors of this paper: the $2m\cos(\theta)$ under the radical should be $4m\cos(\theta)$. This change is reflected in the version of Z_{A12} shown in this paper as Eq. (4.11). The self acoustic impedance of the annular piston is simply derived from Thompson's paper [92, Eq. 1]:

$$Z_{A22} = \left(\frac{b^2 Z_{A33} - a^2 Z_{A11} - 2a^2 Z_{A12}}{b^2 - a^2}\right). \quad \textbf{(4.12)}$$

Equations (4.1) through (4.12) are the equations used in this paper for the enhanced loudspeaker model.

4.5.2 STEP 2: DIRECTLY MEASURE *a*, *b*, *BL*, R_E, AND L_E

Several loudspeaker parameters can be measured directly and therefore do not need to be determined from the parameter extraction method: *a, b, BL,* R_E*, and* L_E. The two representative radii for the loudspeaker can be measured with calipers. The first radius, *a*, is measured from the center of the cone to a point located halfway across the width of the surround. The second radius, *b*, is measured from the center of the cone to the outside edge of the surround. The electrical voice-coil resistance R_E, the electrical voice-coil inductance L_E, and the force-factor *BL* can be measured using existing Thiele-Small parameter extraction methods. These parameters can be determined in a matter of minutes using commercially available packages such as the MLSSA (maximum-length sequence system analyzer) system [93].

4.5.3 STEP 3: MEASURE $\hat{u}_1/\hat{e}_g$ and $\hat{u}_2/\hat{e}_g$ USING A SCANNING LASER

The remaining mechanical parameters of the enhanced loudspeaker model (M_{M1}, M_{M2}, C_{M1}, C_{M2}, C_{M12}, R_{M1}, R_{M2}, and R_{M12}) cannot be measured directly. However, these parameters may be determined by curve-fitting measured mobility FRFs to the mobility FRFs of the enhanced analogous circuit model (Eq. (4.1) and Eq. (4.2)). Because the characteristic response quantities of the analogous circuit include surface velocities, it is logical to measure the actual response of the loudspeaker using $\hat{u}_1/\hat{e}_g$ and $\hat{u}_2/\hat{e}_g$. A scanning laser Doppler vibrometer (SLDV) is capable of making these measurements. An SLDV is a non-destructive, non-invasive measurement system, so there are no mass or stiffness loading effects—this is critical to accurately measuring the loudspeaker parameters without having to compensate for the measurement method.

An SLDV is a precision measurement tool. The mirrors inside the scanning head can be positioned with an angular resolution of 0.002° and with a 1 m stand-off distance, the spot size of the laser is 73 μm. The velocity noise floor of the SLDV is typically less than 1 μm/s/(Hz)$^{1/2}$ [94]. In addition, the scanning laser can take measurements at hundreds of points on the surfaces of the cone and surround in a matter of minutes. This will be important in the next step of the parameter extraction process when the measured mobility FRFs are spatially averaged.

The SLDV measurement took place in a fully anechoic chamber. The loudspeaker under test was mounted in the center of a 2.5 m x 2.5 m baffle, which was raised 0.3 m off the cable floor. The deck of the baffle was constructed from several sections of 1.3 cm thick MDF with rabbeted edges between the sections so that the surface of baffle was airtight and smooth. The laser head was positioned directly above the loudspeaker under test at a standoff distance of 1.2 m. A photograph of the measurement arrangement is shown in Figure 4-6.

Over four hundred measurement points were taken on the surface of the loudspeaker. The majority of the points were located on the loudspeaker cone, but care was also taken to place at least eight scan points across the width of the surround. Three different scan point grid patterns were investigated (rectilinear, honeycomb, and radial) but the radial grid pattern provided the easiest way to later separate the measured scan points into cone and surround categories. A typical scan point density used in this paper is shown in Figure 4-7. The boundaries for the cone and surround are superimposed on top of the image.

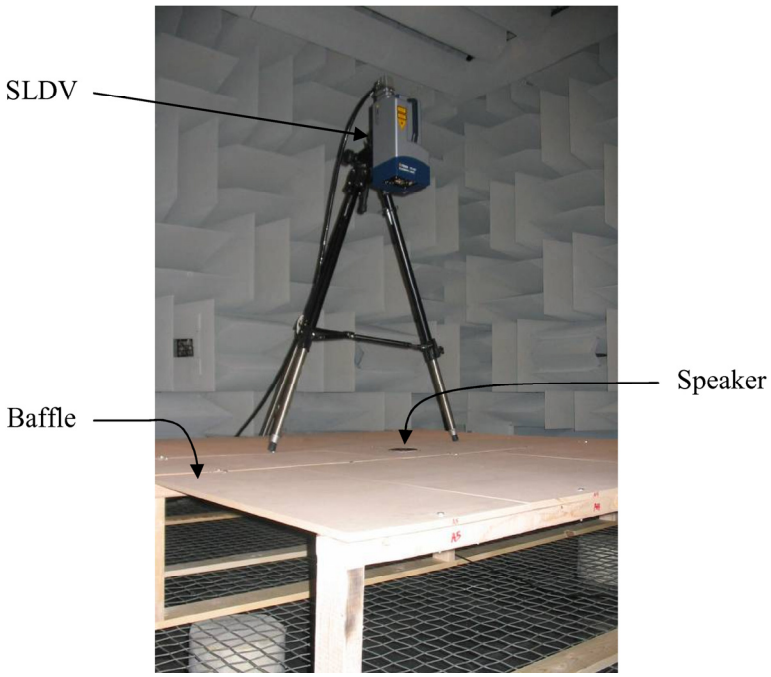

Figure 4-6. SLDV measurement setup.

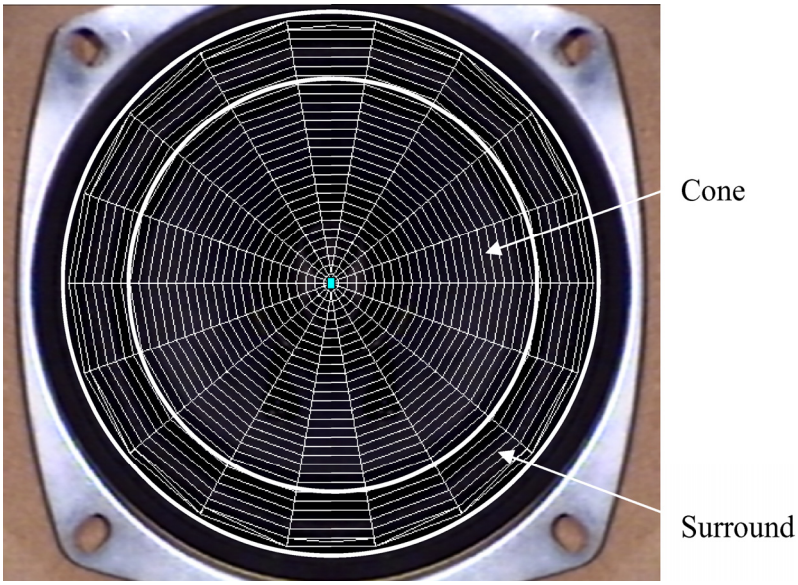

Figure 4-7. Example of the SLDV scan point density.

The fine spatial resolution of the laser is critical to measuring enough points on the cone and the surround so that a good spatial average can be obtained for the surface velocities. It should be noted that the laser will only measure the component of the surface velocity in the direction of the laser beam (which can be approximately normal to the surface of the loudspeaker with sufficient stand-off distance between the laser head and the loudspeaker under test).

For this research, the loudspeaker was excited by white noise and $\hat{u}_1/\hat{e}_g$ and $\hat{u}_2/\hat{e}_g$ were measured at each scan point with the laser vibrometer. It should be noted that the reason for measuring the mobility FRFs (instead of just $\hat{u}_1$ and $\hat{u}_2$) is because this formulation suppresses random variations in the measured surface velocity due to random fluctuations in the excitation voltage. This leads to more consistent and repeatable measurements as the laser scans from point to point across the surface.

4.5.4 STEP 4: COMPUTE $(\hat{u}_1/\hat{e}_g)_{avg}$ AND $(\hat{u}_2/\hat{e}_g)_{avg}$ FOR THE MEASURED DATA

The analogous circuit model assumes that the cone and surround are vibrating uniformly at all spatial positions. In order to approximate uniform vibration from the measured data, spatial averaging was used. The data from the scan points was separated into two categories: points located on the cone and points located on the surround. The cone data points were spatially averaged to obtain $(\hat{u}_1/\hat{e}_g)_{avg}$. This computation was performed by averaging together the real part of the FRF from each cone point and then by averaging together the imaginary part of the FRF from each cone point. The average real and imaginary parts were recombined to form $(\hat{u}_1/\hat{e}_g)_{avg}$. Likewise, the surround points were spatially averaged to obtain $(\hat{u}_2/\hat{e}_g)_{avg}$. These two quantities are complex

valued and provide the 'measured data' from which the parameters of the enhanced model will be extracted. An example of the measured real and imaginary parts of $(\hat{u}_1/\hat{e}_g)_{avg}$ and $(\hat{u}_2/\hat{e}_g)_{avg}$ are shown in Figure 4-8 for a Radio Shack 40-1197 loudspeaker.

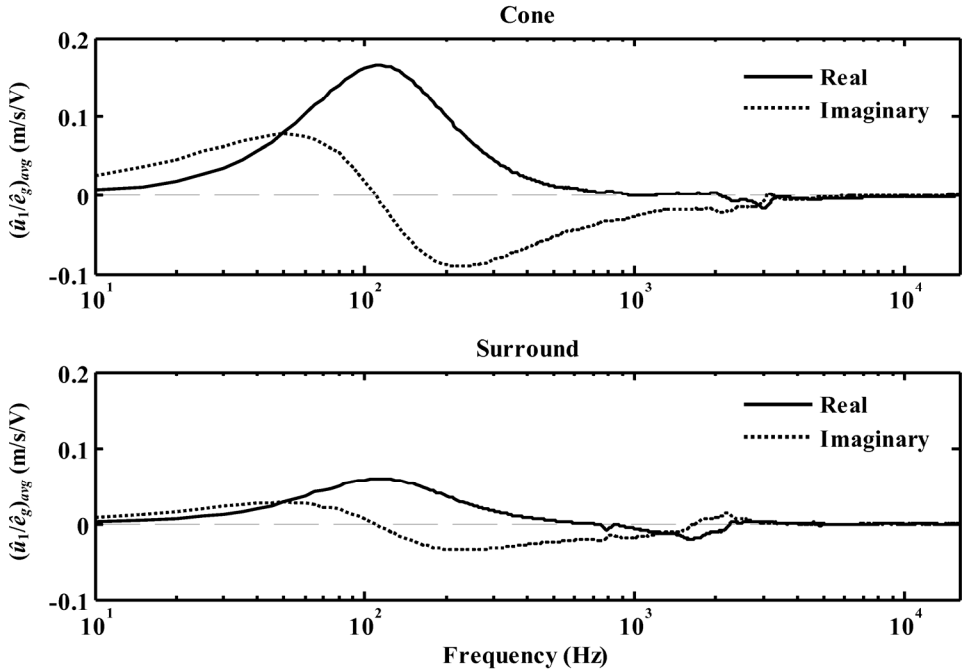

Figure 4-8. Spatially averaged mobility FRFs from a Radio Shack 40-1197 cone (top) and surround (bottom).

4.5.5 STEP 5: DETERMINE f_{surr} TO SERVE AS A CONSTRAINT IN THE CURVE-FIT

The ability to uniquely and reliably identify the surround resonance frequency f_{surr} is an important step in the parameter extraction process. The measured frequency for f_{surr} will serve as a constraint in the curve-fit. This will constrain the model to have a surround resonance at the same frequency as the measured loudspeaker. This section presents a reliable way to determine f_{surr}.

For mobility FRFs, resonance frequencies correspond to where the imaginary part of $(\hat{u}_1/\hat{e}_g)_{avg}$ or $(\hat{u}_2/\hat{e}_g)_{avg}$ crosses zero [95, pg. 461]. According to this criterion, the first resonance frequency of the cone and surround is identifiable from the measured data shown in Figure 4-8 and occurs near 110 Hz. While the cone resonance frequency can usually be identified by inspection after plotting the real and imaginary parts of $(\hat{u}_1/\hat{e}_g)_{avg}$, the surround resonance frequency is more difficult to ascertain by this method. An alternative method must be used to consistently identify this frequency.

After the mobility FRFs were measured with the laser and $(\hat{u}_1/\hat{e}_g)_{avg}$ or $(\hat{u}_2/\hat{e}_g)_{avg}$ were computed, the modal indicator function (MIF) [96] was utilized to clearly identify both the cone and surround resonance frequencies. For a mobility FRF, the MIF is defined as the imaginary part of the FRF divided by the magnitude of the FRF at each frequency ($n = 1$ for the cone and $n = 2$ for the surround):

$$MIF_n = \frac{\mathrm{Im}\left(\hat{u}_n/\hat{e}_g\right)_{avg}}{\left|\left(\hat{u}_n/\hat{e}_g\right)_{avg}\right|}. \qquad \textbf{(4.13)}$$

When plotted on a log scale, resonances show up as strong dips in the MIF. This is due to the fact that the imaginary part of the FRF passes through zero at the point of resonance while the absolute value of the FRF is large in this same region. The overall effect is to divide a number very close to zero by a large number, which when plotted on a log scale will appear as a sharp notch which tends towards negative infinity.

The MIF was computed for both $(\hat{u}_1/\hat{e}_g)_{avg}$ and $(\hat{u}_2/\hat{e}_g)_{avg}$ for the Radio Shack 40-1197 loudspeaker and is shown in Figure 4-9. This figure suggests that the cone and surround undergo a mutual resonance near 110 Hz but that only the surround experiences

a resonance near 1.67 kHz. It was interesting to discover that the cone did not experience a resonance (according to the MIF) at f_{surr}.

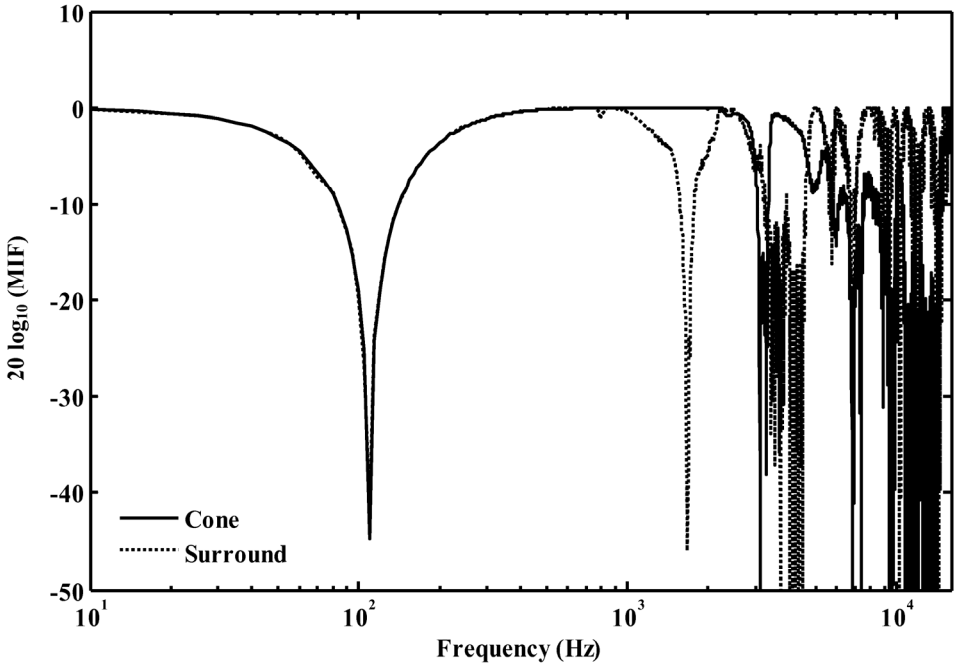

Figure 4-9. MIFs for the cone and surround of a Radio Shack 40-1197 loudspeaker.

If the surround MIF is divided by the cone MIF, the result should produce a curve wherein the first dip corresponds to the primary resonance frequency of the surround. The division of the surround MIF by the cone MIF will be referred to as the surround resonance indicator function (SRIF) and is computed according to

$$SRIF = \frac{MIF_{surround}}{MIF_{cone}}. \tag{4.14}$$

Both the MIF and the SRIF functions increase the observational sensitivity to the cone and surround resonance frequencies. Furthermore, the SRIF was created so that the primary surround resonance was easily identifiable. The SRIF for the Radio Shack 40-

1197 loudspeaker is shown in Figure 4-10. From this plot it was verified that the primary surround resonance occurs at 1.67 kHz. This is the frequency at which the surround experiences uniform motion that is out of phase with the uniform motion of the cone. All of the clear dips and peaks above 2 kHz correspond to frequencies at which the cone and surround break up and no longer satisfy lumped-parameter approximations. This additional characteristic of the SRIF shows where the cone and surround break-up resonances are independent of each other. Independent surround break-ups point downward and independent cone break-ups point upward on the SRIF plot.

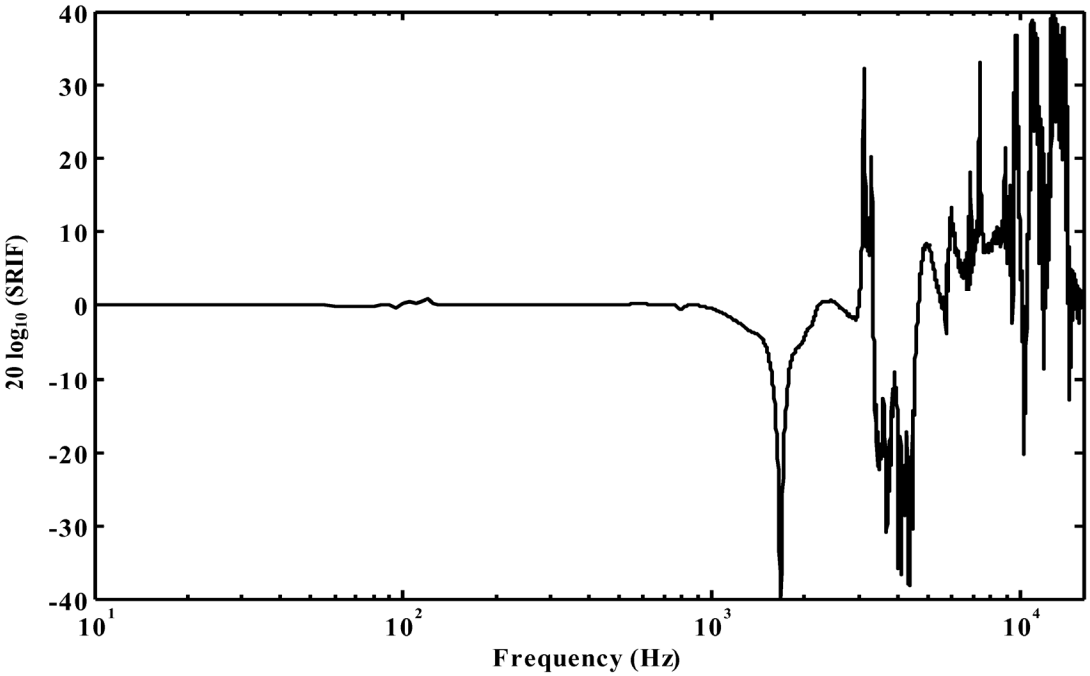

Figure 4-10. SRIF plot for the Radio Shack 40-1197 loudspeaker.

The accuracy of the SRIF function was verified by graphically examining the operating deflection shape of the loudspeaker at 1.67 kHz. It is seen in Figure 4-11 that the cone and surround move out of phase at f_{surr}.

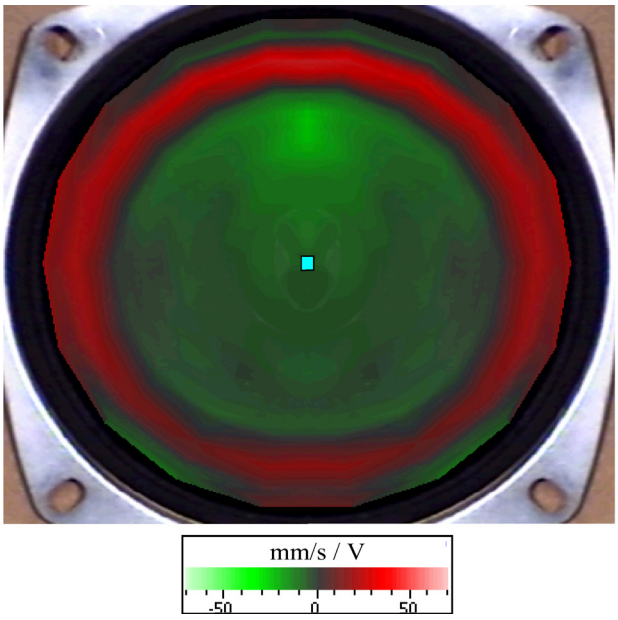

Figure 4-11. Operating deflection shape at f_{surr} for the Radio Shack 40-1197 loudspeaker.

4.5.6 STEP 6: CURVE-FIT THE MODEL TO THE MEASURED DATA TO EXTRACT THE UNKNOWN MODEL PARAMETERS

The purpose of the curve-fit is to extract the unknown enhanced model parameter values from the measured, spatially averaged, mobility FRFs. A MATLAB constrained optimization function (fmincon) was used to accomplish this. As is often done in Thiele-Small parameter measurement methods, the enhanced model was curve-fitted to the measured data by adjusting parameter values to minimize the sum of the squared error (SSE). A fitness function was constructed to compute the SSE between the real and imaginary parts of the measured FRFs and the real and imaginary parts of the FRFs predicted by the enhanced model. The fitness function was defined as

$$Fitness = \sum_f \frac{1}{4} \left\{ \begin{array}{l} \left[\mathrm{Re}\left(\frac{\hat{u}_1}{\hat{e}_g} \right)_{\substack{avg, \\ meas}} - \mathrm{Re}\left(\frac{\hat{u}_1}{\hat{e}_g} \right)_{\substack{avg, \\ pred}} \right]^2 + \left[\mathrm{Im}\left(\frac{\hat{u}_1}{\hat{e}_g} \right)_{\substack{avg, \\ meas}} - \mathrm{Im}\left(\frac{\hat{u}_1}{\hat{e}_g} \right)_{\substack{avg, \\ pred}} \right]^2 \\ + \left[\mathrm{Re}\left(\frac{\hat{u}_2}{\hat{e}_g} \right)_{\substack{avg, \\ meas}} - \mathrm{Re}\left(\frac{\hat{u}_2}{\hat{e}_g} \right)_{\substack{avg, \\ pred}} \right]^2 + \left[\mathrm{Im}\left(\frac{\hat{u}_2}{\hat{e}_g} \right)_{\substack{avg, \\ meas}} - \mathrm{Im}\left(\frac{\hat{u}_2}{\hat{e}_g} \right)_{\substack{avg, \\ pred}} \right]^2 \end{array} \right\}. \quad \textbf{(4.15)}$$

The resonance frequency of the surround in the model was constrained during the curve-fit to occur at the same frequency as the measured surround resonance (as indicated by the SRIF). In addition, all model values were constrained to be greater than zero. Since the fmincon function requires an initial guess for the values of the parameters, the Thiele-Small parameters (M_{MD}, C_{MS}, R_{MS}) were used as the starting guesses for the respective unknown variables (M_{M1}, M_{M2}, C_{M1}, C_{M2}, C_{M12}, R_{M1}, R_{M2}, and R_{M12}). Upper and lower bounds were placed on the allowable values for the unknown variables. Although the initial guess for the bounds was somewhat arbitrary, the bounds were relaxed in the event that they became binding during the curve-fit.

The curve-fitting process was performed and the extracted enhanced parameter values for the Radio Shack 40-1197 loudspeaker are shown in Table 4-2, along with the previously measured Thiele-Small parameters. Recall that BL, L_E, and R_E from the Thiele-Small parameter measurement were used as known values in the enhanced parameter extraction method.

The curve-fit from the enhanced model and the measured data for the cone are shown in Figure 4-12. The quality of the curve-fit for the enhanced model was very good as evidenced by the close graphical agreement between it and the measured data. The $\hat{u}_D/\hat{e}_g$ curve predicted by the classical model (with the measured Thiele-Small parameters)

is also included in the figure in order to show the improved accuracy that is obtained with the enhanced model.

Table 4-2. Parameter values for the Radio Shack 40-1197.

Measured Thiele-Small Parameters			Extracted Enhanced Model Parameters		
Parameter	Value	Units	Parameter	Value	Units
BL	4.648	TM	M_{M1}	3.0007	g
C_{MS}	751.7	μm/N	M_{M2}	0.0296	g
f_s	117.2	Hz	C_{M1}	2500.0	μm/N
L_E	0.161	mH	C_{M2}	293.73	μm/N
M_{MD}	2.454	g	C_{M12}	534.19	μm/N
R_{MS}	0.442	kg/s	R_{M1}	0.6755	kg/s
R_E	7.648	Ω	R_{M2}	0.1596	kg/s
S_D	47.78	cm^2	R_{M12}	0.0558	kg/s

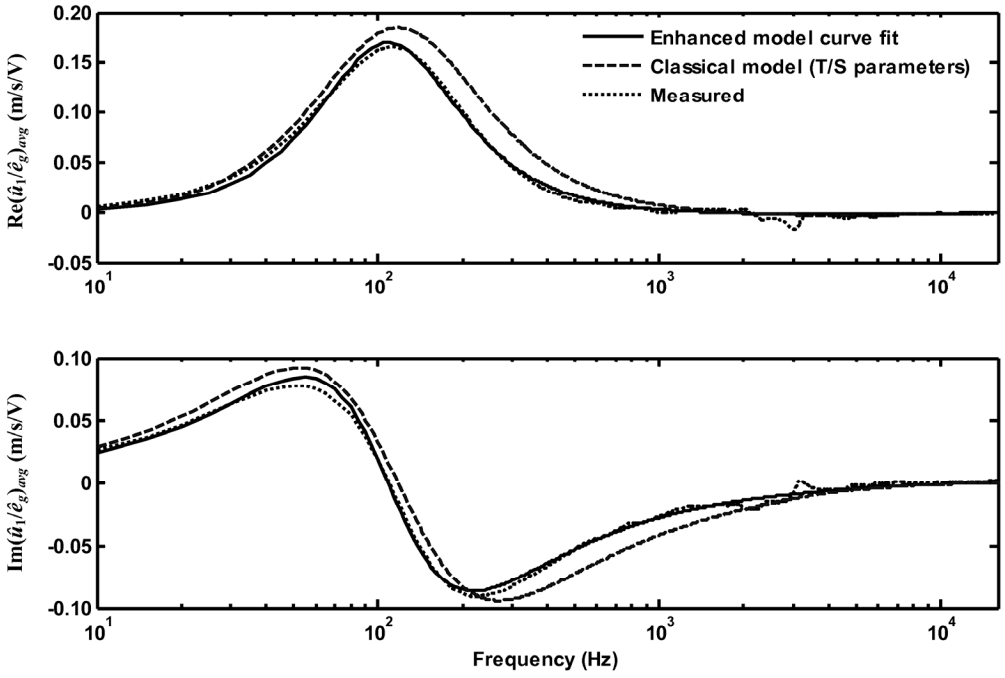

Figure 4-12. Curve-fitted and measured data for the cone FRF of the Radio Shack 40-1197 loudspeaker in comparison to the classical model.

The curve-fit for the enhanced model and the measured data for the surround are shown in Figure 4-13. Again, the quality of the curve-fit for the enhanced model was very good. In this case, it was not possible to show how the classical model compared to the enhanced model since the classical model is not even capable of predicting the vibration of the surround.

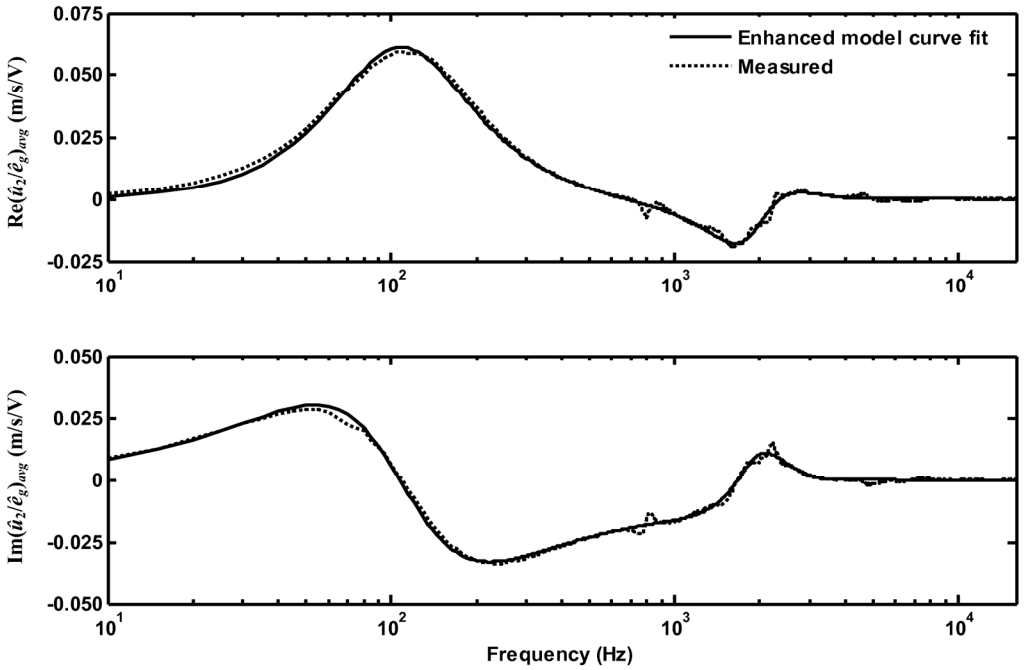

Figure 4-13. Curve-fitted and measured data for the surround FRF of the Radio Shack 40-1197 loudspeaker.

The values of the parameters that were returned from the curve-fitting process are a result of minimizing the SSE between the measured curves and the modeled curves. As with most multi-parameter curve-fitting processes, it is impossible to guarantee that this is a unique solution. However, to gain confidence that the solution reported in this paper is repeatable, the curve-fitting process was started with multiple starting values for the

enhanced parameters. The curve-fitting process produced parameter values within a few percent of the same final value regardless of the starting point. The values that were extracted are also on the same order of magnitude as the Thiele-Small parameter values. This adds another measure of confidence in the results.

4.6 ENHANCED MODEL PARAMETERS FOR SEVEN LOUDSPEAKERS

The parameter extraction method was used to determine the model parameters for seven different loudspeakers. The extracted parameter values are shown in Table 4-3 alongside the measured Thiele-Small parameter values for all seven loudspeakers tested. A legend for the loudspeaker names is included at the bottom of the table. Loudspeakers of various sizes were tested; the smallest loudspeaker was the HiVi A2S (4.4 cm in diameter) and the largest loudspeaker was the Fostex prototype (nearly 18 cm in diameter).

Two general trends were noticed in the extracted parameter values. First, the mass of the cone was always significantly larger than the mass of the surround. Second, the compliance of the spider was always substantially larger than either of the compliances associated with the surround. Saying that the spider has a large compliance is equivalent to saying that it has a low stiffness. In other words, the stiffness of the spider is small compared to the stiffness of the inner and outer portions of the surround. This result may indicate that the effect of the spider on the overall behavior of the system is negligible. However, the damping provided by the spider does not appear to be negligible compared to the damping provided by the surround.

Table 4-3. Measured and extracted parameter values for seven different loudspeakers.

Measured Parameter	Loudspeaker Number (legend at bottom)							Units
	1	2	3	4	5	6	7	
a	2.00	3.10	3.90	4.00	4.15	4.20	8.05	cm
b	2.20	3.50	4.35	4.55	4.55	4.60	8.90	cm
BL	2.971	3.648	5.442	4.648	3.541	3.506	11.19	Tm
C_{MS}	163.8	552.9	421.7	751.7	675.8	899.3	332.5	μm/N
L_E	0.108	0.154	0.173	0.161	0.230	0.165	0.682	mH
M_{MD}	2.527	2.113	4.872	2.454	5.429	2.999	39.10	g
R_E	6.319	6.757	5.820	7.648	6.483	7.252	6.592	Ω
R_{MS}	0.758	0.621	1.080	0.441	0.509	0.432	2.533	kg/s

Extracted Parameter	Loudspeaker Number (legend at bottom)							Units
	1	2	3	4	5	6	7	
M_{M1}	2.8170	2.2825	6.4019	3.0007	6.5051	3.6572	54.489	g
M_{M2}	0.0028	0.0045	0.0170	0.0296	0.0034	0.0327	0.3678	g
C_{M1}	898.46	1448.2	1114.7	2500.0	2395.0	5500.0	2500.0	μm/N
C_{M2}	100.53	400.66	308.13	293.73	459.97	382.66	184.58	μm/N
C_{M12}	201.73	232.31	269.40	534.19	286.25	434.56	78.409	μm/N
R_{M1}	0.6193	0.3390	1.1373	0.6755	0.4827	0.4123	0.4262	kg/s
R_{M2}	0.2324	0.0021	0.2565	0.1596	0.0330	0.1594	3.2592	kg/s
R_{M12}	0.0707	0.0049	0.0495	0.0558	0.0010	0.0600	2.3055	kg/s

1	HiVi A2S	5	HiVi M4N
2	Aura Sound NS3 8D	6	Aura Sound NS4 8A
3	Audax HP100MO	7	Fostex prototype
4	Radio Shack 40-1197		

4.7 ACOUSTICAL VALIDATION

The enhanced parameter values reported in the previous section cannot be checked against published data since other methods to measure the enhanced parameter values do not currently exist. An alternative method to validate the parameter values is presented in this section.

4.7.1 THEORETICAL ON-AXIS PRESSURE

One of the tests used to illustrate the usefulness of the enhanced model and to verify the accuracy of the extracted parameters is to predict the on-axis pressure produced by a loudspeaker in an "infinite" baffle. The enhanced model is capable of predicting a dip in the pressure response near the frequency where the surround has its primary resonance. This dip in pressure would be caused by the surround (with its associated area) moving out of phase with the cone (with its associated area).

A general equation for the on-axis radiated pressure at a distance r for a circular piston of radius r_p and normal surface velocity $\hat{u}_n$ in an infinite plane rigid baffle is given by Eq. (4.16) [97]. This equation could be used to predict the on-axis radiated pressure produced by the classical loudspeaker model by replacing $\hat{u}_n$ with $\hat{u}_D$.

$$\hat{p}(r,0) = j2\rho_0 c\hat{u}_n \sin\left[\frac{k}{2}\left(\sqrt{r^2 + r_p{}^2} - r\right)\right] e^{-j\frac{k}{2}\left(\sqrt{r^2+r_p{}^2}+r\right)}. \qquad \textbf{(4.16)}$$

A formula for the on-axis radiated pressure due to a circular piston (with uniform complex velocity amplitude $\hat{u}_1$) surrounded by a concentric annular ring (with uniform complex velocity amplitude $\hat{u}_2$) was derived using the principle of superposition and Eq. (4.16). The total on-axis pressure can be found by summing the on-axis pressures for three concentric pistons A, B, and C as shown in Figure 4-14. Piston A plus piston B yields the motion of the surround with uniform surface velocity $\hat{u}_2$ while piston C is the motion of the cone with uniform surface velocity $\hat{u}_1$.

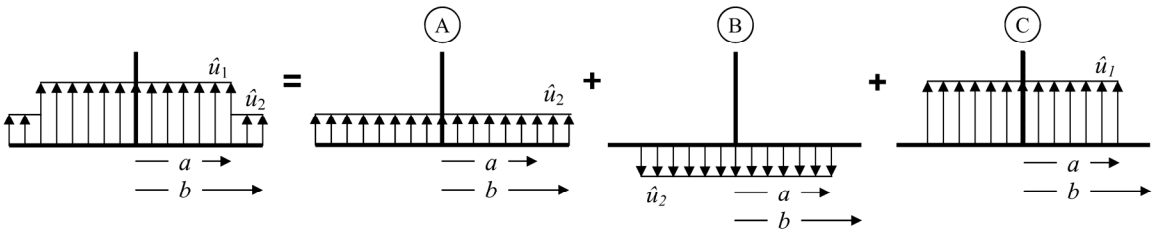

Figure 4-14. The total on-axis pressure for a circular piston surrounded by a concentric annular piston can be found by superposing the pressures of three circular pistons represented by A, B, and C.

The total complex pressure at an on-axis field point r for the enhanced model of a loudspeaker can then be written as:

$$\hat{p}(r,0) = j2\rho_0 c(\hat{u}_2)\sin\left[\frac{k}{2}\left(\sqrt{r^2+b^2}-r\right)\right]e^{-j\frac{k}{2}\left(\sqrt{r^2+b^2}+r\right)} + j2\rho_0 c(\hat{u}_1-\hat{u}_2)\sin\left[\frac{k}{2}\left(\sqrt{r^2+a^2}-r\right)\right]e^{-j\frac{k}{2}\left(\sqrt{r^2+a^2}+r\right)}. \quad \textbf{(4.17)}$$

4.7.2 MEASURED ON-AXIS PRESSURE

The FRF between the input voltage for each of the seven loudspeakers and the baffled on-axis pressure was measured in an anechoic chamber. A GRAS 26AC precision microphone was used to measure the pressure. Broadband excitation was used and a coherence value greater than 0.98 was achieved between the input voltage to the loudspeaker and the output voltage from the microphone at all frequencies above 50 Hz. A photograph of the pressure measurement setup is shown in Figure 4-15.

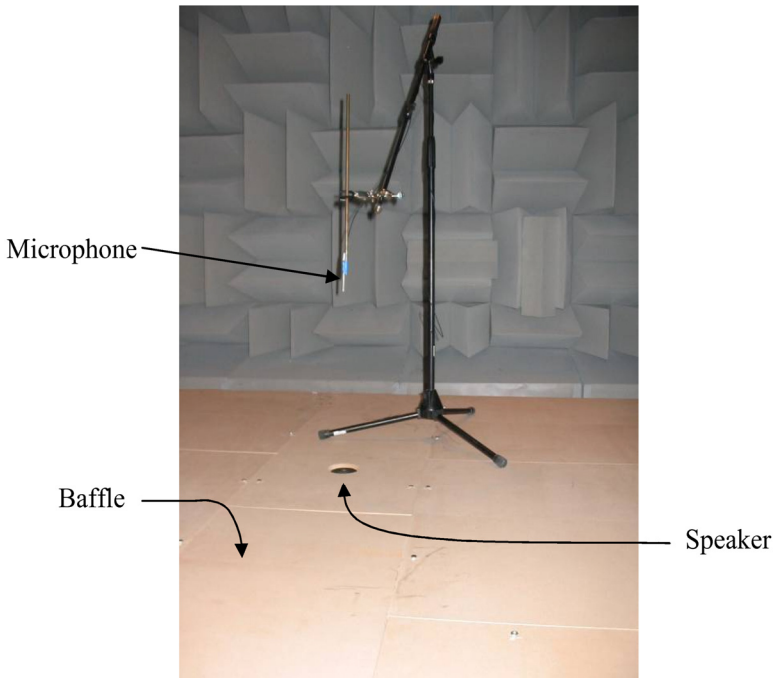

Figure 4-15. Pressure measurement setup.

A preliminary numerical analysis was performed with Eq. (4.17) to make sure that the pressure was measured in the acoustic far-field of the loudspeaker where the frequency dependence had inverse dependence on r for all frequencies of interest. It was found that the acoustic far-field was well established at a distance of 23 cm away from the plane of the baffle with a frequency band of 0 Hz to 20 kHz for all of the loudspeakers except the Fostex (the upper bandwidth of the Fostex was limited to 10 kHz). It was desirable to conduct the measurement as close to the loudspeaker as possible while still remaining in the acoustic far-field because it was found experimentally that the assumption of an infinite baffle broke down as the microphone was moved away from the plane of the baffle. This effect is shown in Figure 4-16 for several microphone positions with the HiVi M4N loudspeaker.

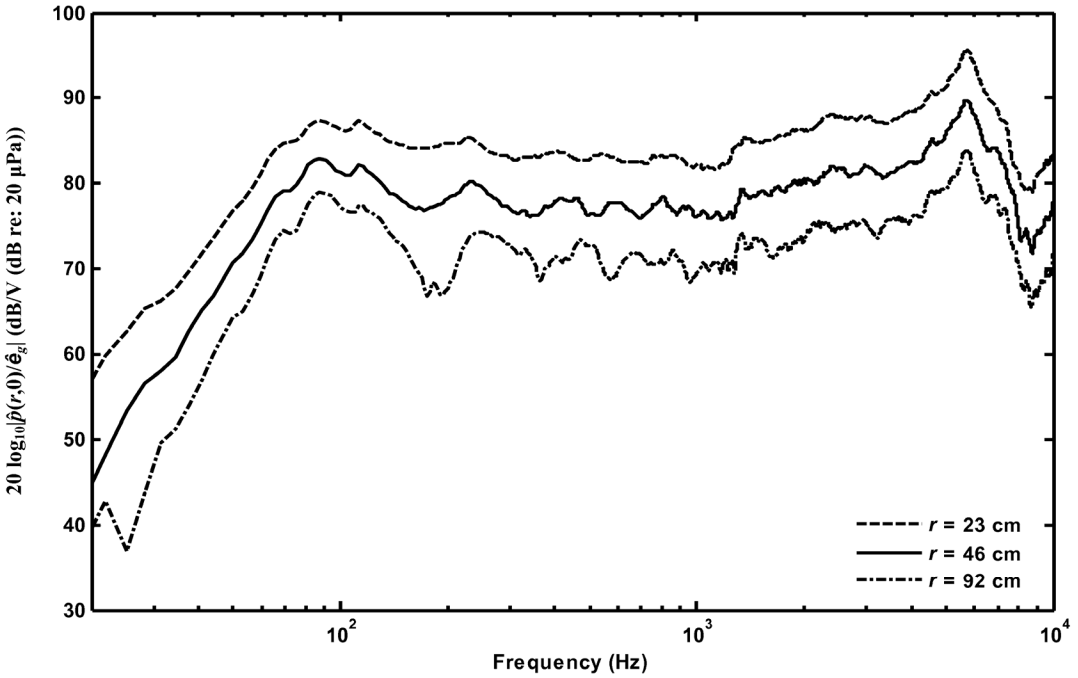

Figure 4-16. Baffle diffraction effects for three microphone locations.

The diffraction of acoustic pressure from behind the baffle to the microphone position in front of the baffle produced interference patterns in the measured FRFs. As can be seen from the figure, the diffraction effect became more pronounced in the measured data as *r* was increased. The diffraction effects are also more severe at low frequencies than they are at high frequencies. The diffraction effect shown in Figure 4-16 was consistent regardless of the loudspeaker being tested.

Olson hypothesized that the destructive interference caused by diffraction around the edges of a square baffle could be reduced by using an "irregular" baffle [65, pg. 128-129]. For a loudspeaker mounted in the center of a square baffle, the acoustic path length from the front to the back is approximately the same for all possible paths. This causes strong interference patterns over relatively narrow frequency bands. If an irregular baffle is used instead, the path lengths from front to back are different depending on the path. An

irregular baffle can be achieved by mounting the loudspeaker off-center, by changing the shape of the baffle, or both. Destructive interference still occurs, but the interference is smeared over a much wider frequency band. Consequently, the measured frequency response will be smoother when an irregular baffle is used. The measurements shown in Figure 4-16 were taken with the loudspeaker positioned in the center of the baffle. Figure 4-17 illustrates the difference between the diffraction effects of the centered loudspeaker in a square baffle and the diffraction effects when the loudspeaker was moved 45 cm off-center and one of the corner panels of the baffle was removed. The irregular baffle configuration was used for all of the validation measurements because of the smoother frequency response measurement.

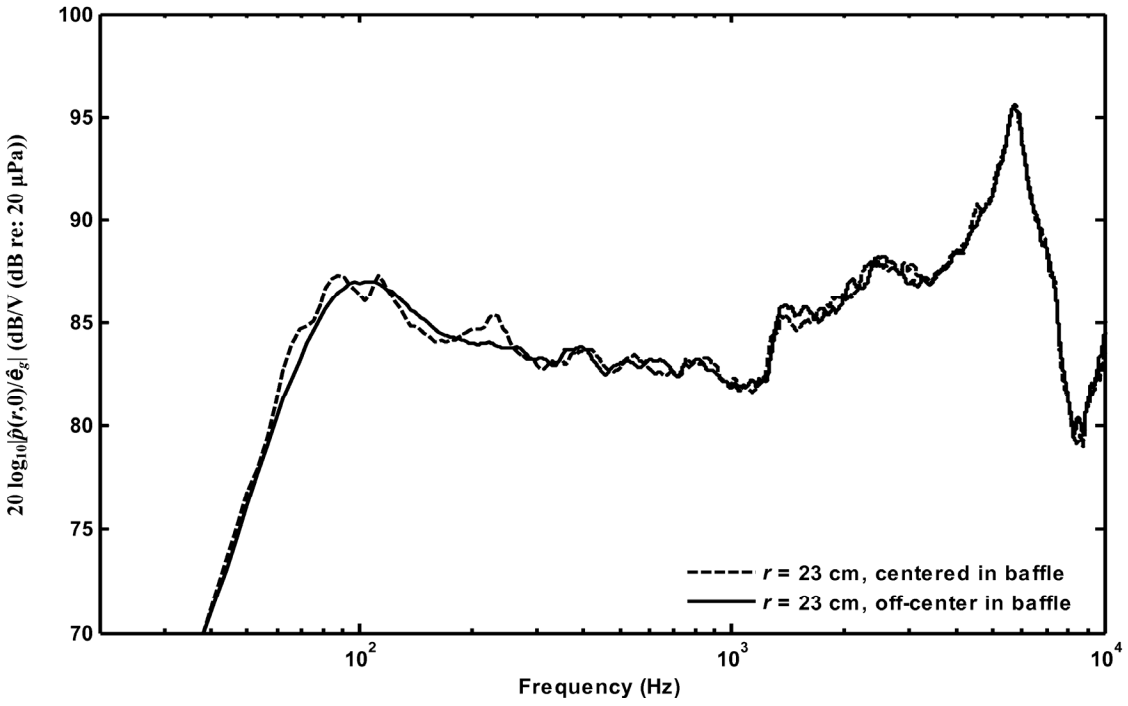

Figure 4-17. Diffraction effect for a square vs. an irregular baffle.

4.7.3 RESULTS

Only a few of the loudspeakers whose parameters are listed in Table 4-3 had enhanced models that predicted dips in the radiated on-axis pressure FRF. One of the most pronounced dips was that of the Aura Sound NS3 8D loudspeaker. Figure 4-18 shows the measured data at r = 23 cm for the Aura Sound NS3 8D, along with the predictions from both the classical model and the enhanced model.

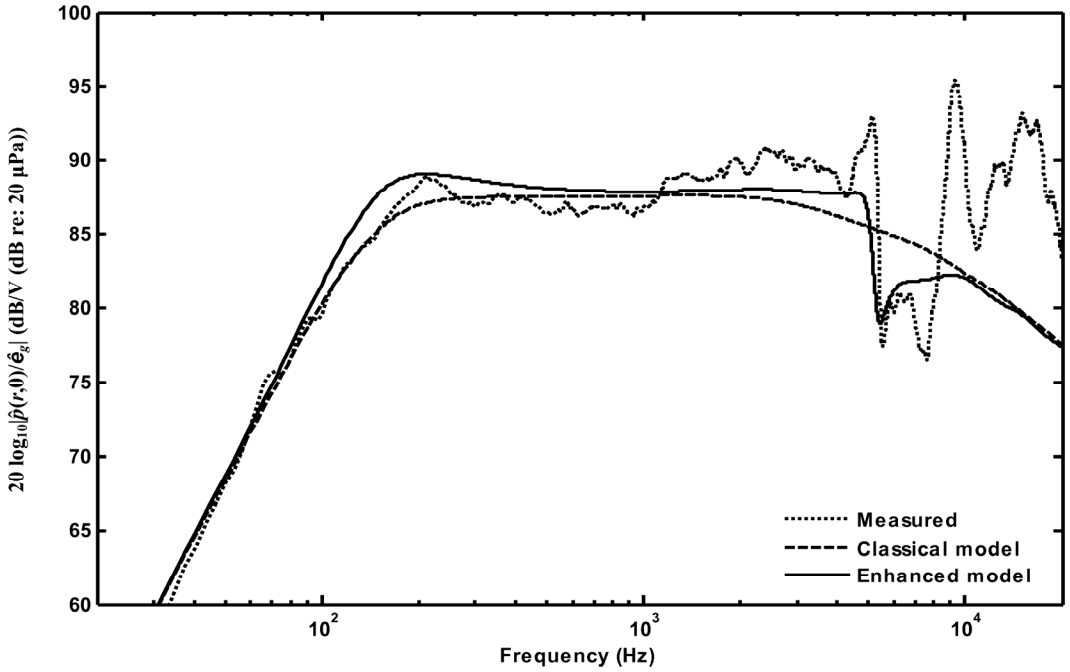

Figure 4-18. Measured on-axis pressure FRF for the Aura Sound NS3 8D loudspeaker.

At 5.5 kHz, this particular loudspeaker exhibits a dip in the radiated pressure that is caused by the surround vibrating out of phase with the cone. The classical model is not capable of predicting this spectral feature, but the enhanced model predicts this dip

reasonably well. Neither model is capable of predicting the resonances due to the cone or surround breaking up which occur in the measured data near 9.3 kHz.

Figure 4-18 also demonstrates that the extracted parameters for this loudspeaker are valid in the sense that they provide an accurate description of actual behavior. It was also observed that the classical model and the enhanced model have near perfect agreement at low frequencies (below 100 Hz). The amplitudes of both models are very close to the measured data in this same region, although a slight discrepancy still occurs at frequencies below 40 Hz. It is hypothesized that this slight discrepancy is due to diffraction around the sides of the baffle that still exists in the measured data at these low frequencies, despite using an irregular baffle.

As a second example, Figure 4-19 shows the measured data for the Radio Shack 40-1197, along with the predictions from both the classical model and the enhanced model. Once again, a dip in the radiated pressure was measured (near 2 kHz) and a corresponding dip was predicted by the enhanced model. Since the enhanced model still assumes uniform motion, it does not account for resonances that correspond to break-ups of either the cone or the surround. The complete effect of the primary surround resonance in the measured data is masked somewhat by the strong cone break-up that occurs at the nearby frequency of 3.2 kHz (recall that the cone break-up frequency was identified from the SRIF of Figure 4-10). It is hypothesized that the measured data would more closely match the enhanced model curve if this strong cone break-up resonance did not exist. It was also noticed from Figure 4-19 that the enhanced model had a more accurate amplitude prediction up to the surround resonance frequency (f_{surr}). The classical model tends to over predict the radiated pressure by 1-3 dB in the bandwidth

from f_s to f_{surr} and is nearly 5 dB in error at f_{surr}. The ability to more accurately predict the amplitude between f_s and f_{surr} indicates that the enhanced model is a higher fidelity model than the classical model.

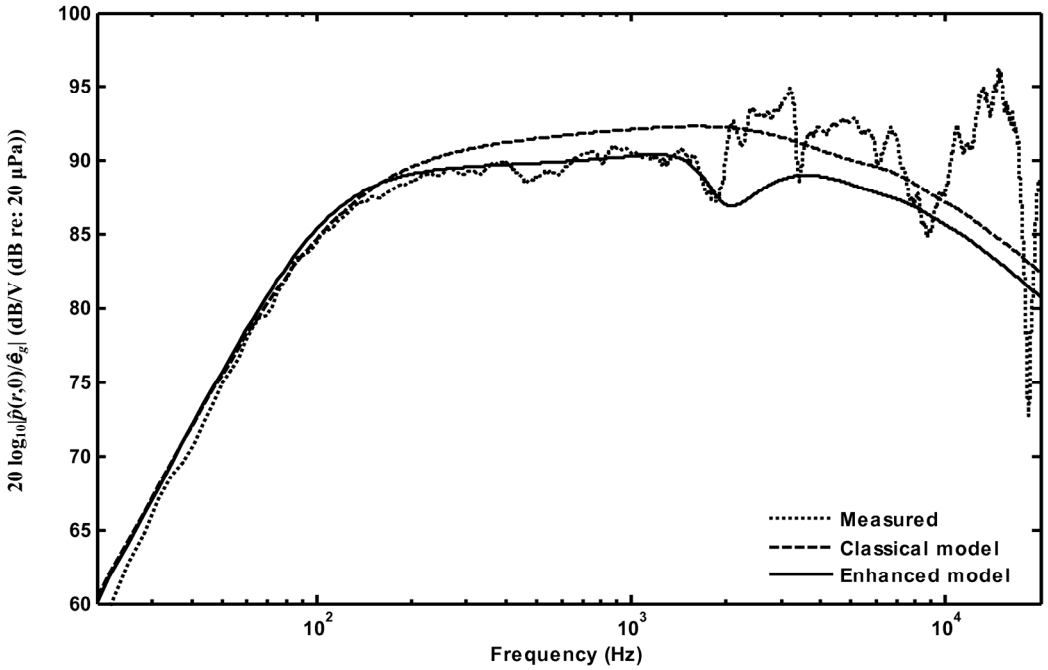

Figure 4-19. Measured on-axis pressure FRF for the Radio Shack 40-1197 loudspeaker.

As a third example, consider the measured and predicted FRFs of the Audax HP100MO shown in Figure 4-20. The enhanced model of this loudspeaker predicts a slight dip in the radiated pressure near 3.1 kHz. This dip is not nearly as pronounced as the dips shown in the previous examples. However, the measured Audax FRF does not have a pronounced dip like the Aura Sound NS3 8D or the Radio Shack 40-1197. Once again, the amplitude prediction of the enhanced model for the Audax loudspeaker provides better agreement with the measured data than the classical model up to, and in this case exceeding, f_{surr}. This particular speaker provides a nice test case because the

first cone break-up (near 6.1 kHz) is far away in frequency from the primary surround resonance.

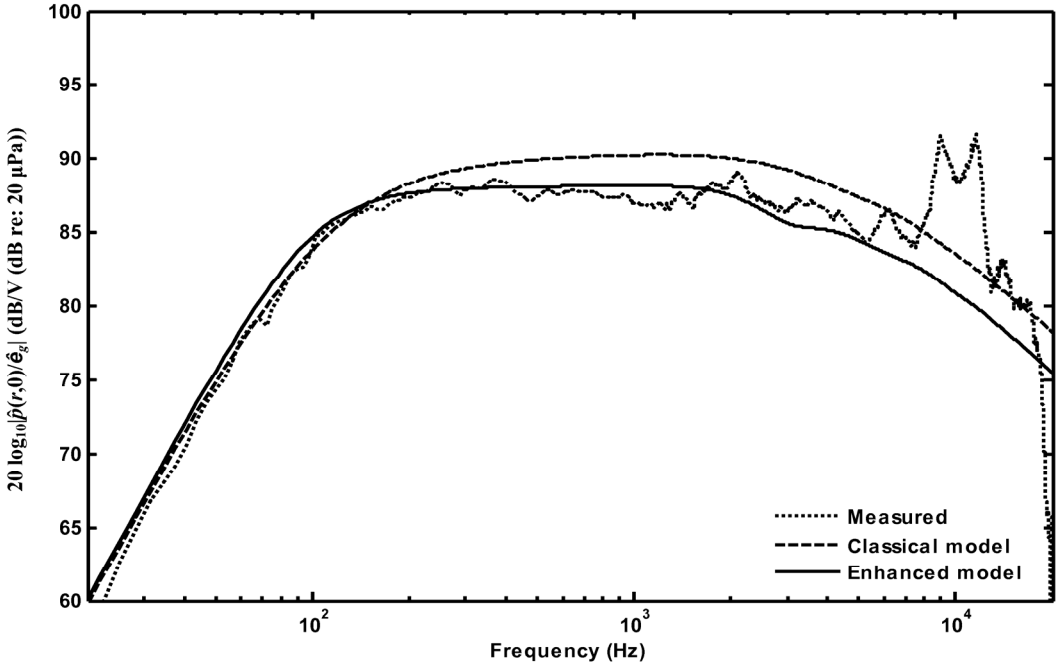

Figure 4-20. Measured on-axis pressure FRF for the Audax HP100MO loudspeaker.

Some of the loudspeakers did not have pronounced dips (predicted or measured) in the on-axis pressure FRF; for these loudspeakers there was simply not a strong enough interaction between the radiating areas to produce the narrow-band degradation in the radiated pressure. The largest loudspeaker measured for this paper was a Fostex prototype driver with a 20 cm diameter—the measured and predicted responses for this loudspeaker are shown in Figure 4-21. Although this loudspeaker has a surround resonance in its measured SRIF at 1.45 kHz, the interactions of the radiating areas are such that a pronounced dip in the radiated pressure does not occur. The dip did not occur in the measured pressure FRF and the enhanced model was successful in the sense that it

did not predict a dip that did not exist. It was observed again that the enhanced model provides a better amplitude prediction in the frequency band between f_s and f_{surr}.

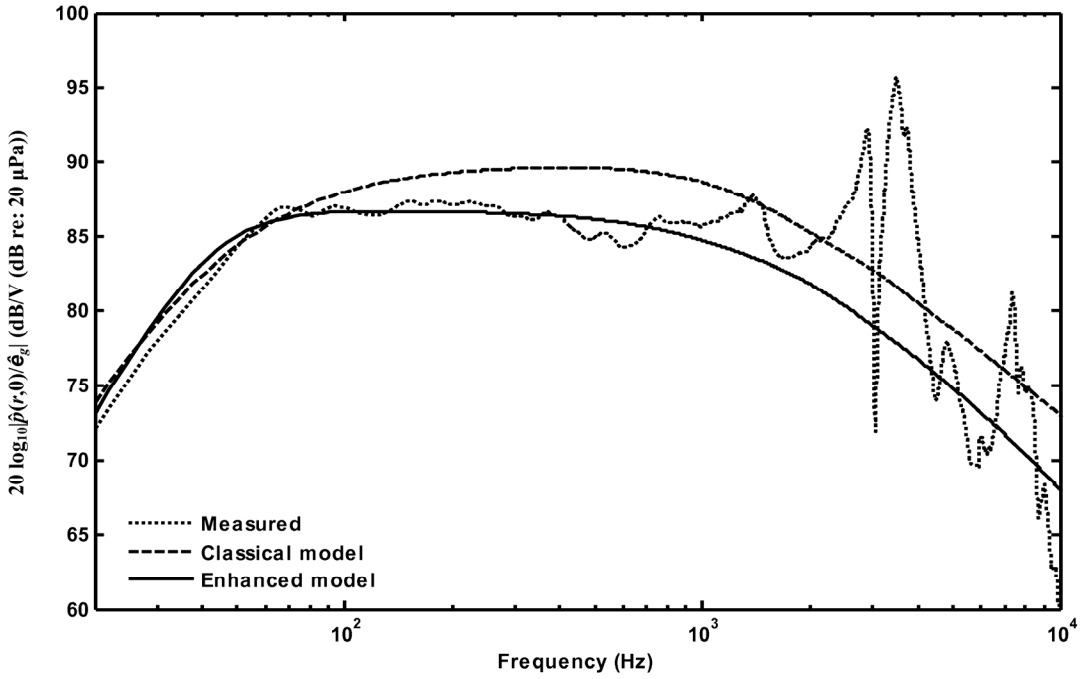

Figure 4-21. Measured on-axis pressure FRF for the Fostex prototype loudspeaker.

To quantify the improvement of the enhanced model over the classical model in the on-axis pressure validation experiment, the SSE was computed between each of the two models (classical and enhanced) and the measured mobility FRF. The SSE was computed in the linear scale (the units of each mobility FRF in the linear scale are Pa/V; the units of the SSE are Pa^2/V^2). The upper frequency limit for the sum of squared error computation was limited to f_{surr} for each loudspeaker. It is not useful to continue the summation above this frequency since neither the classical model nor the enhanced are able to predict the part of the curve that corresponds to the break-ups of the cone and

surround. The percent reduction in the SSE between the classical model and the enhanced model was computed from

$$\%\ \text{Reduction (SSE)} = 100 \cdot \left(1 - \frac{\text{SSE}_{\text{enhanced model}}}{\text{SSE}_{\text{classical model}}} \right). \tag{4.18}$$

The surround resonance frequency, SSE, and percent reduction in the SSE are shown in Table 4-4 for the seven loudspeakers tested. Reductions in the SSE were obtained for all of the loudspeakers. This suggests that the enhanced model provides a more accurate prediction in the on-axis, baffled pressure response than the classical model.

The improvement in the prediction capability comes because the surround is more appropriately modeled in the enhanced model. Even though not all of the loudspeakers exhibited a drastic degradation in the radiated pressure at the surround resonance frequency, the enhanced model provided a better amplitude prediction up to f_{surr}.

Table 4-4. Reduction in SSE between the classical model and the enhanced model.

	Loudspeaker Number (legend at bottom)							
	1	2	3	4	5	6	7	Units
f_{surr}	9105	3920	2310	1670	3430	1680	1440	Hz
$SSE_{classical}$	23.0	22.9	16.8	11.6	1.4	6.7	12.0	Pa^2/V^2
$SSE_{enhanced}$	13.1	13.7	1.7	0.60	1.1	1.7	2.4	Pa^2/V^2
% Red.	**43.0**	**40.2**	**89.9**	**94.6**	**21.4**	**74.6**	**80.0**	-

1	HiVi A2S	5	HiVi M4N
2	Aura Sound NS3 8D	6	Aura Sound NS4 8A
3	Audax HP100MO	7	Fostex prototype
4	Radio Shack 40-1197		

4.8 CONCLUSION

This paper introduced an enhanced model of a moving-coil loudspeaker that has greater predictive capabilities than the classical model. The enhanced model extends previous analogous circuit modeling techniques to include the first resonance of the surround.

A measurement scheme using a scanning laser Doppler vibrometer was introduced to obtain the data from which the unknown enhanced model parameters would be determined. The mobility frequency response function of the loudspeaker was measured at each of several hundred scan points located on the cone and the surround. The data from the cone points were spatially averaged to produce an estimate of $\hat{u}_1/\hat{e}_g$ and the data from the surround points were spatially averaged to produce an estimate of $\hat{u}_2/\hat{e}_g$. A surround resonance indicator function (SRIF) was developed to easily identify the primary surround resonance frequency.

The unknown parameters in the enhanced model were then extracted by curve-fitting the enhanced model to the measured data. A MATLAB constrained optimization function was used to minimize the sum of the squared error between the model prediction and the measured data by adjusting the values of the unknown parameters: M_{M1}, M_{M2}, C_{M1}, C_{M2}, C_{M12}, R_{M1}, R_{M2}, and R_{M12}.

The effectiveness of the enhanced model and the parameter extraction method was demonstrated by an on-axis pressure radiation measurement. The enhanced model predicted a dip in the radiated on-axis pressure for several loudspeakers which aligned with experimental results. The amplitude of the on-axis pressure was also observed to be

more accurate than the classical model in the frequency band from f_s to f_{surr} for all of the loudspeakers that were tested.

The enhanced model provides a way to accurately model the primary surround resonance of a moving-coil loudspeaker. This tool will enable loudspeaker designers to modify the properties of the cone and surround in order to increase the flat bandwidth of the loudspeaker. This work will also be useful to researchers trying to model sound transmission through devices that are physically similar to loudspeakers.

4.9 APPENDIX: SRIF VALIDATION FOR ADDITIONAL LOUDSPEAKERS

The measured SRIF and a surface velocity plot at f_{surr} are shown for six additional loudspeakers. These plots are included here to show the reliability of the SRIF in finding the frequency at which the surround moves out of phase with the cone (both areas experience nearly uniform motion).

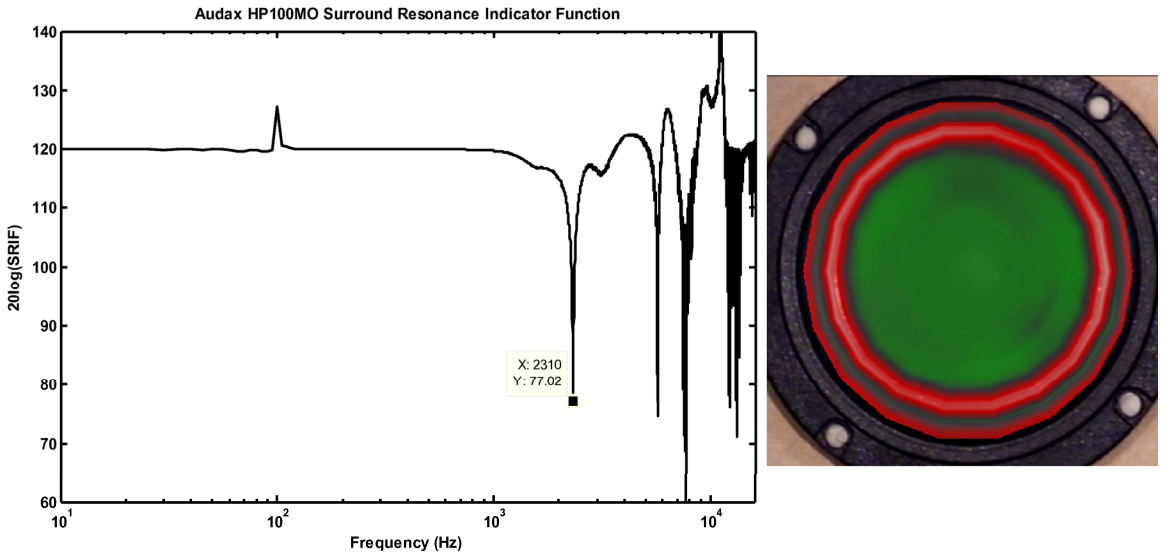

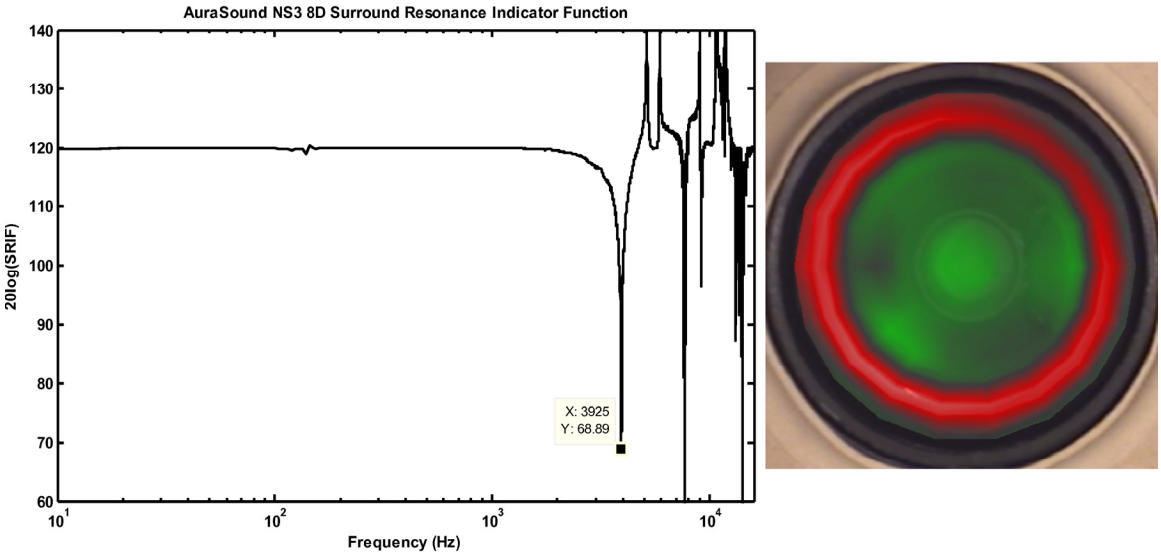

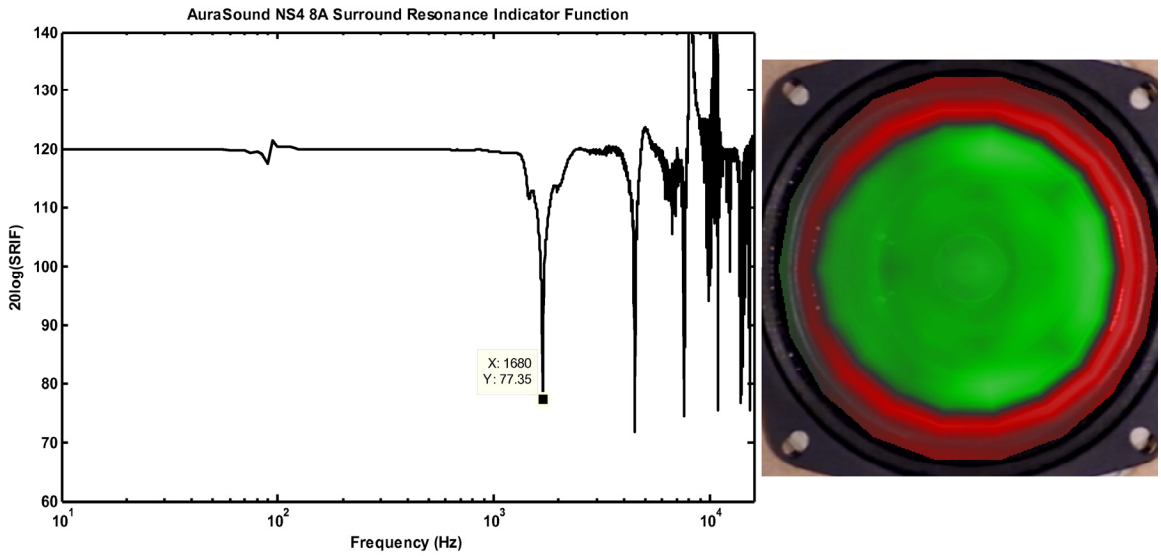

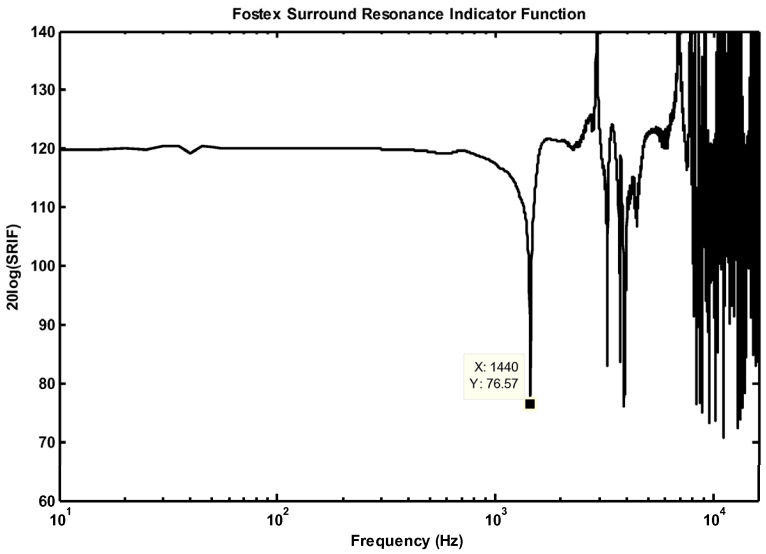

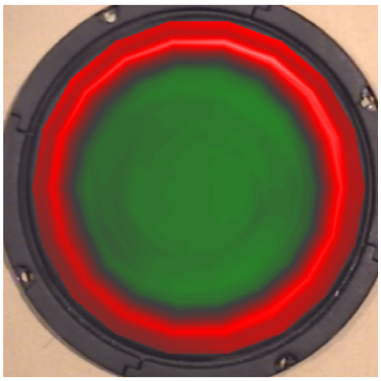

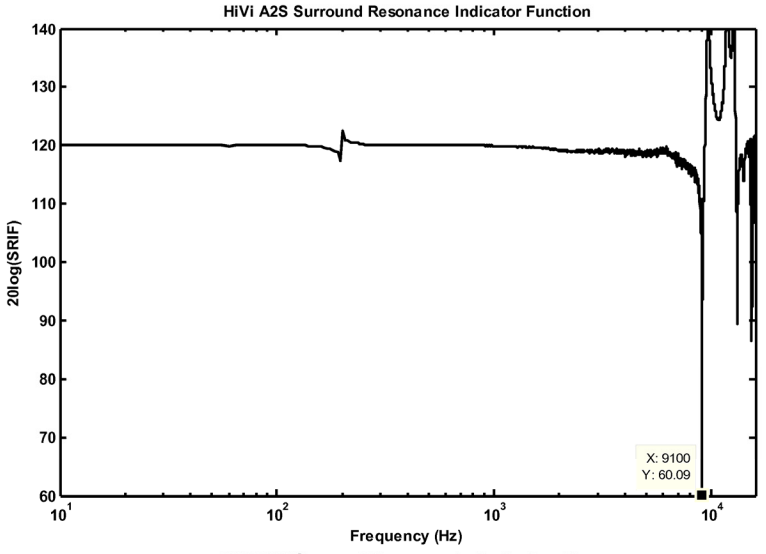

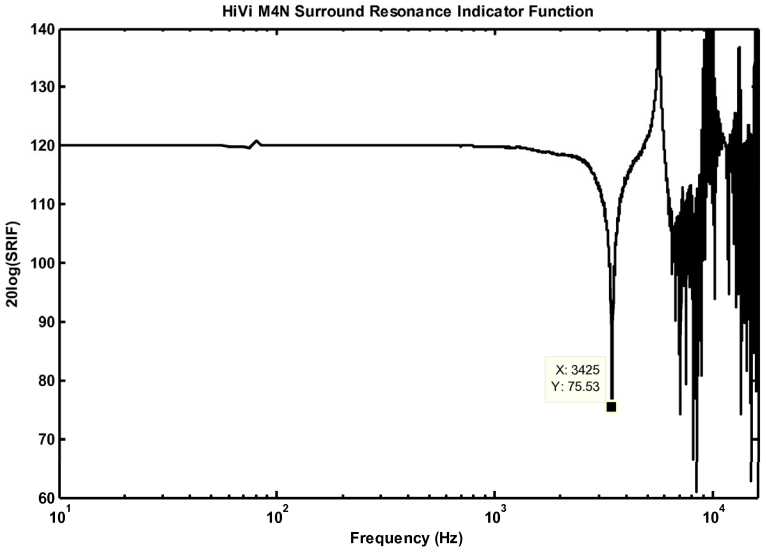

5 ACTIVE SOUND TRANSMISSION CONTROL OF A DOUBLE-PANEL ASP MODULE USING DECOUPLED ANALOG FEEDBACK CONTROLLERS: NUMERICAL MODEL

This chapter presents a paper submitted to the Journal of the Acoustical Society of America. The formatting of the paper has been modified to meet the formatting requirements of this thesis.

5.1 CONTRIBUTING AUTHORS AND AFFILIATIONS

Jason D. Sagers
Department of Mechanical Engineering, 435 CTB, Brigham Young University, Provo, UT 84602; email: jsagers@byu.edu

Timothy W. Leishman
Department of Physics and Astronomy, N247 ESC, Brigham Young University, Provo, UT 84602; email: tim_leishman@byu.edu

Jonathan D. Blotter
Department of Mechanical Engineering, 435 CTB, Brigham Young University, Provo, UT 84602; email: jblotter@byu.edu

5.2 ABSTRACT

Low-frequency sound transmission has long plagued the sound isolation performance of lightweight partitions. Over the last two decades, researchers have investigated actively controlled structures to prevent sound transmission from a source space into a receiving space. An approach using active segmented partitions (ASPs) [46] seeks to significantly improve their low-frequency sound isolation capability. An ASP is a partition which has been mechanically and acoustically segmented into a number of

small individually controlled modules. This paper provides a theoretical and numerical development of a new ASP module configuration, wherein each face of a double-panel structure is independently actuated and controlled by an analog feedback controller. A numerical model is developed to estimate frequency response functions for the purpose of controller design, to understand the effect of acoustic coupling between the panels, to predict the TL of the module in both passive and active states, and to demonstrate that the proposed ASP module will produce bidirectional sound isolation.

5.3 NOMENCLATURE

$\hat{a}_n$ Normal acceleration of the n^{th} panel

BL_n Force factor of the n^{th} moving-coil loudspeaker

c Speed of sound in the fluid medium

c_n Complex frequency response function of the n^{th} controller

C_n Electrical capacitance of the n^{th} capacitor in the control circuit

C_{Mn} Effective mechanical compliance of the n^{th} module element

C_{Mmn} Effective mechanical compliance coupling the m^{th} and n^{th} module elements ($m \neq n$)

$\hat{e}_{gn}$ Complex control voltage forcing the n^{th} moving-coil loudspeaker

f Frequency (Hz)

G_A Acoustic ground (ambient reference pressure)

G_M Mechanical ground (zero reference velocity)

$\tilde{k}$ Complex acoustic wave number, $= \omega/c - j\alpha$

L Effective cavity length of the module

L_{En} Electrical inductance of the voice coil in the n^{th} moving-coil loudspeaker

m Integer index value

M_{Mn} Effective mechanical mass of the n^{th} module element

n Integer index value

$\hat{p}_q$ Complex acoustic pressure at location q in the analogous circuit

$\hat{p}_{in}$ Normally incident complex acoustic pressure on the n^{th} side of the module

$\hat{p}_{tm}$ Normal transmitted complex acoustic pressure on the m^{th} side of the module

R_n Electrical resistance of the n^{th} resistor in the control circuit

R_{En} Electrical resistance of the voice coil in the n^{th} moving-coil loudspeaker

R_g Output resistance of the electrical control source

R_{Mn} Effective mechanical resistance of the n^{th} module element

R_{Mmn} Effective mechanical resistance coupling the m^{th} and n^{th} module elements ($m \neq n$)

S Total cross-sectional area of the module, $= S_1 + S_2 = S_3 + S_4$

s Laplace domain frequency variable, $= j\omega$

S_n Cross-sectional area of the n^{th} module element

TL Normal-incidence sound TL

$\hat{u}_n$ Complex normal velocity amplitude of the n^{th} module element

$\hat{U}_n$ Complex volume velocity on the n^{th} side of module, ex: $\hat{U}_1 = \hat{u}_1 S_1 + \hat{u}_2 S_2$

Z_{A1} Acoustic impedance substitution for waveguide network, $= j(\omega\rho_o/\tilde{k}S)\ tan(\tilde{k}L/2)$

Z_{A2} Acoustic impedance substitution for waveguide network, $= -j(\omega\rho_o/\tilde{k}S)\ csc(\tilde{k}L)$

Z_{En} Total electrical impedance of the n^{th} moving-coil loudspeaker, $= R_g + R_{En} + j\omega L_{En}$

α Absorption coefficient of filler material used in the cavity

ρ_o Ambient density of the fluid medium

ω Angular frequency (rad/s), = $2\pi f$

Π Acoustic sound power

5.4 INTRODUCTION

There has long been interest in the use of partitions to reduce sound transmission into noise-sensitive environments. There is particular need for improvement of partitions at lower frequencies where passive sound isolation is inadequate. This is the case in both single- and double-panel partitions where the TL is severely degraded at low frequencies due to resonance effects [4]. A common passive method to reduce sound transmission is to add mass to the partition [10, ch. 9, 98, ch. 8]. However, this solution is not feasible for situations where extra weight cannot be tolerated, such as in aerospace vehicles, large ceiling structures, high rise building walls, etc. A promising solution to this problem is active structural control of lightweight partitions.

Two active control strategies that have been utilized to improve the sound isolation performance of partitions at low frequencies include active structural acoustic control (ASAC) and active segmented partitions (ASPs). The ASAC approach involves actuating a continuous panel in such a way as to reduce the efficiency of acoustic radiation into the receiving space. This approach has been explored thoroughly [12-14, 17-22, 24, 25]. ASAC is typically implemented by locating several actuators over the continuous panel and by locating the sensors either on the panel or in the receiving space. A control algorithm is then used which alters the radiating mode shapes of the panel. The performance of the algorithm is typically quantified by using microphones to measure the attenuation in sound pressure level at several locations in the receiving space. In general,

receiving-side attenuations with ASAC have been small. Typical results have been roughly 5 to 10 dB of attenuation in narrow frequency bands. However, a concise summary of ASAC results is difficult because the measurement techniques in the literature are inconsistent. The major challenges of the ASAC approach are the large number of fully-coupled controllers, the need for microphones as error sensors in the receiving space, the spatial control spillover that inevitably results when using a continuous transmitting panel, and the minimal attenuation achieved in narrow frequency bands.

An alternative active control approach is to use an active segmented partition. An effective ASP array has been implemented by Leishman et al. [2, 28-30] wherein a partition was subdivided into an array of small modules that were both acoustically and mechanically segmented. Using multiple single-channel digital feed-forward controllers and an array of four modules, Leishman achieved very high TL results (near 60 dB for sinusoidal signals) over a frequency band of 30 Hz to 290 Hz [48]. The primary limitations of Leishman's configuration were its unidirectional TL performance, its lack of broadband random-noise control capabilities, and the expense of digital feed-forward controllers.

The segmentation of the partition has several advantages. First, it allows for independent control of each module, thus eliminating the impracticality of a large number of fully-coupled controllers that exists for ASAC control. Second, the segmentation simplifies the active control problem by allowing the long-wavelength assumption to exist in the exposed module surfaces and cavities. Finally, the simplification of the active

control problem permits the error sensors to be placed inside the partition, thus eliminating the need for microphones in the acoustic space outside of the partition.

A practical active partition (be it an ASAC or ASP approach) should satisfy a few important criteria. First, it should be bidirectional for many applications, or capable of providing sound isolation in both directions through the partition. Second, it should be capable of controlling both tonal and broadband disturbances. Third, it should be self-contained, meaning that all of the necessary sensing and actuation hardware is located on or inside the partition. Finally, the partition should provide global attenuation of acoustic energy in the receiving space.

The purpose of this paper is to develop a numerical model that will demonstrate the sound isolation potential of a new design for an ASP module. The design allows for decoupled bidirectional control of each panel in a double-panel partition. It may be used for both tonal and broadband sound transmission control. The key components of the panels, sensors, actuators, and controllers are included in the numerical model. The purpose of the model is to:

- estimate the plant frequency response functions.
- understand the effects of acoustic coupling between the panels.
- predict the TL of the module in both passive and active states.
- demonstrate that the module design will produce bidirectional sound isolation.

5.5 DESIGN CONSIDERATIONS OF THE NEW MODULE

The design considerations for the new module are introduced in this section. They include both the physical description and the active control description.

5.5.1 PHYSICAL DESCRIPTION

The proposed design for an individual ASP module is shown in Figure 5-1. The design consists of two parallel panels separated by an air space. Each panel is connected to the lightweight but rigid interstitial structure by a resilient connection, or surround. The surround allows the panels to vibrate with some independence from the interstitial structure. In this way, the mechanical coupling path is reduced between the two panels in the same module and between any two modules in the array, thus enhancing the ability to successfully implement decoupled controllers. An actuator and sensor pair is connected to each panel in the module. The actuators are contained inside the cavity and the sensors can be mounted on either side of the panel. The actuators are also connected to the interstitial structure by means of lightweight supports. The output of the sensor is fed into the controller and then the output of the controller is fed into the actuator (shown schematically for the leftmost panel in Figure 5-1). Although not shown in the figure, the necessary electronics for the controllers could be compactly designed so that they can be contained within the module. The remainder of the cavity is filled with acoustically absorbent fiberglass insulation (not shown in Figure 5-1) to help improve the passive sound isolation performance of the module at high frequencies.

Different types of actuators such as inertial shakers, piezoelectric stacks, and moving-coil loudspeaker drivers could be used in the module; the actuators used in this research are moving-coil loudspeaker drivers. Likewise, different types of sensors could be used in the module; the sensors used in this research are accelerometers. Although the types of sensors and actuators could be changed in a different design, it is critical to the

validity of the model that all of the important dynamics of the panel, surround, actuator, and sensor are included.

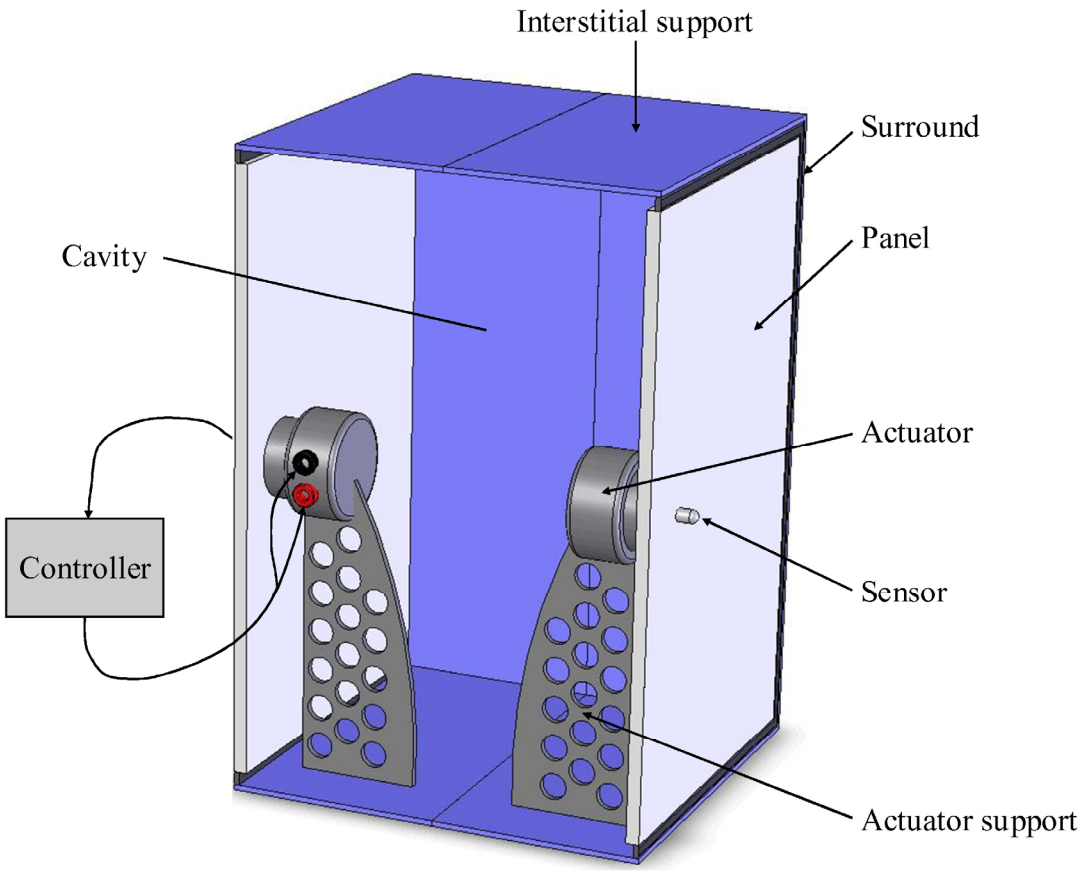

Figure 5-1. A cutaway view of a double-panel ASP module.

5.5.2 ACTIVE CONTROL DESCRIPTION

An analog feedback controller was selected for this module because of its potential for broadband control as well as its relative ease of implementation, low cost, and low mass. Two independent controllers whose complex frequency response functions are represented by c_1 and c_2 were used (one for each panel). For this research,

the controllers were second-order, analog Fleischer-Tow biquad circuits [57, 58, 99]. They use resistors, capacitors, and operational amplifiers to create a transfer function between the input and output voltages. The shape of the transfer function is determined by choosing the values of the resistors and capacitors. The electrical schematic of the controller is shown in Figure 5-2.

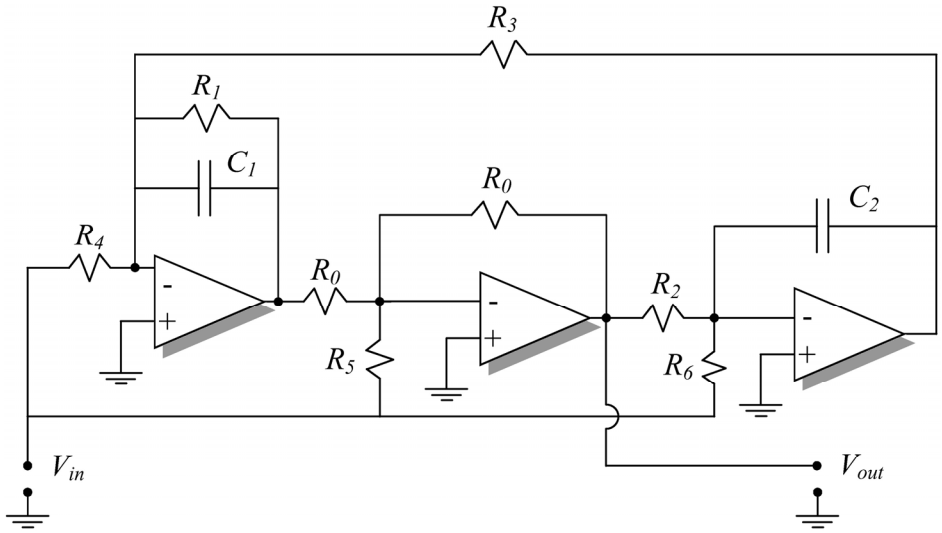

Figure 5-2. Electrical schematic of a second-order Fleischer-Tow biquad circuit.

The output voltage signal from the accelerometer is the input voltage (V_{in}) to the controller. The output voltage from the controller (V_{out}) is the input voltage to the actuator. The Laplace domain transfer function between the input and output voltage of the controller is given by

$$\frac{V_{out}}{V_{in}} = -\frac{\frac{R_0}{R_5}s^2 + \frac{1}{R_1C_1}\left(\frac{R_0}{R_5} - \frac{R_1}{R_4}\right)s + \frac{1}{R_3R_6C_1C_2}}{s^2 + \frac{1}{R_1C_1}s + \frac{1}{R_2R_3C_1C_2}}. \quad \textbf{(5.1)}$$

Two important physical design choices made it possible to use a controller that was only second-order. First, it was important that collocated sensor and actuator pairs be used to eliminate undesirable delay in the plant due to acoustic propagation. Second, the airspace between the two panels was filled with absorptive material to dampen high-frequency cavity resonances which could unnecessarily complicate the control scheme [59].

5.6 NUMERICAL MODEL

Analogous circuit modeling techniques will be used in this paper to develop the numerical model of the new ASP module. A discussion of these techniques can be found in the literature [16, 67] and will not be repeated here, except as necessary to highlight specific areas of interest. The analogous circuit model is a multiple-domain (electrical, mechanical, and acoustical) representation of the ASP module that provides a straightforward way to write the equations of motion for the system.

5.6.1 SCHEMATIC DRAWING

A schematic drawing of the module is shown in Figure 5-3. Since the two halves of the module contain identical components, only a detailed discussion of the left half will be given. The mass of the panel is represented by M_{M1} and the mass of the surround is represented by M_{M2}. The panel and the surround each act as a radiating surface area (S_1 and S_2 respectively). These surfaces are assumed to vibrate with uniform complex velocity amplitudes $\hat{u}_1$ and $\hat{u}_2$. This assumption has a bandwidth limitation as higher-order modal patterns will begin to appear in both the cone and surround at sufficiently high frequencies.

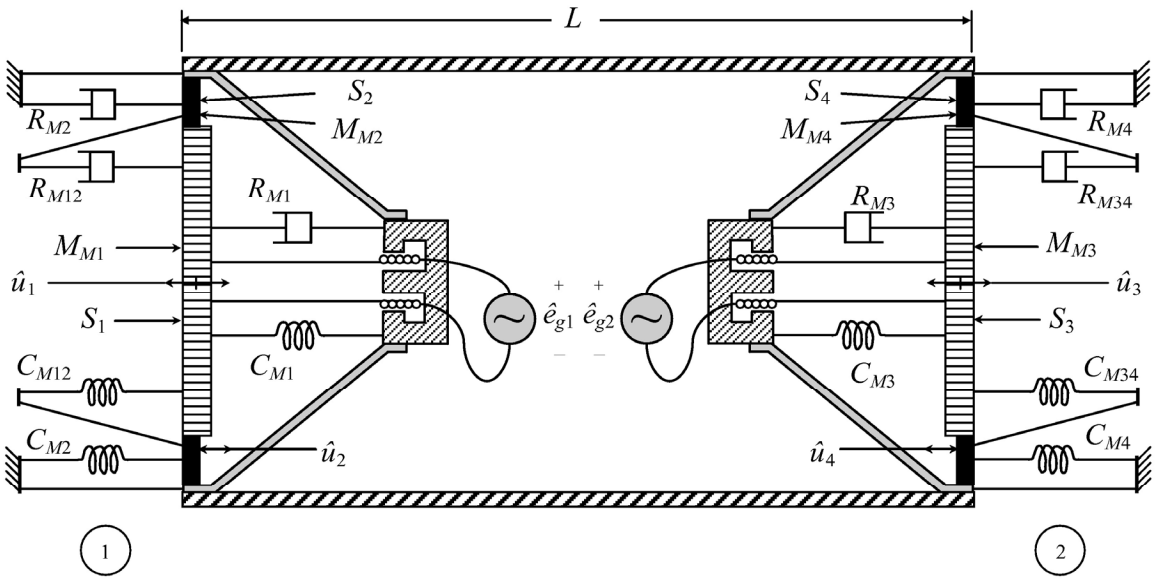

Figure 5-3. Cross-sectional schematic view of the ASP module.

The connection between the surround and the interstitial support is modeled with a resistance and a compliance (R_{M2} and C_{M2} respectively) as is the connection between the surround and the panel (R_{M12} and C_{M12} respectively). The lumped-elements are assumed to extend uniformly around the perimeter of the module. Because of the possible asymmetry in the properties of the surround after it has been installed, R_{M2} is generally not assumed to be equal to R_{M12} and C_{M2} is generally not assumed to be equal to C_{M12}. Finally, the secondary suspension, or spider, of the moving-coil actuator is modeled with its own resistance and compliance values (R_{M1} and C_{M1} respectively).

Each half of the module incorporates a two degree of freedom (DOF) mechanical system. The first DOF is contained in the motion of the panel, while the second DOF is contained in the motion of the surround. The added DOF of the surround constitutes what will be hereafter referred to as the enhanced model of a loudspeaker driver.

The moving-coil driver has intrinsic electrical and mechanical properties which also describe its behavior. Although the driver is an electrical device, it will be modeled in the mechanical mobility domain as an ideal flow source, with a value of $(\hat{e}_{g1}BL_1)/Z_{E1}$, in parallel with its internal mobility, Z_{E1}/BL_1^2. The complex control voltage that is output from the controller and input into the actuator is represented by $\hat{e}_{g1}$.

The benefit of using the enhanced model as shown in Figure 5-3 (as opposed to the classical model of the loudspeaker, see [16, ch. 7]) is that it allows the surround to vibrate as a lumped element, with its own DOF. As a result, the model should better predict the TL that will occur if the panel is effectively frozen by the active control scheme while the surround is still permitted to vibrate. It is anticipated that any residual vibration of the surround could significantly degrade the TL performance of the module.

One of the difficulties with the enhanced model is the determination of the additional mechanical mass, mechanical resistance, and mechanical compliance values of the surround. Measurement methods exist to determine the composite parameters of the classical model [54-71], but the individual values shown in Figure 5-3 are much more difficult to ascertain. To solve this problem, the author developed a laser-based measurement method from which the unknown parameters (M_{M1}, M_{M2}, C_{M1}, C_{M2}, C_{M12}, R_{M1}, R_{M2}, R_{M12} and M_{M3}, M_{M4}, C_{M3}, C_{M4}, C_{M34}, R_{M3}, R_{M4}, R_{M34}) were extracted (Ch. 4).

As mentioned previously, the airspace between the two panels was filled with a porous material to provide acoustic absorption. To account for the absorption in this model, the absorption coefficient α of a sample of R-13 fiberglass insulation was measured using a plane-wave tube [60-62] and the resulting values were used in the complex wave number $\tilde{k}$.

5.6.2 ANALOGOUS CIRCUIT

The multiple-domain analogous circuit representation of the ASP module is shown in Figure 5-4. The left and right halves of the module are represented in the left and right sides of the circuit. Eight gyrator elements were used in the circuit to couple the acoustic impedance domain and the mechanical mobility domain. The electrical components of the moving-coil driver shown in the circuit have already been transferred from the electrical impedance domain to the mechanical mobility domain. A one-dimensional waveguide network is used in the center of the circuit to acoustically couple the left and right halves of the module. Appropriate mechanical and acoustical grounds are represented by G_M and G_A respectively.

Constant incident acoustic pressure sources are modeled on each side of the module ($\hat{p}_{i1}$ and $\hat{p}_{i2}$). Disturbance pressures are thus allowed to impinge upon the device from the left (side 1), right (side 2), or both sides simultaneously. It should be noted that the analogous circuit assumes normal plane-wave incidence and transmission with respect to each panel, as well as steady-state time-harmonic excitation and control.

Several variables that describe pressures, normal surface velocities, and volume velocities are labeled in the figure. These annotations were included in order to make the derivation of the governing equations more apparent. Some variables (such as $\hat{u}_1$, $\hat{u}_2$, $\hat{u}_3$, and $\hat{u}_4$) have obvious physical meaning while the physical significance of other variables (such as $\hat{p}_A$, $\hat{p}_B$, $\hat{p}_C$, and $\hat{p}_D$) is less obvious. All mechanical variables are designated by the subscript M (e.g. M_{M1}).

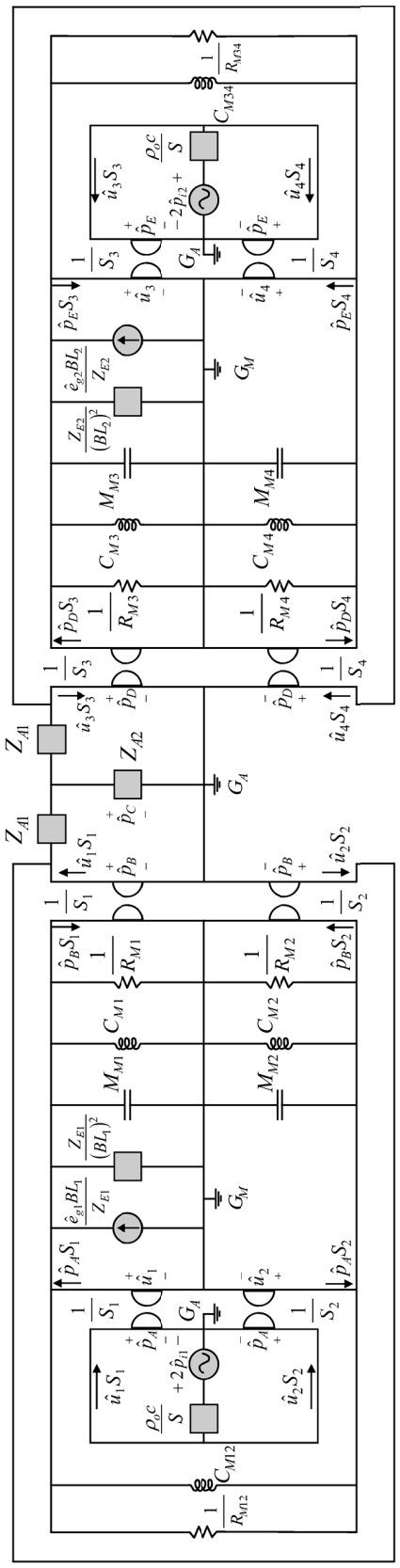

Figure 5-4. Multiple-domain analogous circuit representing the ASP module.

5.6.3 NUMERICAL DEVELOPMENT

Nodal analysis was used to write nine equations in nine unknowns ($\hat{u}_1$, $\hat{u}_2$, $\hat{u}_3$, $\hat{u}_4$, $\hat{p}_A$, $\hat{p}_B$, $\hat{p}_C$, $\hat{p}_D$, and $\hat{p}_E$) for the circuit:

$$\frac{\hat{e}_{g1}BL_1}{Z_{E1}} + (\hat{p}_A - \hat{p}_B)S_1 - (\hat{u}_1 - \hat{u}_2)Z_{M12} - \hat{u}_1 Z_{M1} = 0 \tag{5.2}$$

$$(\hat{p}_A - \hat{p}_B)S_2 + (\hat{u}_1 - \hat{u}_2)Z_{M12} - \hat{u}_2 Z_{M2} = 0 \tag{5.3}$$

$$\hat{p}_A = 2\hat{p}_{i1} - \hat{U}_1 \frac{\rho_0 c}{S} \tag{5.4}$$

$$\hat{U}_1 - \frac{(\hat{p}_B - \hat{p}_C)}{Z_{A1}} = 0 \tag{5.5}$$

$$\frac{(\hat{p}_B - \hat{p}_C)}{Z_{A1}} - \frac{(\hat{p}_C - \hat{p}_D)}{Z_{A1}} - \frac{\hat{p}_C}{Z_{A2}} = 0 \tag{5.6}$$

$$\frac{(\hat{p}_C - \hat{p}_D)}{Z_{A1}} - \hat{U}_2 = 0 \tag{5.7}$$

$$\frac{\hat{e}_{g2}BL_2}{Z_{E2}} + (\hat{p}_D - \hat{p}_E)S_3 - (\hat{u}_3 - \hat{u}_4)Z_{M34} - \hat{u}_3 Z_{M3} = 0 \tag{5.8}$$

$$(\hat{p}_D - \hat{p}_E)S_4 + (\hat{u}_3 - \hat{u}_4)Z_{M34} - \hat{u}_4 Z_{M4} = 0 \tag{5.9}$$

$$\hat{p}_E = 2\hat{p}_{i2} - \hat{U}_2 \frac{\rho_o c}{S} \tag{5.10}$$

Six mechanical impedance substitutions (Z_{M1}, Z_{M2}, Z_{M3}, Z_{M4}, Z_{M12}, and Z_{M34}) are used in the above equations and are defined in the appendix. The nine nodal equations can be reduced to four coupled equations of motion with $\hat{u}_1$, $\hat{u}_2$, $\hat{u}_3$, and $\hat{u}_4$ as the unknown

variables. The solution to the equations of motion for $\hat{u}_1$, $\hat{u}_2$, $\hat{u}_3$, and $\hat{u}_4$ required careful algebraic reduction by means of impedance substitutions. The full solution is much too lengthy to include in this paper. Instead, the primary governing equations are presented in the body of the paper and all of the algebraic impedance substitutions are defined in the appendix. The impedance definitions were created and labeled sequentially during the solution process with the following letter order: B, C, D, and F (the letters A and E were skipped to avoid confusion with acoustic and electrical impedance definitions). The reader should be aware that the impedance substitutions are not intended to have specific physical significance, but are primarily used to enable the presentation of a compact solution.

Several quantities of interest can be obtained from the solution to the equations of motion. The model will first be used to predict both plant FRFs. The plant FRF can be used to design a new controller or to evaluate the stability margins of an existing controller. Second, the model will be used to estimate the acoustic coupling strength between the two panels. This will be accomplished by looking at the FRF between the control voltage of one actuator and the acceleration of the other panel. It is expected that an acoustic coupling path will exist between the panels, but that its effect will not require coupled feedback controllers. Third, the model will be used to predict the unidirectional TL through the module. This will be accomplished by letting $\hat{p}_{i1}$ equal unity while $\hat{p}_{i2}$ is set to zero for the left-to-right TL, and vice versa for the right-to-left TL. Finally, the model will be used to predict the bidirectional capabilities of the module. This will be accomplished by letting both $\hat{p}_{i1}$ and $\hat{p}_{i2}$ be arbitrarily defined over different frequency bands.

5.6.4 PLANT ACCELERANCE FRFS

The plant *P* is defined for active control schemes as "the system between the input to the secondary [(control)] actuator and the output of the sensor used to measure the residual error signal" [49, pg.105]. Knowledge of the plant FRF allows for the design of an appropriate controller. Two plants exist in this model (one for each panel) and are defined as the frequency response from the input control voltage of the actuator to the output of the error sensing accelerometer

$$P(f) = \frac{\text{Accelerometer Output}}{\text{Actuator Input}}. \tag{5.11}$$

The voltage output of the panel-mounted accelerometer was used as the reference signal for the feedback controller. The solution of the equations of motion yields the normal surface velocity for each panel

$$\hat{u}_1 = 2\hat{p}_{i1}Z_{D1} + 2\hat{p}_{i2}Z_{D7} + \hat{e}_{g1}BL_1Z_{D2} + \hat{e}_{g2}BL_2Z_{D3}, \tag{5.12}$$

$$\hat{u}_3 = 2\hat{p}_{i1}Z_{F1} + 2\hat{p}_{i2}\left(Z_{F4} - Z_{F5}\right) + \hat{e}_{g1}BL_1Z_{F3} + \hat{e}_{g2}BL_2Z_{F2} \quad . \tag{5.13}$$

The acceleration of each panel can then be found by using a simple relationship:

$$\hat{a}_1 = j\omega\hat{u}_1, \tag{5.14}$$

$$\hat{a}_3 = j\omega\hat{u}_3. \tag{5.15}$$

The accelerance FRF of the first plant (between $\hat{e}_{g1}$ and $\hat{a}_1$) is readily found from Eqs. (5.12) and (5.14) by setting $\hat{p}_{i1}$, $\hat{p}_{i2}$, and $\hat{e}_{g2}$ equal to zero:

$$P_{11} = \frac{\hat{a}_1}{\hat{e}_{g1}} = j\omega B L_1 Z_{D2} \,. \tag{5.16}$$

Similarly, the accelerance FRF of the second plant (between $\hat{e}_{g2}$ and $\hat{a}_3$) can be found from Eqs. (5.13) and (5.15) by setting $\hat{p}_{i1}$, $\hat{p}_{i2}$, and $\hat{e}_{g1}$ equal to zero:

$$P_{22} = \frac{\hat{a}_3}{\hat{e}_{g2}} = j\omega B L_2 Z_{F2} \tag{5.17}$$

5.6.5 ACOUSTIC COUPLING FRFS

The two halves of the module in this analysis are assumed to be structurally isolated from one another, so the only physical coupling path between them is through the air cavity. A qualitative measure of the strength of this coupling path is the FRF between the acceleration of one panel due to an excitation of the other panel. The magnitude of the acoustic coupling FRF will be large when cavity resonances exist. A measure of the strength of the acoustic coupling path between the actuator of one panel and the acceleration of the other panel can be found by using Eqs. (5.12) through (5.15) and by solving for the cross FRFs, meaning the acceleration of one panel due to a control voltage on the other actuator (after $\hat{p}_{i1}$, $\hat{p}_{i2}$, and the uninvolved control voltage is set to zero):

$$P_{21} = \frac{\hat{a}_1}{\hat{e}_{g2}} = j\omega B L_2 Z_{D3}\,, \tag{5.18}$$

$$P_{12} = \frac{\hat{a}_3}{\hat{e}_{g1}} = j\omega B L_1 Z_{F3}\,. \tag{5.19}$$

5.6.6 TRANSMISSION LOSS

The TL of the module is defined in terms of the time-averaged incident sound power, $<\Pi_i>_t$, and the time-averaged transmitted sound power $<\Pi_t>_t$ [100]:

$$\mathrm{TL} = 10\log\left(\frac{\langle \Pi_i \rangle_t}{\langle \Pi_t \rangle_t}\right). \tag{5.20}$$

Since the total surface area of side 1 is the same as the total surface area of side 2 ($S = S_1 + S_2 = S_3 + S_4$) and since plane-wave propagation is assumed, Eq. (5.20) can be reduced to

$$\mathrm{TL} = 10\log\left(\left|\frac{\hat{p}_{in}}{\hat{p}_{tm}}\right|^2\right), \tag{5.21}$$

where $\hat{p}_{in}$ is the incident pressure on side n and $\hat{p}_{tm}$ is the transmitted pressure on side m due to $\hat{p}_{in}$. For the left-to-right TL through the module, $\hat{p}_{in}$ is $\hat{p}_{i1}$ and $\hat{p}_{tm}$ is $\hat{p}_{t2}$. The pressure $\hat{p}_{t2}$ is equal to the product of the total volume velocity of side 2, $\hat{U}_2$, and the acoustic impedance $\rho_o c/S$ seen by the module on side 2 (assumed anechoic).

Manipulation of the analogous circuit equations presented in Sec. 5.6.3 yields the left-to-right TL through the module

$$TL_{12} = 10\log_{10}\left(\left|\frac{\hat{p}_{i1}S}{(\rho_o c)\begin{bmatrix} 2\hat{p}_{i1}(Z_{A2}Z_{B1})(S_1Z_{D1} - S_2Z_{D4}) \\ +2\hat{p}_{i2}[Z_{A2}Z_{B1}(S_1Z_{D7} - S_2Z_{D8}) - Z_{B1}] \\ +\hat{e}_{g1}BL_1(Z_{A2}Z_{B1})(S_1Z_{D2} - S_2Z_{D5}) \\ +\hat{e}_{g2}BL_2\left[Z_{A2}Z_{B1}(S_1Z_{D3} - S_2Z_{D6}) + \frac{Z_{B2}}{Z_{E2}}\right] \end{bmatrix}}\right|^2\right). \quad \textbf{(5.22)}$$

It can be seen from this expression that if $\hat{p}_{i2}$ were zero, the equation would reduce to the unidirectional left-to-right (side 1 to side 2) TL through the module based solely on the disturbance pressure $\hat{p}_{i1}$. The presence of $\hat{p}_{i2}$ will act to reduce the 'measurable' TL (but perhaps not the 'perceived' TL) through the module because an observer on side 2 cannot distinguish the sound pressure that is transmitted through the module due to $\hat{p}_{i1}$ and the sound pressure that is reflected from panel 2 due to $\hat{p}_{i2}$. Equation (5.22) can predict the TL of the module in its passive configuration (both $\hat{e}_{g1}$ and $\hat{e}_{g2}$ set equal to zero and both Z_{E1} and Z_{E2} set to infinity to represent open-circuited actuator terminals). It can also predict the TL of a configuration with only a single-panel active (either $\hat{e}_{g1}$ or $\hat{e}_{g2}$ equal to zero and either Z_{E1} and Z_{E2} set to infinity, respectively) or a configuration with both panels active (both $\hat{e}_{g1}$ and $\hat{e}_{g2}$ nonzero and $Z_{En} = R_g + R_{En} + j\omega L_{En}$).

Alternately, the right-to-left TL through the module is given by:

$$TL_{21} = 10\log_{10}\left(\left|\frac{\hat{p}_{i2}S}{(\rho_o c)\begin{bmatrix}2\hat{p}_{i1}(S_1Z_{D1}-S_2Z_{D4})+2\hat{p}_{i2}(S_1Z_{D7}-S_2Z_{D8})\\+\hat{e}_{g1}BL_1(S_1Z_{D2}-S_2Z_{D5})+\hat{e}_{g2}BL_2(S_1Z_{D3}-S_2Z_{D6})\end{bmatrix}}\right|^2\right). \quad \textbf{(5.23)}$$

The control voltages for use in Eqs. (5.22) and (5.23) are given by the product of the acceleration of the panel and the frequency response function of the control circuit:

$$\hat{e}_{g1} = j\omega c_1 \hat{u}_1 , \quad \textbf{(5.24)}$$

$$\hat{e}_{g2} = j\omega c_2 \hat{u}_3 . \quad \textbf{(5.25)}$$

Equations (5.12), (5.13), (5.24), and (5.25) can be solved simultaneously for the control voltages $\hat{e}_{g1}$ and $\hat{e}_{g2}$. The appropriate terms need to be set equal to zero or infinity for the specific control configuration. For example, if only panel 1 was actively controlled and there was only a single disturbance source $\hat{p}_{i1}$, then $\hat{p}_{i2}$ and $\hat{e}_{g2}$ in Eq. (5.12) would be set to zero and Z_{E2} would be set to infinity. Simultaneously solving Eq. (5.12) with Eq. (5.24) would yield the resulting control voltage

$$\hat{e}_{g1} = \frac{2\hat{p}_{i1} j\omega c_1 Z_{D1}}{1 - j\omega c_1 B L_1 Z_{D2}} . \quad \textbf{(5.26)}$$

Control voltages for the other configurations can be solved in a similar fashion. As was briefly mentioned, the presence of a downstream disturbance source will reduce

the 'measurable' TL through the module when both $\hat{p}_{i1}$ and $\hat{p}_{i2}$ posses the same spectral content with similar amplitudes. However, when the same spectral content is present in both disturbance sources but one of the sources has much higher amplitude than the other, the TL prediction should approach what it would be when the smaller pressure amplitude is set to zero. Likewise, the predicted TL should appear unaltered when $\hat{p}_{i1}$ and $\hat{p}_{i2}$ contain altogether different frequency content.

5.7 MODEL PREDICTIONS

The numerical parameter values for the enhanced loudspeaker model used in this research are given in Table 5-1. The cavity depth L was 0.15 m and acoustic damping was included in the cavity through the complex wave number, $\tilde{k}$. Both halves of the module were constructed from identical components so that $BL_1 = BL_2$, $L_{E1} = L_{E2}$, etc.

Table 5-1. Enhanced model parameters used in the numerical analysis.

Parameter	Value	Units	Parameter	Value	Units
BL_1, BL_2	3.54	Tm	M_{M2}, M_{M4}	0.15	g
L_{E1}, L_{E2}	0.23	mH	C_{M1}, C_{M3}	2300	μm/N
R_{E1}, R_{E2}	6.48	Ω	C_{M2}, C_{M4}	448	μm/N
R_{g1}, R_{g2}	0.10	Ω	C_{M12}, C_{M34}	272	μm/N
S_1, S_3	30.0	cm^2	R_{M1}, R_{M3}	0.57	kg/s
S_2, S_4	3.00	cm^2	R_{M2}, R_{M4}	0.30	kg/s
M_{M1}, M_{M3}	7.21	g	R_{M12}, R_{M34}	0.30	kg/s

5.7.1 PREDICTED PLANT ACCELERANCE FRFS

The normalized accelerance FRF P_{11} predicted by Eq. (5.16) is shown in Figure 5-5. This curve represents the acceleration seen by panel 1 due to an excitation voltage

on its actuator, $\hat{e}_{g1}$. For this analysis, panel 2 has the same parameters as panel 1 and so P_{22} is identical to P_{11}.

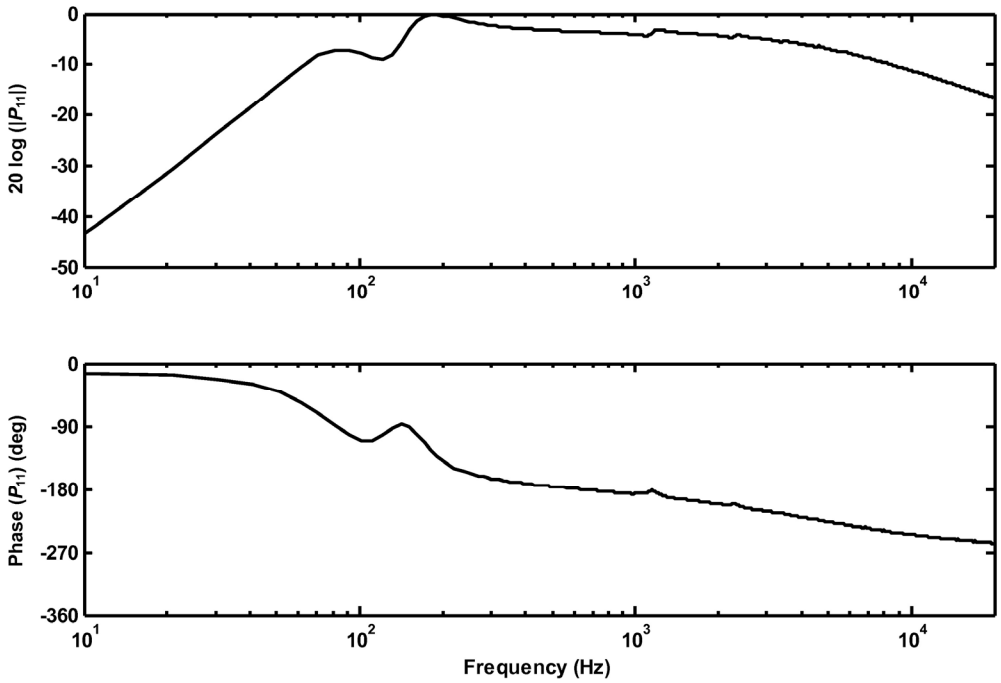

Figure 5-5. Normalized accelerance FRF for the module.

The first peak seen near 80 Hz is the primary mechanical resonance of the loudspeaker. The magnitude of the FRF falls off at 12 dB per octave below this frequency. The second peak near 185 Hz is the mass-air-mass resonance frequency of the double-panel partition. The magnitude of the FRF is relatively flat above the mass-air-mass resonance frequency until it begins to roll off at high frequencies due to the inductance of the voice coil.

The accelerance FRF can be used to design a controller or to test the stability margins of an existing controller. The control circuit used in this research was presented in section 5.5.2. The resistor and capacitor values chosen for this analysis produced a

low-pass FRF for the controller. The resistor and capacitor values are given in Table 5-2 and the frequency response of the controller is shown in Figure 5-6.

Table 5-2. Resistor and capacitor values used in the analog controller.

Parameter	Value	Units	Parameter	Value	Units
R_0	10,000	Ω	R_5	10,000	Ω
R_1	430	Ω	R_6	1,300	Ω
R_2	13,120	Ω	C_1	0.047	μF
R_3	1,000	Ω	C_2	0.047	μF
R_4	452	Ω			

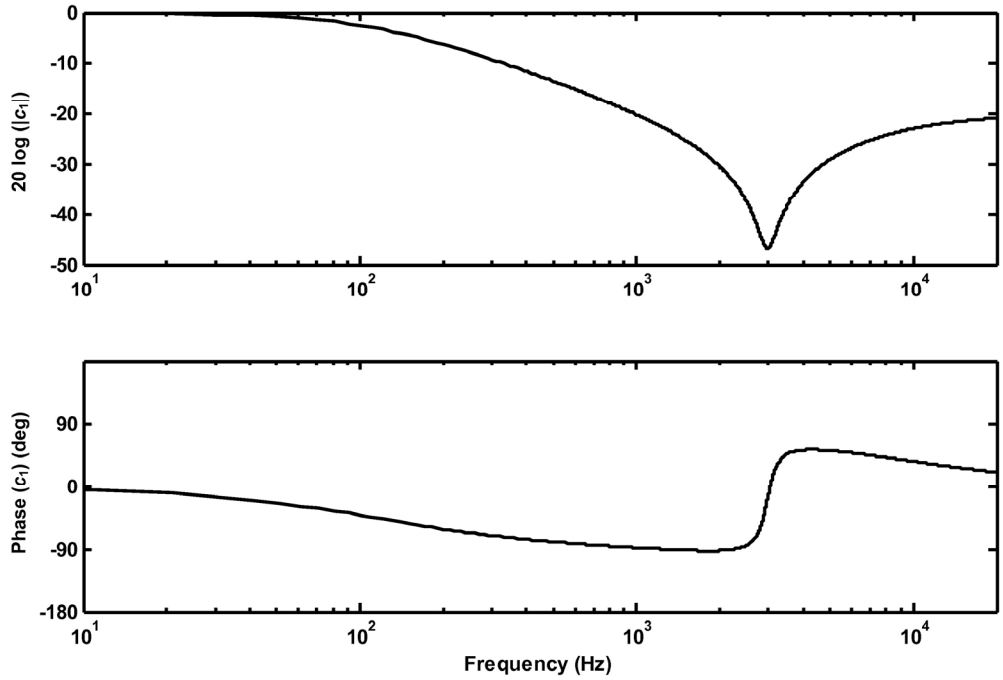

Figure 5-6. Predicted FRF of the controller.

5.7.2 PREDICTED ACOUSTIC COUPLING FRFS

The cross-coupling FRF, P_{12}, between the acceleration of one panel due to an input excitation on the other is shown in Figure 5-7. The mass-air-mass resonance is evident at 185 Hz and represents the strongest coupling path from one panel to the other. The axial cavity resonances are also clearly evident with the first resonance occurring near 1.1 kHz. However, the magnitude of the first cavity resonance is nearly 20 dB down from the mass-air-mass resonance. The P_{21} cross-coupling FRF is identical to the one shown in Figure 5-7.

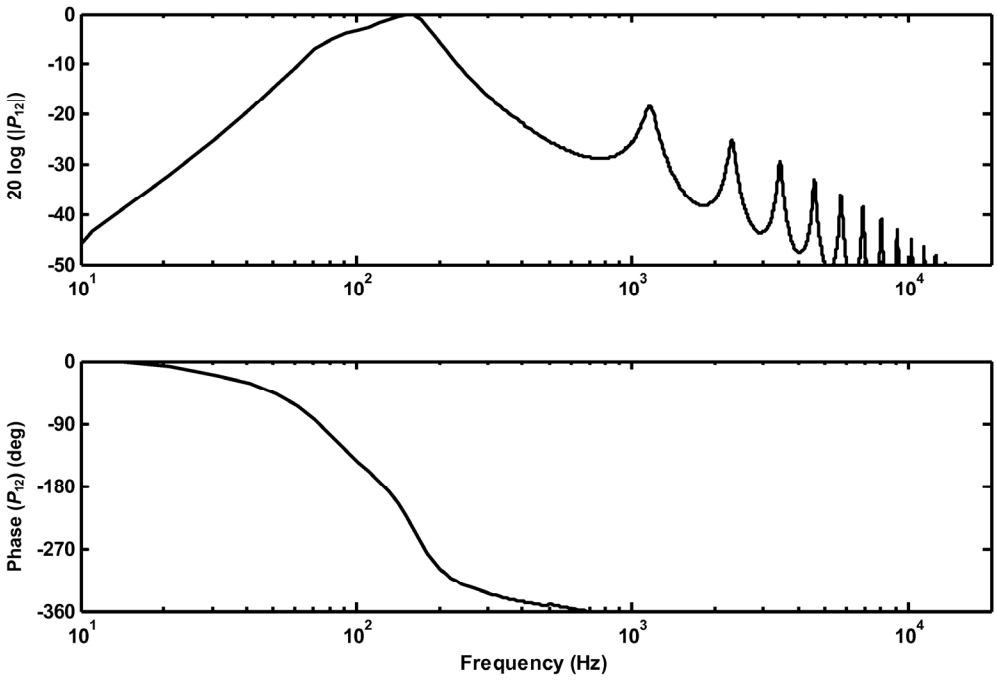

Figure 5-7. Cross-coupling accelerance FRF.

The effect of the cavity depth, L, on the acoustic coupling strength was investigated. The results for three different cavity depths are shown in Figure 5-8. It was

found that the peak magnitude of the acoustic coupling FRF increased roughly 3 dB per halving of distance. The amplitude of P_{12} was independent of L at frequencies well below the mass-air-mass resonance. The general amplitude dependence of P_{12} was also independent of L at frequencies far above the first axial cavity resonance (excluding, of course, the frequency-dependent location of the peaks that varied with L).

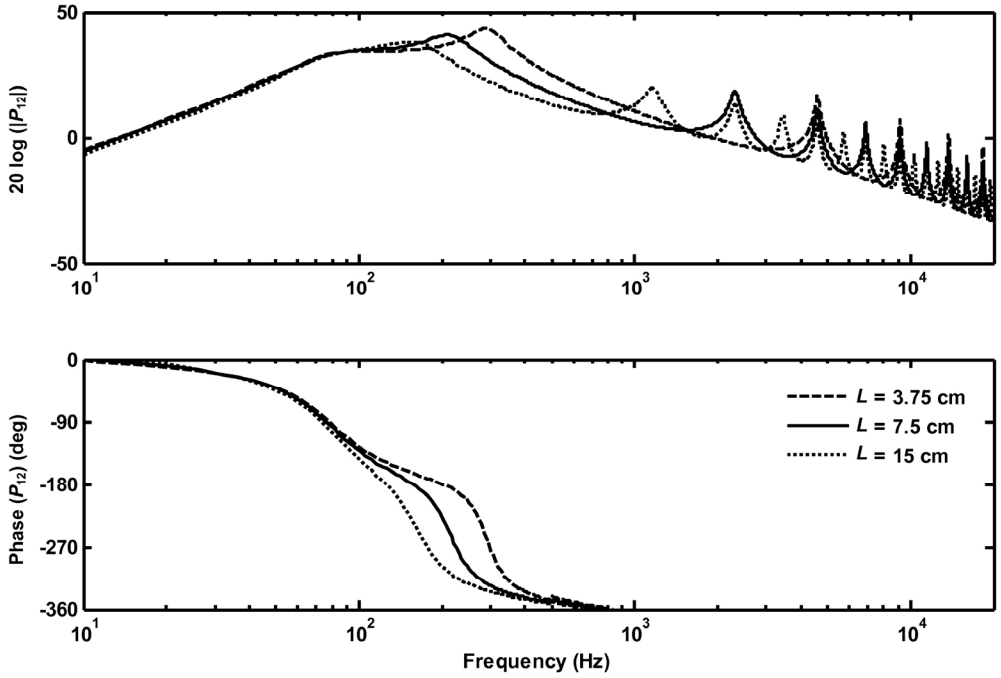

Figure 5-8. Cross-coupling accelerance FRFs for three different cavity depths.

5.7.3 PREDICTED TL

The unidirectional TL (e.g., from left-to-right) through the module is plotted in Figure 5-9 for three control configurations. The passive configuration exhibits the characteristic response of a double-panel partition [4]. The TL increases at 18 dB per octave immediately above the mass-air-mass resonance frequency while the slope

decreases slightly to 12 dB per octave at higher frequencies. The axial cavity resonances are also clearly seen.

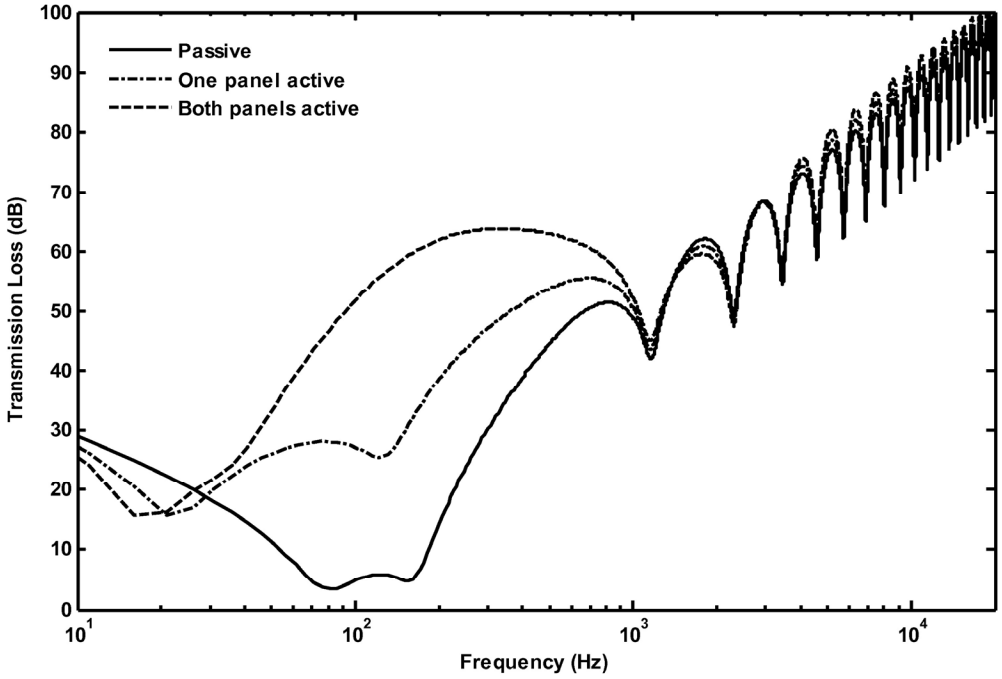

Figure 5-9. Unidirectional TL through the module.

The configuration wherein only a single panel of the double-panel partition was actively controlled is also shown in the figure. The predicted TL is the same regardless of whether panel 1 or panel 2 is actively controlled. The maximum increase in the TL for this control scheme is 27 dB at 165 Hz. The arithmetic average increase in the TL from 50 Hz to 500 Hz is 18 dB. This represents a sizeable increase in TL at low frequencies, with only a single panel of control. The control filters were designed such that the module transitions back into its passive state near 1 kHz. The single-panel control does not completely eliminate the TL effect that is caused by the mass-air-mass resonance frequency. This is due to the strong acoustic coupling that exists between the panels at

this frequency. Any uncontrolled residual vibration that exists on panel 1 is readily transmitted to panel 2 at this frequency.

The predicted TL increases further when both panels are controlled simultaneously. The maximum increase in the TL for this scheme is 55 dB at 165 Hz. The average increase in the TL from 50 Hz to 500 Hz is 36 dB—twice that produced by single-panel control. The effect of the mass-air-mass resonance is no longer apparent.

It should be remembered that the enhanced model permits each panel surround to have an additional degree of freedom. The classical model of the loudspeaker presented by Beranek [16] and others does not possess this characteristic. It is conceivable that the surround could freely vibrate at some frequency even if the vibration of the panel was significantly reduced. This type of system response may have a significant effect on the maximum obtainable TL.

The effect of the ratio of surround area to panel area on the TL was explored. Three different ratios of S_2/S_1 (and likewise S_4/S_3) were examined for the case when both panels were actively controlled. The total surface area of the module was kept at 33 cm^2 and the ratio of S_2/S_1 was varied to produce ratios of 0, 0.125, and 0.250. The results of this analysis are shown in Figure 5-10. The degradation of the TL when S_2 is increased is dramatic at some frequencies. It should be noted that the TL prediction for the classical model of the loudspeaker is the same as the $S_2/S_1 = 0$ curve (i.e., no surround area). To obtain the best overall TL, the area that is not directly actuated (S_2 and S_4) should be minimized while maintaining sufficient resilience for isolation of interstitial structures and adjacent panels.

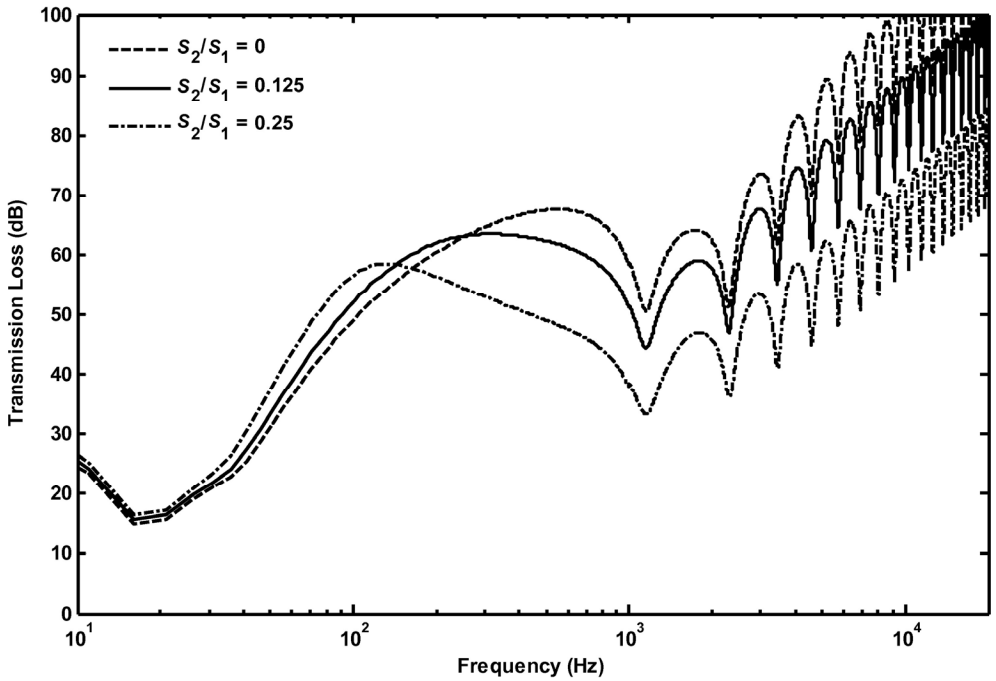

Figure 5-10. The effect of the area ratio S_2/S_1 on the TL when both panels are actively controlled.

The right-to-left unidirectional TL for the module is exactly the same as the results presented in Figure 5-10. This fact represents a significant improvement in performance over other ASAC and ASP methods. The physical hardware, along with the independent controllers enable the module to exhibit the same unidirectional sound TL in both directions through the module.

The effect of cavity depth on TL was also explored. It was shown earlier that the acoustic coupling strength increases in the vicinity of the mass-air-mass resonance as the space between the panels is diminished. This reduces the TL that can be achieved in the control bandwidth. The predicted TL for three different cavity depths is shown in Figure 5-11. It was found that the average achievable TL in the control bandwidth (20 Hz to 1 kHz) increases by approximately 6 dB each time the cavity depth (L) is doubled. The

low and high-frequency regions of the TL curve remain unaffected by the cavity depth (although the cavity resonances shift in frequency).

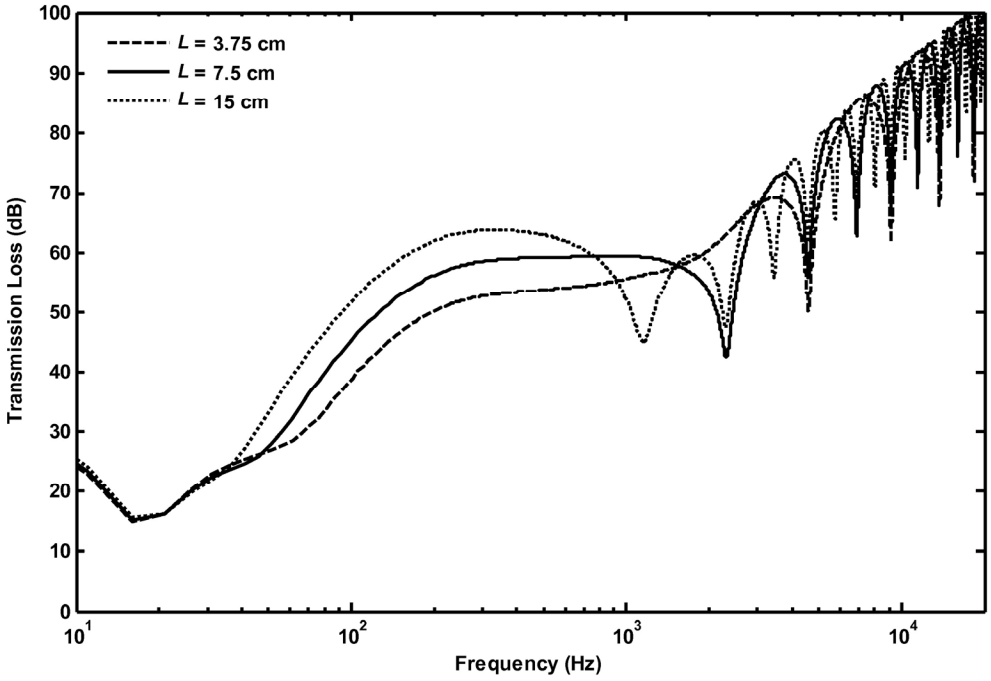

Figure 5-11. Effect of cavity depth *L* on the TL when both panels are actively controlled.

5.7.4 PREDICTED BIDIRECTIONAL TL

The final performance test of this ASP module is how the TL is affected when there is a pressure disturbance on both sides of the module. The previous section showed the results for the unidirectional TL—the TL when only $\hat{p}_{i1}$ or $\hat{p}_{i2}$ is present. The bidirectional TL is the TL through the module when both $\hat{p}_{i1}$ and $\hat{p}_{i2}$ are simultaneously present.

Suppose the primary disturbance source is $\hat{p}_{i1}$ and is located on the left side of the module. The TL from left-to-right through the module is given in Eq. (5.22). If the

pressure $\hat{p}_{i2}$ on the right side of the module is zero, then the equation reduces to the left-to-right unidirectional TL. The 'measurable' left-to-right TL of the module will be degraded if $\hat{p}_{i2}$ exists. The degradation to the 'measurable' TL will only occur at frequencies contained in $\hat{p}_{i2}$ and the amount of degradation will depend on the relative amplitude of $\hat{p}_{i2}$ to $\hat{p}_{i1}$. For the sake of illustration, let $\hat{p}_{i1}$ have a magnitude of unity at all frequencies and $\hat{p}_{i2}$ be zero everywhere outside of the bandwidth of 200-400 Hz but allowed to take on various amplitudes within that bandwidth: 0, 0.1, 1.0, 10. The apparent TL with both panels actively controlled is shown in Figure 5-12.

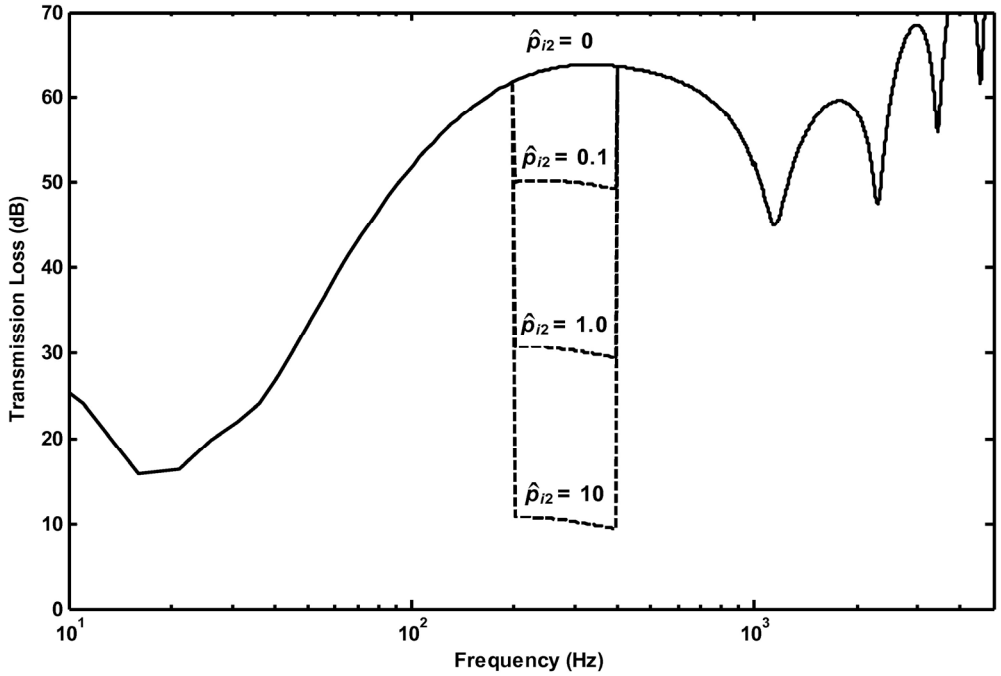

Figure 5-12. Apparent left-to-right TL through the module when a second disturbance source of different amplitude is present.

It is obvious that the 'measurable' TL is reduced when a second disturbance source is present in the receiving-side of the module. The reduction in the TL depends on

the amplitude of the second disturbance source. However, this should not represent any major concern about the effectiveness of the device. It is seen in Figure 5-12 that the active control of the device is not affected at frequencies outside of the bandwidth of $\hat{p}_{i2}$. In fact, the controlled module is actually attenuating the sound energy that is passing through the module from left to right but the presence of a second source on the receiving-side inhibits the ability to quantify the TL. This is almost a moot point for acoustic observers located on either side of the module; what they hear between 200 and 400 Hz would be dominated by the acoustic source that resides on their side of the module.

5.8 CONCLUSION

The TL performance of a feedback-controlled double-panel ASP module was examined. An enhanced model of a loudspeaker was used (instead of the classical loudspeaker model) wherein the surround was modeled with an additional degree of freedom. The TL predictions were developed for sound propagating in both directions through the module.

It was shown that the TL for the passive double-panel module exhibited the classical resonance effects at low frequencies. Active feedback control of a single panel improved the TL performance in this region and the model predicted an average TL boost of 18 dB from 50 Hz to 500 Hz. However, the mass-air-mass resonance dip was still apparent in the predicted TL curve due to the strong acoustic coupling in the cavity at this frequency. Simultaneous active feedback control of both panels improved the TL performance further, and the model predicted an average boost in the TL of 36 dB from

50 Hz to 500 Hz (over the passive case). It also completely eliminated the dip in the TL at the mass-air-mass resonance frequency.

The enhanced model of the loudspeaker illustrates the effect of having an uncontrolled vibrating surface area as part of the panel. In this particular application, the surround of the loudspeaker is still permitted to vibrate even if the vibration of the cone is significantly reduced. The residual vibration of the surround permits flanking around the cone and degrades the TL performance of the module at some frequencies. This effect can be reduced by minimizing the area of the surround. This effect represents an important consideration when designing ASP modules.

The cavity depth between the two panels also affected the maximum achievable TL. Smaller cavity depths intensified the strength of the acoustic coupling between the panels. On average, the achievable TL in the control bandwidth is reduced by 6 dB every time the cavity depth is cut in half. This effect is primarily seen at frequencies within the active control bandwidth. The TL at frequencies well below the mass-air-mass resonance is not affected, nor is the TL affected at sufficiently high frequencies above the control bandwidth.

This research demonstrated that simultaneous feedback control of each panel in a double-panel module is an effective way to actively increase TL at low frequencies. From this research, it also appears that the analog feedback controllers can be independent from one another. It was shown that the ASP module design, in conjunction with the analog feedback controllers, allowed the module to have bidirectional TL capabilities.

5.9 IMPEDANCE DEFINITION APPENDIX

Mechanical impedance substitutions

$$Z_{M1} \equiv \frac{(BL_1)^2}{Z_{E1}} + R_{M1} + \frac{1}{j\omega C_{M1}} + j\omega M_{M1} \quad \textbf{(5.27)}$$

$$Z_{M2} \equiv R_{M2} + \frac{1}{j\omega C_{M2}} + j\omega M_{M2} \quad \textbf{(5.28)}$$

$$Z_{M3} \equiv \frac{(BL_2)^2}{Z_{E2}} + R_{M3} + \frac{1}{j\omega C_{M3}} + j\omega M_{M3} \quad \textbf{(5.29)}$$

$$Z_{M4} \equiv R_{M4} + \frac{1}{j\omega C_{M4}} + j\omega M_{M4} \quad \textbf{(5.30)}$$

$$Z_{M12} \equiv R_{M12} + \frac{1}{j\omega C_{M12}} \quad \textbf{(5.31)}$$

$$Z_{M34} \equiv R_{M34} + \frac{1}{j\omega C_{M34}} \quad \textbf{(5.32)}$$

$$Z_{M1.PR} \equiv Z_{M1} + Z_{M12} \quad \textbf{(5.33)}$$

$$Z_{M2.PR} \equiv Z_{M2} + Z_{M12} \quad \textbf{(5.34)}$$

$$Z_{M3.PR} \equiv Z_{M3} + Z_{M34} \quad \textbf{(5.35)}$$

$$Z_{M4.PR} \equiv Z_{M4} + Z_{M34} \quad \textbf{(5.36)}$$

Acoustic impedance substitutions

$$Z_{AA} \equiv \frac{\rho_0 c}{S} + Z_{A1} + Z_{A2} \tag{5.37}$$

$$Z_{AB} \equiv Z_{AA} \tag{5.38}$$

B impedance substitutions

$$Z_{B1} \equiv \frac{S_3^{\,2} Z_{M4.PR} + 2S_3 S_4 Z_{M34} + S_4^{\,2} Z_{M3.PR}}{S_3^{\,2} Z_{AB} Z_{M4.PR} + S_4^{\,2} Z_{AB} Z_{M3.PR} + Z_{M3.PR} Z_{M4.PR} + 2S_3 S_4 Z_{AB} Z_{M34} - Z_{M34}^{\,2}} \tag{5.39}$$

$$Z_{B2} \equiv \frac{S_3 Z_{M4.PR} + S_4 Z_{M34}}{S_3^{\,2} Z_{AB} Z_{M4.PR} + S_4^{\,2} Z_{AB} Z_{M3.PR} + Z_{M3.PR} Z_{M4.PR} + 2S_3 S_4 Z_{AB} Z_{M34} - Z_{M34}^{\,2}} \tag{5.40}$$

C impedance substitutions

$$Z_{C1} \equiv S_1^{\,2} Z_{A2}^{\,2} Z_{B1} - S_1^{\,2} Z_{AA} - Z_{M1.PR} \tag{5.41}$$

$$Z_{C2} \equiv S_1 S_2 Z_{A2}^{\,2} Z_{B1} + Z_{M12} - S_1 S_2 Z_{AA} \tag{5.42}$$

$$Z_{C3} \equiv S_2^{\,2} Z_{A2}^{\,2} Z_{B1} - S_2^{\,2} Z_{AA} - Z_{M2.PR} \tag{5.43}$$

D impedance substitutions

$$Z_{D1} \equiv \frac{Z_{E1} Z_{E2} \left(S_1 Z_{C3} - S_2 Z_{C2} \right)}{Z_{E1} Z_{E2} \left(Z_{C2}^{\,2} - Z_{C1} Z_{C3} \right)} \tag{5.44}$$

$$Z_{D2} \equiv \frac{Z_{E2} \left(Z_{C3} \right)}{Z_{E1} Z_{E2} \left(Z_{C2}^{\,2} - Z_{C1} Z_{C3} \right)} \tag{5.45}$$

$$Z_{D3} \equiv \frac{Z_{E1}Z_{A2}Z_{B2}\left(S_1Z_{C3} - S_2Z_{C2}\right)}{Z_{E1}Z_{E2}\left(Z_{C2}{}^2 - Z_{C1}Z_{C3}\right)} \quad \textbf{(5.46)}$$

$$Z_{D4} \equiv \frac{Z_{E1}Z_{E2}\left(S_1Z_{C2} - S_2Z_{C1}\right)}{Z_{E1}Z_{E2}\left(Z_{C2}{}^2 - Z_{C1}Z_{C3}\right)} \quad \textbf{(5.47)}$$

$$Z_{D5} \equiv \frac{Z_{E2}\left(Z_{C2}\right)}{Z_{E1}Z_{E2}\left(Z_{C2}{}^2 - Z_{C1}Z_{C3}\right)} \quad \textbf{(5.48)}$$

$$Z_{D6} \equiv \frac{Z_{E1}Z_{A2}Z_{B2}\left(S_1Z_{C2} - S_2Z_{C1}\right)}{Z_{E1}Z_{E2}\left(Z_{C2}{}^2 - Z_{C1}Z_{C3}\right)} \quad \textbf{(5.49)}$$

$$Z_{D7} \equiv \frac{Z_{E1}Z_{E2}Z_{A2}Z_{B1}\left(S_2Z_{C2} - S_1Z_{C3}\right)}{Z_{E1}Z_{E2}\left(Z_{C2}{}^2 - Z_{C1}Z_{C3}\right)} \quad \textbf{(5.50)}$$

$$Z_{D8} \equiv \frac{Z_{E1}Z_{E2}Z_{A2}Z_{B1}\left(S_2Z_{C1} - S_1Z_{C2}\right)}{Z_{E1}Z_{E2}\left(Z_{C2}{}^2 - Z_{C1}Z_{C3}\right)} \quad \textbf{(5.51)}$$

F impedance substitutions

$$Z_{F1} \equiv \frac{\left(S_1Z_{D1} - S_2Z_{D4}\right)\left(S_3Z_{A2}Z_{E2}Z_{M4.PR} + S_4Z_{M34}Z_{A2}Z_{E2}\right)}{Z_{E2}\left(S_3{}^2Z_{AB}Z_{M4.PR} + S_4{}^2Z_{AB}Z_{M3.PR} + Z_{M3.PR}Z_{M4.PR} + 2S_3S_4Z_{AB}Z_{M34} - Z_{M34}{}^2\right)} \quad \textbf{(5.52)}$$

$$Z_{F2} \equiv \frac{\left(S_1Z_{D3} - S_2Z_{D6}\right)\left(S_3Z_{A2}Z_{E2}Z_{M4.PR} + S_4Z_{M34}Z_{A2}Z_{E2}\right) + \left(S_4{}^2Z_{AB} + Z_{M4.PR}\right)}{Z_{E2}\left(S_3{}^2Z_{AB}Z_{M4.PR} + S_4{}^2Z_{AB}Z_{M3.PR} + Z_{M3.PR}Z_{M4.PR} + 2S_3S_4Z_{AB}Z_{M34} - Z_{M34}{}^2\right)} \quad \textbf{(5.53)}$$

$$Z_{F3} \equiv \frac{\left(S_1Z_{D2} - S_2Z_{D5}\right)\left(S_3Z_{A2}Z_{E2}Z_{M4.PR} + S_4Z_{M34}Z_{A2}Z_{E2}\right)}{Z_{E2}\left(S_3{}^2Z_{AB}Z_{M4.PR} + S_4{}^2Z_{AB}Z_{M3.PR} + Z_{M3.PR}Z_{M4.PR} + 2S_3S_4Z_{AB}Z_{M34} - Z_{M34}{}^2\right)} \quad \textbf{(5.54)}$$

$$Z_{F4} \equiv \frac{\left(S_1Z_{D7} - S_2Z_{D8}\right)\left(S_3Z_{A2}Z_{E2}Z_{M4.PR} + S_4Z_{M34}Z_{A2}Z_{E2}\right)}{Z_{E2}\left(S_3{}^2Z_{AB}Z_{M4.PR} + S_4{}^2Z_{AB}Z_{M3.PR} + Z_{M3.PR}Z_{M4.PR} + 2S_3S_4Z_{AB}Z_{M34} - Z_{M34}{}^2\right)} \quad \textbf{(5.55)}$$

$$Z_{F5} \equiv \frac{Z_{E2}\left(S_3Z_{M4.PR} + S_4Z_{M34}\right)}{Z_{E2}\left(S_3{}^2Z_{AB}Z_{M4.PR} + S_4{}^2Z_{AB}Z_{M3.PR} + Z_{M3.PR}Z_{M4.PR} + 2S_3S_4Z_{AB}Z_{M34} - Z_{M34}{}^2\right)} \quad \textbf{(5.56)}$$

5.10 THESIS APPENDIX: ALTERNATE MODELS

This section contains more information on analogous circuit modeling that was not included as part of the manuscript that primarily composed the chapter. Its purpose is to present the circuits and equations necessary to model different TL configurations such as a single-panel partition with the classical model, a single-panel partition with the enhanced model, and a double-panel partition with the classical model. This section also contains TL results for each configuration that give insight into active panel partitions. *The impedance substitutions presented in this appendix are only valid for the particular section in which they are presented; they should not be used across sections unless specifically stated.*

5.10.1 CLASSICAL MODEL: SINGLE-PANEL TL

The classical model of a loudspeaker in a duct is shown in Figure 5-13. The mechanical components that the key parameters represent are included in the figure. Notice the lumped element parameters (C_{MS}, M_{MD}, R_{MS}) and the single radiating surface area (S_D). A resilient surround connecting the basket to the cone is not shown in this figure since it is not accounted for in the model. The voltage input to the loudspeaker is represented by $\hat{e}_g$ and the presumably uniform normal surface velocity of the cone is represented by $\hat{u}_D$. The composite parameters C_{MS}, M_{MD}, and R_{MS} can be measured using existing loudspeaker parameter measurement methods. The incident and transmitted pressures ($\hat{p}_i$ and $\hat{p}_t$ respectively) are also shown in the figure.

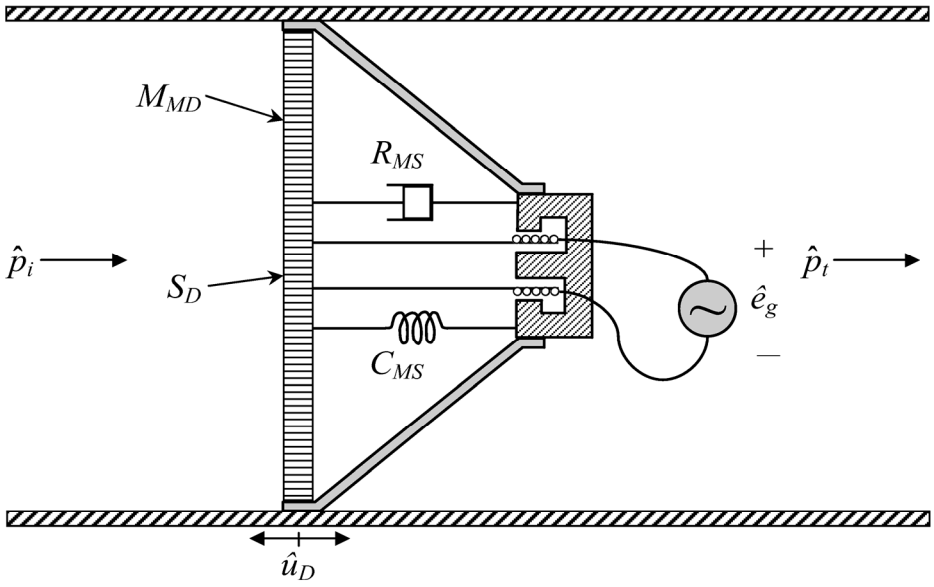

Figure 5-13. Cross-sectional view of a classical model of a loudspeaker in a duct.

The multiple-domain analogous circuit model for this configuration is shown in Figure 5-14. The left and right-most branches of the circuit are represented in the acoustic impedance domain while the center section is represented in the mechanical mobility domain. Three nodal equations can be written for this circuit.

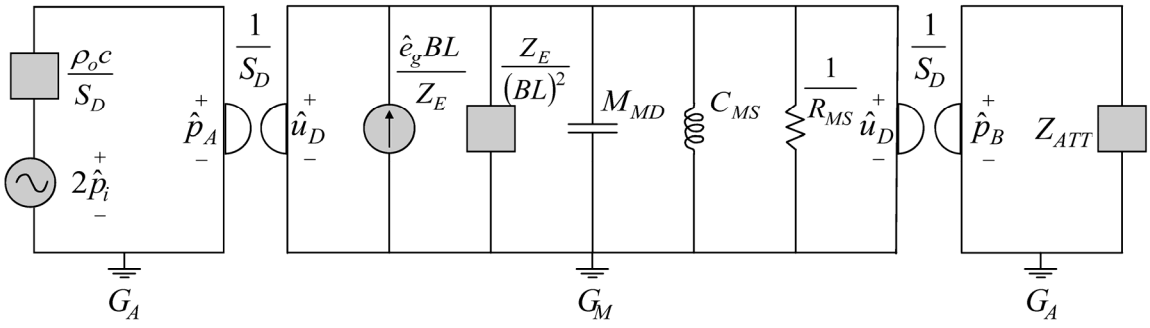

Figure 5-14. Multiple-domain analogous circuit model for a single-panel partition module using the classical model of a loudspeaker.

The development of the equations is not presented here, but the final equations needed to model the TL are summarized briefly in Eq. (5.57) through Eq. (5.61).

$$TL = 10\log\left(\left|\frac{\hat{p}_i}{\hat{u}_D \rho_0 c}\right|^2\right) \tag{5.57}$$

$$\hat{u}_D = \frac{1}{Z_E\left(2\rho_0 c S_D + Z_{M1}\right)}\left[\hat{e}_g BL + 2\hat{p}_i S_D Z_E\right] \tag{5.58}$$

$$Z_{M1} = \frac{(BL)^2}{Z_E} + R_{MS} + \frac{1}{j\omega C_{MS}} + j\omega M_{MD} \tag{5.59}$$

Passive (open circuit) case:

$$\begin{aligned} Z_E &\to \infty \\ \hat{e}_g &= 0 \end{aligned} \tag{5.60}$$

Active case (feedback control):

$$\begin{aligned} Z_E &= R_g + R_{E1} + j\omega L_{E1} \\ \hat{e}_g &= \frac{2j\omega c_1 \hat{p}_i S_D Z_E}{Z_E\left(2\rho_o c S_D + Z_{M1}\right) - j\omega BL_1 c_1} \end{aligned} \tag{5.61}$$

The Thiele-Small parameters for a HiVi M4N loudspeaker were measured using a maximum length sequence system analyzer (MLSSA). The electrical impedance of the loudspeaker was first measured in free-air in an anechoic chamber. Then a 7.7 g test mass was mounted on the cone and the impedance measurement was repeated. The Thiele-Small parameters were extracted from the measured data. The values that were used in the numerical analysis are shown in Table 5-3.

Table 5-3. Classical model parameters used in the single-panel numerical analysis.

Parameter	Value	Units
BL	3.541	Tm
C_{MS}	700	μm/N
L_E	0.230	mH
M_{MD}	6.129	g
R_E	6.483	Ω
R_{MS}	0.492	kg/s
S_D	30.00	cm^2

The predicted TL for the passive and active states is shown in Figure 5-15. The dips in the TL at 15 Hz and 2.2 kHz are effects of the controller—these frequencies are near the instability points of the closed-loop feedback control system and so there is a slight degradation in the TL.

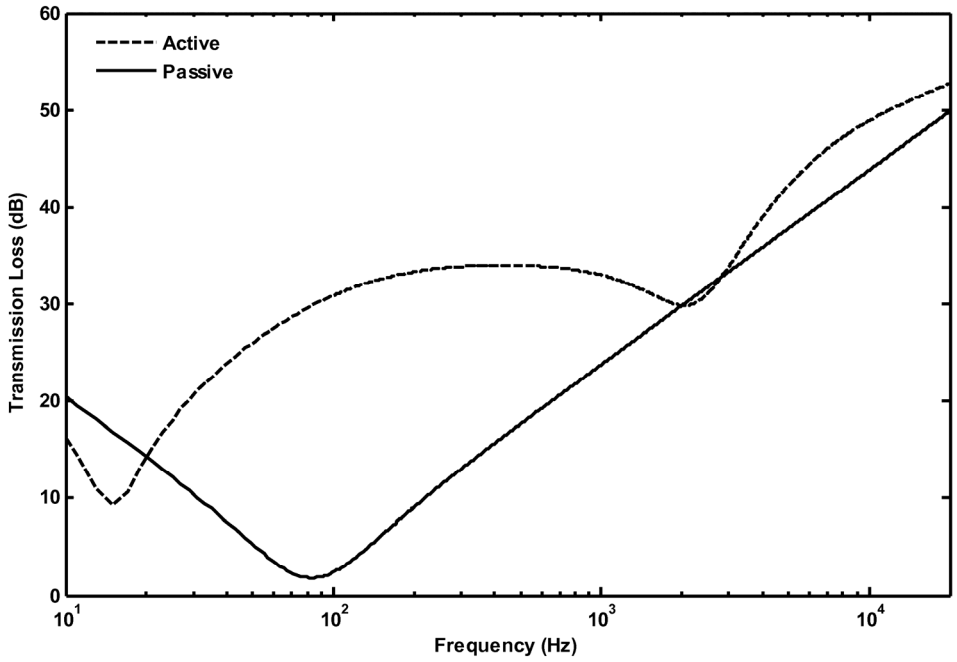

Figure 5-15. Predicted TL of a single-panel partition module using the classical model of a loudspeaker for passive and active states.

An important question about the results presented in Figure 5-15 is whether or not the very low-frequency (< 30 Hz) performance can be improved by altering the controller. Although the answer to this question is not a simple one, it can be approached from several angles. First recall Eq. (5.58). The only way to drive $\hat{u}_D$ to zero is to constrain the actuation force to be equal in magnitude and opposite in phase to the acoustic disturbance force. Equating the two mathematically and solving for the required control voltage $\hat{e}_g$ yields

$$\hat{e}_g = \frac{-2\hat{p}_i S_D Z_E}{BL} \tag{5.62}$$

This "optimum" control voltage only has frequency dependence in the Z_E term, and even then, the only frequency dependence is at high frequencies due to the inductance of the voice coil. The optimum control voltage for a uniform amplitude disturbance pressure is shown in Figure 5-16. This result indicates that very low amplitude control voltages can produce an actuation force capable of balancing the incident acoustic force.

While there is no obvious limitation in the figure for the frequency range of interest (meaning that the magnitude of the required control voltage is definitely achievable), there is a subtle practical limitation: there is no way to sense $\hat{p}_i$ directly. A microphone mounted in the source space outside the module would have difficulty measuring $\hat{p}_i$ for all but one-dimensional cases. A single microphone could only measure the total pressure (the sum of the incident and reflected pressures) at the measurement location. This limitation makes the generation of the optimal control voltage extremely difficult.

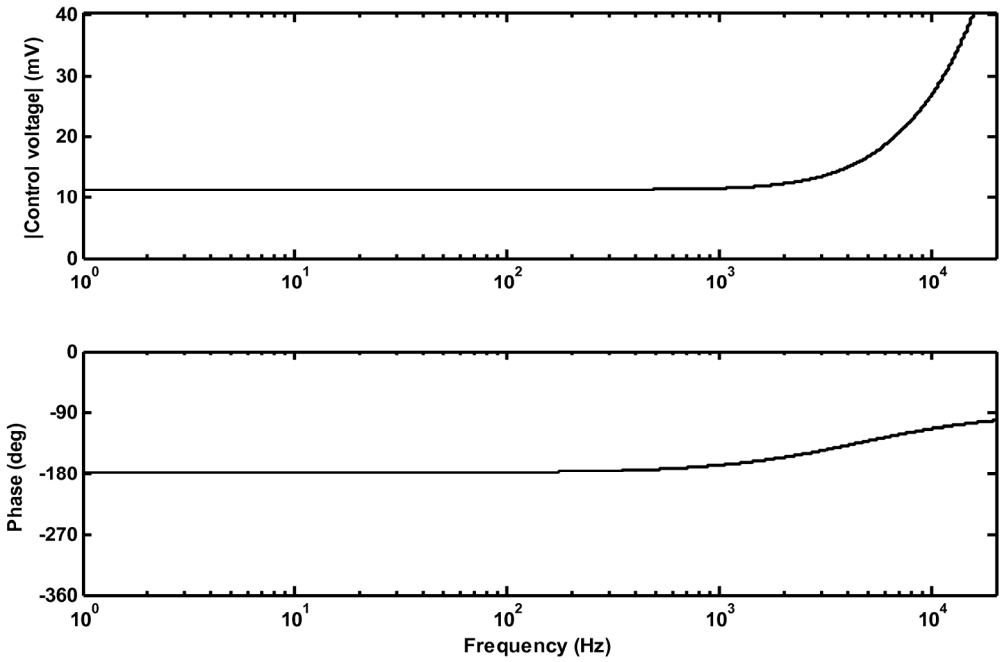

Figure 5-16. Optimum control voltage for a uniform amplitude incident pressure upon a single-panel partition module (classic model).

A vibro-acoustic quantity that can be reasonably sensed is the panel acceleration, which is essentially a filtered version of the incident pressure. Substituting Eq. (5.61) into Eq. (5.58) yields the surface velocity of the panel $\hat{u}_D$ while under feedback control (i.e., the reference signal for the controller originated from the acceleration of the panel)

$$\hat{u}_D = \frac{2\hat{p}_i S_D Z_E}{Z_E(2\rho_0 c S_D + Z_{M1})}\left[\frac{j\omega BLc_1}{Z_E(2\rho_0 c S_D + Z_{M1}) - j\omega BLc_1} + 1\right]. \qquad \textbf{(5.63)}$$

Simplification of this equation yields

$$\hat{u}_D = \frac{2\hat{p}_i S_D Z_E}{Z_E(2\rho_0 c S_D + Z_{M1}) - j\omega BLc_1}. \qquad \textbf{(5.64)}$$

The objective of the feedback controller is to force $\hat{u}_D$ towards zero, and an optimal controller would force $\hat{u}_D$ to equal zero. Using Eq. (5.64) with $\hat{u}_D$ set to equal zero requires the following expression to be true:

$$2\hat{p}_i S_D Z_E = 0. \tag{5.65}$$

Neither $\hat{p}_i$ nor S_D is permitted to be zero. Note that this equation has no dependence on the feedback controller transfer function c_1. Therefore, Eq. (5.65) highlights the important fact that the *only* way to force $\hat{u}_D$ to zero when the acceleration of the panel is used as a reference signal is to constrain Z_E to be zero. This means that *any* feedback controller can never completely force $\hat{u}_D$ to be zero. Because $\hat{u}_D$ can never be zero, this equation also indicates that infinite TL is not possible for an ASP module under feedback control. However, reducing the electrical impedance of the electromechanical motor will tend to reduce $\hat{u}_D$ and thus increase the TL.

The electrical impedance of the loudspeaker Z_E has three terms: R_g, R_E, and L_E. R_E and L_E are properties of the voice coil while R_g is the output resistance of the controller. The effect of changing R_E was investigated while leaving c_1 fixed. The active TL results for three different voice coil resistances are shown in Figure 5-17. Each halving of the voice coil resistance increased the TL by 6 dB across the entire control bandwidth.

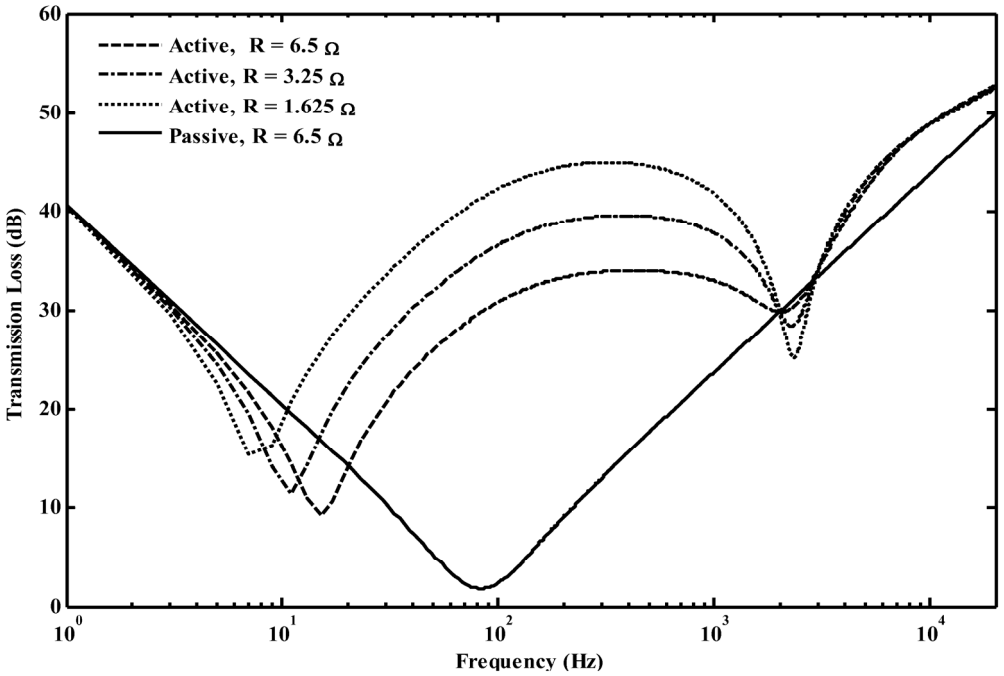

Figure 5-17. TL predictions of an active single-panel partition for three different voice coil resistances.

Although Eq. (5.65) indicates that changing Z_E has the most profound effect upon the possible TL, other mechanical properties of the loudspeaker could also be changed. The effect of changing the mechanical compliance of the loudspeaker was also investigated. The nominal compliance value used in the analysis was doubled and then doubled again. The results for all three cases are shown in Figure 5-18. It can be seen that changing the compliance value by a factor of 2 has a 6 dB effect on the passive TL results below the resonance frequency of the loudspeaker. However, the increase in the TL produced by active control at the lowest frequencies is unimpressive. This corresponds to what was predicted by Eq. (5.65); changing mechanical properties of the driver has a minimal effect on the active TL result.

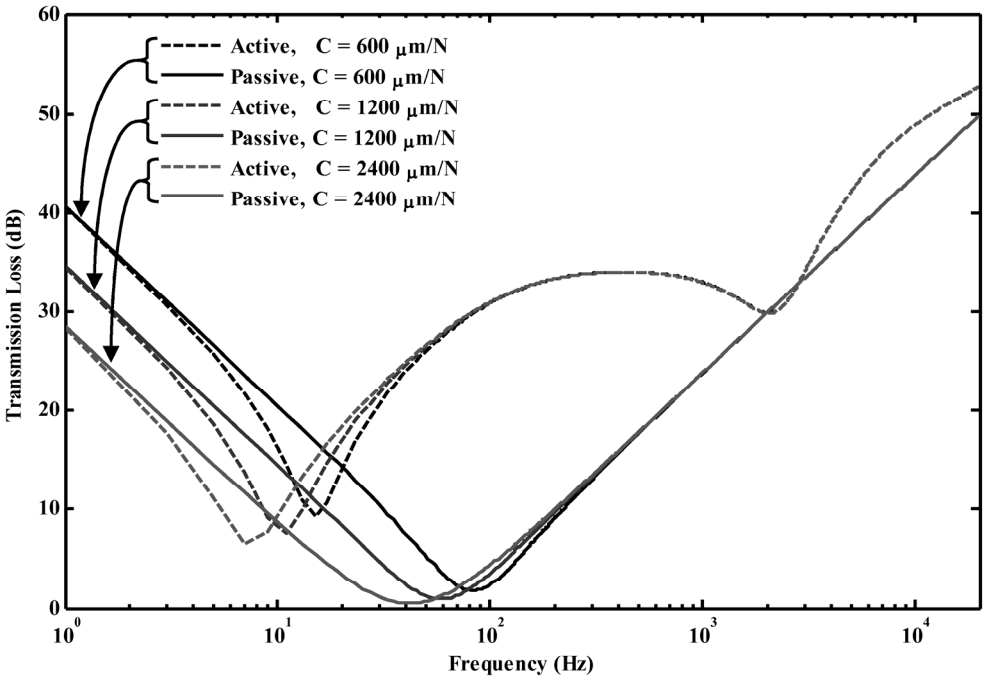

Figure 5-18. Effect of changing the mechanical compliance on the TL for both passive and active cases.

It might be suggested that a special filter be placed in-line so that the signal from the accelerometer could be processed to look like $\hat{p}_i$. Although this solution is commonly proposed, Nelson and Elliott discussed this approach this in section 7.3 of their book [50, pg. 213]. They make the following comment:

> "At first sight, this would appear to be a simple problem to solve. However, we are constrained considerably in our choice of $G(j\omega)$ [c_1 in the treatment of this thesis]. First, $G(j\omega)$ must be realizable, that is, it must have a causal impulse response – we are not at liberty to introduce a filter which produces its output prior to its input (the problem would indeed be simpler if we could!) Second, we have to ensure that the closed-loop system that we produce is *stable*."

This approach would result in the filter shown in Figure 5-19. This filter is not practical for several reasons. First, the high gain at low frequencies would produce very high voltages for low frequencies that would overdrive the actuator. Second, the shape of this filter is fairly smooth for the model and could possibly be created in an analog filter device, but the high-frequency spectrum of an actual electromagnetic loudspeaker would make the FRF more difficult to achieve with an analog filter. It is simply not feasible to use this type of filter as a feedback controller.

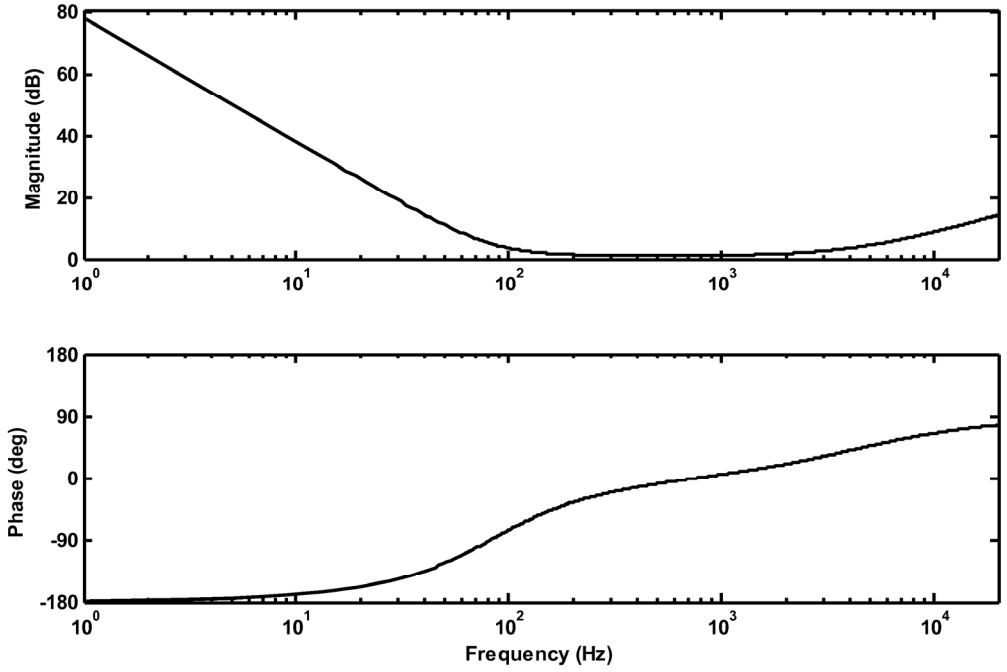

Figure 5-19. Possible control filter for a single-panel active partition module.

5.10.2 ENHANCED MODEL: SINGLE-PANEL TL

The enhanced model of a loudspeaker in a duct is shown in Figure 5-20. In this case, there are two transmitting surface areas, S_1 and S_2. The composite parameters of the classical model have been broken down into individual parameters. A new measurement method for extracting these parameters was presented in Ch. 4.

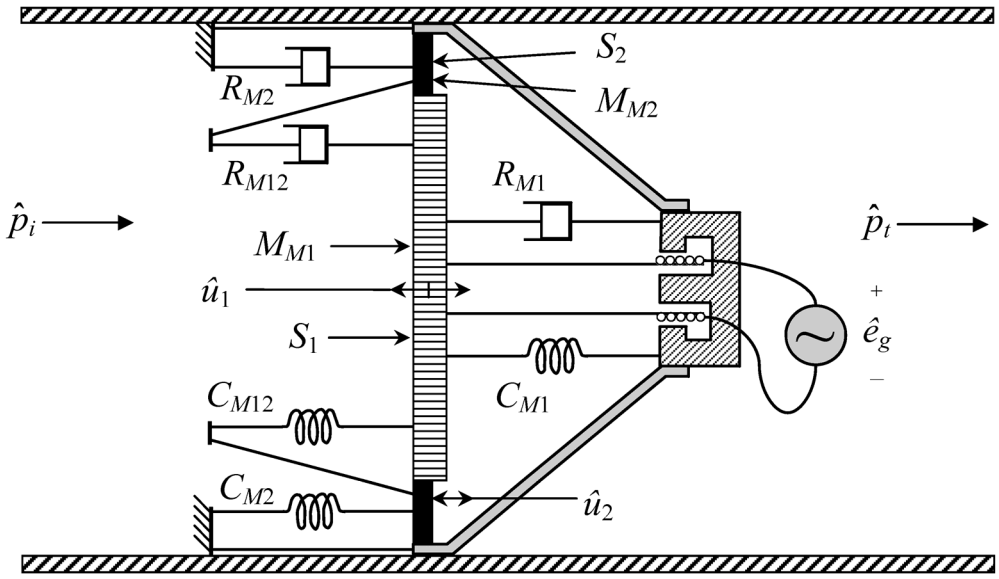

Figure 5-20. Cross-sectional view of an enhanced model of a loudspeaker in a duct.

The analogous circuit model for this configuration is shown in Figure 5-21 [after 46]. The left and right-most branches of the circuit are represented in the acoustic impedance domain while the center section is represented in the mechanical mobility domain. Four nodal equations can be written for this circuit.

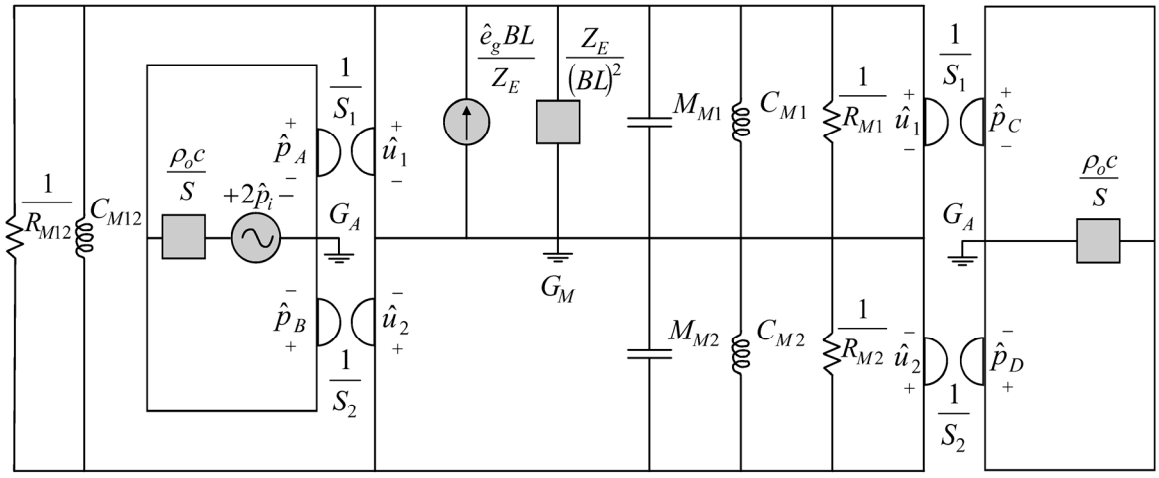

Figure 5-21. Multiple-domain analogous circuit model for a single-panel partition module using the enhanced model of a loudspeaker.

The development of the equations is not presented here, but the final equations needed to model the TL are summarized briefly in Eq. (5.66) through Eq. (5.81). The measured parameter values used in the enhanced model are shown in Table 5-4.

$$TL = 10\log\left(\left|\frac{\hat{p}_i S}{\hat{U}_1 \rho_0 c}\right|^2\right) \tag{5.66}$$

$$\hat{U}_1 = \hat{u}_1 S_1 + \hat{u}_2 S_2 \tag{5.67}$$

$$\hat{u}_1 = 2\hat{p}_i Z_{C1} - \hat{e}_g BL Z_{C2} \tag{5.68}$$

$$\hat{u}_2 = 2\hat{p}_i Z_{C3} + \hat{e}_g BL Z_{C4} \tag{5.69}$$

$$Z_{M1} = \frac{(BL)^2}{Z_E} + R_{MS} + \frac{1}{j\omega C_{MS}} + j\omega M_{MD} \tag{5.70}$$

$$Z_{M2} = R_{M2} + \frac{1}{j\omega C_{M2}} + j\omega M_{M2} \tag{5.71}$$

$$Z_{M12} = R_{M12} + \frac{1}{j\omega C_{M12}} \tag{5.72}$$

$$Z_{B1} = 2S_1{}^2 \frac{\rho_0 c}{S} + Z_{M1} + Z_{M12} \tag{5.73}$$

$$Z_{B2} = 2S_1 S_2 \frac{\rho_0 c}{S} - Z_{M12} \tag{5.74}$$

$$Z_{B3} = 2S_2{}^2 \frac{\rho_0 c}{S} + Z_{M2} + Z_{M12} \tag{5.75}$$

$$Z_{C1} = \frac{\left(S_2 Z_{B2} - S_1 Z_{B3}\right)}{\left(Z_{B2}{}^2 - Z_{B1} Z_{B3}\right)} \tag{5.76}$$

$$Z_{C2} = \frac{Z_{B3}}{Z_E\left(Z_{B2}{}^2 - Z_{B1} Z_{B3}\right)} \tag{5.77}$$

$$Z_{C3} = \frac{\left(S_1 Z_{B2} - S_2 Z_{B1}\right)}{\left(Z_{B2}{}^2 - Z_{B1} Z_{B3}\right)} \tag{5.78}$$

$$Z_{C4} = \frac{Z_{B2}}{Z_E\left(Z_{B2}{}^2 - Z_{B1} Z_{B3}\right)} \tag{5.79}$$

Passive case (open circuit):

$$\begin{aligned} Z_E &\to \infty \\ \hat{e}_g &= 0 \end{aligned} \tag{5.80}$$

Active case (feedback control):

$$\begin{aligned} Z_E &= R_g + R_E + j\omega L_E \\ \hat{e}_g &= \frac{2j\omega c_1 \hat{p}_i Z_{C1}}{j\omega BLZ_{C2} c_1 + 1} \end{aligned} \tag{5.81}$$

Table 5-4. Enhanced model parameters used in the single-panel numerical analysis.

Parameter	Value	Units	Parameter	Value	Units
BL	3.541	Tm	M_{M2}	0.146	g
L_E	0.230	mH	C_{M1}	2297.0	μm/N
R_E	6.483	Ω	C_{M2}	448.0	μm/N
R_g	0.100	Ω	C_{M12}	272.0	μm/N
S_1	30.00	cm^2	R_{M1}	0.570	kg/s
S_2	3.00	cm^2	R_{M2}	0.300	kg/s
M_{M1}	7.205	g	R_{M12}	0.300	kg/s

The predicted TL for the passive and active states is shown in Figure 5-22. There are still dips in the TL at 15 Hz and 2.2 kHz, which are effects of the controller. These frequencies are near the instability points of the closed-loop feedback control system, so there is a slight degradation in the TL. These dips were also seen in Figure 5-15. However, a new dip has emerged in the enhanced model near 1 kHz. This dip is caused by the movement of the surround when the vibration of the cone is reduced through actuation.

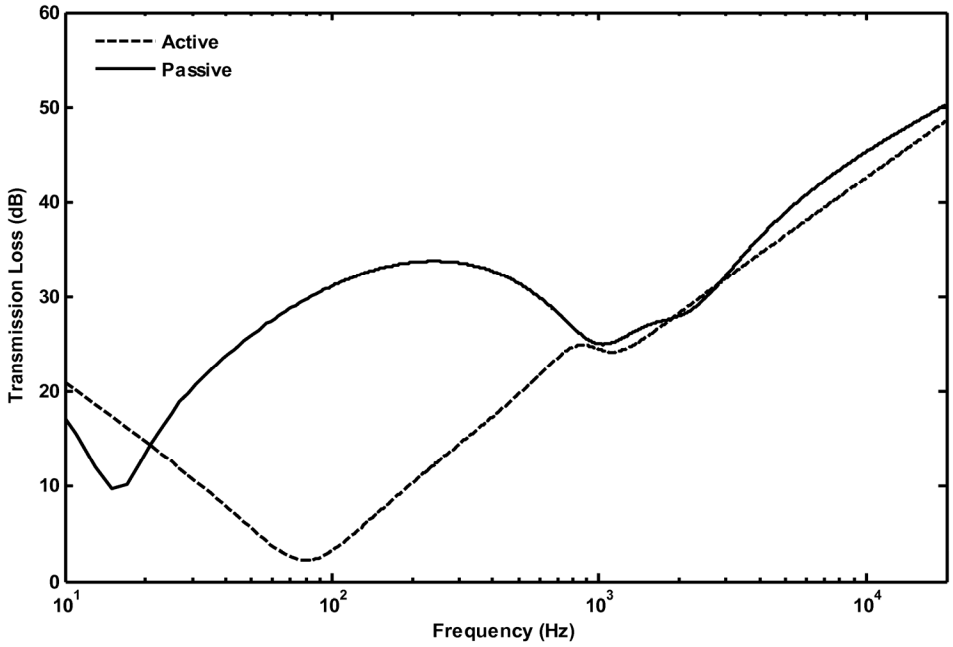

Figure 5-22. Predicted TL of a single-panel partition module using the enhanced model of a loudspeaker for passive and active states.

A comparison of the passive and active states for the classical and enhanced single-panel models is shown in Figure 5-23. Accounting for the independent area of the surround degrades the TL by 9 dB at 1 kHz. The TL is not affected below 200 Hz, where the cone and the surround move in phase with one another.

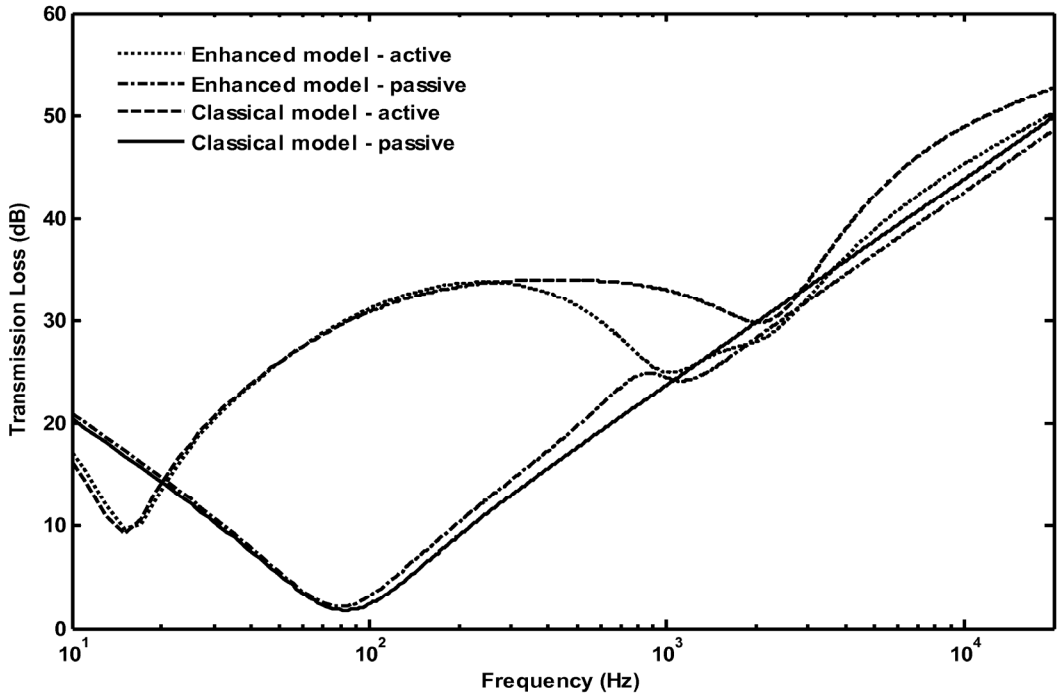

Figure 5-23. Comparison of the active and passive TL predictions for the classical model and the enhanced model of a single-panel partition module.

5.10.3 CLASSICAL MODEL: DOUBLE-PANEL TL

A double-panel partition composed of two loudspeakers placed back-to-back is shown in Figure 5-24. The classical model of the loudspeaker was used to analyze the TL through the device. There is one radiating surface area for each panel, S_D. Although there is actually a resilient surround that connects the panel to the interstitial structure, the

surround is not shown in Figure 5-24 because it is not included in the model. This analysis assumes that the loudspeakers have identical properties, but the control voltages are different. The cavity depth L is the distance between the two panels.

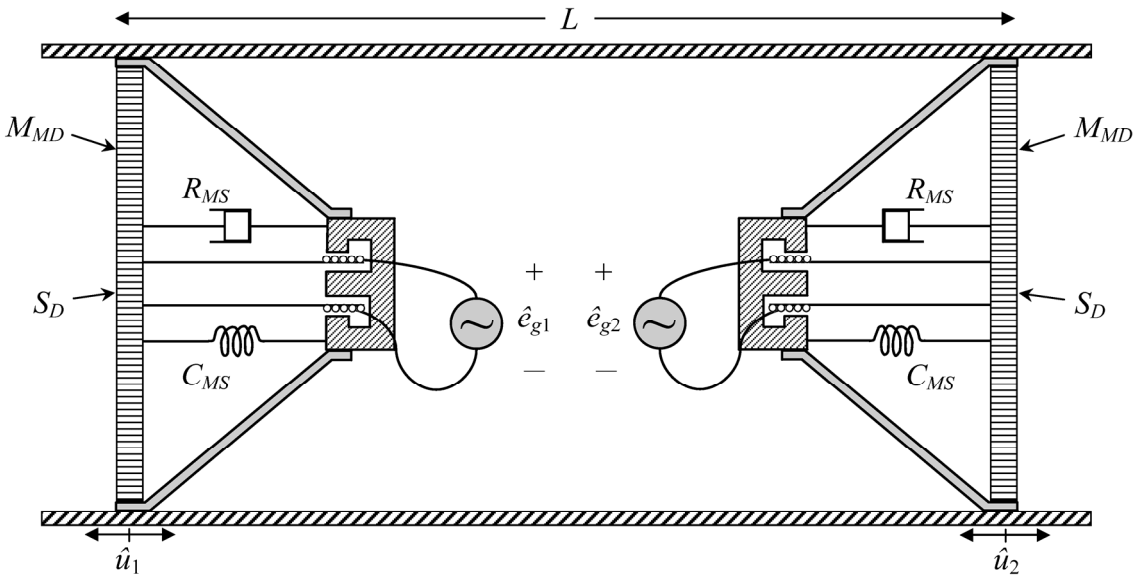

Figure 5-24. Cross-sectional view of a bidirectional double-panel partition module using a classical model of a loudspeaker.

The multiple-domain analogous circuit for this configuration is shown in Figure 5-25. The leftmost loudspeaker in the module is represented by the left side of the circuit and the rightmost loudspeaker is represented by the right side of the circuit. The acoustic impedance portions of the circuit are identifiable by the acoustic ground designator G_A. The two mechanical mobility portions of the circuit are identifiable by the mechanical ground designator G_M. The acoustic T-network located in the center of the circuit models the one-dimensional acoustic space between the panels.

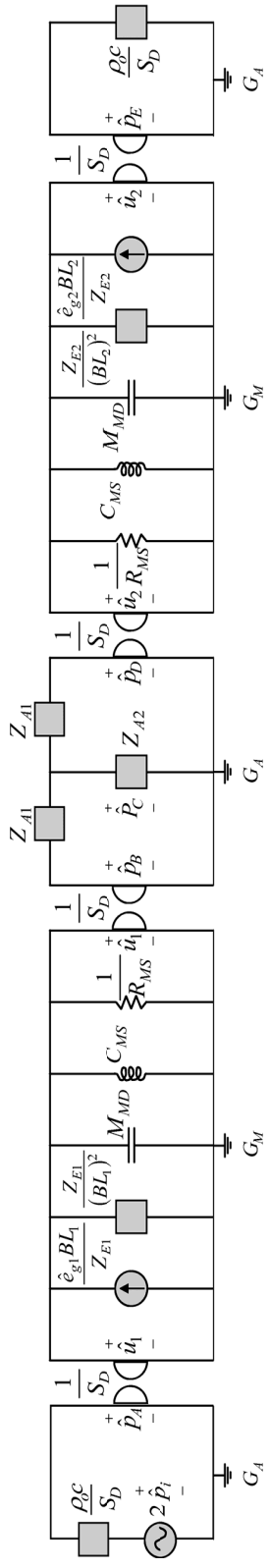

Figure 5-25. Multiple-domain analogous circuit representing a bidirectional double-panel partition module using the classical model of a loudspeaker.

The development of the equations is not presented here, but the final equations needed to model the TL are summarized in Eq. (5.82) through Eq. (5.97).

$$TL = 10\log\left(\left|\frac{\hat{p}_i}{\hat{u}_2\rho_0 c}\right|^2\right) \tag{5.82}$$

$$\hat{u}_1 = 2\hat{p}_i Z_{D1} + \hat{e}_{g1} BL_1 Z_{D2} + \hat{e}_{g2} BL_2 Z_{D3} \tag{5.83}$$

$$\hat{u}_2 = 2\hat{p}_i Z_{D4} + \hat{e}_{g1} BL_1 Z_{D5} + \hat{e}_{g2} BL_2 Z_{D6} \tag{5.84}$$

$$Z_{M1} = \frac{(BL_1)^2}{Z_{E1}} + R_{MS} + \frac{1}{j\omega C_{MS}} + j\omega M_{MD} \tag{5.85}$$

$$Z_{M2} = \frac{(BL_2)^2}{Z_{E2}} + R_{MS} + \frac{1}{j\omega C_{MS}} + j\omega M_{MD} \tag{5.86}$$

$$Z_B = S_D\rho_o c + {S_D}^2(Z_{A1} + Z_{A2}) \tag{5.87}$$

$$Z_{D1} = \frac{S_D(Z_{E1}Z_{E2})(Z_B + Z_{M2})}{Z_{E1}Z_{E2}\left({Z_B}^2 - {S_D}^4{Z_{A2}}^2 + Z_B Z_{M1} + Z_B Z_{M2} + Z_{M1}Z_{M2}\right)} \tag{5.88}$$

$$Z_{D2} = \frac{(Z_{E2})(Z_B + Z_{M2})}{Z_{E1}Z_{E2}\left({Z_B}^2 - {S_D}^4{Z_{A2}}^2 + Z_B Z_{M1} + Z_B Z_{M2} + Z_{M1}Z_{M2}\right)} \tag{5.89}$$

$$Z_{D3} = \frac{(Z_{E1})\left({S_D}^2 Z_{A2}\right)}{Z_{E1}Z_{E2}\left({Z_B}^2 - {S_D}^4{Z_{A2}}^2 + Z_B Z_{M1} + Z_B Z_{M2} + Z_{M1}Z_{M2}\right)} \tag{5.90}$$

$$Z_{D4} = \frac{{S_D}^3(Z_{E1}Z_{E2})(Z_{A2})}{Z_{E1}Z_{E2}\left({Z_B}^2 - {S_D}^4{Z_{A2}}^2 + Z_B Z_{M1} + Z_B Z_{M2} + Z_{M1}Z_{M2}\right)} \tag{5.91}$$

$$Z_{D5} = \frac{(Z_{E2})\left({S_D}^2 Z_{A2}\right)}{Z_{E1}Z_{E2}\left({Z_B}^2 - {S_D}^4{Z_{A2}}^2 + Z_B Z_{M1} + Z_B Z_{M2} + Z_{M1}Z_{M2}\right)} \tag{5.92}$$

$$Z_{D6} = \frac{(Z_{E1})(Z_B + Z_{M1})}{Z_{E1}Z_{E2}\left({Z_B}^2 - {S_D}^4{Z_{A2}}^2 + Z_B Z_{M1} + Z_B Z_{M2} + Z_{M1}Z_{M2}\right)} \tag{5.93}$$

Passive case (both loudspeakers with open circuits):

$$\begin{aligned} Z_{E1} &\to \infty \\ Z_{E2} &\to \infty \\ \hat{e}_{g1} &= 0 \\ \hat{e}_{g2} &= 0 \end{aligned} \tag{5.94}$$

Panel 1 active case (feedback control on panel 1,open circuit on loudspeaker 2):

$$\begin{aligned} Z_{E1} &= R_g + R_{E1} + j\omega L_{E1} \\ Z_{E2} &\to \infty \\ \hat{e}_{g1} &= \frac{2j\omega c_1 \hat{p}_i Z_{D1}}{1 - j\omega BL_1 Z_{D2} c_1} \\ \hat{e}_{g2} &= 0 \end{aligned} \tag{5.95}$$

Panel 2 active case (feedback control on panel 2,open circuit on loudspeaker 1):

$$\begin{aligned} Z_{E1} &\to \infty \\ Z_{E2} &= R_g + R_{E2} + j\omega L_{E2} \\ \hat{e}_{g1} &= 0 \\ \hat{e}_{g2} &= \frac{2j\omega c_2 \hat{p}_i Z_{D4}}{1 - j\omega BL_2 Z_{D6} c_2} \end{aligned} \tag{5.96}$$

Both panels active case (feedback control on both panels):

$$\begin{aligned} Z_{E1} &= R_g + R_{E1} + j\omega L_{E1} \\ Z_{E2} &= R_g + R_{E2} + j\omega L_{E2} \\ \hat{e}_{g1} &= \frac{-2\hat{p}_i j\omega c_1 \left(Z_{D1} - j\omega BL_2 c_2 Z_{D1} Z_{D6} + j\omega BL_2 c_2 Z_{D3} Z_{D4}\right)}{j\omega c_1 BL_1 Z_{D2} + j\omega c_2 BL_2 Z_{D6} - j^2\omega^2 c_1 c_2 BL_1 BL_2 Z_{D2} Z_{D6} + j^2\omega^2 c_1 c_2 BL_1 BL_2 Z_{D3} Z_{D5} - 1} \\ \hat{e}_{g2} &= \frac{-2\hat{p}_i j\omega c_2 \left(Z_{D4} + j\omega BL_1 c_1 Z_{D1} Z_{D5} - j\omega BL_1 c_1 Z_{D2} Z_{D4}\right)}{j\omega c_1 BL_1 Z_{D2} + j\omega c_2 BL_2 Z_{D6} - j^2\omega^2 c_1 c_2 BL_1 BL_2 Z_{D2} Z_{D6} + j^2\omega^2 c_1 c_2 BL_1 BL_2 Z_{D3} Z_{D5} - 1} \end{aligned} \tag{5.97}$$

The measured parameter values that were used in this analysis are shown in Table 5-5. These parameters were measured with a MLSSA system in an anechoic chamber. Since the two halves of the module are identical (i.e., the same type of loudspeaker was used on each side), $BL_1 = BL_2$, $L_{E1} = L_{E2}$, etc.

Table 5-5. Classical model parameters used in the double-panel numerical analysis.

Parameter	Value	Units
BL_1, BL_2	3.541	Tm
C_{MS}	700.0	μm/N
L_{E1}, L_{E2}	0.230	mH
M_{MD}	6.129	g
R_{E1}, R_{E2}	6.483	Ω
R_{MS}	0.492	kg/s
S_D	30.00	cm^2

The predicted TL for three control configurations of the module is shown in Figure 5-26. The effects of the control spillover from the feedback controller are again visible at 15 Hz and 2.2 kHz. The effect of the axial cavity resonances are clearly seen by the sharp dips in the TL beginning at 1.2 kHz.

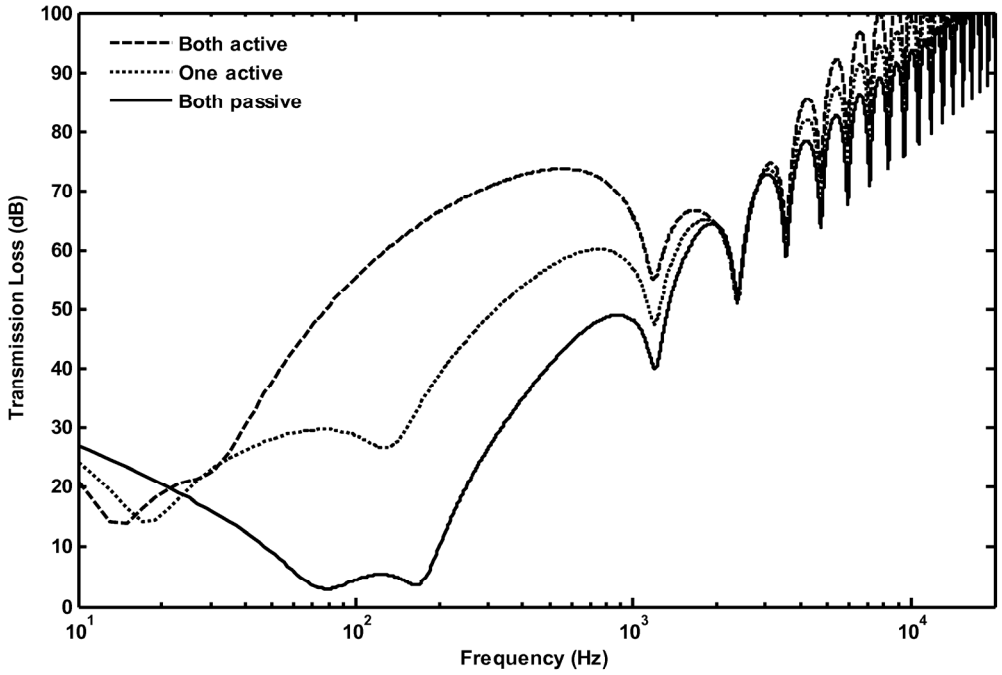

Figure 5-26. Predicted TL of a double-panel partition module using the classical model of a loudspeaker for passive and two active states.

It is instructive to compare the classical model presented in this section to the enhanced model presented previously. The predicted TL results are shown in Figure 5-27. Careful inspection of this figure reveals all of the fundamental behaviors of the model and highlights the difference between the classical and enhanced models. First, the enhanced model predicts degradation in the TL of the double-panel partition due to the effects of the surround, especially in the range from 100 Hz to 2 kHz. Second, the model predicts a slight degradation in the TL caused by near instability of the feedback controller at 15 Hz and 2.2 kHz. Third, the model predicts the axial cavity resonances beginning at 1.2 kHz.

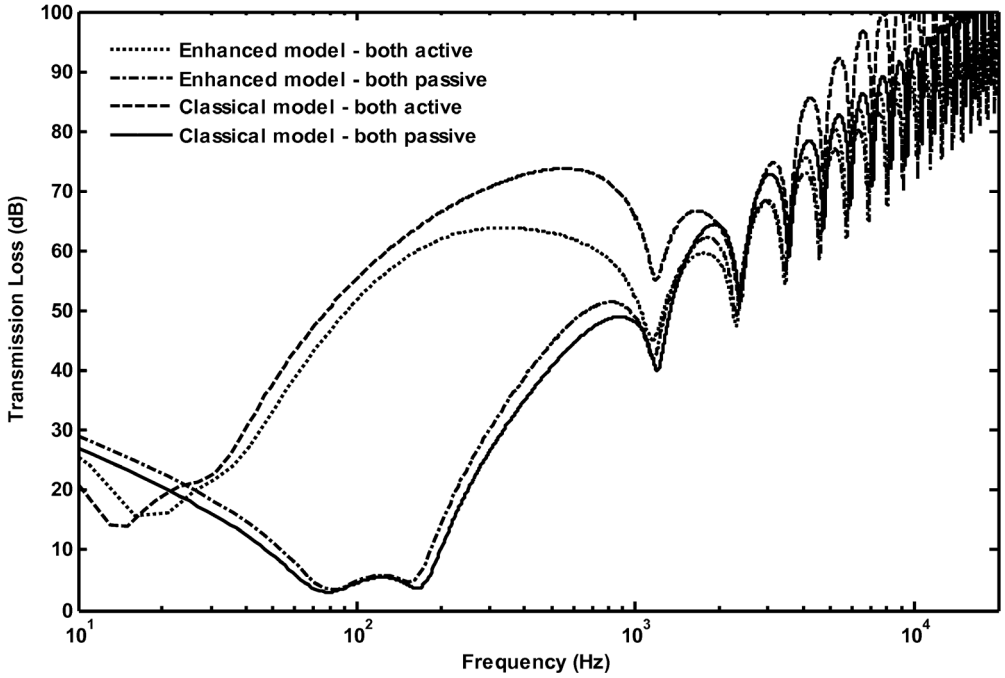

Figure 5-27. Comparison of the active and passive TL predictions for the classical and enhanced model of a double-panel partition module.

Finally, the control phenomenon illustrated by Eq. (5.65), $2\hat{p}_i S_D Z_E = 0$, was investigated to see if the trend held up for the double-panel case. This effect was analyzed numerically for the double-panel case because the necessary impedance substitutions made it difficult to draw insight from the resulting analytical equation. Instead, the effect was analyzed by running the classical model of the double-panel module for two different loudspeakers: the Aura Sound NS4-8A and the Aura Sound NS4-4A. These loudspeakers have nearly identical parameters except for their DC voice coil resistances (8 Ω and 4 Ω respectively). The compared TLes for the two loudspeakers in a double-panel partition module are shown in Figure 5-28.

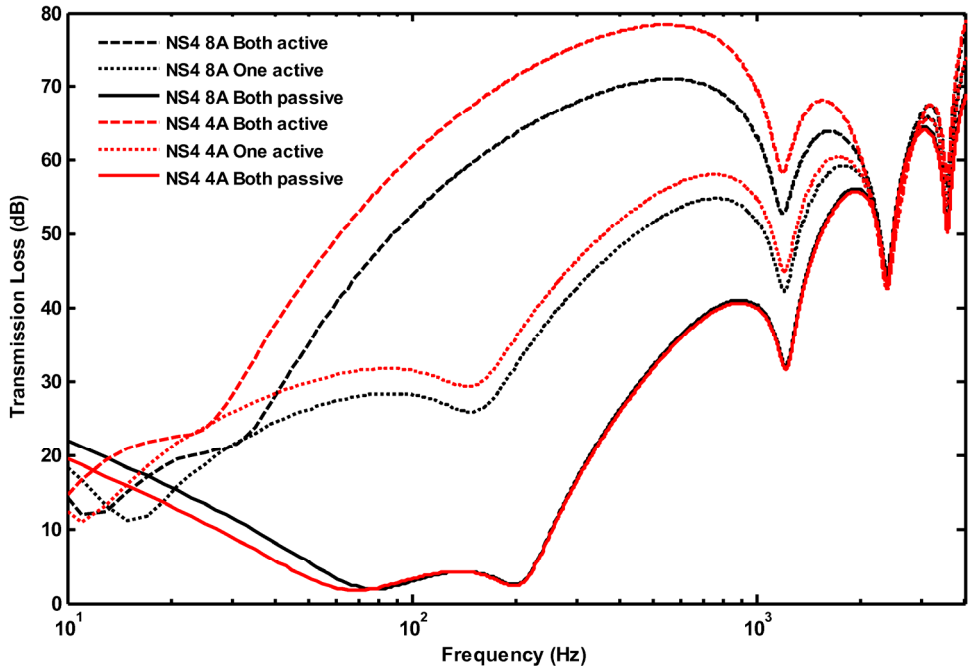

Figure 5-28. Comparison of two Aura Sound loudspeakers with different voice coil resistances in a double-panel module.

Very little difference was observed in the passive TL between the two loudspeakers. However, the TL curve for the active case, in which both panels were controlled, was 8 dB higher in the loudspeaker with the 4 Ω voice coil resistance than the loudspeaker with the 8 Ω voice coil resistance. It is hypothesized that the effect of reducing the electrical impedance of the loudspeaker translates into the ability to send more electrical power into the device, which ultimately results in better TL during active control.

6 ACTIVE SOUND TRANSMISSION CONTROL OF A DOUBLE-PANEL ASP MODULE USING DECOUPLED ANALOG FEEDBACK CONTROL: EXPERIMENTAL RESULTS

This chapter presents a paper submitted to the Journal of the Acoustical Society of America. The formatting of the paper has been modified to meet the formatting requirements of this thesis.

6.1 CONTRIBUTING AUTHORS AND AFFILIATIONS

Jason D. Sagers
Department of Mechanical Engineering, 435 CTB, Brigham Young University, Provo, UT 84602; email: jsagers@byu.edu

Timothy W. Leishman
Department of Physics and Astronomy, N247 ESC, Brigham Young University, Provo, UT 84602; email: tim_leishman@byu.edu

Jonathan D. Blotter
Department of Mechanical Engineering, 435 CTB, Brigham Young University, Provo, UT 84602; email: jblotter@byu.edu

6.2 ABSTRACT

Low-frequency sound transmission has always plagued the sound isolation performance of lightweight partitions. Over the last two decades, researchers have investigated actively controlled structures to better reduce sound transmission through a partition from a source space into a receiving space. These approaches often focus on the improvement of low-frequency TL through lightweight partitions. One promising approach involves active segmented partitions (ASPs) wherein partitions are segmented

into separately controlled modules. This paper provides an experimental analysis of a new double-panel ASP module wherein each panel is independently controlled by an analog feedback controller. The experimental results are compared to numerical predictions. Plant frequency response functions, acoustic coupling strength frequency response functions, and the TL of single- and double-panel partitions are presented. The averaged measured TL from 20 Hz to 1 kHz for an actively controlled single-panel module was 29 dB, compared to 14 dB for the passive case. The average measured TL over the same bandwidth for the actively controlled double-panel module was 57 dB, compared to 31 dB for the passive case.

6.3 INTRODUCTION

Passive single- and double-panel partitions have long been used to reduce sound transmission into noise-sensitive environments. Although both types of partitions can provide reasonable sound isolation at high frequencies, their performance at low frequencies is severely degraded due to resonance effects [4, 98]. A common passive method to reduce the low-frequency sound transmission is to add mass to the partition. There are applications when weight is not an issue and this approach is fine. However, there are many applications such as sound isolation for aircraft cabins, rocket payloads, large ceilings, and high-rise buildings where this solution is not viable because of weight penalties. Active control was proposed as a means to improve the low-frequency sound isolation of single- and double-panel partitions without adding additional mass. Two main categories of active control approaches are present in the literature: active structural acoustic control (ASAC) and active segmented partitions (ASP).

The term active structural acoustic control, or ASAC, was coined to describe a range of active control strategies where control forces are applied directly to a continuous panel in order to reduce the radiated acoustic pressure [12]. ASAC methods have been explored thoroughly [13, 14, 17-25]. In general, receiving-side attenuations with single-panel ASAC methods have been small (on the order of 5-10 dB). Additionally, comparing the performance of one ASAC implementation to another is difficult because the measurement techniques have been inconsistent. The major drawbacks to the ASAC approach are the large number of fully-coupled actuator/sensor pairs, the need for microphones in the receiving space, and the spatial control spillover that inevitably results when controlling a continuous panel. In short, the complexities of ASAC control for large scale implementations have been daunting.

An alternate approach to ASAC is active segmented partitions (ASP), which has been implemented by Leishman [8, 45]. In this approach, a single or double-panel partition is subdivided into an array of discrete modules that are mechanically segmented from each other. The mechanical segmentation of the partition eliminates the spatial control spillover that occurs when trying to control a continuous panel. In the case of double-panel partitions, the interior space between the panels is also acoustically segmented with an acoustically rigid interstitial structure. The acoustic segmentation simplifies the control problem by imposing long-wavelength conditions for the individual modules and by reducing acoustic cross-talk between modules inside the partition.

Leishman produced numerical models for two single-panel and two double-panel ASP modules [46]. The control objective for each module was to minimize the surface velocity of the transmitting panel. His most effective configuration was a double-panel

module in which a composite source-side panel was used to minimize the volume velocity into the cavity and thus "freeze" the transmitting panel. The normal-incidence TL was measured in a plane-wave tube for both an individual module and a 2 x 2 array of modules [47, 48]. Using a digital feed-forward active noise control scheme, Leishman achieved TL results near 80 dB over a band of 40 Hz to 1.0 kHz for the individual module. The array of four modules produced TL results near 55 dB over a band of 40 Hz to 300 Hz.

Two drawbacks were identified with Leishman's double-panel ASP module. First, the module used a feed-forward active controller. The time-advanced reference signal needed for feed-forward control is not available in many applications. In addition, the feed-forward controller used by Leishman was only capable of attenuating single-tone disturbances. There are some applications where an advanced reference signal is available and only single-tone disturbances exist—Leishman's configuration would work well in those situations. However, since these luxuries are not available in many sound isolation applications an alternate module design is needed. Second, the volume velocity approach used by Leishman produced a unidirectional module—attenuation of sound was only possible in one direction. Many applications would require bidirectional TL capabilities where the module is capable of attenuating sound in both directions.

A new ASP module was proposed wherein each panel of the double-panel module is directly sensed and actuated with a feedback controller (Ch. 5). The feedback control scheme eliminates the need for a time-advanced reference signal and minimizing the surface velocity of both panels (instead of just the transmitting panel) also allows for bidirectional performance. The purpose of this paper is to present the experimental test

setup, report the experimental results for the new ASP module, and validate the modeling results presented previously (Ch. 5). The frequency response functions (FRFs) for each plant, the acoustic coupling FRF between the panels, the TL in both passive and active states, and the bidirectional capabilities of the module are investigated.

6.4 EXPERIMENTAL APPARATUS

A plane-wave tube was used to measure the normal-incidence TL of the new ASP module. The plane-wave tube was constructed from a 10 cm inside diameter acrylic tube, with airtight microphone ports located every 5 cm along its length. The tube was split into two sections: the source-side tube and the receiving-side tube. The primary disturbance source was located at one end of the source tube and a 1.5 m anechoic termination was located at the far end of the receiving tube. The primary disturbance source was a 10 cm full-range driver with an enclosed rear chamber. The anechoic termination was constructed by cutting a wedge from a cylinder of open-cell foam. The module was located between the source and receiving tubes. A photograph of the experimental apparatus is shown in Figure 6-1.

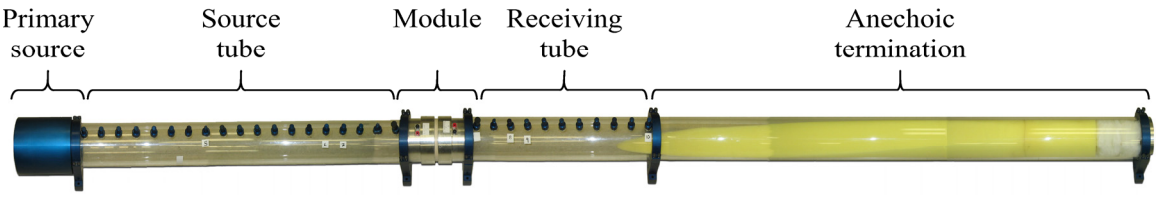

Figure 6-1. Photograph of the TL measurement apparatus.

Mechanical or acoustic flanking paths in the measurement apparatus can severely affect the TL measurement, especially during the measurement of devices with high TL. Special consideration was taken to reduce the strength of any flanking path that may exist in the measurement apparatus. The source tube was placed on a different table than the receiving tube so that vibrational energy could not exit the source tube, transmit through the table and into the receiving tube, and then re-radiate as acoustic energy into the receiving tube. Furthermore, the table that the source tube was placed on was a vibration isolation table with a separate concrete foundation from the rest of the laboratory. In addition, a resilient connection was used to join the two halves of the double-panel module so that vibrational energy could not easily transmit directly through the mechanical structure of the module into the receiving space.

The two-microphone transfer-function technique developed by Chung and Blaser [60, 61] was used to measure the TL through the module. This method provided a way to decompose the sound field in the source tube so that only the pressure incident upon the module was used in the TL calculation. The downstream field was also decomposed to reduce error associated with any non-anechoic performance of the termination. Two microphone pairs were actually used on each side of the module; a pair with large spacing and a pair with small spacing. The space between each microphone in a pair determines the usable measurement bandwidth according to the following rule of thumb, where c is the speed of sound in the medium and d is the diameter of the tube [101]:

$$0.05\left(\frac{c}{d}\right) < f < 0.4\left(\frac{c}{d}\right). \qquad \textbf{(6.1)}$$

A large spacing of 40 cm was used for one microphone pair with a corresponding usable bandwidth of 40 Hz to 345 Hz. A small spacing of 5 cm was used for the other microphone pair, with a corresponding usable bandwidth of 345 Hz to 2.7 kHz. The two measurements were spliced together at 345 Hz to provide a single measurement from 40 Hz to 2.7 kHz. All of the microphones were placed at least 1.5 duct diameters away from the module to reduce the effects of evanescent cross modes in the acoustic near field of the partition.

The first cross mode of the 10 cm diameter plane-wave tube is approximately 2 kHz. Only plane waves propagate in the duct below this frequency, provided that the frequency content of the primary disturbance source remains below 2 kHz. Some cross modes will inevitably be excited during the measurement but the amplitude of these modes should sufficiently evanesce as the waves reach the microphone locations.

Each microphone was calibrated to an absolute reference (114 dB at 1 kHz), then a switching calibration routine was used between each pair of microphones. The switching routine produced a relative calibration in both magnitude and phase of one microphone to the other. Post-processing with the relative calibration removes the frequency-dependent characteristics of the microphones, preamplifiers, and front-end of the data acquisition system.

The performance of the measurement apparatus was qualified in two ways. First, the frequency-dependent absorption coefficient of the anechoic wedge was measured to determine the anechoic cutoff frequency. The cutoff frequency is defined as the frequency above which the absorption coefficient consistently exceeds 0.99. The measured absorption coefficient of the anechoic termination is shown in Figure 6-2. The

plot is zoomed into low frequencies to identify the cutoff frequency. The absorption coefficient remains above 0.99 beginning at 67 Hz. The termination also provides an absorption coefficient exceeding 0.70 down to 26 Hz.

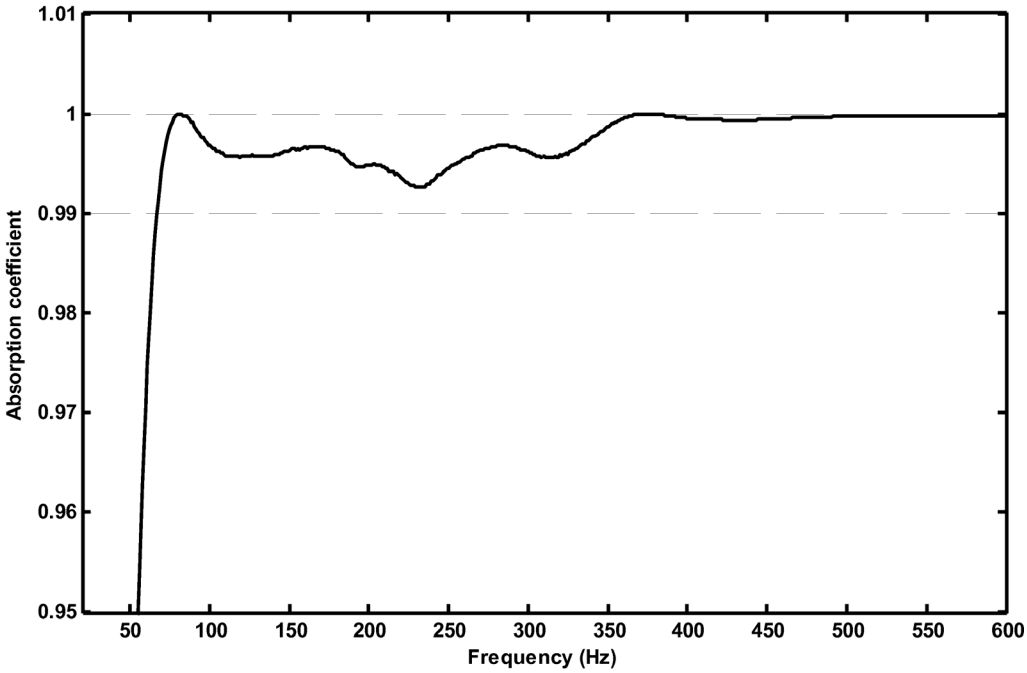

Figure 6-2. Measured absorption coefficient for the 1.5 m anechoic termination. The dashed line at 0.99 represents the anechoic limit for the termination.

The second qualification of the measurement apparatus was the measurement of the TL of the apparatus without the module in the duct. The measurement apparatus was arranged as if a TL measurement were to be conducted, but the actuators (loudspeakers) were removed from the module before the measurement. The TL through a section of air with the same length as the module should be nearly equal to zero. The measured TL of this configuration is shown in Figure 6-3. The figure shows that the measurement error introduced by the apparatus will be very small over the useable measurement bandwidth—

the average error between 67 Hz and 1.8 kHz is 0.42 dB. It should be noted that larger errors may be introduced below the 67 Hz anechoic termination cutoff frequency and in the region of the 2 kHz duct cross mode. The error at low frequencies was most likely attributed to the non-ideal anechoic termination below 67 Hz while the error near 2 kHz is likely due to cross mode propagation.

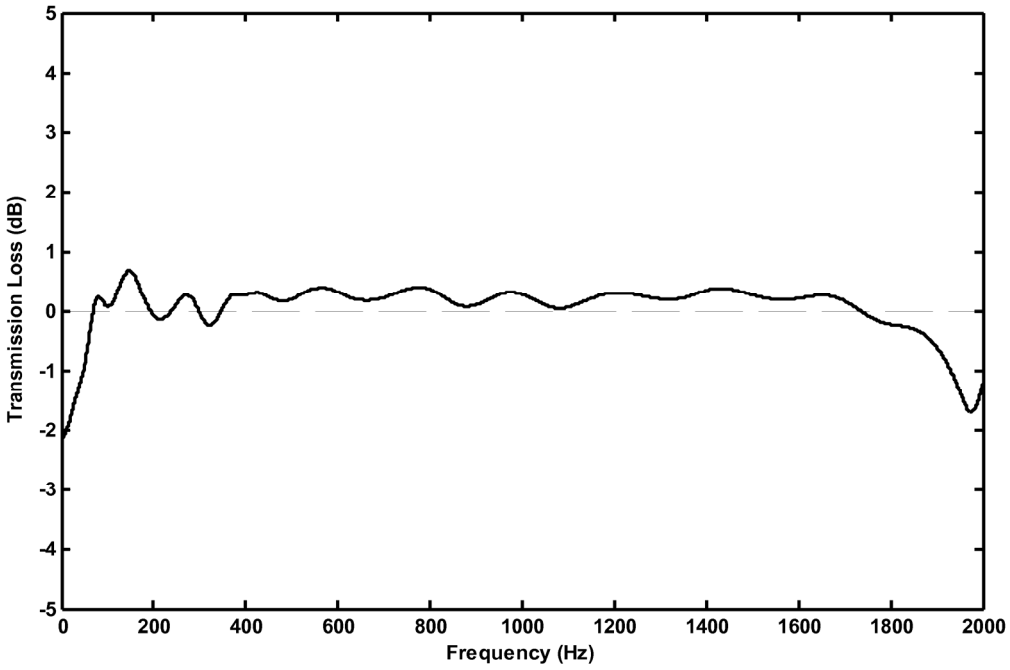

Figure 6-3. TL of the measurement apparatus without the module.

Both of the aforementioned tests provide some validation that the measurement apparatus is qualified to make accurate TL measurements between 67 Hz and 1.8 kHz. The experimental results immediately outside of these ranges could still be valid, but may have slightly larger levels of experimental error.

6.5 TRANSDUCERS

Several transducers were used in the experimental module. The loudspeakers were 10 cm diameter HiVi M4N full-range drivers. The surface areas that comprised the cone and the surround of the loudspeaker made up the 'panel' of the partition. The magnet and voice coil assembly of the loudspeaker provided the actuation of the panel. The measured Thiele-Small parameters and the extracted enhanced parameters (see Ch. 4) for this loudspeaker are shown in Table 6-1.

Table 6-1. Thiele-Small and enhanced parameters for the HiVi M4N loudspeaker.

Thiele Small Parameters			Enhanced parameters		
Parameter	Value	Units	Parameter	Value	Units
BL	3.541	Tm	BL	3.541	Tm
C_{MS}	700.0	μm/N	L_E	0.230	mH
f_s	83.11	Hz	R_E	6.483	Ω
L_E	0.230	mH	R_g	0.100	Ω
M_{MD}	5.429	g	S_1	30.00	cm^2
R_E	6.483	Ω	S_2	3.00	cm^2
R_g	0.100	Ω	M_{M1}	7.205	g
R_{MS}	0.492	kg/s	M_{M2}	0.146	g
S_D	54.11	cm^2	C_{M1}	2297	μm/N
			C_{M2}	448.0	μm/N
			C_{M12}	272.0	μm/N
			R_{M1}	0.570	kg/s
			R_{M2}	0.300	kg/s
			R_{M12}	0.300	kg/s

A 0.7 g PCB 352B10 accelerometer was used to measure the acceleration of each loudspeaker cone. The accelerometer was mounted in the center of the cone to sense the normal surface acceleration. In the case of the double-panel partition, the basket of each loudspeaker was oriented toward the interior of the cavity. The electrical terminal

connections for the loudspeakers were made using airtight banana jacks. A cutaway view of the experimental module is shown in Figure 6-4. A piece of fiberglass insulation (not shown) was inserted into the cavity to dampen the axial cavity resonances during the measurement of the double-panel partition and provide greater passive TL at higher frequencies.

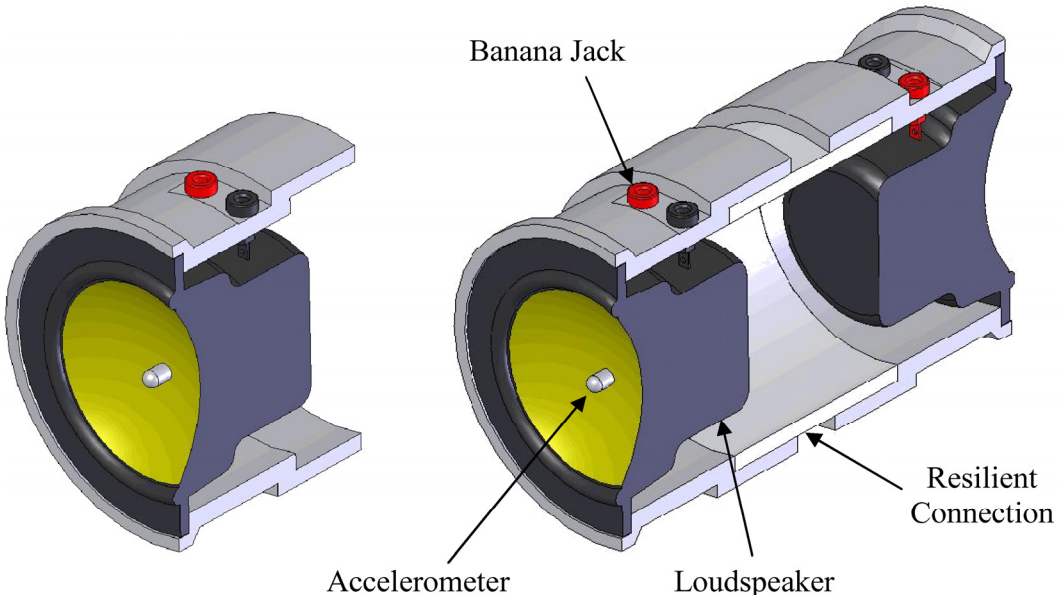

Figure 6-4. Cutaway view of the ASP module for an active single-panel partition (left) and an active double-panel partition (right).

The microphones used in the measurement apparatus were Larson Davis 377A02 precision microphones with Larson Davis PRM426 preamplifiers. The microphones were positioned along the length of the duct in airtight microphone ports mounted at 5 cm intervals. All unused ports were sealed with plugs. A photograph of the receiving-side tube is shown in Figure 6-5.

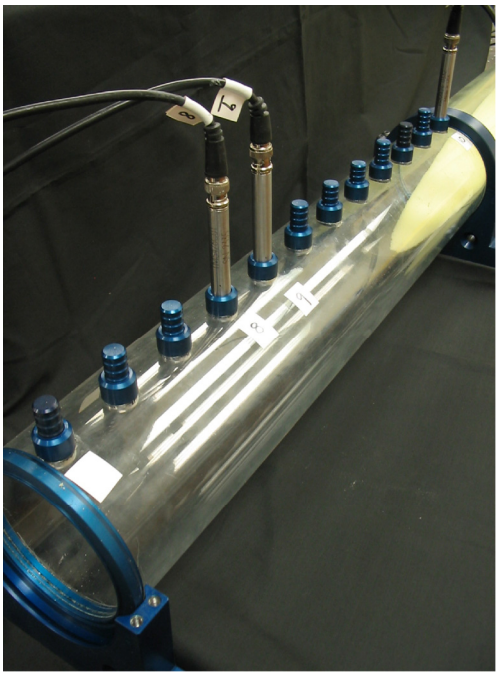

Figure 6-5. Photograph of the receiving-side tube of the measurement apparatus. The microphone ports are spaced 5 cm apart and the tip of the anechoic wedge is visible in the upper right.

6.6 FEEDBACK CONTROLLERS

The design of the feedback controller was introduced the preceding chapter. The Fleischer-Tow biquad circuit is a second-order filter whose response can be shaped by appropriate choices of resistor and capacitor values. A schematic of the circuit design is shown in Figure 6-6. The filter response for this application was designed to be a low-pass filter with a slight notch near 3 kHz.

The predicted and measured controller responses are shown in Figure 6-7. The slight discrepancy between the two curves is due to inexact resistor and capacitor component values used in the actual circuit.

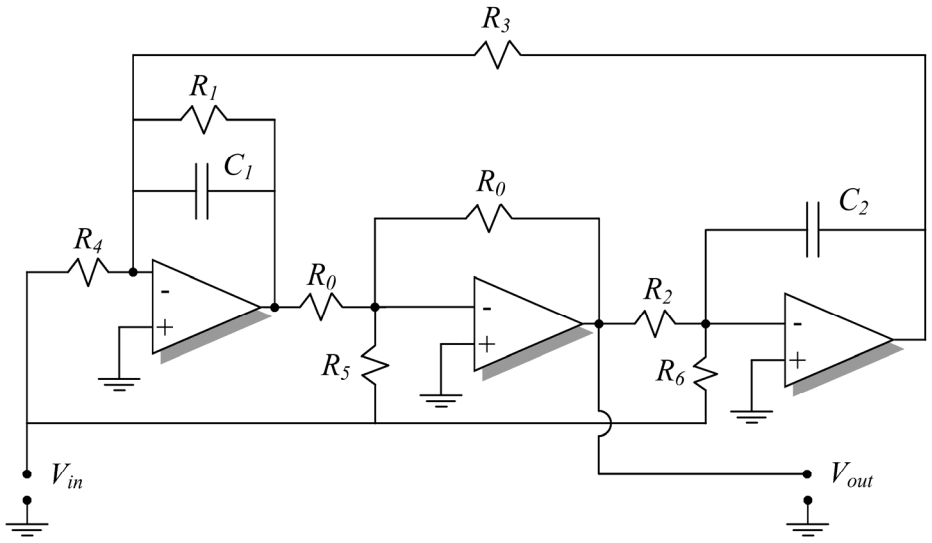

Figure 6-6. Electrical schematic for a second-order Fleischer-Tow biquad circuit.

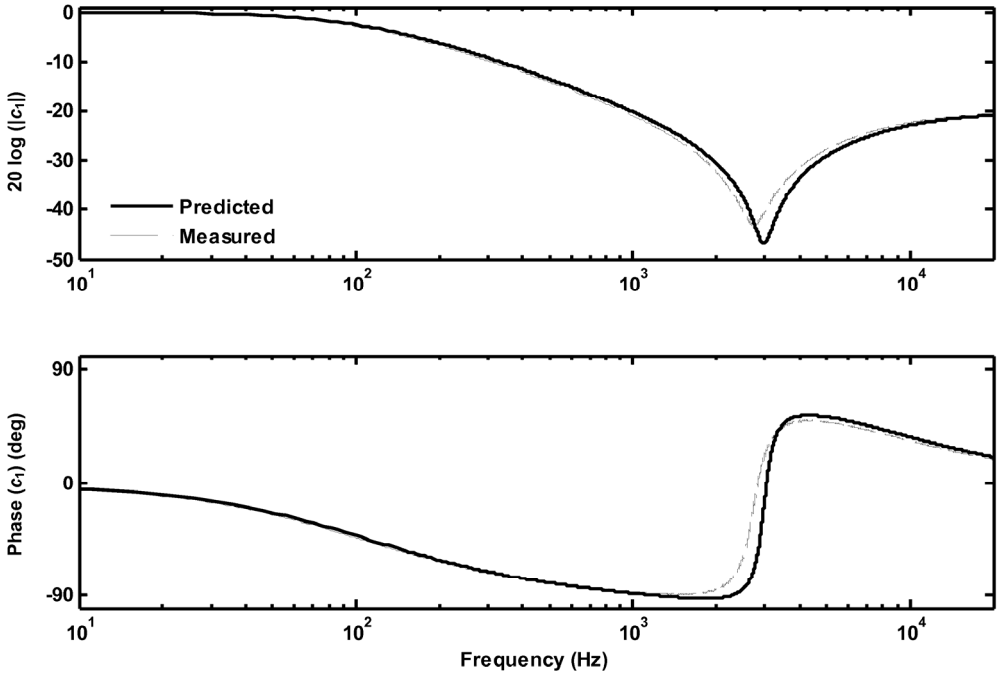

Figure 6-7. Predicted and measured controller FRFs for a Fleischer-Tow biquad controller.

The two control circuits were implemented on an electrical breadboard. National Semiconductor LM837N quad operational amplifier chips were used; three out of the four op-amps on the chip were needed for each control circuit. A photograph of one controller is shown in Figure 6-8. The output of each accelerometer was fed as the input into one of the control circuits. The output of each control circuit was then passed through a two-channel variable-gain Crown DC300A stereo amplifier. The amplifier was used to control the gain of each controller for experimental purposes. Finally, each output of the amplifier was fed into one of the loudspeakers in the active double-panel partition module.

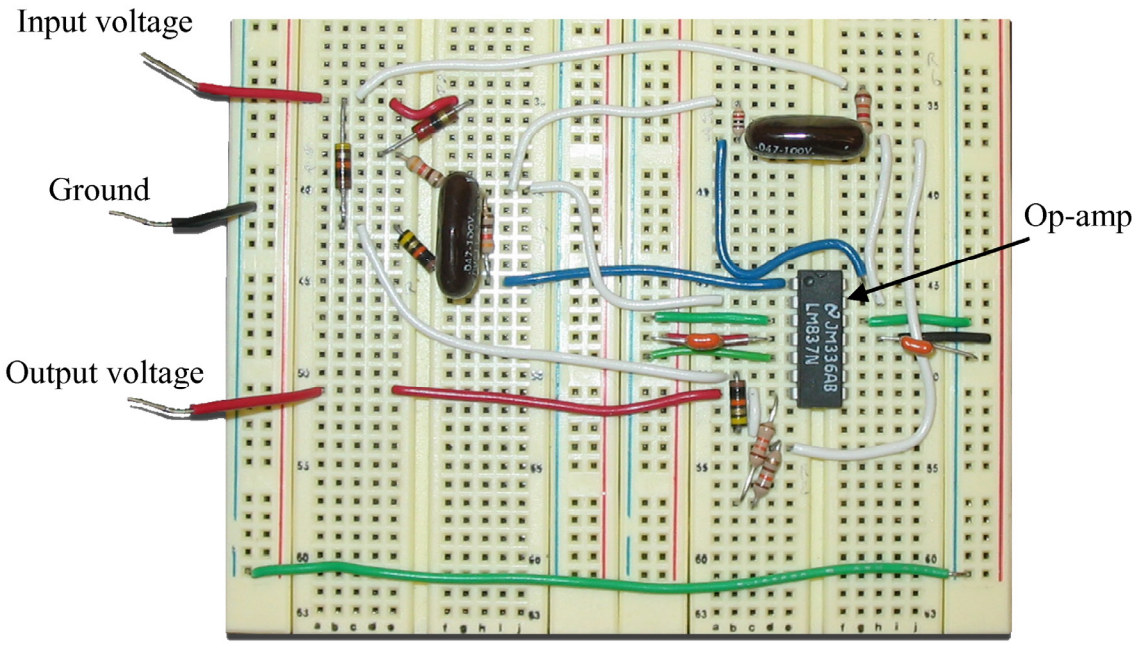

Figure 6-8. Photograph of a single Fleischer-Tow control circuit on a breadboard.

6.7 PLANT ACCELERANCE FRFS

The accelerance FRF (the acceleration output divided by the voltage input) of the plant was predicted with the enhanced double-panel TL model in the preceding chapter. For the accelerance FRF measurement, the plant was located in free-air, not in the measurement apparatus. The predicted and measured plant responses are shown in Figure 6-9. The model matches the measured data extremely well up to 2 kHz. The model assumptions of lumped-parameter behavior break down above 2 kHz when the cone begins to exhibit strong resonance behavior. The model prediction is useful in making design decisions that affect the low-frequency response and stability, but the *measured* frequency response function is needed to account for the high frequency dynamics of the plant which the model is unable to predict.

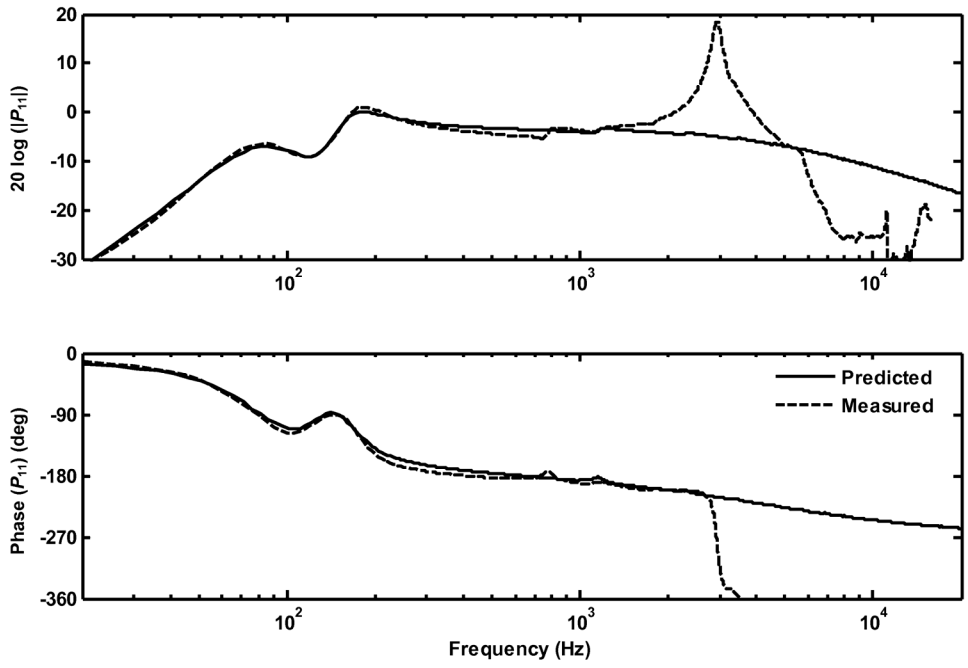

Figure 6-9. Predicted and measured plant FRF.

One of the advantages to the controller that was chosen for this research (a low-pass filter with a notch) is the ability to place the notch at the same frequency as the first break-up frequency of the cone (~3kHz). This removes the effect of the resonant response from the closed-loop system by significantly reducing the excitation voltage fed to the loudspeaker near this frequency.

6.8 ACOUSTIC COUPLING FRFS

The acoustically coupled FRF of the plant was predicted with the enhanced double-panel TL model in chapter 5 of this thesis. For this FRF measurement, the plant was located in free-air, not in the measurement apparatus. The predicted and measured acoustically coupled plant FRFs are shown in Figure 6-10.

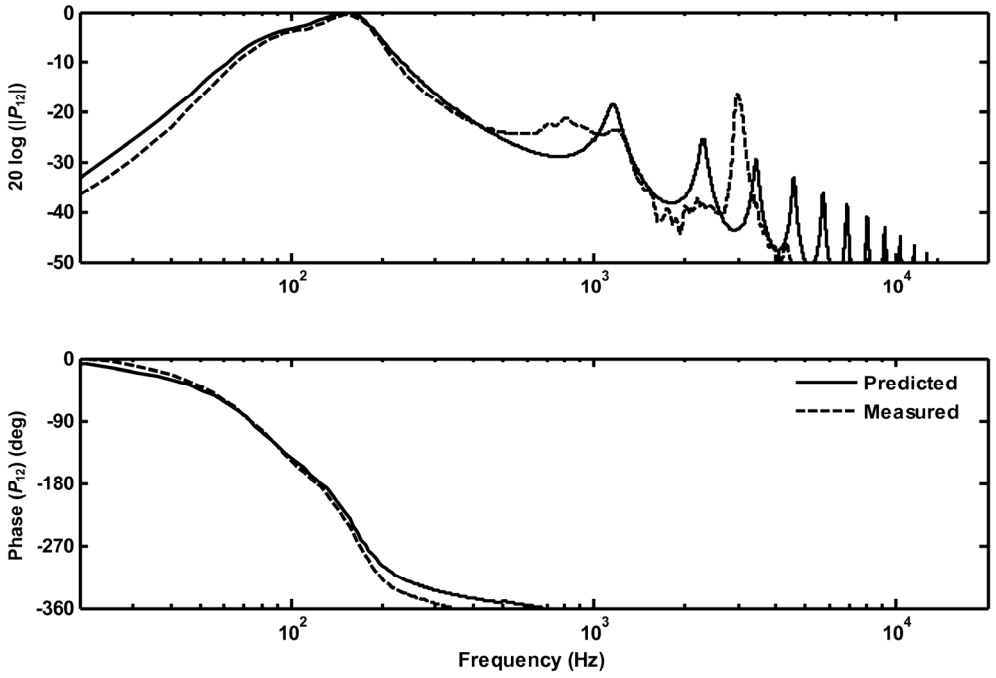

Figure 6-10. Predicted and measured cross-coupling accelerance FRFs.

Once again, the model is shown to provide very good predictions of the strength of the acoustic coupling path at low frequencies. As is expected in a double-panel partition, the strength of the acoustic coupling is greatest at the mass-air-mass resonance frequency, which is 155 Hz for this partition. The strength of the acoustic coupling rises at 12 dB per octave well below the mass-air-mass resonance frequency, 6 dB per octave in the immediate vicinity, and falls at 18 dB per octave immediately above it.

The acoustic coupling works in favor of the control scheme used in this module. To illustrate this, suppose that a disturbance wave is incident upon the first panel of the partition. If it is set into vibratory motion, the acoustic coupling will also cause the second panel to vibrate. The amplitude at which the second panel vibrates depends on the magnitude of the acoustic coupling path. Consequently, if the first panel is actively controlled so that it cannot vibrate, then the acoustic coupling strength will force the second panel to follow suit. Likewise, active control of the second panel will encourage the first panel not to vibrate. It should also be noted that the panels will tend to act independently of one another at frequencies where the acoustic coupling path is not strong.

6.9 TRANSMISSION LOSS

The TL through the module was predicted and measured for several different schemes. The first scheme was with only one active panel in place (i.e, a single-panel partition). The second scheme was a double-panel partition with only one primary disturbance source on the source-side of the measurement apparatus. The final scheme was the double-panel partition with disturbance sources located on both the source and

receiving-sides of the tube. The TL results of each scheme are presented in this section and are compared to the model predictions developed in chapter 5.

6.9.1 SINGLE-PANEL PARTITION TL RESULTS

The single-panel partition was produced by removing the second active partition from the module as shown in Figure 6-4. The module was oriented so that the cone of the loudspeaker was facing the disturbance source. The TL was measured for both passive and active module states. The predicted and measured TL is plotted in Figure 6-11. Note that the measurement bandwidth is restricted to 2 kHz because this measurement was made in the plane-wave tube apparatus.

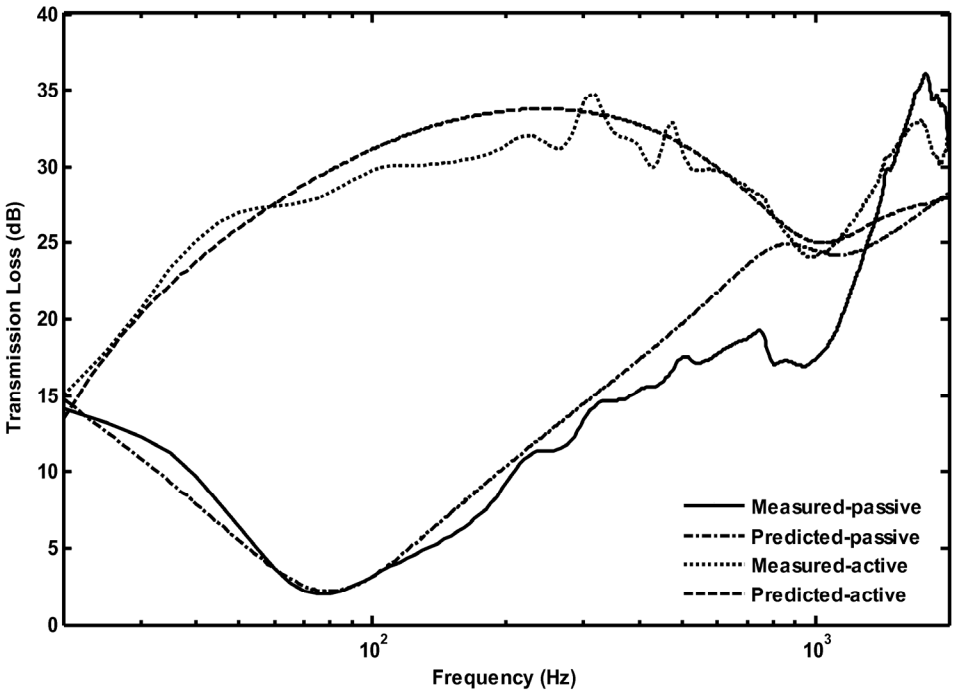

Figure 6-11. Predicted and measured TL of a single-panel partition in passive and active states.

The measured TL agrees quite well with the predicted TL up to 1 kHz. It is uncertain why the measured passive TL does not perform as well as the model predicts in the region around 1 kHz. One hypothesis is that although the model allows the surround to move independent from the cone, it does not account for the self and mutual radiation impedances between the two areas. This might cause the observed deviation of the model from the experimental results near the area where the surround resonance is the strongest.

The degradation in the active TL near 1 kHz is caused by two separate phenomena. The first effect is due to slight control instability in the region. The phase of the closed-loop system crosses the -360° point at 1 kHz causing small amplification of the disturbance signal to occur at this frequency. The second effect is due to the area of the surround moving with its own resonance near 1 kHz. This effect cannot be actively controlled because there is no way to directly actuate the surround area. This effect was verified by scanning the face of the single-panel partition with a scanning laser Doppler vibrometer in both the passive and active states. The scan results are shown at 100 Hz and at 1 kHz in Figure 6-12 (note the different color legends between the two frequencies). The surround resonance is clearly seen under active control at 1 kHz but is not exhibited under active control at 100 Hz. The substantial reduction in the RMS surface velocity from the passive to active states is also verified in the figure. The reduction in the RMS surface velocity at the centermost scan point is 27.7 dB at 100 Hz and 13.3 dB at 1 kHz.

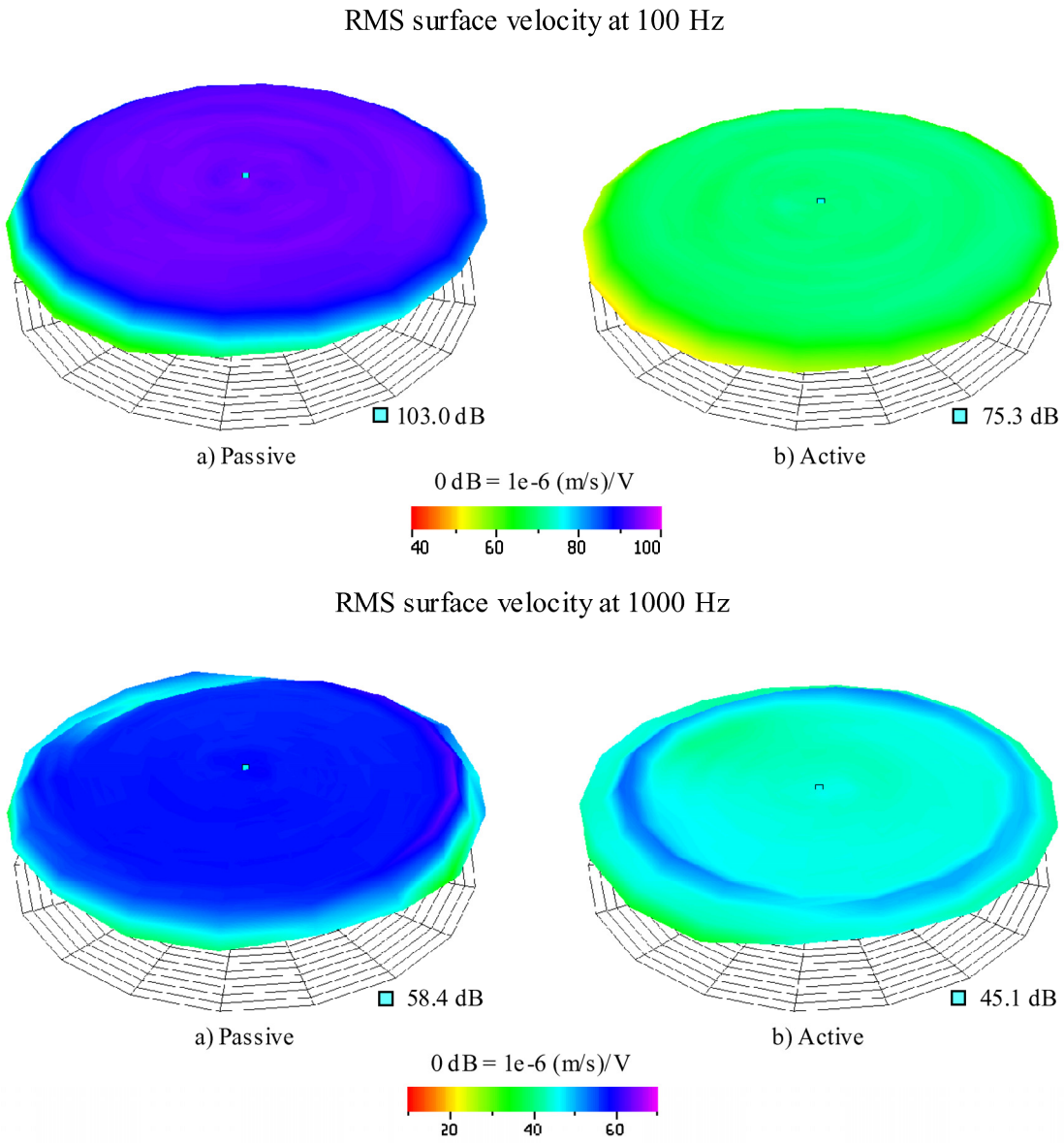

Figure 6-12. Scanning laser Doppler vibrometer measurements of the RMS surface velocities for a single-panel partition at 100 Hz and 1 kHz in passive and active control states.

6.9.2 DOUBLE-PANEL PARTITION TL RESULTS

The double-panel partition was configured as shown in Figure 6-4. The TL was measured for both passive and active module states. The predicted and measured TL is

plotted in Figure 6-13. In this configuration, three different active control states were possible: active control of panel 1 only, active control of panel 2 only, and active control of both panels simultaneously.

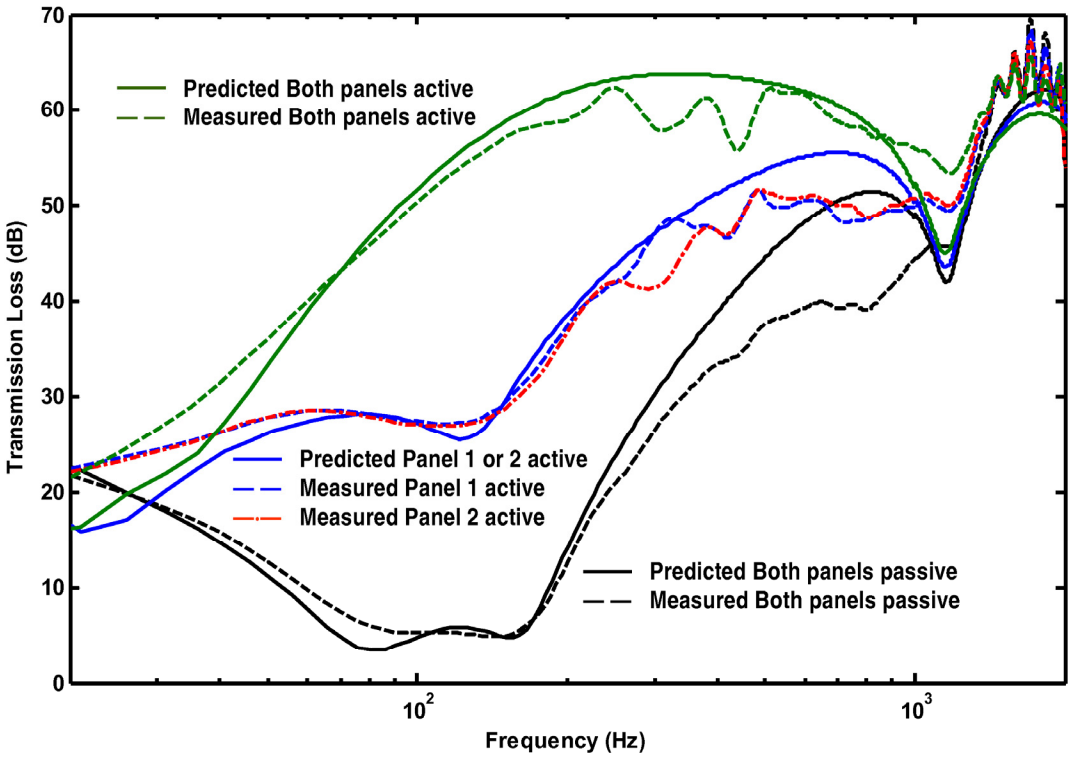

Figure 6-13. Predicted and measured TL of a double-panel partition in passive and active states.

The experimental results agree well with the predictions from the model. One obvious discrepancy between the predictions and the model is the prediction of a dominant axial cavity resonance at 1.15 kHz. This resonance does appear in the measured data, but is much less severe than what the model predicted.

It was interesting to find that the TL performance was essentially identical when only panel 1 or panel 2 was actively controlled. This indicates that it does not matter

whether the disturbing sound wave first interacts with a passive partition or with an active partition, as long as one of the two panels of the partition is actively controlled. However, the mass-air-mass resonance feature is still observed in the spectral response when only a single-panel of control occurs, whereas this spectral feature is completely eliminated when both panels are simultaneously controlled.

The average TL (arithmetic averaging) between 20 Hz and 1 kHz (both measured and predicted) was computed for the single- and double-panel partitions in all of their control states. The results are shown in Table 6-2. The results show that active panel control can provide effective broadband TL, even in the single-panel case. The double-panel partition with active control on each panel provides a tremendous increase in the broad, low-frequency TL performance of the module. The results also show that the model accurately predicts the TL of the module over a wide frequency range.

Table 6-2. Average TL (arithmetic) between 20 Hz and 1 kHz for the single- and double-panel partition in each control state.

	Measured average TL (20 Hz to 1 kHz)	Predicted average TL (20 Hz to 1 kHz)
Single-panel, passive	14 dB	11 dB
Single-panel, active	29 dB	31 dB
Double-panel, passive	31 dB	37 dB
Double-panel, panel 1 active	45 dB	48 dB
Double-panel, panel 2 active	45 dB	48 dB
Double-panel, both panels active	57 dB	58 dB

The maximum increase in the TL from the passive state to the active state of each module was also computed (both measured and predicted). Again, the maximum increase in the TL from passive to active states is substantial for both the single-panel and

double-panel partition. It was also observed that actively controlling both panels of the double-panel partition effectively doubles the TL performance (in dB) of the module over actively controlling a single panel of the double-panel partition. This is true for the maximum increase in TL from passive to active states (Table 6-3).

Table 6-3. Maximum increase in TL from passive to active states for the single- and double-panel partition in each control state.

	Maximum measured *increase* in TL from passive to active state	Maximum predicted *increase* in TL from passive to active state
Single-panel, passive	N/A	N/A
Single-panel, active	27 dB @ 95 Hz	28 dB @ 95 Hz
Double-panel, passive	N/A	N/A
Double-panel, panel 1 active	26 dB @ 175 Hz	27 dB @ 165 Hz
Double-panel, panel 2 active	25 dB @ 155 Hz	27 dB @ 165 Hz
Double-panel, both panels active	52 dB @ 160 Hz	55 dB @ 160 Hz

6.9.3 BIDIRECTIONAL RESULTS

Broadband bidirectional TL is not possible to measure using conventional testing techniques. The presence of a second disturbance source in the receiving-side of the measurement apparatus will simply act to degrade the measured TL through the module. However, a special test provides some insight into the bidirectional capabilities of the module. Two distinct tones were used to ensure that the module could attenuate in either direction as the sounds passed through the module—even if the tones were present at the same time.

In order to carry out this experiment, a side-branch tube was added to the receiving-side tube of the measurement apparatus shown in Figure 6-1. A second disturbance source was placed at the end of the side branch tube. The upstream disturbance source broadcast a 75 Hz tone and the downstream disturbance source broadcast a 150 Hz tone. The sound pressure level (SPL) was measured with two microphones, one located in the source-side tube and one located in the receiving-side tube. The difference in SPL between the two microphones in the direction of sound propagation for the tone was used as an estimate of the sound isolation of the module. The results for the double-panel partition are shown in Table 6-4. The values for the expected TL came from Figure 6-13 at 75 Hz and 150 Hz.

Table 6-4. Bidirectional sound isolation results for two tones passing through the module in different directions.

	Δ SPL	Expected TL
Passive		
75 Hz	13 dB	7 dB
150 Hz	12 dB	5 dB
Panel 1 active		
75 Hz	33 dB	28 dB
150 Hz	31 dB	29 dB
Panel 2 active		
75 Hz	33 dB	28 dB
150 Hz	31 dB	29 dB
Both panels active		
75 Hz	48 dB	45 dB
150 Hz	50 dB	57 dB

The first observation was that the ΔSPL is not as good of a metric as the TL. One reason for this is that the SPL in the upstream tube is a strong function of frequency due to its axial modes. This can cause peaks in the SPL as much as 20 dB higher at axial resonances than at other frequencies. However, the magnitude of the measured attenuation in SPL was on the same order of magnitude of the predicted TL. The second and more important observation from the measured data is that the module can provide the same attenuation when sound is propagating in both directions through the module as it can when sound is only propagating in one direction through the module.

6.10 ELECTRICAL POWER CONSUMPTION

The increase in the TL from passive to active states comes at the expense of electrical power consumption. A natural question to ask is how much power the active device requires relative to the sound power that is incident upon it. This question was answered, at least in part, by measuring the steady state RMS voltage across the loudspeaker terminals of the module and then by measuring the steady state RMS current through the terminals. The total electrical power in mW was measured for each active control case. The total incident sound power in mW was also measured for each active control case. The electrical power was then divided by the incident sound power upon the device to form a power factor. The results are shown in Table 6-5.

When only a single panel was actuated at a time, it was observed that panel 1 uses almost twice the power as panel 2. It is interesting to note, however, that the same TL is achieved by controlling either panel 1 or panel 2 by itself. This indicates that the passive TL characteristics within the module are not fully leveraged if the first panel of a

unidirectional transmission path is actuated. Consequently, if foreknowledge about the direction of sound transmission through the device was possible, it would be more economical to only actuate the second panel in the device.

Table 6-5. Total electrical power used to actuate the module, incident sound power, and power factor for the double-panel partition under various control states.

	Total RMS Electrical Power	RMS Incident Sound Power	Power Factor
Double-panel, passive	0 mW	16.2 mW	0
Double-panel, panel 1 active	45.6 mW	15.9 mW	2.9
Double-panel, panel 2 active	22.0 mW	15.6 mW	1.4
Double-panel, both panels active	48.2 mW	16.1 mW	3

The best TL performance was achieved when both panels were actively controlled. This scheme only consumes about 2.5 mW more power than controlling panel 1 alone but nearly doubles (in dB) the TL performance of the module.

A power factor of 3 was calculated for the case in which both panels were actively controlled. If the relationship between the electrical power and the incident sound power is linear with an increase in sound power, the device would require three times more electrical power than the acoustic power incident upon it. For example, 30 W of electrical power would be required to produce the same TL if the incident sound power upon the device was increased to 10 W. It should be noted that the module could not be experimentally tested with lower incident sound power because the high TL of the module caused the signal-to-noise ratio to be too low in the receiving-side tube.

6.11 CONCLUSION

The analogous circuit model was validated using an experimental ASP module. It was shown experimentally that direct panel control of a double-panel partition using an analog feedback controller is an effective way to produce high TL at low frequencies. The average TL from 20 Hz to 1 kHz for a fully active double-panel partition was 57 dB, whereas the average passive TL for the same device was only 31 dB over the same frequency band. It was also shown that the new ASP module provides bidirectional TL control. The electrical power consumption of the active device was also investigated. It was found that a ratio of electrical power to sound power of 3:1 was typical for the active device under the measurement conditions presented in the paper. It was observed that the TL performance could be doubled by actuating both panels, which required only 2.6 mW more electrical power than actively controlling the first panel alone.

7 CONCLUSION

The work of this thesis demonstrated that a relatively simple analog feedback control scheme could be used to actively increase the transmission loss (TL) through an ASP module. Feedback control represents a more practical way to implement an actively controlled acoustic partition since the time-advanced reference signal needed for feed-forward control is often unavailable. The analog feedback controller used in this research successfully attenuated noise from a broadband random-noise disturbance source.

It was demonstrated in this thesis that an analog feedback controller can be successful in a panel control scheme. An analog feedback controller is simple to implement, inexpensive, and lightweight; all of which contribute to the overall goal of a practical and lightweight sound isolation product. From a control standpoint, the minimal latency of the analog circuit is well suited for narrowband, broadband, and transient disturbances.

A simple yet novel combination of actuators and sensors was introduced in this thesis in order to produce a bidirectional TL module. This property did not exist in previous ASP modules. Analogous circuit models were created to predict the performance of the new scheme and to explore the effects of various model parameters on the TL of the device. It was found that the classical model of a loudspeaker was unable to explain significant effects in the measured TL at mid frequencies. The observed effects were caused by the surround of the loudspeaker vibrating with an

independent degree of freedom from the cone. An enhanced model of a loudspeaker was then used, wherein the surround was modeled with this additional degree of freedom.

The ability to measure parameters for use in the enhanced model became critical. A laser-based measurement technique was developed to extract unknown model parameters. Self and mutual radiation impedances of the loudspeaker cone and surround were carefully accounted for while extracting these parameters. Several examples were given which demonstrated the ability of the enhanced model to give more accurate predictions for the on-axis radiated pressure response. The extraction routine presented in this thesis is the first published parameter extraction routine for the enhanced loudspeaker model.

The effect of changing parameter values in the analogous circuit model was explored. It was found that the ratio of the surround area over the cone area had a major impact on the active TL potential of the device. The maximum TL was reduced as the area of the surround was increased relative to the area of the cone. This impact was frequency dependent; the degradation to the TL was more severe at mid and high frequencies. It was also found that the cavity depth of the module had a slight but predictable effect on the TL potential. The maximum TL was reduced by approximately 6 dB for each halving of the cavity depth. This effect was a constant function of frequency over the active control bandwidth. It was also found that decreasing the electrical resistance of each actuator voice coil provided the single largest increase in the TL potential; it was an effect manifest uniformly at all frequencies. Each halving of the voice coil resistance produced a 6 dB increase in the predicted TL through the device.

It was shown from the analogous circuit model that it was impossible to obtain an optimal control voltage when using the acceleration of the panel as a reference signal. Consequently, the aim of the feedback controller was to maximize the gain of the open-loop transfer function over the control bandwidth while maintaining proper stability margins. If the incident pressure could be sensed directly, it would be possible to produce an optimal control voltage signal of reasonable amplitude. However, sensing the incident pressure is fundamentally equivalent to performing feed-forward active control.

A prototype module was built using off-the-shelf components and measured in a plane-wave tube. The normal-incidence TL was measured for several passive and active configurations. The measured results were shown to approximately match the numerical predictions. The average arithmetic TL from 20 Hz to 1 kHz for a fully active double-panel partition was 57 dB, whereas the average passive TL for the same device was only 31 dB. This represents a sizeable improvement in the TL through the device at low frequencies. The module was also shown to have bidirectional TL capabilities. This was manifested in two ways: identical broadband TL in both directions through the module and by simultaneous attenuation of two distinct sinusoidal tones traveling in different directions through the module.

Although major advancements in the design of ASP modules have been made in the course of this thesis work, many opportunities exist for future research. Recommendations for future work on the ASP module presented in this thesis include:

- Measuring the normal-incidence TL on larger experimental modules with the same basic design.

- Developing miniature electronics (including amplifiers, control filters, and power supplies) that can be mounted inside the module.
- Developing a new actuator with minimum weight and thickness in mind.
- Minimizing the overall depth of the modules.
- Maximizing the surface area of the panels in the experimental module.
- Minimizing the surface area of the surrounds in the experimental module.
- Creating more elaborate feedback controllers.
- Addressing the mechanical and electrical connection between adjacent modules in an array.
- Performing oblique and random incidence TL tests on an array of experimental modules.
- Calculating electrical power consumption as a function of incident sound power for an array of experimental modules.
- Investigating continuous skin surfaces for ASP arrays (for aesthetic purposes).

8 REFERENCES

1. *Making soundproof walls*, in *New York Times*. January 28, 1912: New York.

2. *Sound-proof walls sought*, in *New York Times*. October 16, 1927: New York.

3. *Soundproof wall is expected soon; U.S. Bureau of standards experiments point the way to better, cheaper, and more durable buildings*, in *New York Times*. October 25, 1925: New York.

4. Fahy, F., *Sound and structural vibration : radiation, transmission, and response*. 1985, London ; Orlando: Academic Press. xx, 309 p.

5. Fuller, C.R. and Jones, J.D., *Experiments on reduction of propeller induced interior noise by acive control of cylinder vibration.* Journal of Sound and Vibration, 1987. **112**(2): p. 389-395.

6. Sacarcelik, O. and Johnson, M., *Active control of noise transmission into payload fairings using distributed active vibration absorbers and loudspeakers*, in *NoiseCon 2004*. 2004: Baltimore, MD. p. 889-898.

7. Beranek, L.L., *Noise and vibration control*. 1971, New York: McGraw-Hill. x, 650 p.

8. Leishman, T.W., *Active control of sound transmission through partitions composed of discretely controlled modules*, in *The Graduate Program in Acoustics*. 2000, The Pennsylvania State University: University Park.

9. Leishman, T.W., *Class notes - ME562 Analysis of Acoustic Systems*. 2008, BYU. p. 7-11.

10. Beranek, L.L. and Vér, I.L., *Noise and vibration control engineering : principles and applications*. 1992, New York: Wiley. x, 804 p.

11. Kinsler, L.E., Frey, A.R., Coppens, A.B., and Sanders, J.V., *Fundamentals of acoustics*. 4th ed. 2000, New York: John Wiley & Sons, Inc. xii, 548 p.

12. Fuller, C.R. and Silcox, R.J., *Acoustics 1991: Active structural acoustic control.* Journal of the Acoustical Society of America, 1992. **91**(1): p. 519.

13. Fuller, C.R., Hansen, C.H., and Snyder, S.D., *Active control of sound radiation from a vibrating rectangular panel by sound sources and vibration inputs: an experimental comparision.* Journal of Sound and Vibration, 1991. **148**(2): p. 355-360.

14. Thomas, D.R., Nelson, P.A., Elliott, S.J., and Pinnington, R.J., *Experimental investigation into the active control of sound transmission through stiff light composite panels.* Noise Control Engineering Journal, 1993. **41**(1): p. 273-279.

15. Elliott, S.J. and Johnson, M.E., *Radiation modes and the active control of sound power.* Journal of the Acoustical Society of America, 1993. **94**(4): p. 2194-2204.

16. Beranek, L.L., *Acoustics*. 1954, New York: McGraw-Hill. 481 p.

17. Johnson, M.E. and Elliott, S.J., *Active control of sound radiation using volume velocity cancellation.* Journal of the Acoustical Society of America, 1995. **98**(4): p. 2174-2186.

18. Pierre, R.L.J., Koopman, G.H., and Chen, W., *Volume velocity control of sound transmission through composite panels.* Journal of Sound and Vibration, 1998. **210**(4): p. 441-460.

19. Hirsch, S.M., et al., *Experimental study of smart segmented trim panels for aircraft interior noise control.* Journal of Sound and Vibration, 2000. **231**(4): p. 1023-1037.

20. Hirsch, S.M., Sun, J.Q., and Jolly, M.R., *Analytical study of interior noise control using segmented panels.* Journal of Sound and Vibration, 2000. **231**(4): p. 1007-1021.

21. Bingham, B., Atalla, M.J., and Hagood, N.W., *Comparison of structural-acoustic control designs on an active composite panel.* Journal of Sound and Vibration, 2001. **244**(5): p. 761-778.

22. Petitjean, B., Legrain, I., Simon, F., and Pauzin, S., *Active control experiments for acoustic radiation reduction of a sandwich panel: Feedback and feedforward investigations.* Journal of Sound and Vibration, 2002. **252**(1): p. 19-36.

23. Bianchi, E., Gardonio, P., and Elliott, S.J., *Smart panel with multiple decentralized units for the control of sound transmission. Part III: Control system implementation.* Journal of Sound and Vibration, 2004. **274**(1-2): p. 215-232.

24. Gardonio, P., Bianchi, E., and Elliott, S.J., *Smart panel with multiple decentralized units for the control of sound transmission. Part I: Theoretical predictions.* Journal of Sound and Vibration, 2004. **274**(1-2): p. 163-192.

25. Gardonio, P., Bianchi, E., and Elliott, S.J., *Smart panel with multiple decentralized units for the control of sound transmission. Part II: Design of the decentralized control units.* Journal of Sound and Vibration, 2004. **274**(1-2): p. 193-213.

26. Gagliardini, L. and Bouvet, P., *DPA: The active controlled double wall*, in *Internoise 1993*. 1993: Leuven, Belgium. p. 107-109.

27. Sas, P., Bao, C., Augusztinovicz, F., and Desmet, W., *Active control of sound transmission through a double panel partition.* Journal of Sound and Vibration, 1995. **180**(4): p. 609.

28. Bao, C. and Pan, J., *Experimental study of different approaches for active control of sound transmission through double walls.* Journal of the Acoustical Society of America, 1997. **102**(3): p. 1664-1670.

29. Pan, J. and Bao, C., *Analytical study of different approaches for active control of sound transmission through double walls.* Journal of the Acoustical Society of America, 1998. **103**(4): p. 1916-1922.

30. Bao, C. and Pan, J., *Active acoustic control of noise transmission through double walls: Effect of mechanical paths.* Journal of Sound and Vibration, 1998. **215**(2): p. 395-398.

31. Cheng, L., Li, Y.Y., and Gao, J.X., *Energy transmission in a mechanically-linked double-wall structure coupled to an acoustic enclosure.* Journal of the Acoustical Society of America, 2005. **117**(5): p. 2742-2751.

32. Li, Y.Y. and Cheng, L., *Active noise control of a mechanically linked double panel system coupled with an acoustic enclosure.* Journal of Sound and Vibration, 2006. **297**: p. 1068-1074.

33. Pan, X., Sutton, T.J., and Elliott, S.J., *Active control of sound transmission through a double-leaf partition by volume velocity cancellation.* Journal of the Acoustical Society of America, 1998. **104**(5): p. 2828.

34. De Fonseca, P., Sas, P., Van Brussel, H., and Henrioulle, K. *Active reduction of sound transmission through double panel partitions - A physical analysis of the observed phenomena*. 2000. Leuven, Belgium: Katholieke Universiteit Leuven, Heverlee, B-3001, Belgium.

35. De Fonseca, P., Sas, P., Van Brussel, H., and Henrioulle, K., *Active reduction of sound transmission through double panel partitions - A physical analysis of the observed phenomena.* Proceedings of the 25th International Conference on Noise and Vibration Engineering, ISMA, Proceedings of the 25th International Conference on Noise and Vibration Engineering, ISMA, 2000: p. 43-50.

36. Paurobally, R., Pan, J., and Bao, C., *Feedback control of noise transmission through a double-panel partition*, in *1999 International Symposium on Active Control of Sound and Vibration*. 1999: Fort Lauderdale, FL. p. 375-386.

37. Carneal, J.P. and Fuller, C.R., *An analytical and experimental investigation of active structural acoustic control of noise transmission through double panel systems.* Journal of Sound and Vibration, 2004. **272**(3-5): p. 749-771.

38. Carneal, J.P. and Fuller, C.R., *Active structural acoustic control of noise transmission through double panel systems.* American Institute of Aeronautics and Astronautics Journal, 1995. **33**(4): p. 618-623.

39. DeMan, P., Francois, A., and Preumont, A., *Active control of noise transmission through double wall structures An overview of possible approaches*, in *6th National Congress on Theoretical and Applied Mechanics*. 2003: Ghent.

40. Zhu, H., Rajamani, R., and Stelson, K.A., *Active control of acoustic reflection, absorption, and transmission using thin panel speakers.* Journal of the Acoustical Society of America, 2003. **113**(2): p. 852(19).

41. Zhu, H., Rajamani, R., and Stelson, K.A., *Development of thin panels for active control of acoustic reflection, absorption and transmission.* Proceedings of the American Control Conference, 2002. **2**: p. 909-914.

42. Zhu, H., Rajamani, R., and Stelson, K.A., *Active control of sound reflection, absorption and transmission using thin panels.* Noise and Vibration Worldwide, 2004. **35**(5): p. 8-20.

43. Zhu, H., Yu, X., Rajamani, R., and Stelson, K.A., *Active control of glass panels for reduction of sound transmission through windows.* Mechatronics, 2004. **14**(7): p. 805-819.

44. Xun, Y., Rajamani, R., Stelson, K.A., and Tianhong, C., *Active Control of Sound Transmission Through Windows With Carbon Nanotube-Based Transparent Actuators.* Control Systems Technology, IEEE Transactions on, 2007. **15**(4): p. 704-714.

45. Leishman, T.W. and Tichy, J., *A fundamental investigation of the active control of sound transmission through segmented partition elements.* INCE Conference Proceedings, 1997. **103**(2): p. 137-148.

46. Leishman, T.W. and Tichy, J., *A theoretical and numerical analysis of vibration-controlled modules for use in active segmented partitions.* Journal of the Acoustical Society of America, 2005. **118**(3): p. 1424-1438.

47. Leishman, T.W. and Tichy, J., *An experimental investigation of two module configurations for use in active segmented partitions.* Journal of the Acoustical Society of America, 2005. **118**(3 I): p. 1439-1451.

48. Leishman, T.W. and Tichy, J., *An experimental investigation of two active segmented partition arrays.* Journal of the Acoustical Society of America, 2005. **118**(5): p. 3050-3063.

49. Elliott, S.J., *Signal processing for active control*. 2001, San Diego, Calif. London: Academic. xviii, 511 p.

50. Nelson, P.A. and Elliott, S.J., *Active control of sound*. 1992, London ; San Diego: Academic Press. xii, 436 p.

51. Pawelczyk, M., *Analogue active noise control.* Applied Acoustics, 2002. **63**(11): p. 1193-1213.

52. Green, M., *Feedback Applications in Active Noise Control for Small Axial Cooling Fans*, in *Physics and Astronomy* 2006, Brigham Young University Provo, UT. p. 69.

53. Franklin, G.F., Powell, J.D., and Emami-Naeini, A., *Feedback control of dynamic systems*. 5th ed. 2006, Upper Saddle River, N.J.: Pearson Prentice Hall. xvii, 910 p.

54. Richards, R.J., *An introduction to dynamics and control*. 1979, London ; New York: Longman. xi, 522 p.

55. Andre, J. and Michael, M., *Enhancement of the transmission loss of double panels by means of actively controlling the cavity sound field.* INCE Conference Proceedings, 1999. **107**(1): p. 363-374.

56. Yu, S.-H. and Hu, J.-S., *Controller design for active noise cancellation headphones using experimental raw data.* IEEE/ASME Transactions on Mechatronics, 2001. **6**(4): p. 483-490.

57. Su, K.L., *Analog filters*. 2nd ed. 2002, Norwell: Kluwer Academic Publishers. xv, 406 p.

58. Herpy, M. and Berka, J.-C., *Active RC filter design*. 1986, New York: Elsevier 306 p.

59. Wheeler, P.D., *Voice communications in the cockpit noise environment - the role of active noise reduction*. 1986, Southampton University: Southampton.

60. Chung, J.Y. and Biaser, D.A., *Transfer function method of measuring in-duct acoustic properties, Part I: Theory.* Journal of the Acoustical Society of America, 1980. **68**(3): p. 907-913.

61. Chung, J.Y. and Blaser, D.A., *Transfer function method of measuring in-duct acoustic properties, Part II: Experiment.* Journal of the Acoustical Society of America, 1980. **68**(3): p. 914-921.

62. Chung, J.Y., *Cross-spectral method of measuring acoustic intensity without error caused by instrument phase mismatch.* Journal of the Acoustical Society of America, 1978. **64**(6): p. 1613-1616.

63. Leishman, T.W., *Class notes - ME562 Analysis of Acoustic Systems*. 2008, BYU. p. 2.12-2.13.

64. Beranek, L.L., *Loudspeakers and microphones.* Journal of the Acoustical Society of America, 1954. **26**(5): p. 618-629.

65. Olson, H.F., *Elements of acoustical engineering*. 1940, New York: Van Nostrand. xv, 344 p.

66. Olson, H.F., *Dynamical analogies*. First ed. 1943, New York: D. Van Nostrand Company, Inc. 196.

67. Leach, M., *Introduction to Electroacoustics and Audio Amplifier Design*. 3rd ed. 2003, Dubuque, IA: Kendall-Hunt Publishing.

68. Olson, H.F., Preston, J., and May, E.G., *Recent developments in direct-radiator high-fidelity loudspeakers.* Journal of the Audio Engineering Society, 1954. **2**(4): p. 219-227.

69. Anderson, B.E., *Derivation of moving-coil loudspeaker parameters using plane wave tube techniques*, in *Department of Physics and Astronomy*. 2003, Brigham Young University: Provo. p. 175.

70. Anderson, B.E. and Leishman, T.W., *An acoustical measurement method for the derivation of loudspeaker parameters*, in *Convention of the Audio Engineering Society*. 2003, Audio Engineering Society: New York, NY.

71. Ashley, J.R. and Swan, M.D., *Experimental determination of low-frequency loudspeaker parameters.* Journal of the Audio Engineering Society, 1969. **17**(5): p. 525-531.

72. Ashley, J.R. and Swan, M.D., *Improved measurement of loudspeaker parameters*, in *Convention of the Audio Engineering Society*. 1971.

73. Berkhoff, A.P., *Impedance analysis of subwoofer systems.* Journal of the Audio Engineering Society, 1994. **42**(1/2): p. 4-14.

74. Blind, H., Phillips, A., and Geddes, E., *Efficient loudspeaker parameter estimation - an extension*, in *Convention of the Audio Engineering Society*. 1992: San Francisco, CA.

75. Cabot, R.C., *Automated measurements of loudspeaker small-signal parameters.* Journal of the Audio Engineering Society, 1986. **34**(12): p. 1032-1032.

76. Cabot, R.C., *Automated measurements of loudspeaker small signal parameters*, in *Convention of the Audio Engineering Society*. 1986: Los Angeles, CA.

77. Clark, D., *Precision measurement of loudspeaker parameters.* Journal of the Audio Engineering Society, 1997. **45**(3): p. 129-141.

78. Geddes, E. and Phillips, A., *Efficient loudspeaker linear and nonlinear parameter estimation*, in *Convention of the Audio Engineering Society*. 1991: New York, NY.

79. Gomez-Meda, R., *Measurement of the Thiele-Small parameters for a given loudspeaker, without using a box*, in *Convention of the Audio Engineering Society*. 1991: New York, NY.

80. Hoge, W.J.J., *The measurement of loudspeaker driver parameters*, in *Convention of the Audio Engineering Society*. 1977: New York, NY.

81. Keele, D.B.J., *Sensitivity of Thiele's vented loudspeaker enclosure alignments to parameter variations.* Journal of the Audio Engineering Society, 1973. **21**(4): p. 246-255.

82. Knudsen, M.H., Jensen, J.G., Julskjaer, V., and Rubak, P., *Determination of loudspeaker driver parameters using a system identification technique.* Journal of the Audio Engineering Society, 1989. **37**(9): p. 700-708.

83. Moreno, J.N., *Measurement of loudspeaker parameters using a laser velocity transducer and 2-channel FFT analysis.* Journal of the Audio Engineering Society, 1991. **39**(4): p. 243-249.

84. Moreno, J.N., *Measurement of loudspeaker parameters using a laser velocity transducer and two-channel FFT analysis*, in *Convention of the Audio Engineering Society*. 1990: Montreux.

85. Small, R.H., *Efficiency of direct-radiator loudspeaker systems.* Journal of the Audio Engineering Society, 1971. **19**(10): p. 862-863.

86. Small, R.H., *Direct radiator loudspeaker system analysis.* Journal of the Audio Engineering Society, 1972. **20**(5): p. 383-395.

87. Thiele, A.N., *Loudspeakers in Vented Boxes: Part I.* Journal of the Audio Engineering Society, 1971. **19**(5): p. 382-392.

88. Thiele, A.N., *Loudspeakers in vented boxes: Part II.* Journal of the Audio Engineering Society, 1971. **19**(6): p. 471-483.

89. Stepanishen, P.R., *Evaluation of mutual radiation impedances between circular pistons by impulse response and asymptotic methods.* Journal of Sound and Vibration, 1978. **59**(2): p. 221-235.

90. Stepanishen, P.R., *The impulse response and mutual radiation impedance between a circular piston and a piston of arbitrary shape.* Journal of the Acoustical Society of America, 1973. **54**(3): p. 746-754.

91. Stepanishen, P.R., *Impulse response and radiation impedance of an annular piston.* Journal of the Acoustical Society of America, 1974. **56**(2): p. 305-312.

92. Thompson, W., *The computation of self- and mutual-radiation impedances for annular and elliptical pistons using Bouwkamp's integral.* Journal of Sound and Vibration, 1971. **17**(2): p. 221-233.

93. Rife, D., *MLSSA SPO - Speaker Parameter Option Reference Manual*. 2005, DRA Laboratories.

94. Polytec, *Polytec Scanning Vibrometer PSV 400 Hardware manual*. 2003.

95. Gatti, P.L. and Ferrari, V., *Applied mechanical and structural vibrations : theory, methods, and measuring instrumentation*. 1999, london ; New York: E & FN Spon. xiv, 826 p.

96. Avitabile, P., *MODAL SPACE: What is the Difference Between all the Mode Indicator Functions? What Do They all Do?* Experimental Techniques, 2007. **31**(2): p. 15-16.

97. Leishman, T.W., *Class notes - ME562 Analysis of Acoustic Systems*. 2008, BYU. p. 4-66.

98. Bies, D.A. and Hansen, C.H., *Engineering noise control : theory and practice*. 1988, London Boston: Unwin Hyman. xvii, 414 p.

99. Fleischer, P.E. and Tow, J., *Design formulas for biquad active filters using three operational amplifiers.* Proceedings of the IEEE, 1973. **61**(5): p. 662-663.

100. Pierce, A.D., *Acoustics: an introduction to its physical principles and applications*. 1981, New York: McGraw-Hill Book Co. xxiii, 642 p.

101. Boden, H. and Abom, M., *Influence of errors on the two-microphone method for measuring acoustic properties in ducts.* Journal of the Acoustical Society of America, 1986. **79**(2): p. 541-549.